



Universidad de Guanajuato

---

Doctorado en Ciencia y Tecnología del Agua

**STUDY ON MoS<sub>2</sub> NANOSHEETS FOR DESALINATION AND  
HEAVY METALS REMOVAL FROM WATER**

**TESIS DOCTORAL**

QUE PARA OBTENER EL GRADO DE DOCTORADO EN CIENCIAS Y  
TECNOLOGÍA DEL AGUA

PRESENTA

**Qingmiao Wang**

ASESORES

**Dra. Yanmei Li**

**Dr. Shaoxian Song Hu**

PATROCINADO POR CONACyT Beca número 868976

**Guanajuato. July 2020**

---



Universidad de Guanajuato

---

Doctorado en Ciencia y Tecnología del Agua

**STUDY ON MoS<sub>2</sub> NANOSHEETS FOR DESALINATION  
AND HEAVY METALS REMOVAL FROM WATER**

**TESIS DOCTORAL**

QUE PARA OBTENER EL GRADO DE DOCTORADO EN CIENCIAS Y  
TECNOLOGÍA DEL AGUA

PRESENTA

**Qingmiao Wang**

ASESORES

**Dra. Yanmei Li**

**Dr. Shaoxian Song Hu**

**Sinodales**

**Dr. José Luis Nava Montes de Oca** \_\_\_\_\_

**Dr. José René Rangel Méndez** \_\_\_\_\_

**Dra. Mildred Quintana** \_\_\_\_\_

**Dr. Mario Alberto Corona Arroyo** \_\_\_\_\_

**Dr. Germán Cuevas Rodríguez** \_\_\_\_\_

**Guanajuato. July 2020**

---

## Acknowledgments

The financial supports of this work from the National Natural Science Foundation of China under the projects Nos. 51674183, 51974216 and 51704220, the Natural Science Foundation of Hubei Province (No. 2016CFA013), and the Research Fund Program of Key Laboratory of Rare Mineral, Ministry of Land and Resources (KLRM-KF201802), are gratefully acknowledged. I would also like to gratefully acknowledge the *Consejo Nacional de Ciencia y Tecnología de Mexico* for offering me the scholarship under the grant No. 868976 during my ph.D. studies.

I greatly appreciate my supervisors-Dra. Yanmei Li, Dr. Shaoxian Song and Dra. Feifei Jia for their plenty of care, guidance, and encouragement to me. I can't make much progress in academic research during my ph.D. studies without their valuable suggestions, supports and push. Their rigorous academic attitudes, profound academic attainments and inexhaustible kindness to others, set up a bright beacon for my whole life.

Great gratefulness also should be given to Dr. Mario Alberto Corona Arroyo, Dr. Feng Rao, Dr. Horacio Hernandez and Ms. Rong An. With their enthusiastic help, studying and living in a foreign country turn out much easier and more reassuring for me.

Also, I want to thank my friends: Xu Liao, Dante Vargas, Viridiana Piña, Changyou Wang, Dr. Cheng Liu, Hao Yi, Wei Wang, Zhili Li, Xiang Tian, Tianxing Chen, Lang Yang, Wei Ge, Kaige Sun, Chang Liu, Min Dai, Hui Liu, and so on, for their help and accompany in Mexico and China.

I really appreciate the people in Guanajuato, since I receive lots of enthusiastic help from people in this city, even though we are not familiar with each other at all.

Especially, I greatly appreciate my parents, my sisters and brothers, and especially my wife-Huiling Qin for their financial and spiritual supports, which gives me much confidence to overcome any difficulties in my study and life.

Finally, facing the COVID-19 outbreak, I greatly appreciate the medical staff, experts, and scholars and other guys from the whole world who are struggling in the frontline to fight against the epidemic. I hope we human beings can overcome the difficulties as soon as possible.

## Abstract

MoS<sub>2</sub>-based nanosheets hold great potential in some flexible and low-cost applications for the removal of heavy metal ions and desalination from water due to their excellent electrochemical activity, mechanical and thermal stability, high surface area and abundant negatively charged surfaces, etc. This work studies the properties and mechanisms of MoS<sub>2</sub> nanosheets as solar absorbers for solar desalination, as electrode materials for capacitive deionization (CDI) and as adsorbents for heavy metals removal. Meanwhile, some progress has been made to overcome the specified difficulties facing MoS<sub>2</sub> nanosheets in these applications. The details of the experimental and results are displayed below.

Three elaborate and promising designs of MoS<sub>2</sub> nanosheets as the solar absorbers for solar desalination were provided in this work:

(I) Magnetic MoS<sub>2</sub> nanosheets as recyclable photo-absorbers for high-performance solar steam generation. The magnetic MoS<sub>2</sub> nanosheets showed a superhigh solar absorption of over 96% within the whole wavelength range of 200-2500 nm. As a result, a high evaporation efficiency of up to 79.2% under the low illumination of 2.5 kW m<sup>-2</sup> was achieved. In addition, the magnetic MoS<sub>2</sub> nanosheets not only showed the long-term well dispersion in aqueous solution due to the introduction of hydrophilic PDA but also exhibited a fast and effective separation from aqueous solution with the help of the decorating nano Fe<sub>3</sub>O<sub>4</sub>, which much benefited to the continuously efficient solar steam generation and its good recyclability, respectively.

(II) Nanoscale MoS<sub>2</sub> embed in 3D double-layer structure for high-efficiency solar desalination. With low cost, facile construction pathway and good mechanical flexibility, the MPU-PPU evaporator simultaneously exhibited high evaporation efficiency of 85% under a low illumination of 1.0 kW m<sup>-2</sup> and superhigh evaporation efficiencies over 90% under higher solar illumination (1.5–2.5 kW m<sup>-2</sup>), which outperformed many other reported advanced materials for solar desalination.

(III) Facile preparation of high-quality 3D MoS<sub>2</sub> aerogel for highly efficient solar desalination. This 3D MoS<sub>2</sub> aerogel has an excellent light-absorbing efficiency of over 95% within the whole solar spectrum range, enabling the high evaporation efficiency of 88.0% under low solar irradiation of 1.0 kW m<sup>-2</sup> and superhigh evaporation efficiencies of over 90% under the slightly enhanced solar irradiation of 1.5-3.0 kW m<sup>-2</sup> as well as the remarkable desalination performance. In addition, the excellent mechanical stability of this MoS<sub>2</sub> aerogel renders it to be reused for at least 10 cycles with stable water productivity.

Despite MoS<sub>2</sub> nanosheets has already been used in CDI, their poor water wettability remained as one of the primary weaknesses for MoS<sub>2</sub> nanosheets being used in CDI. In this case, the hydrophilic MoS<sub>2</sub>/polydopamine (PDA) nanocomposites have been used as the electrode to enhance the capacitive deionization performance. Consequently, MoS<sub>2</sub> modified by PDA for 4 h (MoS<sub>2</sub>/PDA-4) could exhibit not only lower inner resistances due to its better wettability but also much higher specific capacitance because of the incorporation of electroactive PDA compared to original MoS<sub>2</sub>, resulting in the enhanced electrosorption rate (less than 9 min) and desalination capacity (14.80 mg g<sup>-1</sup>).

MoS<sub>2</sub> nanosheets were used as adsorbents to remove Cd (II) from water. The strong complexation between Cd<sup>2+</sup> and the intrinsic S planes was proposed for the high adsorption of Cd<sup>2+</sup> on MoS<sub>2</sub> nanosheets. Aiming at overcoming the difficulty of solid-liquid separation which severely restricted the practical applications of nanoscale MoS<sub>2</sub>, the mussel-inspired Fe<sub>3</sub>O<sub>4</sub>@polydopamine (PDA)-MoS<sub>2</sub> core-shell nanospheres were prepared and used as the adsorbent for the removal of Pb<sup>2+</sup> from water. As a result, the as-prepared nanocomposites not only exhibited a high adsorption capacity of Pb<sup>2+</sup> but also showed an easy and fast separation from aqueous solutions within 120 s by an external magnet as well as a facile regeneration by general acid treatment.

**Keywords:** MoS<sub>2</sub> nanosheets; Clean freshwater production; Solar desalination; Capacitive deionization; Adsorption; Working mechanisms

# CONTENTS

|  |     |
|--|-----|
| Acknowledgements.....  | I   |
| Abstract.....  | II  |
| List of Figures.....   | VII |
| List of Tables.....  | XII |
| CHAPTER I .....  | 1   |
| Introduction.....  | 1   |
| 1.1. Justification.....  | 1   |
| 1.2. Objectives.....   | 3   |
| 1.2.1. General objective.....  | 3   |
| 1.2.2. Goals.....  | 3   |
| CHAPTER II.....  | 5   |
| Antecedents.....   | 5   |
| 2.1. Species of metal ions in water and their impacts on humanity .....  | 6   |
| 2.1.1. Light metal ions and their main impacts on humanity .....   | 6   |
| 2.1.2. Heavy metal ions and their main effects on humanity .....   | 7   |
| 2.2. Technologies of water desalination and purification .....   | 8   |
| 2.2.1. Thermal-based distillation.....   | 8   |
| 2.2.2. Membrane-based technologies .....   | 9   |
| 2.2.3. Electrochemistry-based technologies.....  | 11  |
| 2.2.4. Solar-driven technologies.....  | 12  |
| 2.2.5. Solid-liquid separation technologies .....  | 13  |
| 2.3. Fundamental origins of applying MoS <sub>2</sub> for water desalination and purification.....                         | 14  |
| 2.3.1. Various structures and numerous preparation methods of MoS <sub>2</sub> .....                                       | 14  |
| 2.3.2. Main potential applications of MoS <sub>2</sub> in water desalination and purification                              | 16  |
| CHAPTER III .....  | 20  |
| Magnetic MoS <sub>2</sub> nanosheets as recyclable photo-absorbers for high-performance solar steam generation .....       | 20  |
| 3.1. Introduction .....  | 20  |
| 3.2. Experimental section.....   | 21  |
| 3.2.1. Materials .....   | 21  |
| 3.2.2. Preparation of magnetic MoS <sub>2</sub> nanosheets.....  | 21  |
| 3.2.3. Characterization methods .....  | 22  |
| 3.2.4. Solar steam generation test.....  | 22  |
| 3.3. Results and discussion. ....  | 23  |
| 3.3.1. Preparation and characterization.....   | 23  |
| 3.3.2. Evaluation of evaporation performances .....  | 27  |
| 3.3.3. Recyclability .....   | 32  |
| 3.4. Conclusions. ....   | 33  |
| CHAPTER IV.....  | 36  |
| Nanoscale MoS <sub>2</sub> nanosheets embed in 3D double layer structure (DLS) for high-efficiency solar desalination..... | 36  |
| 4.1. Introduction .....  | 36  |

|  |           |
|--|-----------|
| 4.2. Experimental sections .....   | 37        |
| 4.2.1. Materials .....   | 37        |
| 4.2.2. Fabrication of MPU-PPU evaporator .....   | 37        |
| 4.2.3. Characterization methods .....  | 39        |
| 4.2.4. Experiments of solar desalination .....   | 39        |
| 4.3. Results and discussion .....  | 40        |
| 4.3.1. Preparation and characterization .....  | 40        |
| 4.3.2. Solar desalination performance .....  | 43        |
| 4.3.3. Working mechanisms of high-efficiency solar desalination .....  | 49        |
| 4.4. Conclusions .....   | 51        |
| CHAPTER V .....  | 55        |
| <b>Facile preparation of high-quality 3D MoS<sub>2</sub> aerogel for highly efficient solar desalination ..</b>            | <b>55</b> |
| 5.1. Introduction .....  | 55        |
| 5.2. Experimental section .....  | 56        |
| 5.3. Results and Discussion .....  | 58        |
| 5.4. Conclusion .....  | 69        |
| CHAPTER VI .....   | 75        |
| <b>Hydrophilic MoS<sub>2</sub>/polydopamine nanocomposites as the electrode for enhanced capacitive deionization .....</b> | <b>75</b> |
| 6.1. Introduction .....  | 75        |
| 6.2. Experimental .....  | 76        |
| 6.2.1. Materials .....   | 76        |
| 6.2.2. Synthesis of MoS <sub>2</sub> .....   | 76        |
| 6.2.3. Synthesis of MoS <sub>2</sub> /PDA nanocomposites .....   | 77        |
| 6.2.4. Characterizations .....   | 77        |
| 6.2.5. Electrochemical measurement .....   | 78        |
| 6.2.6. CDI test .....  | 78        |
| 6.3. Results and discussion .....  | 80        |
| 6.3.1. Characterizations .....   | 80        |
| 6.3.2. CDI performance .....   | 86        |
| 6.3.3. The origins of the enhanced CDI performance .....   | 88        |
| 6.3.4. Cycling performance .....   | 90        |
| 6.4. Conclusions .....   | 92        |
| CHAPTER VII .....  | 96        |
| <b>Removal of Cd (II) from water by using nanoscale MoS<sub>2</sub> sheets as adsorbents .....</b>                         | <b>96</b> |
| 7.1. Introduction .....  | 96        |
| 7.2. Materials and methods .....   | 97        |
| 7.2.1. Materials .....   | 97        |
| 7.2.2. Methods .....   | 98        |
| 7.3. Results and discussion .....  | 99        |
| 7.3.1. Characterization .....  | 99        |
| 7.3.2. Effect of pH on cadmium ion adsorption on nano-scale molybdenum disulphide sheets .....                             | 102       |
| 7.3.3. Adsorption kinetics of cadmium on nano-scale molybdenum disulphide  |           |

|   |     |
|---|-----|
| sheets .....  | 103 |
| 7.3.4. Adsorption isotherms of cadmium ions on nano-scale molybdenum disulphide sheets.....   | 105 |
| 7.3.5. Mechanism analysis of adsorption .....   | 108 |
| 7.4. Conclusions .....  | 109 |
| CHAPTER VIII.....   | 115 |
| Mussel-inspired Fe <sub>3</sub> O <sub>4</sub> @polydopamine (PDA)- MoS <sub>2</sub> core–shell nanosphere as a promising adsorbent for removal of Pb <sup>2+</sup> from water..... | 115 |
| 8.1. Introduction .....   | 115 |
| 8.2. Materials and methods .....  | 116 |
| 8.2.1. Chemical Materials .....   | 116 |
| 8.2.2. Fabrication of Fe <sub>3</sub> O <sub>4</sub> @PDA-MoS <sub>2</sub> nanocomposites .....   | 116 |
| 8.2.3. Characterization.....  | 117 |
| 8.2.4. Batch adsorption test .....  | 118 |
| 8.2.5. Stability test of adsorbents .....   | 118 |
| 8.3. Results and discussion .....   | 119 |
| 8.3.1. Preparation and characterizations .....  | 119 |
| 8.3.2. Stability of adsorbents .....  | 123 |
| 8.3.3. Effect of solution pH .....  | 125 |
| 8.3.4. Adsorption kinetics and isotherms .....  | 126 |
| 8.3.5. Adsorption thermodynamics and mechanisms.....  | 129 |
| 8.3.6. Cyclic stability and reusability.....  | 132 |
| 8.4. Conclusions .....  | 133 |
| CHAPTER IX.....   | 138 |
| Conclusions .....   | 138 |
| Appendix.....   | 140 |
| Publications .....  | 140 |
| 1. Articles published in international journals during the Ph.D. studying .....   | 140 |
| 2. Articles to be published in international journals during the Ph.D. studying .....   | 141 |



## List of Figures

|  |    |
|--|----|
| Fig. 1.1 Structure of MoS <sub>2</sub> nanosheets.....   | 2  |
| Fig. 2.1 Map of projected physical and economic water scarcity in 2025.....  | 5  |
| Fig. 2.2 Schematics of (a) a typical MSF process, (b) a typical MSF process and (c) a typical CV process.....  | 8  |
| Fig. 2.3 Schematics of (a) Membrane osmosis desalination (FO-forward osmosis, PRO- pressure retarded osmosis and RO- reverse osmosis), (b) Membrane distillation.....  | 10 |
| Fig. 2.4. Schematics of (a) a typical ED process, (b) a typical CDI process.....   | 11 |
| Fig. 2.5 Schematics of the main two system designs for solar desalination: (a) the volumetric systems, (b) the interfacial systems .....   | 12 |
| Fig. 2.6. Schematics of (a) adsorption and (b) ion exchange.....   | 13 |
| Fig. 2.7 Potential applications of MoS <sub>2</sub> -based nanomaterials in environment-related fields .....   | 16 |
| Fig. 3.1. Schematic diagram of the experimental set-up.....  | 23 |
| Fig. 3.2 Schematic diagram of the preparation procedure of magnetic MoS <sub>2</sub> nanosheets.....   | 24 |
| Fig. 3.3 (a) XRD patterns of the pristine MoS <sub>2</sub> nanosheets, nano Fe <sub>3</sub> O <sub>4</sub> and the magnetic MoS <sub>2</sub> nanosheets. SEM images of (b) the pristine MoS <sub>2</sub> nanosheets and (c) the magnetic MoS <sub>2</sub> nanosheets. (d) EDS analysis of the magnetic MoS <sub>2</sub> nanosheets according to (c). (e) The magnetic property of nano Fe <sub>3</sub> O <sub>4</sub> and magnetic MoS <sub>2</sub> nanosheets. (f) UV–Vis–NIR absorption spectroscopy of the magnetic MoS <sub>2</sub> nanosheets.....  | 26 |
| Fig. 3.4. Stability of pristine MoS <sub>2</sub> dispersion and magnetic MoS <sub>2</sub> dispersion for different time..  | 26 |
| Fig. 3.5 (a) Mass change of water over illumination time for different concentrations of magnetic MoS <sub>2</sub> dispersions under illumination of 1.0 kW m <sup>-2</sup> , and (b) temperature variations for various magnetic MoS <sub>2</sub> dispersions with concentration of 0, 0.5, 1.0, and 2.0 g L <sup>-1</sup> under illumination of 1.0 kW m <sup>-2</sup> . (c) The corresponding evaporation rates and evaporation efficiency. (d) Mass change of water over illumination time for 1.0 g L <sup>-1</sup> magnetic MoS <sub>2</sub> dispersions under various illumination of 0, 1.0, 1.5, 2.0 and 2.5 kW m <sup>-2</sup> , and (e) temperature variations for magnetic MoS <sub>2</sub> dispersions with concentration of 1.0 g L <sup>-1</sup> under various illuminations of 0, 1.0, 1.5, 2.0 and 2.5 kW m <sup>-2</sup> . (f) The corresponding evaporation rates and evaporation efficiency..... | 29 |
| Fig. 3.6. The solar-to-heat efficiency and solar-to-steam efficiency of magnetic MoS <sub>2</sub> dispersions with various concentration under solar irradiation of 1.0 kW m <sup>-2</sup> .....   | 30 |
| Fig. 3.7. Calculating the evaporation rates of magnetic MoS <sub>2</sub> dispersions under various solar irradiation.....  | 30 |
| Fig. 3.8 (a) Concentration of magnetic MoS <sub>2</sub> dispersions as a function of the separation time by an external magnet. (b). The stable evaporation rates and evaporation efficiency of 1.0 g L <sup>-1</sup>  |    |

|   |    |
|---|----|
| magnetic MoS <sub>2</sub> nanosheets for 10 successive cycles (Each cycle: 1.0 kW m <sup>-2</sup> , 60 min illumination) .....  | 32 |
| Fig. 4.1. Optical images of PU sponge immersed in MoS <sub>2</sub> dispersions for 6 h (a) without being pressed, (b) with being repeatedly pressed for 20 times, and (c) with being repeatedly pressed for 50 times. (d) the cross-section image of (c).....   | 38 |
| Fig. 4.2. (a) Illustration of constructing the MPU-PPU evaporator with DLSs. (b) Schematic illustration of solar desalination system by MPU-PPU evaporator.....   | 41 |
| Fig. 4.3 (a) XRD spectrum and (b) SEM images of the synthesized MoS <sub>2</sub> . (c) Mass of MoS <sub>2</sub> loaded on PU over immersing time. (d) SEM images of raw PU sponge and (e) MoS <sub>2</sub> supported on PU sponge. (f) Optical image of the flexible evaporators (Layer thickness: top: 0.5 cm, bottom: 1.0 cm) .....   | 42 |
| Fig. 4.4 Optical images and SEM images of (a) raw PU, (b) MoS <sub>2</sub> supported on PU (MPU) and (c) PDA modified PU (PPU). (Diameter: 5.0 cm, thickness: 2.0 cm) .....   | 43 |
| Fig. 4.5. (a) The optic image of solar steam generation derived from MPU-PPU evaporator under illumination of 1.0 kW m <sup>-2</sup> at ~20 min. (b) Mass change over time of various evaporators under illumination of 1.0 kW m <sup>-2</sup> . (c) Evaporation rates and the corresponding evaporation efficiency of various evaporators. (d) Effect of the thickness of top MPU layer on the evaporation efficiency of MPU-PPU evaporators. (e) Evaporation rates and corresponding efficiency of under illumination of 0, 1.0, 1.5, 2.0 and 2.5 kW m <sup>-2</sup> . (f) Comparison of the ion concentrations in aqueous solutions before and after solar desalination by MPU-PPU evaporator..... | 44 |
| Fig. 4.6. Linear fitting results of the mass change curves of various evaporators under solar irradiation of 1.0 kW m <sup>-2</sup> .....   | 44 |
| Fig. 4.7. Effect of the thickness of top MPU layer inside the DLSs on their evaporation rates.....  | 46 |
| Fig. 4.8. Optical images of MPU layer with different thickness (0.2, 0.5, 1.0 and 1.5 cm) under illumination of 1.0 kW m <sup>-2</sup> .....  | 47 |
| Fig. 4.9. Mass change over time of the MPU-PPU evaporator under illuminations of 0, 1.0, 1.5, 2.0 and 2.5 kW m <sup>-2</sup> .....  | 47 |
| Fig. 4.10. Concentration of Na <sup>+</sup> and Cl <sup>-</sup> in the simulated seawater and evaporated water.....   | 48 |
| Fig. 4.11. Optical images of the top surface of MPU-PPU after 1 <sup>th</sup> , 5 <sup>th</sup> and 10 <sup>th</sup> cycles.....  | 49 |
| Fig. 4.12. (a) Solar absorption property of the synthesized nanoscale MoS <sub>2</sub> . (b) Temperature variations on the top surfaces of seawater, PU-PU, MPU-PU and MPU-PPU evaporators as a function of time under illumination of 1.0 kW m <sup>-2</sup> . (c) The thermal conductivity of the bottom layers of the evaporators. (d) Contact angles of PPU as a function of treated time in PDA solution. (e) Schematic diagram of working mechanisms of the MPU-PPU evaporator for  |    |

|  |    |
|--|----|
| solar desalination.....  | 50 |
| Fig. 5.1 Residual plot of the thermal conductivity of the 3D MoS <sub>2</sub> aerogel based on the transient plane source method.....  | 57 |
| Fig. 5.2. Schematic diagram of preparation strategy of 3D MoS <sub>2</sub> aerogels.....   | 58 |
| Fig. 5.3. SEM images of (a) single MoS <sub>2</sub> nanosheets and (b) MoS <sub>2</sub> aerogels. Optical images of MoS <sub>2</sub> -based aerogels prepared by (c) functionalized MoS <sub>2</sub> nanosheets and (d) single MoS <sub>2</sub> nanosheets after being pressed.....  | 59 |
| Fig. 5.4. The location of functionalized MoS <sub>2</sub> nanosheets in the 3D MoS <sub>2</sub> aerogels.....  | 60 |
| Fig. 5.5. N <sub>2</sub> adsorption/desorption isotherm of MoS <sub>2</sub> aerogels prepared from the functionalized MoS <sub>2</sub> nanosheets.....   | 60 |
| Fig. 5.6. (a) Compression stress-strain curves of MoS <sub>2</sub> aerogels prepared by the functionalized MoS <sub>2</sub> nanosheets. (b) FTIR spectra of chitosan, single MoS <sub>2</sub> nanosheets, functionalized MoS <sub>2</sub> nanosheets and MoS <sub>2</sub> aerogels. (c) Zeta potentials of chitosan and functionalized MoS <sub>2</sub> nanosheets. (d) Light absorption spectra of pure chitosan, single MoS <sub>2</sub> nanosheets, functionalized MoS <sub>2</sub> nanosheets and MoS <sub>2</sub> aerogels.....   | 61 |
| Fig. 5.7. Tensile stress-strain curve of the 3D MoS <sub>2</sub> aerogel.....  | 62 |
| Fig. 5.8. Zeta potentials of single MoS <sub>2</sub> nanosheets within the wide pH range of 2.0-12.0.....  | 63 |
| Fig. 5.9. Contact angle of the 3D MoS <sub>2</sub> aerogel.....  | 64 |
| Fig. 5.10. (a) Mass change of water over time under solar irradiation of 1.0 kW m <sup>-2</sup> with MoS <sub>2</sub> aerogels as solar absorbers. (b) Evaporation performance of water with the MoS <sub>2</sub> aerogels under solar irradiation of 1.0-3.0 kW m <sup>-2</sup> . (c) Desalination performance achieved by MoS <sub>2</sub> aerogels. (d) Temperature variations on the top surface of MoS <sub>2</sub> aerogels during the solar desalination (under solar irradiation of 3.0 kW m <sup>-2</sup> ), the inset image is the temperature distribution of the device during evaporation recorded by an IR camera..... | 65 |
| Fig. 5.11. Linear fitting results of the time-dependent mass change of water with the 3D MoS <sub>2</sub> aerogels and pure water under solar irradiation of 1.0 kW m <sup>-2</sup> .....  | 66 |
| Fig. 5.12. Linear fitting results of the time-dependent mass change of water with the 3D MoS <sub>2</sub> aerogels under solar irradiations of 0, 1.0, 1.5, 2.0 and 3.0 kW/m <sup>2</sup> .....  | 67 |
| Fig. 5.13. Cycling performance of MoS <sub>2</sub> aerogels under solar irradiation of 1.0 kW m <sup>-2</sup> .....  | 68 |
| Fig. 6.1. Sketch of the possible polymerization process of dopamine in this work(25°C, pH 8.5).  | 77 |
| Fig. 6.2. (a) Sketch of the self-made CDI unit. (b) Diagram of the CDI device in this work.....  | 79 |
| Fig. 6.3. The relationship between the concentration and conductivity of NaCl aqueous solution.  | 79 |
| Fig. 6.4. (a) XRD and (b) FTIR spectra of the original MoS <sub>2</sub> and various MoS <sub>2</sub> /PDA nanocomposites.....  | 81 |
| Fig. 6.5. SEM images of (a) original MoS <sub>2</sub> , (b) MoS <sub>2</sub> /PDA-2, (c) MoS <sub>2</sub> /PDA-4, (d) MoS <sub>2</sub> /PDA-12   |    |

|   |    |
|---|----|
| and (e, f) MoS <sub>2</sub> /PDA-24.....  | 81 |
| Fig. 6.6. Water contact angles of (a) original MoS <sub>2</sub> , (b) MoS <sub>2</sub> /PDA-4, (c) MoS <sub>2</sub> /PDA-12 and (d) MoS <sub>2</sub> /PDA-24.....   | 82 |
| Fig. 6.7 (a) XPS survey scans of various MoS <sub>2</sub> /PDA nanocomposites. High-resolution spectra of (b) Mo 3s, (c) C 1s and (d) N 1s of various MoS <sub>2</sub> /PDA nanocomposites.....   | 84 |
| Fig. 6.8. CV curves of (a) MoS <sub>2</sub> modified by PDA for 0, 2, 4, 8, 12, 18, 24 h at 20 mV/s, (b) original MoS <sub>2</sub> and (c) MoS <sub>2</sub> /PDA-4 with scanning rates ranging from 5 mV/s to 100mV/s. (d) Cycling performance of MoS <sub>2</sub> /PDA-4 at 20 mV/s (Inset: CV curves in 1 <sup>th</sup> , 50 <sup>th</sup> and 100 <sup>th</sup> cycles). All measurements were performed in 1.0 M NaCl solution..... | 85 |
| Fig. 6.9. (a) Electrosorption capacity of origin MoS <sub>2</sub> and MoS <sub>2</sub> /PDA-4 in 200 mg/L NaCl solution at different times. (b) Electrosorption capacity of original MoS <sub>2</sub> and MoS <sub>2</sub> /PDA-4 in NaCl solutions with various concentrations and their corresponding Langmuir fitting curves.....  | 86 |
| Fig. 6.10. (a) Specific capacitance of various MoS <sub>2</sub> /PDA nanocomposites obtained at scanning rate of 20 mV/s in 1.0 M NaCl solution. (b) Nyquist plots of various MoS <sub>2</sub> /PDA nanocomposites. (Inset: Equivalent electrical circuit) .....  | 89 |
| Fig. 6.11. Surface charge of MoS <sub>2</sub> and MoS <sub>2</sub> /PDA-4.....  | 90 |
| Fig. 6.12. (a) Cycling performances of MoS <sub>2</sub> /PDA-4 electrodes in 200 mg/L NaCl solution. (b) Dissolution results of the PDA in MoS <sub>2</sub> /PDA-4 electrodes during the continuous CDI operation.....  | 91 |
| Fig. 7.1. (a) XRD patterns and (b) Raman spectra of molybdenite before and after exfoliation...100  |    |
| Fig. 7.2. (a) TEM images of nano-scale molybdenum disulphide sheets; (b) HRTEM image of bilayer molybdenum disulphide with folded edges; (c) HRTEM image of the basal plane; (d) SAED pattern with a typical hexagonal structure of molybdenum disulphide nanosheets...101  |    |
| Fig. 7.3. AFM characterisation of molybdenum disulphide nanosheets: (a) typical AFM image of molybdenum disulphide nanosheets, (b) corresponding cross-sectional profile of the molybdenum disulphide nanosheets marked in panel (a), and (c) histogram of the thickness distribution of molybdenum disulphide nanosheets.....102   |    |
| Fig. 7.4. (a) Effect of solution pH on cadmium adsorption with nano-scale molybdenum disulphide sheets. (b) Plot of % distribution of ionic species against solution pH (20°C) ...103   |    |
| Fig. 7.5. (a) Adsorption kinetics of cadmium ions on nano-scale molybdenum disulphide sheets. (b) Intraparticle diffusion plot for the adsorption of cadmium ions onto nano-scale molybdenum disulphide sheets.....104  |    |
| Fig. 7.6. Adsorption isotherms of cadmium ions on nano-scale molybdenum disulphide sheets..106  |    |
| Fig. 7.7. XPS of nano-scale molybdenum disulphide sheets, with and without Cd <sup>2+</sup> ions loaded. (a) All surveys, with and without Cd <sup>2+</sup> loaded, (b) Cd 3d spectra, (c) S 2p spectra, (d) O 1s   |    |

|  |     |
|--|-----|
| spectra (the points are the original data, while the outermost black lines are the fitting curves).....  | 109 |
| Fig. 8.1. Optical images of Fe <sub>3</sub> O <sub>4</sub> @PDA-MoS <sub>2</sub> immersed in 10 mL, 0.01mol/L HNO <sub>3</sub> for different time.....   | 119 |
| Fig. 8.2. Schematic diagram of the fabrication of Fe <sub>3</sub> O <sub>4</sub> @PDA-MoS <sub>2</sub> nanocomposites.....   | 119 |
| Fig. 8.3. TEM images of (a, b) Fe <sub>3</sub> O <sub>4</sub> nanospheres, (c, d) Fe <sub>3</sub> O <sub>4</sub> @PDA nanospheres and (e, f) Fe <sub>3</sub> O <sub>4</sub> @PDA-MoS <sub>2</sub> nanospheres. (g) XRD spectrum of Fe <sub>3</sub> O <sub>4</sub> nanospheres, Fe <sub>3</sub> O <sub>4</sub> @PDA, pure MoS <sub>2</sub> and Fe <sub>3</sub> O <sub>4</sub> @PDA-MoS <sub>2</sub> ..... | 120 |
| Fig. 8.3 Nitrogen adsorption-desorption isotherm plot of Fe <sub>3</sub> O <sub>4</sub> , Fe <sub>3</sub> O <sub>4</sub> @PDA, pure MoS <sub>2</sub> and Fe <sub>3</sub> O <sub>4</sub> @PDA-MoS <sub>2</sub> nanospheres.....   | 121 |
| Fig. 8.4. SEM image of pure MoS <sub>2</sub> .....   | 121 |
| Fig. 8.5. Nitrogen adsorption-desorption isotherm plot of Fe <sub>3</sub> O <sub>4</sub> , Fe <sub>3</sub> O <sub>4</sub> @PDA, pure MoS <sub>2</sub> and Fe <sub>3</sub> O <sub>4</sub> @PDA-MoS <sub>2</sub> nanospheres.....  | 122 |
| Fig. 8.6. Magnetic hysteresis loop of the original Fe <sub>3</sub> O <sub>4</sub> , Fe <sub>3</sub> O <sub>4</sub> @PDA and Fe <sub>3</sub> O <sub>4</sub> @PDA-MoS <sub>2</sub> nanospheres. (Inset photographs illustrated the magnetic separability of Fe <sub>3</sub> O <sub>4</sub> @PDA-MoS <sub>2</sub> nanospheres from aqueous solution in 120 s.) .....  | 123 |
| Fig. 8.7 Stability test of Fe <sub>3</sub> O <sub>4</sub> @MoS <sub>2</sub> and Fe <sub>3</sub> O <sub>4</sub> @PDA-MoS <sub>2</sub> nanospheres in strong acid solution.....  | 124 |
| Fig. 8.8. XRD pattern of Fe <sub>3</sub> O <sub>4</sub> @MoS <sub>2</sub> .....  | 124 |
| Fig. 8.9. (a) Effect of solution pH on Pb <sup>2+</sup> adsorption with Fe <sub>3</sub> O <sub>4</sub> @PDA-MoS <sub>2</sub> nanospheres. (b) Zeta potential of Fe <sub>3</sub> O <sub>4</sub> @PDA-MoS <sub>2</sub> nanospheres.....  | 126 |
| Fig. 8.10. (a) Adsorption kinetic of Pb <sup>2+</sup> on Fe <sub>3</sub> O <sub>4</sub> @PDA-MoS <sub>2</sub> nanospheres and the fitting results, (b) Adsorption isotherm of Pb <sup>2+</sup> on Fe <sub>3</sub> O <sub>4</sub> @PDA-MoS <sub>2</sub> nanospheres and the fitting results.....  | 126 |
| Fig. 8.11. Fitting results of Langmuir-Freundlich models for Pb <sup>2+</sup> on Fe <sub>3</sub> O <sub>4</sub> @PDA-MoS <sub>2</sub> nanospheres at 293 K, 303 K and 313 K.....   | 130 |
| Fig. 8.12. Plots of ln(Q <sub>e</sub> /C <sub>e</sub> ) versus Q <sub>e</sub> at various temperatures.....   | 130 |
| Fig. 8.13. Van't Hoff plot for Pb <sup>2+</sup> on Fe <sub>3</sub> O <sub>4</sub> @PDA-MoS <sub>2</sub> nanospheres.....   | 131 |
| Fig. 8.14. Adsorption capacity of Fe <sub>3</sub> O <sub>4</sub> @PDA-MoS <sub>2</sub> nanospheres in ten cycles of regeneration.....  | 133 |

## List of Tables

|  |     |
|--|-----|
| Table 2.1 Light metal ions from various sources and their impacts on humanity.....   | 7   |
| Table 2.2 Various species of heavy metal ions and their impacts on humanity.....   | 7   |
| Table 2.3 Comparison of nanoscale MoS <sub>2</sub> with different synthesizing methods .....   | 15  |
| Table 3.1 Element ratio in magnetic MoS <sub>2</sub> nanosheets.....   | 27  |
| Table 3.2. The calculation of the thermal efficiency and the evaporation efficiency of working fluids with various concentrations under irradiation of 1.0 kW m <sup>-2</sup> .....                                  | 31  |
| Table 3.3. Comparison of various solar absorbers in the volumetric systems.....  | 31  |
| Table 4.1. Recent works of solar steam generation systems.....   | 45  |
| Table 5.1 Calculation details of the evaporation efficacies under 1.0-3.0 kW m <sup>-2</sup> .....   | 67  |
| Table 5.2 The evaporation performance of various advanced materials in recent works.....   | 67  |
| Table 6.1 Parameters of Langmuir fitting models for the electrosorption of NaCl on original MoS <sub>2</sub> and MoS <sub>2</sub> /PDA-4.....  | 87  |
| Table 6.2 Comparisons of CDI performances between the electrode materials in this work and other recently reported electrode materials.....  | 87  |
| Table 6.3. Dissolution results of the PDA in MoS <sub>2</sub> /PDA-4 electrodes during the continuous CDI operation.....   | 91  |
| Table 7.1. Kinetic parameters of cadmium ion adsorption on nanoscale MoS <sub>2</sub> sheets.....  | 104 |
| Table 7.2. Parameters of Langmuir, Freundlich, and Langmuir-Freundlich isotherm models for cadmium ion adsorption on nano-scale molybdenum disulphide sheets.....  | 106 |
| Table 7.3. Comparison of cadmium adsorption performances by various adsorbents.....  | 107 |
| Table 8.1. ICP results of Fe <sub>3</sub> O <sub>4</sub> @PDA–MoS <sub>2</sub> nanocomposites.....   | 121 |
| Table 8.2. The Fe <sup>3+</sup> /Fe <sup>2+</sup> leakage of Fe <sub>3</sub> O <sub>4</sub> @MoS <sub>2</sub> and Fe <sub>3</sub> O <sub>4</sub> @PDA-MoS <sub>2</sub> nanospheres in acid solutions (pH=1.98) ..... | 125 |
| Table 8.3. Parameters of the pseudo-first-kinetic, pseudo-second-kinetic and intraparticle diffusion models for Pb <sup>2+</sup> adsorption on Fe <sub>3</sub> O <sub>4</sub> @PDA-MoS <sub>2</sub> at 293 K.....    | 127 |
| Table 8.4. Langmuir, Freundlich and Langmuir-Freundlich isotherms parameters for Pb <sup>2+</sup> adsorption on Fe <sub>3</sub> O <sub>4</sub> @PDA-MoS <sub>2</sub> nanospheres at 293 K.....                       | 128 |
| Table 8.5. Comparison of adsorption performances of Pb <sup>2+</sup> by various adsorbents.....  | 129 |
| Table 8.6. Fitting results of Pb <sup>2+</sup> on Fe <sub>3</sub> O <sub>4</sub> @PDA-MoS <sub>2</sub> nanospheres at 293 K, 303 K and 313 K by Langmuir-Freundlich isotherm model.....                              | 130 |
| Table 8.7. Parameters of Van't Hoff plot for Pb <sup>2+</sup> on Fe <sub>3</sub> O <sub>4</sub> @PDA-MoS <sub>2</sub> nanospheres.....   | 131 |
| Table 8.8. Thermodynamic constants for the adsorption of Pb <sup>2+</sup> on Fe <sub>3</sub> O <sub>4</sub> @PDA-MoS <sub>2</sub> nanospheres.....   | 132 |

# CHAPTER I

## Introduction

### 1.1. Justification

Freshwater shortage is the main aspect of freshwater-related problems faced by human society, which will be a long-term and worldwide social problem in the 21st century. Although almost 70% of the earth surface is covered by water, only 2.5% of that water is freshwater and only 0.3% of freshwater is easily accessible to human beings [1]. By 2025, two-thirds of the world's population may face water shortages [2]. Freshwater shortage severely restricts the sustainable development of economy and society since clean water is at the heart of social, economic and environmental growth [3]. Recovering freshwater from undrinkable water bodies such as oceans and brackish waters by means of desalination has been widely regarded as the effective solution to alternative the freshwater shortage [4].

Water pollution derived from heavy metals is another serious problem of the freshwater resources. With the fast development of metallurgy, mining, nuclear energy and chemical manufacturing in recent decades, a large number of heavy metal ions ( $\text{Pb}^{2+}$ ,  $\text{Cd}^{2+}$ ,  $\text{Hg}^{2+}$ ,  $\text{Ag}^+$ , etc.) have been released into the natural environment, posing a serious threat to surface water and groundwater. Due to the continuous accumulation, high toxicity and strong permeability, heavy metal ions in water are easily accumulated in living organisms, causing long-term damage to humans and other animals. Thus, it is of great significance to remove heavy metals from water.

In the past two decades, nanomaterials have attracted extensive researches in providing new solutions or enhancing existing solutions to remove heavy metals and salts from water. In particular, two-dimensional (2D) graphene-based nanomaterials have been widely studied in adsorptive removal of heavy metals [5], photocatalytic reduction of heavy metals (for example, from  $\text{Cr}^{6+}$  with high toxicity to  $\text{Cr}^{3+}$  with few toxicity and easy par) [6], electrosorption and membrane-based separation of salt ions [7,8], due to their high specific surface area and intriguing properties that are typically unavailable in their bulk forms.

Recently, with the intrinsic graphene-like architecture, molybdenum disulfide ( $\text{MoS}_2$ ) nanosheets have also received increasing attention in recent years. The monolayer of  $\text{MoS}_2$  consists of a molybdenum (Mo) atom layer sandwiched between two sulfur (S) atom layers, and the interlayer spacing of  $\text{MoS}_2$  monolayers is 0.62 nm with a free spacing of 0.30 nm (Fig. 1.1).

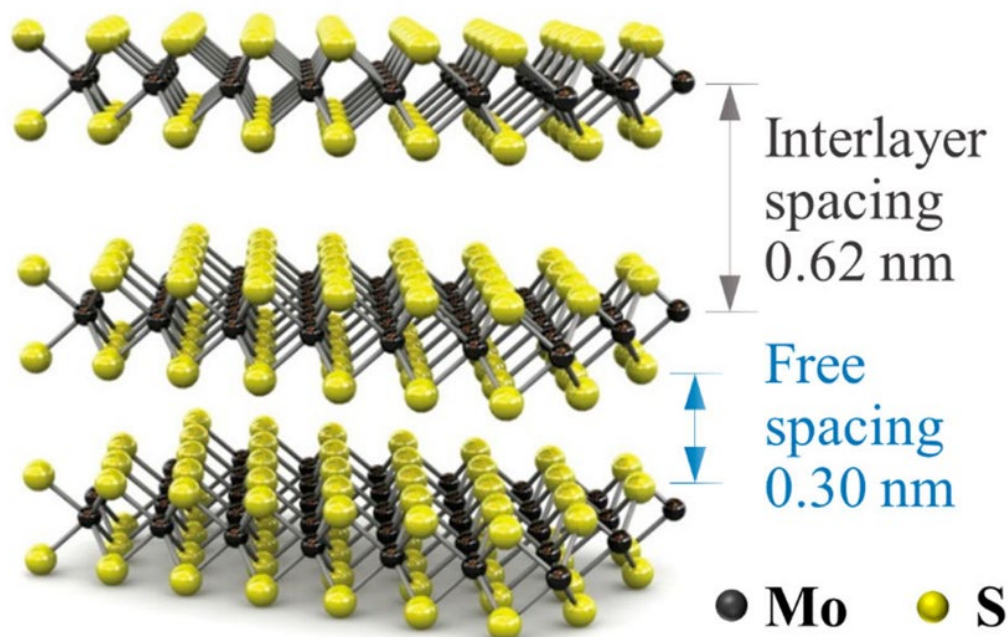


Fig. 1.1 Structure of MoS<sub>2</sub> nanosheets. (Source [9])

Due to the unique structures and distinct electrical, physicochemical and mechanical properties, MoS<sub>2</sub> nanosheets are expected to have promising applications in providing new solutions or enhancing existing solutions to solve a series of pressing environmental problems from water shortage to water pollution. For instance, the direct and narrow bandgaps (1.89 eV) of MoS<sub>2</sub> nanosheets contribute to the easy separation and migration of carriers at the interfaces, guaranteeing its excellent absorbance of ultra-violet lights (UV, wavelengths < 200 nm) and visible lights (Vis, wavelengths: 200-660 nm) and laying foundation for its excellent photothermal conversion property. Therefore, MoS<sub>2</sub> nanosheets hold great potential as the photo-absorber in the novel application of solar desalination. The abundant negative charges on the surface of MoS<sub>2</sub> nanosheets can significantly contribute to the ion intercalation/transportation and electrostatic attraction of ions, rendering MoS<sub>2</sub> nanosheets a promising electrode material for capacitive deionization (CDI) [10]. Given the abundance of exposed sulfur atoms on its surface, MoS<sub>2</sub> nanosheets could sever as an efficient adsorbent for the removal of heavy metal ions due to the strong Lewis acid and base soft-soft interactions between heavy metals and sulfur atoms [9].

However, some inherent properties of MoS<sub>2</sub> nanosheets also severely restrict their practical applications in the aforementioned fields. For instance, when served as



the adsorbents for removing pollutants from water, the used MoS<sub>2</sub> nanosheets usually suffer from the difficulty of uneasy separation because of their extremely tiny sizes, thus resulting in high material consumption and secondary environment pollutions. When used as the electrodes in CDI, the inherent poor water wettability of MoS<sub>2</sub> nanosheets is detrimental to the access of electrolyte to its surfaces. This will lead to not only the high transfer resistance at the solid-liquid interfaces but also the inefficient utilization of the electrochemical surfaces of MoS<sub>2</sub> nanosheets, severely limiting their CDI performance. In solar desalination, the difficulty of MoS<sub>2</sub> nanosheets is mainly attributed to the fact that single MoS<sub>2</sub> nanosheets are usually free or lack of strong connecting/bonding sites-the functional groups which however play the critical role in constructing the high-quality evaporation system.

Therefore, it is of great significance to conduct in-depth study of MoS<sub>2</sub> nanosheets in removal of heavy metals and water desalination, which might provide one promising solution to the problem of freshwater resource.

## **1.2. Objectives**

### **1.2.1. General objective**

To conduct the in-depth study of MoS<sub>2</sub> nanosheets for desalination and heavy metals removal from water, and to solve the problems facing MoS<sub>2</sub> nanosheets in these applications, and finally to approach into their working mechanisms.

### **1.2.2. Goals**

- (1) To investigate the magnetic MoS<sub>2</sub> nanosheets as recyclable photo-absorbers for high-performance solar steam generation.
- (2) To investigate the MoS<sub>2</sub> nanosheets @sponge with double layer structure for high-efficiency solar desalination.
- (3) To investigate the facile preparation of high-quality 3D MoS<sub>2</sub> aerogel for highly efficient solar desalination.
- (4) To investigate the hydrophilic MoS<sub>2</sub>/polydopamine nanocomposites as the electrode for enhanced capacitive deionization
- (5) To investigate the removal performances and mechanisms of cadmium ions (Cd<sup>2+</sup>) from water by using MoS<sub>2</sub> nanosheets as the absorbents.
- (6) To investigate the removal performances and mechanisms of lead ions (Pb<sup>2+</sup>) from water by using MoS<sub>2</sub> nanosheet-based nanocomposites as the absorbents with easy separation and excellent recyclability.

**REFERENCES**

- [1] United Nations Environment Programme, Water Distribution on Earth, (2013) 0–1. <https://www.nationalgeographic.org/media/water-distribution-earth/>.
- [2] J. Eliasson, The rising pressure of global water shortages, *Nature*. 517 (2015) 6. doi:10.1038/517006a.
- [3] J. Leijon, C. Boström, Freshwater production from the motion of ocean waves – A review, *Desalination*. 435 (2018) 161–171. doi:10.1016/j.desal.2017.10.049.
- [4] M. Baghbanzadeh, D. Rana, C.Q. Lan, T. Matsuura, Zero thermal input membrane distillation, a zero-waste and sustainable solution for freshwater shortage, *Applied Energy*. 187 (2017) 910–928. doi:10.1016/j.apenergy.2016.10.142.
- [5] W. Peng, H. Li, Y. Liu, S. Song, A review on heavy metal ions adsorption from water by graphene oxide and its composites, *Journal of Molecular Liquids*. 230 (2017) 496–504. doi:10.1016/j.molliq.2017.01.064.
- [6] Y. Li, W. Cui, L. Liu, R. Zong, W. Yao, Y. Liang, Y. Zhu, Removal of Cr(VI) by 3D TiO<sub>2</sub>-graphene hydrogel via adsorption enriched with photocatalytic reduction, *Applied Catalysis B: Environmental*. 199 (2016) 412–423. doi:10.1016/j.apcatb.2016.06.053.
- [7] P. Liu, T. Yan, L. Shi, H.S. Park, X. Chen, Z. Zhao, D. Zhang, Graphene-based materials for capacitive deionization, *Journal of Materials Chemistry A*. 5 (2017) 13907–13943. doi:10.1039/C7TA02653F.
- [8] N. Song, X. Gao, Z. Ma, X. Wang, Y. Wei, C. Gao, A review of graphene-based separation membrane: Materials, characteristics, preparation and applications, *Desalination*. 437 (2018) 59–72. doi:10.1016/j.desal.2018.02.024.
- [9] Z. Wang, B. Mi, Environmental Applications of 2D Molybdenum Disulfide (MoS<sub>2</sub>) Nanosheets, *Environmental Science and Technology*. 51 (2017) 8229–8244. doi:10.1021/acs.est.7b01466.
- [10] F. Xing, T. Li, J. Li, H. Zhu, N. Wang, X. Cao, Chemically exfoliated MoS<sub>2</sub> for capacitive deionization of saline water, *Nano Energy*. 31 (2017) 590–595. doi:10.1016/j.nanoen.2016.12.012.

## CHAPTER II

### Antecedents

The lack of access to freshwater can reduce basic quality of living and restrict regional economic development, thus having major impacts on people's well-being. To deal with the freshwater scarcity, numerous technologies have been developed to produce clean water from seawater/brackish water or polluted water. Among these technologies, the multiple stage flash (MSF), multiple effect distillation (MED) and reverse osmosis (RO) are the most generally used, which however mainly applied in developed countries and areas due to their requirements of large-scale infrastructure construction and high operation cost (high temperature and high pressure) [1].

Unfortunately, about four billion people, or two-thirds of the world's population, face severe water shortages at least 1 month of the year, especially in remote and underdeveloped areas (Fig. 2.1), far more than was previously thought, according to reported results of Professor Arjen Y. Hoekstra [2] and the international water management institute (IWMI).

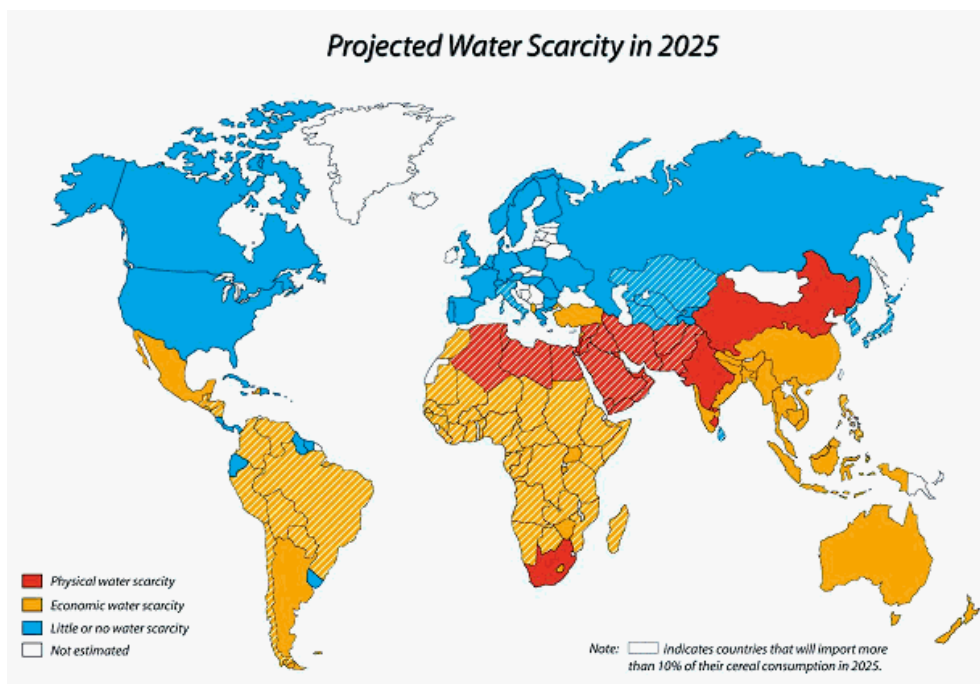


Fig. 2.1. Map of projected physical and economic water scarcity in 2025. (Source: IWMI, 2000)

In this case, some flexible and low-cost technologies, such as capacitive deionization (CDI), solid-liquid separation and solar desalination, etc., have recently become hot spots for water desalination and purification aiming to relieve the terrible

water scarcity especially in these aforementioned areas. Note that the performances of these flexible and low-cost methods for water desalination and purification highly rely on the species and the property of materials used in their systems. For instance, the electrodes used in CDI devices usually are carbon-based and metal oxide-based materials, which typically possess high specific capacitance. Adsorbents used in solid-liquid extraction processes usually are clay-based, metal oxide-based and carbon-base materials, which generally possess high specific areas and porous structures or charged surfaces. Solar absorbers used in solar desalination usually are carbon-based and plasma metal-based materials, which generally hold the property of high light-absorbing and solar-to-heat conversion capacity.

## **2.1. Species of metal ions in water and their impacts on humanity**

Generally, the species of metal ions in water can be divided into (1) light metal ions (such as  $K^+$ ,  $Na^+$ ,  $Mg^{2+}$ ,  $Ca^{2+}$  and  $Al^{3+}$  etc.) with density  $< 4.5 \text{ g cm}^{-3}$  and (2) heavy metal ions (typically  $Hg^{2+}$ ,  $Pb^{2+}$ ,  $Cd^{2+}$ ,  $Cu^{2+}$ ,  $As^{+3}$  and  $Cr^{5+}$  etc.) with density  $> 4.5 \text{ g cm}^{-3}$ . Both light metal ions and heavy metal ions have significant effects on human beings and other creatures, suggesting the necessity of their removals from some specified water systems. In many academic researches, the removal of light metal ions from water is often called as water desalination, while the removal of heavy metal ions from water is generally named as water purification.

### **2.1.1. Light metal ions and their main impacts on humanity**

Several light metal ions, such as  $K^+$ ,  $Na^+$ ,  $Ca^{2+}$ , etc., are the necessary nutrients required by the human body and other creatures. However, water systems contain high concentration of light metal ions, such as the seawater (mainly  $Na^+$ ,  $K^+$ ,  $Ca^{2+}$ ,  $Mg^{2+}$  and  $Sr^{2+}$ , etc.), brackish water (mainly  $Mg^{2+}$  and  $Ca^{2+}$ , etc.) and some industry wastewater (eg: biopharmaceutical wastewater, mainly  $Ca^{2+}$ ,  $Mg^{2+}$ ,  $K^+$  and  $Na^+$ ), have some great and objectionable impacts on humanity and other creatures as shown in Table 2.1. Although light metal ions in water with high concentration generally cannot do severe damage to human body and other organisms, they do have some unwanted and indirection impacts on the life and the production of human beings. In this case, water desalination is of great significance for the current society to improve the levels of production and living.

Table 2.1. Light metal ions from various sources and their impacts on humanity

| Sources                         | Main species   | Main impacts on humanity   |
|---------------------------------|--|--|
| Seawater                        | Na <sup>+</sup> , K <sup>+</sup> , Ca <sup>2+</sup> ,<br>Mg <sup>2+</sup> , Sr <sup>2+</sup> | Cannot be directly used by human beings,<br>plants and other animals.  |
| Brackish water                  | Ca <sup>2+</sup> , Mg <sup>2+</sup>  | Bitter taste, difficult to drink directly,<br>long-term drinking causes gastrointestinal<br>disorders and low immunity |
| Biopharmaceutical<br>wastewater | Ca <sup>2+</sup> , Mg <sup>2+</sup> , K <sup>+</sup> ,<br>Na <sup>+</sup>                    | Often cause water loss and eventually kill<br>the cells during the biochemical treatment<br>of discharges              |

### 2.1.2. Heavy metal ions and their main effects on humanity

Water systems containing heavy metal ions, such as the electroplating wastewater (mainly Cd<sup>2+</sup>, Cr<sup>3+</sup>/Cr<sup>6+</sup>, Cu<sup>2+</sup> etc.) and the mining drainages (mainly As<sup>3+</sup>, Pb<sup>2+</sup>, etc.), can do direct and great damage to the bodies of human and other animals because of their significant toxic effects (as shown in Table 2.2) [3,4]. Therefore, it is necessary to treat wastewaters containing heavy metal ions prior to their discharge to the environment.

Table 2.2. Various species of heavy metal ions and their impacts on humanity

| Species                               | Main sources  | Main impacts on humanity  |
|---------------------------------------|---|---|
| Hg <sup>2+</sup>                      | Electric/light bulb, wood preservatives,<br>leather tanning, ointments, thermometers,<br>adhesives and paints                 | Rheumatoid arthritis, and<br>diseases of the kidneys,<br>circulatory system and nervous<br>system |
| Pb <sup>2+</sup>                      | Petrol based materials, pesticides, leaded<br>gasoline, and mobile batteries  | Damage the fetal brain,<br>diseases of the kidneys,<br>circulatory system and nervous<br>system   |
| Cd <sup>2+</sup>                      | Refined petroleum products, paint pigments,<br>pesticides, galvanized<br>pipes, plastics, polyvinyl and copper<br>refineries. | Kidney damage, renal disorder,<br>human carcinogen  |
| Cr <sup>3+</sup><br>/Cr <sup>6+</sup> | Chrome plating, petroleum refining,<br>electroplating industry, leather, tanning,   | Headache, diarrhea, nausea,<br>vomiting, carcinogen   |

|                                       |   |  |
|---------------------------------------|---|--|
|                                       | textile manufacturing and pulp processing units.  |  |
| $\text{Cu}^{2+}$                      | Electroplating industry, metal refining and industrial emissions  | Liver damage, Wilson disease, insomnia                         |
| $\text{Ni}^{+2}$                      | Galvanization, paint and powder, batteries processing units, metal refining and super phosphate fertilizers | Dermatitis, nausea, chronic asthma, coughing, human carcinogen |
| $\text{As}^{+3}$<br>$/\text{As}^{+5}$ | Automobile exhaust/industrial dust, wood preservatives and dyes   | Skin manifestations, visceral cancers, vascular disease        |

## 2.2. Technologies of water desalination and purification

### 2.2.1. Thermal-based distillation

The thermal-based distillation technology mainly consists of multiple stage flash (MSF), multi effect distillation (MED) and vapor compression (VC), of which their schematics are shown in Fig. 2.2.

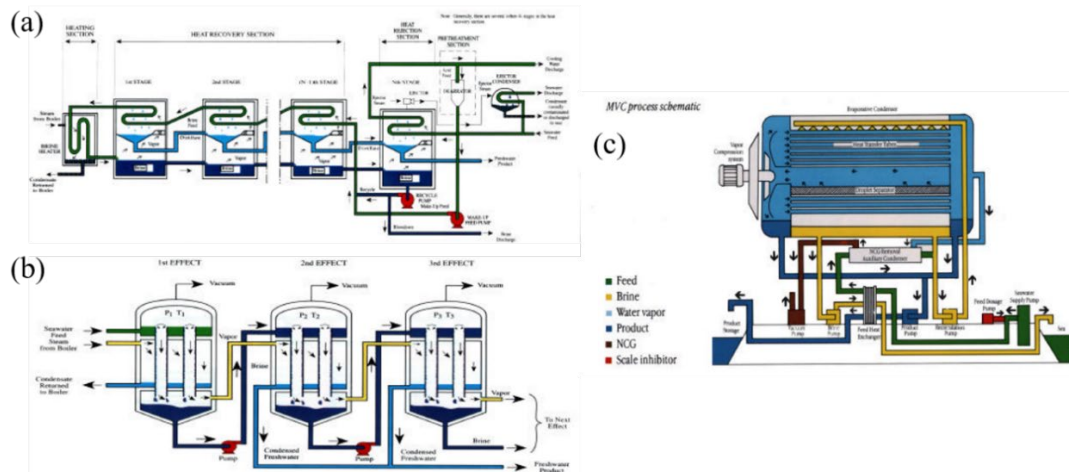


Fig. 2.2. Schematics of (a) a typical MSF process, (b) a typical MED process and (c) a typical VC process. (Source: [5])

The MSF produces pure water by boiling and then condensing saline water. In MSF, the saline feedwater first passes through a series of tubes. This essentially preheats the water before entering the brine heater. It is then heated in the brine heater

using any given form of thermal energy. The heated water is then introduced into a vessel (called stage) where the ambient pressure is lower than the brine heater. This low pressure results in sudden boiling (flashing) of the saline water. The vapors, formed during the boiling, condense on the tubes carrying input saline water and the distillate is collected. Only a small percentage of the heated water is converted into steam depending upon the pressure maintained at each stage. The remaining water is then introduced to the next stage with an even lower pressure, and the process continues until the saline water (now brine) is cooled down and discharged. MSF plants may contain between 4 and 40 stages, but usually they comprise of 18 to 25 stages.

The MED process uses the steam produced by a boiler to successively heat feed water in a series of steps, which are called ‘effects’ [Halcrow Water Services]. Similar to the MSF process described above, each successive effect operates at a lower temperature and pressure to cause further vaporization, and a portion of the feed water vaporizes in each effect while the remainder goes to the next effect. The formation of process residues is, just as in the MSF case, an issue to be avoided or minimized, and the operation of MED plants require ongoing technical and operational capacity. MED plants also require a source of dependable heat, which can be provided by solar and/or fossil fuels, or the use of industrial waste heat.

In the MSF and MED processes, the energy input to drive the distillation was accomplished by simply heating one end of the plant and cooling the other, whereas in the VC process this input is accomplished by using a heat pump to upgrade the low-temperature energy rejected from the distiller and to recycle it back to the hot end as the energy input. The heat pump may take the form of either a mechanical compressor (see Fig. 2.2 (c)) or a thermo-compressor.

These thermal processes are mature and widely used, but meanwhile they often suffer from the high energy consuming, and now desalination plants around the world pay more attention to membrane-based technologies for water desalination.

### **2.2.2. Membrane-based technologies**

Membrane-based water desalination technologies generally involve membrane osmosis desalination (mainly including the forward osmosis-FO, pressure delayed osmosis-PRO and reverse osmosis-RO) and membrane distillation (MD) (see Fig. 2.3). RO is a separation process that uses pressure to force a solution through a membrane that retains the solute on one side and allows the pure solvent to pass to the other side.

The membrane here is semipermeable, meaning it allows the passage of solvent but not for metals. The membranes used for RO have a dense barrier layer in the polymer matrix where most separation occurs. Reverse osmosis can remove many types of molecules and ions from solutions, including bacteria, and is used in both industrial processes. RO involves a diffusive mechanism, so that separation efficiency is dependent on solute concentration, pressure and water flux rat. In the FO process, instead of using hydraulic pressure, as in conventional RO desalination processes, a concentrated draw solution is used to generate high osmotic pressure, which pulls the water across a semipermeable membrane from the feed solution (McCutcheon et al., 2005). The draw solutes are then separated from the diluted draw solution to recycle the solutes and to produce a final product water. PRO, a variation of FO, can produce salinity gradient (blue) energy from a feed and draw solution with an osmotic-pressure gradient, with pressure created by flow of freshwater into saltwater.

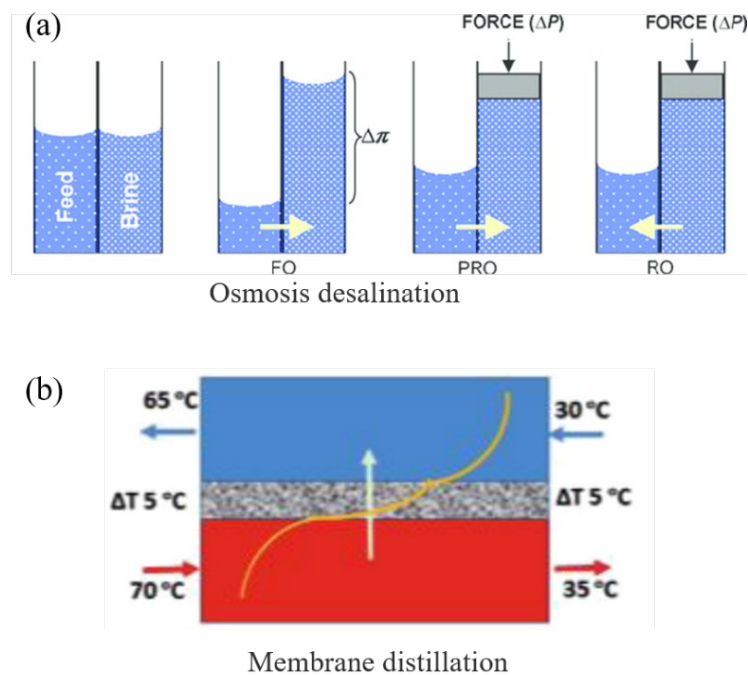


Fig. 2.3. Schematics of (a) Membrane osmosis desalination (FO-forward osmosis, PRO- pressure retarded osmosis and RO- reverse osmosis) (Source:[6] ), (b) Membrane distillation. (Source: [7])

MD is a membrane process, driven by a thermal (temperature) gradient, with water vapor transported across a hydrophobic microporous membrane using a significantly lower temperature than conventional distillation at very low operating pressures (nearly 1 bar). MD requires energy input in two forms: thermal (to drive the separation process) and electrical (to move feed, product, and brine flows).



### 2.2.3. Electrochemistry-based technologies

As displayed in Fig. 2.4(a), electrodialysis (ED) is a membrane separation in which ionized species in the solution are passed through an ion exchange membrane by applying an electric potential. The membranes are thin sheets of plastic materials with either anionic or cationic characteristics. When a solution containing ionic species passes through the cell compartments, the anions migrate toward the anode and the cations toward the cathode, crossing the anion exchange and cation-exchange membranes.

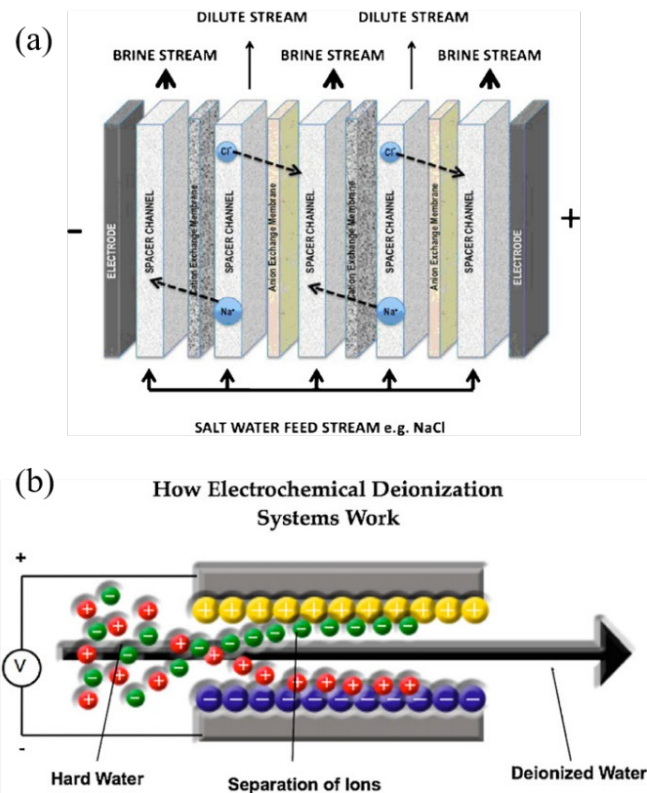


Fig. 2.4. Schematics of (a) a typical ED process, (b) a typical CDI process. (Source: [8])

CDI (Fig. 2.4(b)) has very low energy consumption at low salinity, is easy to operate and is low maintenance. With a low direct voltage (0.8-1.2 V) loaded in a typical CDI process, salt ions in aqueous solution will be transferred into electric double layers (EDLs) at electrode/solution interfaces by electrostatic forces, subsequently stored inside the EDLs, resulting in the desalinated water in the CDI cell. If the electric field is removed, the trapped ions are released back into the aqueous solution, revealing the recoverability and low-cost property of CDI techniques. One of the drawbacks limiting the charge efficiency in CDI is co-ion adsorption, i.e., the adsorption of ions to an electrode carrying the same surface charge.

### 2.2.4. Solar-driven technologies

Solar-driven water evaporation, which utilizes sunlight as a renewable energy source, is an emerging and promising approach to provide solutions for clean water scarcity with minimum environmental impact. According to where the solar absorber materials are placed in the liquid media, the evaporation systems of solar-driven technologies can be classified into two categories (see Fig. 2.5): (1) the volumetric system and (2) the interfacial system.

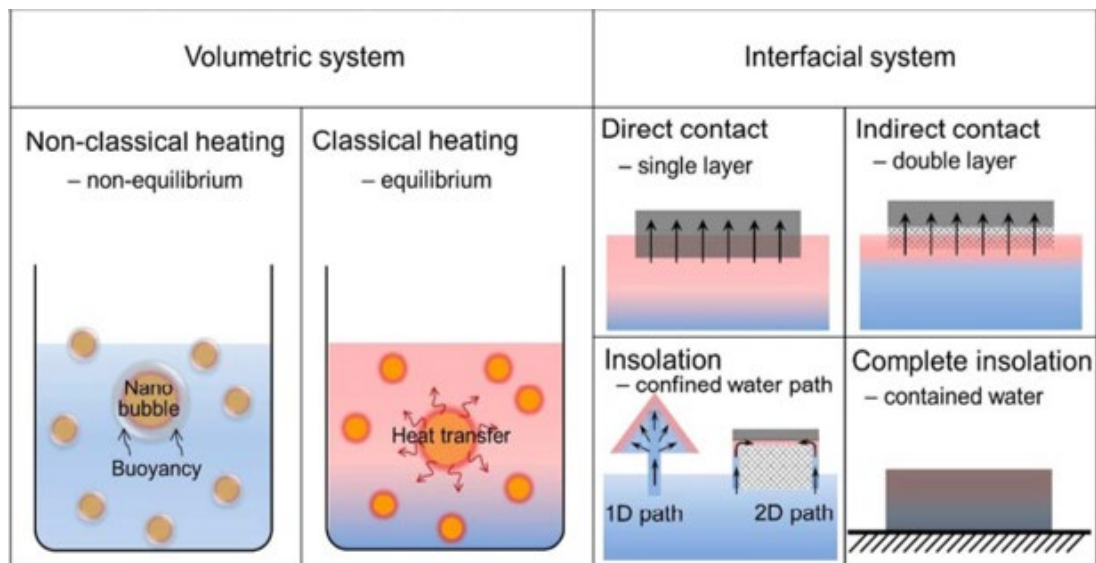


Fig. 2.5. Schematics of the main two system designs for solar desalination: (a) the volumetric systems, (b) the interfacial systems. (Source: [9])

A volumetric system is a straightforward steam generation route via direct nanostructure solar energy absorption. Volumetric absorbers can have surface temperatures lower than the bulk fluid temperature, which explicitly reduces significant heat losses to the surrounding media. The steam generation mechanism is still in dispute for volumetric systems. Two plausible mechanisms including the non-classical heat transfer (non-equilibrium heating) and the classical heat transfer (equilibrium heating) have been proposed to explain the vapor generation phenomenon.

Generally speaking, the volumetric systems show a relatively low steam generation efficiency because the bulk working liquid is inevitably heated up too. This makes it susceptible to radiation, conduction and convection heat losses, and also unnecessary heating of the bulk water that does not participate in steam generation yet consumes considerable energy. To minimize the superfluous energy losses and

improve the energy conversion efficiency, interfacial solar steam generation strategy has recently been losses at the absorber surface; secondly, the temperature of the bulk liquid remains close to the ambient temperature, minimizing heat loss and parasitic use of the converted thermal energy to heat up bulk water. In terms of the relative location of solar absorber to water surface, the interfacial systems can be classified in (a) direct contact configuration, (b) indirect contact configuration and (c) Isolation configuration.

### 2.2.5. Solid-liquid separation technologies

An adsorption process (see Fig. 2.6 (a)) is the transfer of ions from solution phase to the solid phase, actually describes a group of processes, which includes adsorption and precipitation reactions. A stable adsorption process is usually a dynamic equilibrium of adsorbates on the absorbents between the absorption and desorption. Basically, adsorption is a mass transfer process and substances bound by physical and or chemical interactions to solid surface. Various low-cost adsorbents, derived from agricultural waste, industrial by-product, natural material, or modified biopolymers, have been recently developed and applied for the removal of heavy metal ions or organic pollutants for water treatment. This approach has been widely considered as one of the alternative treatment techniques for wastewater because of its low cost, effective treatment and easy operation, etc.

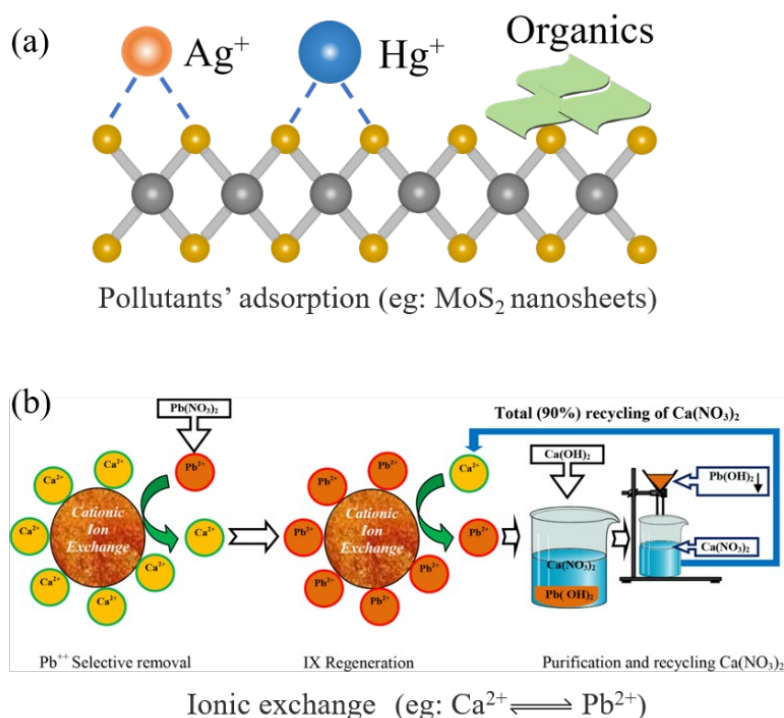


Fig. 2.6. Schematics of (a) adsorption and (b) ion exchange (Source: [10]).

Ion exchange (see Fig. 2.6 (b)) can attract soluble ions from the liquid phase to the solid phase, which is the most widely used method in water treatment industry. As a cost-effective method, ion exchange process normally involves low-cost materials and convenient operations, and it has been proved to be very effective for removing heavy metals from aqueous solutions, particular for treating water with low concentration of heavy metals [29, 30]. In this process cations or anions containing special ion exchanger is used to remove metal ions in the solution. Commonly used ion exchangers are synthetic organic ion exchange resins. It can be used only low concentrated metal solution and this method is highly sensitive with the pH of the aqueous phase. Ion exchange resins are the most used materials in ionic exchange for water desalination and purification.

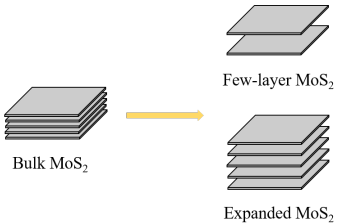
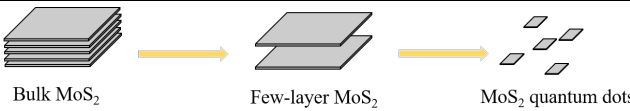
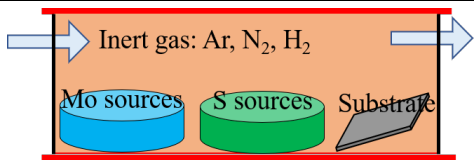
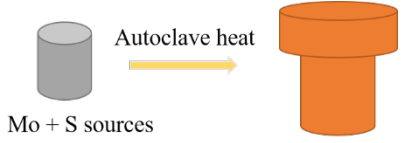
## **2.3. Fundamental origins of applying MoS<sub>2</sub> for water desalination and purification**

### **2.3.1. Various structures and numerous preparation methods of MoS<sub>2</sub>**

Till now, numerous methods have been developed to synthesize monolayer and few-layer MoS<sub>2</sub> materials to suit different applications. These synthesis methods can be categorized into two general types: (I) the top-down method, which mechanically, ultrasonically, or chemically exfoliates bulk materials by overcoming the weak interlayer Van der Waals force and (II) the bottom-up method, which assembles MoS<sub>2</sub> nanosheets using individual atoms. Some typical and representative methods are discussed as follows and summarized in Table 2.3. General speaking, top-down methods can only produce single or few-layer MoS<sub>2</sub> nanosheets while bottom-top methods can synthesize MoS<sub>2</sub> with various different architectures by controlling the reaction conditions. In addition, the morphology and structures of various MoS<sub>2</sub> can be tailored by their preparation methods, resulting in the as-prepared MoS<sub>2</sub> possessing different physical and chemical properties, further leading to the wide applications of MoS<sub>2</sub> in various fields.

As conclusions, MoS<sub>2</sub>-based nanomaterials take the great advantage in easy preparation and multiple property, thus show the promising application in removing heavy metals and desalination from water.

Table 2.3. Comparison of nanoscale MoS<sub>2</sub> with different synthesizing methods.

| Category  | Methods                   | General morphology   | Primary applications  | Refs   |         |
|-----------|---------------------------|--|---|--|---------|
| Top-down  | Mechanical exfoliation    |  <p>Bulk MoS<sub>2</sub> → Few-layer MoS<sub>2</sub> → Expanded MoS<sub>2</sub></p>        | Fundamental study and device performance demonstration                  | [11,12]  |         |
|           | Liquid exfoliation        |  | Electronic devices; Energy storages                                     | [13]   |         |
|           | Chemical exfoliation      |  | Hydrogen evolution reaction; Membranes                                  | [14,15]  |         |
|           | Multi-exfoliation         |  <p>Bulk MoS<sub>2</sub> → Few-layer MoS<sub>2</sub> → MoS<sub>2</sub> quantum dots</p>    | Monolayer nanosheets with lateral sizes < 10 nm                         | Energy transfer                                  | [16]    |
| Bottom-up | Chemical vapor deposition |  <p>Inert gas: Ar, N<sub>2</sub>, H<sub>2</sub></p> <p>Mo sources S sources Substrate</p> | Monolayer nanosheets with lateral size of several micrometers           | Optoelectronics; Electronics; Sensors; Catalysis | [17,18] |
|           | Solvothermal reactions    |  <p>Mo + S sources → Autoclave heat</p>  | Hierarchical hollow MoS <sub>2</sub> nanoparticles                      | Energy storage                                   | [19]    |
|           |                           |  | 3D flower-like MoS <sub>2</sub> with diameter of hundreds of nanometers | Catalysis; Environmental adsorbents              | [20,21] |

### 2.3.2. Main potential applications of MoS<sub>2</sub> in water desalination and purification

Due to their significantly different electrical, physicochemical, biological, and mechanical properties, etc., MoS<sub>2</sub>-based nanomaterials have recently attracted great attention in many fields, such as electronics [17], catalysis [18], biomedical [22], and energy-related fields [19]. MoS<sub>2</sub>-based nanomaterials can be also expected to have novel applications in the environmental fields because of their various excellent properties as displayed in Fig. 2.6. For example, because of its fluorescence quenching ability and mechanical stability, MoS<sub>2</sub> nanosheets can serve as the detection of biomolecules and metal ion contaminants. Due to their photocatalytic properties in semiconducting phase and antibacterial property, the metallic (conductive 1T-phase) MoS<sub>2</sub> nanosheets have shown antibacterial property in a three-step mechanism, including direct bacterium-MoS<sub>2</sub> contact, membrane damage by sharp MoS<sub>2</sub> edges, and disruption of microbial processes in redox reactions.

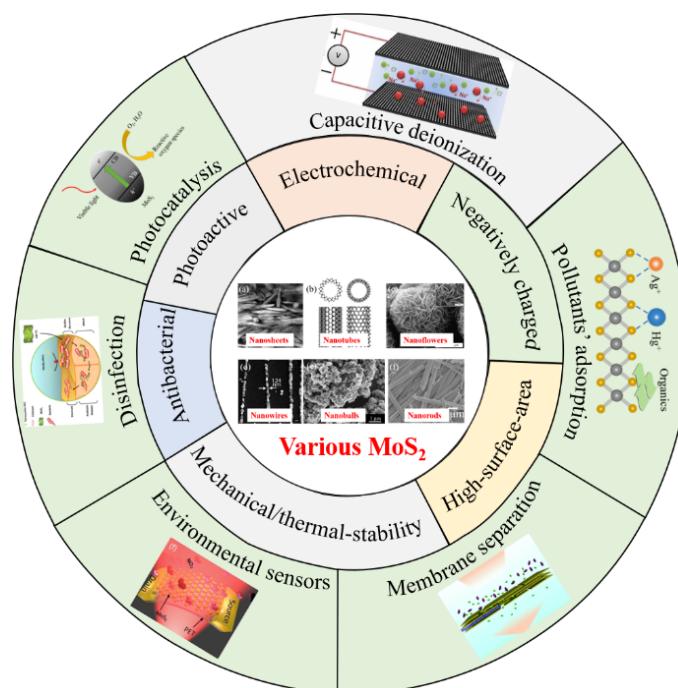


Fig. 2.7. Potential applications of MoS<sub>2</sub>-based nanomaterials in environment-related fields.

Particularly, MoS<sub>2</sub>-based nanomaterials also hold the promising application in water desalination and purification because of some specified properties. For instance, MoS<sub>2</sub> can be applied as an electrode material for capacitive deionization due to its ideal platform and outstanding electrochemical property as aforementioned in Fig. 2.6. Given the abundance of negatively charged surfaces (namely, the exposed sulfur atoms on its surface), MoS<sub>2</sub> can work as an efficient adsorbent for the removal of

heavy metal ions (e.g.,  $\text{Hg}^{2+}$  and  $\text{Ag}^+$ ) due to the strong Lewis acid and base soft-soft interactions. However, each coin has two sides. It should also be pointed out that some unwanted properties of  $\text{MoS}_2$  can have great influences on the applications of other properties. Namely, much progress still should be made during the applications of  $\text{MoS}_2$  in water desalination and purification.

Herein, this work focuses on further developing the potential of  $\text{MoS}_2$  nanomaterials and provides some improvements in the following applications: (1) Providing three promising designs of applying  $\text{MoS}_2$  as the solar absorbers for solar desalination: (a) Magnetic  $\text{MoS}_2$  nanosheets as recyclable photo-absorbers for high-performance solar steam generation; (b) Nanoscale  $\text{MoS}_2$  embed in 3D double layer structure for high-efficiency solar desalination, and (c) Facile preparation of high-quality 3D  $\text{MoS}_2$  aerogel for highly efficient solar desalination. (2) Due to the unwanted poor water wettability which still remained one of the primary weaknesses facing  $\text{MoS}_2$  for its CDI application, the hydrophilic  $\text{MoS}_2$ /polydopamine (PDA) nanocomposites have been used as the electrode for enhanced capacitive deionization. (3) Developing the removal of Cd (II) from water by using nano-scale  $\text{MoS}_2$  sheets as adsorbents, and then displaying the improvement by using the mussel-inspired  $\text{Fe}_3\text{O}_4$ @polydopamine (PDA)- $\text{MoS}_2$  core-shell nanosphere as a promising adsorbent for removal of  $\text{Pb}^{2+}$  from water aiming at overcoming the difficulty of solid-liquid separation via traditional centrifugation and filtration terribly restricted the practical applications of nanoscale  $\text{MoS}_2$ .

## REFERENCES

- [1] T. Mezher, H. Fath, Z. Abbas, A. Khaled, Techno-economic assessment and environmental impacts of desalination technologies, *Desalination*. 266 (2011) 263–273. doi:10.1016/j.desal.2010.08.035.
- [2] M.M. Mekonnen, A.Y. Hoekstra, Sustainability: Four billion people facing severe water scarcity, *Science Advances*. 2 (2016) 1–7. doi:10.1126/sciadv.1500323.
- [3] S.K. Gunatilake, Methods of Removing Heavy Metals from Industrial Wastewater, *Journal of Multidisciplinary Engineering Science Studies*. 1 (2015) 12–18.
- [4] P.K. Gautam, R.K. Gautam, S. Banerjee, M.C. Chattopadhyaya, J.D. Pandey, Heavy metals in the environment: Fate, transport, toxicity and remediation technologies, in: *Heavy Metals: Sources, Toxicity and Remediation Techniques*, 2016: pp. 101–130.
- [5] M.M. Schenkeveld, R. Morris, B. Budding, J. Helmer, *Seawater and Brackish Water Desalination in the Middle East, North Africa and Central Asia*, 2004.

- <http://www.worldbank.org/watsan/bnwp>.
- [6] S. Phuntsho, H.K. Shon, S. Hong, S. Lee, S. Vigneswaran, J. Kandasamy, Fertiliser drawn forward osmosis desalination: The concept, performance and limitations for fertigation, *Reviews in Environmental Science and Biotechnology*. 11 (2012) 147–168. doi:10.1007/s11157-011-9259-2.
- [7] G. Amy, N. Ghaffour, Z. Li, L. Francis, R.V. Linares, T. Missimer, S. Lattemann, Membrane-based seawater desalination: Present and future prospects, *Desalination*. 401 (2017) 16–21. doi:10.1016/j.desal.2016.10.002.
- [8] M.A. Anderson, A.L. Cudero, J. Palma, Capacitive deionization as an electrochemical means of saving energy and delivering clean water. Comparison to present desalination practices: Will it compete?, *Electrochimica Acta*. 55 (2010) 3845–3856. doi:10.1016/j.electacta.2010.02.012.
- [9] L. Zhu, M. Gao, C.K.N. Peh, G.W. Ho, Solar-driven photothermal nanostructured materials designs and prerequisites for evaporation and catalysis applications, *Materials Horizons*. 5 (2018) 323–343. doi:10.1039/c7mh01064h.
- [10] A. Lalmi, K.E. Bouhidel, B. Sahraoui, C. el H. Anfif, Removal of lead from polluted waters using ion exchange resin with  $\text{Ca}(\text{NO}_3)_2$  for elution, *Hydrometallurgy*. 178 (2018) 287–293. doi:10.1016/j.hydromet.2018.05.009.
- [11] B. Radisavljevic, A. Radenovic, J. Brivio, V. Giacometti, A. Kis, Single-layer  $\text{MoS}_2$  transistors, *Nature Nanotechnology*. 6 (2011) 147–150. doi:10.1038/nnano.2010.279.
- [12] A. Splendiani, L. Sun, Y. Zhang, T. Li, J. Kim, C.Y. Chim, G. Galli, F. Wang, Emerging photoluminescence in monolayer  $\text{MoS}_2$ , *Nano Letters*. 10 (2010) 1271–1275. doi:10.1021/nl903868w.
- [13] K. Lee, H.Y. Kim, M. Lotya, J.N. Coleman, G.T. Kim, G.S. Duesberg, Electrical characteristics of molybdenum disulfide flakes produced by liquid exfoliation, *Advanced Materials*. 23 (2011) 4178–4182. doi:10.1002/adma.201101013.
- [14] D. Voiry, M. Salehi, R. Silva, T. Fujita, M. Chen, T. Asefa, V.B. Shenoy, G. Eda, M. Chhowalla, Conducting  $\text{MoS}_2$  nanosheets as catalysts for hydrogen evolution reaction, *Nano Letters*. 13 (2013) 6222–6227. doi:10.1021/nl403661s.
- [15] L. Sun, H. Huang, X. Peng, Laminar  $\text{MoS}_2$  membranes for molecule separation, *Chemical Communications*. 49 (2013) 10718–10720. doi:10.1039/c3cc46136j.
- [16] W. Qiao, S. Yan, X. Song, X. Zhang, X. He, W. Zhong, Y. Du, Luminescent monolayer  $\text{MoS}_2$  quantum dots produced by multi-exfoliation based on lithium intercalation, *Applied Surface Science*. 359 (2015) 130–136. doi:10.1016/j.apsusc.2015.10.089.
- [17] Y.H. Lee, X.Q. Zhang, W. Zhang, M.T. Chang, C. Te Lin, K. Di Chang, Y.C. Yu, J.T.W.



- Wang, C.S. Chang, L.J. Li, T.W. Lin, Synthesis of large-area MoS<sub>2</sub> atomic layers with chemical vapor deposition, *Advanced Materials*. 24 (2012) 2320–2325. doi:10.1002/adma.201104798.
- [18] Y. Shi, H. Li, L.-J. Li, Recent advances in controlled synthesis of two-dimensional transition metal dichalcogenides via vapour deposition techniques, *Chemical Society Reviews*. 44 (2015) 2744–2756. doi:10.1039/C4CS00256C.
- [19] M. Wang, G. Li, H. Xu, Y. Qian, J. Yang, Enhanced lithium storage performances of hierarchical hollow MoS<sub>2</sub> nanoparticles assembled from nanosheets, *ACS Applied Materials and Interfaces*. 5 (2013) 1003–1008. doi:10.1021/am3026954.
- [20] J. Xie, H. Zhang, S. Li, R. Wang, X. Sun, M. Zhou, J. Zhou, X.W.D. Lou, Y. Xie, Defect-Rich MoS<sub>2</sub> Ultrathin Nanosheets with Additional Active Edge Sites for Enhanced Electrocatalytic Hydrogen Evolution, *Advanced Materials*. 25 (2013) 5807–5813. doi:10.1002/adma.201302685.
- [21] X. Wang, J. Ding, S. Yao, X. Wu, Q. Feng, Z. Wang, B. Geng, High supercapacitor and adsorption behaviors of flower-like MoS<sub>2</sub> nanostructures, *J. Mater. Chem. A*. 2 (2014) 15958–15963. doi:10.1039/C4TA03044C.
- [22] T. Liu, C. Wang, X. Gu, H. Gong, L. Cheng, X. Shi, L. Feng, B. Sun, Z. Liu, Drug delivery with PEGylated MoS<sub>2</sub> nano-sheets for combined photothermal and chemotherapy of cancer, *Advanced Materials*. 26 (2014) 3433–3440. doi:10.1002/adma.201305256.

## CHAPTER III

# Magnetic MoS<sub>2</sub> nanosheets as recyclable photo-absorbers for high-performance solar steam generation

### 3.1. Introduction

Desalination technology, as one of the most three effective approaches to deal with the water scarcity that limits the development of human society and economy, has long been one of the research focuses all over the world [1]. The major desalination technologies currently used in the industry for the production of clean freshwater are the thermal distillation method and the membrane-based separation process. Unfortunately, these two desalination technologies are widely classified as the capital and energy-intensive processes because of their high consumption of fossil fuels or electricity causing the large carbon footprints and high cost. As a renewable and clean energy, solar energy, which is often the first energy source to be considered in many energy-consumption related fields [2,3], has also attracted great attention in recent seawater/brackish desalination or water purification [4]. Solar steam generation (also named solar desalination or solar evaporation), a classic method via harvesting solar energy for desalination or water purification, has been widely regarded as one of the promising methods for freshwater production [5]. Among the evaporation systems for solar steam generation, the dispersions containing light-absorbing nanomaterials, also known as the volumetric evaporation systems, have been proved one of the effective designs for producing steam under solar illumination [4]. Various light-absorbing nanomaterials, such as graphene-based [5,6] carbon nanotube (CNT)-based [7,8] and metal oxide-based nanomaterials [9] have been applied in the volumetric evaporation systems for solar steam generation. However, although holding the excellent light absorption and low cost, MoS<sub>2</sub>-based materials have been considered only in four works which involved the interfacial evaporation [1,7,10,11] as far as known. Namely, the application of MoS<sub>2</sub>-based nanomaterials has never been investigated in the volumetric evaporation systems for the solar steam generation yet, which might be ascribed to both its poor dispersibility due to the hydrophobicity and its disappointing recyclability because of its nanoscale size.

Herein, a novel MoS<sub>2</sub>-based solar absorber (magnetic MoS<sub>2</sub> nanosheets), prepared by the in-situ growth of nano Fe<sub>3</sub>O<sub>4</sub> on the polydopamine (PDA)-functionalized MoS<sub>2</sub> nanosheets, has been applied for the volumetric solar

steam generation. To reduce the capital cost of the solar-harvesting system and enhance the possibility of practical industry application, the work mainly paid attention to a low solar density range of 0-2.5 kW m<sup>-2</sup>. Under this illumination, the solar steam generation performances including the evaporation rates and the corresponding evaporation efficiency were evaluated. Aiming at the low capital cost and well evaporation performance, the most appropriate concentration of magnetic MoS<sub>2</sub> nanosheets for solar steam generation was also investigated. It could be expected that with the introduction of hydrophilic PDA coating, nano Fe<sub>3</sub>O<sub>4</sub> ought to readily in-situ grow on the functionalized MoS<sub>2</sub> nanosheets with the help of its abundant functional groups, and magnetic MoS<sub>2</sub> nanosheets exhibited a long-term well dispersion in aqueous solutions which benefited for the high-performance solar steam generation. In addition, due to the introduction of nano Fe<sub>3</sub>O<sub>4</sub>, magnetic MoS<sub>2</sub> nanosheets exhibited excellent recyclability for solar steam generation which avoided both materials waste and environmental pollution, suggesting its great potential in practical desalination or water purification.

## 3.2. Experimental section

### 3.2.1. Materials

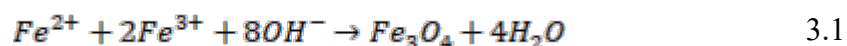
Hexaammonium heptamolybdate tetrahydrate ((NH<sub>4</sub>)<sub>6</sub>Mo<sub>7</sub>O<sub>24</sub>·4H<sub>2</sub>O), thiourea (CN<sub>2</sub>H<sub>4</sub>S), ethanol (C<sub>2</sub>H<sub>6</sub>O), tris(hydroxymethyl)aminomethane (C<sub>4</sub>H<sub>11</sub>NO<sub>3</sub>, Tris), Dopamine hydrochloride (C<sub>8</sub>H<sub>11</sub>NO<sub>2</sub>·HCl) was obtained from Shanghai Aladdin Bio-Chem Technology Co., Ltd. Hydrochloric acid (HCl) was purchased from Merck Pty. Ltd. FeCl<sub>3</sub>·6H<sub>2</sub>O, FeSO<sub>4</sub>·7H<sub>2</sub>O, citric acid monohydrate and NH<sub>4</sub>OH (25%) solution were originated from Sinopharm Chemical Reagent Co., Ltd (Shanghai). All chemicals were of analytical purity and used without further purification. Deionized Milli-Q water (18.2 MΩ cm, Millipore Corporation) was used in all the experiments.

### 3.2.2. Preparation of magnetic MoS<sub>2</sub> nanosheets

**Preparation of nanoflower-like MoS<sub>2</sub>:** To prepare the nanoflower-like MoS<sub>2</sub> [12], 2.48 g of (NH<sub>4</sub>)<sub>6</sub>Mo<sub>7</sub>O<sub>24</sub>·4H<sub>2</sub>O and 4.56 g of CN<sub>2</sub>H<sub>4</sub>S were dissolved in 72 mL of pure water under vigorous stirring for 30 min to form a homogeneous solution, and then transferred into a 100 mL Teflon-lined stainless-steel autoclave which was heated at 220°C for 6 h and finally naturally cooled to room temperature. The resultant sample was washed with ultrapure water and ethanol for three or four times and then dried by vacuum freeze-drying.

**Preparation of PDA-functionalized MoS<sub>2</sub> nanosheets:** Typically, 100 mg of nanoflower-like MoS<sub>2</sub> were dispersed in 75 mL of Tris-buffer aqueous solution (10 mM, pH 8.5) and sonicated at 150 W for 30 min to obtain the exfoliated MoS<sub>2</sub> nanosheets [13]. Afterwards, 150 mg dopamine hydrochloride was added, and the mixture was shaken at 150 rpm for 4 h in a water base at room temperature (25°C). The resultant sample was washed with ultrapure water for three or four times and then dried by vacuum freeze-drying.

**Preparation of magnetic MoS<sub>2</sub> nanosheets:** Magnetic MoS<sub>2</sub> nanosheets were fabricated as follows: Firstly, 100 mg of the PDA-functionalized MoS<sub>2</sub> nanosheets was added into 200 mL of water and sonicated at 150 W for 5 min to obtain a homogeneous solution. Secondly, 6.0 g of FeCl<sub>3</sub>·6H<sub>2</sub>O and 3.1 g of FeSO<sub>4</sub>·7H<sub>2</sub>O were entirely dissolved in the above solution and mechanically stirred at 400 rpm for 1h to ensure the sufficient immobilization of iron ions on the functionalized MoS<sub>2</sub> nanosheets. Thirdly, after the rapid addition of 20 mL of NH<sub>4</sub>OH (25%) solution, 7.0 g of citric acid monohydrate was subsequently added into the mixture, and in this stage the following reactions (Eq. 3.1) mainly occurred [5,7]:



After being vigorously stirred for another 1.0 h, the resultant black precipitates were separated with a magnet and washed at six times with acetone, and finally heated at 65°C in the oven for 1.0 h to evaporate the acetone.

### 3.2.3. Characterization methods

The structure of MoS<sub>2</sub> was analyzed by the X-ray diffraction spectroscopy (XRD, PIXcel-Empyrean). The morphology and chemical composition of samples were obtained from scanning electron microscopy (SEM, Hitachi S-4700) equipped with an energy dispersive spectrometer (EDS). The magnetic property of the samples was measured with a VSM (PPMS-9T, Quantum Design, USA). The solar absorption of samples was measured by an ultraviolet-visible-near infrared diffuser absorption spectrophotometer (LAMBDA950). An ion chromatography (Dionex Aquion) and an inductively coupled plasma atomic emission spectroscopy (ICP-AES, Prodigy 7) were applied to determine the concentrations of anions and cations in solutions, respectively.

### 3.2.4. Solar steam generation test

Schematic diagram of the experimental set-up for the solar steam generation was

displayed in Fig. 3.1. The critical components of the set-up included a solar simulator (Perfectsolar M300), a volumetric solar receiver (acrylic beaker), an electric balance (Shanghai Yueping, YP6002, accuracy: 0.01 g) which was connected to a computer for the real-time measurements of water mass changes. The designed solar receiver consisted of an inner acrylic beaker (Inner diameter: 4.8 mm, height: 30 mm, thickness: 3 mm), an outside acrylic beaker (Inner diameter: 70 mm, height: 40 mm, thickness: 3 mm) and conical cap (diameter: 64 mm, cone angle: 120°). The inner acrylic beaker contained ~40 mL of 3.5wt% NaCl aqueous solution, which often acted as an alternative to the real seawater [5,14]. The probe of an electronic temperature logger (Jingchuang GSP-6), which was also connected to the computer, was inserted into the center of the inner acrylic beaker with an underwater depth of 1.0 cm to record the temperature vibration of the nanofluids. The thickness of each solution was maintained at 20 mm to achieve a fast temperature rise. All experiments of solar steam generation were finished in Wuhan city, Hubei province, China from April 05, 2019, to May 20, 2019, during which the ambient temperature had been kept at  $23 \pm 2^\circ\text{C}$  by the air conditioner and the ambient humidity had been  $30 \pm 5\%$ .

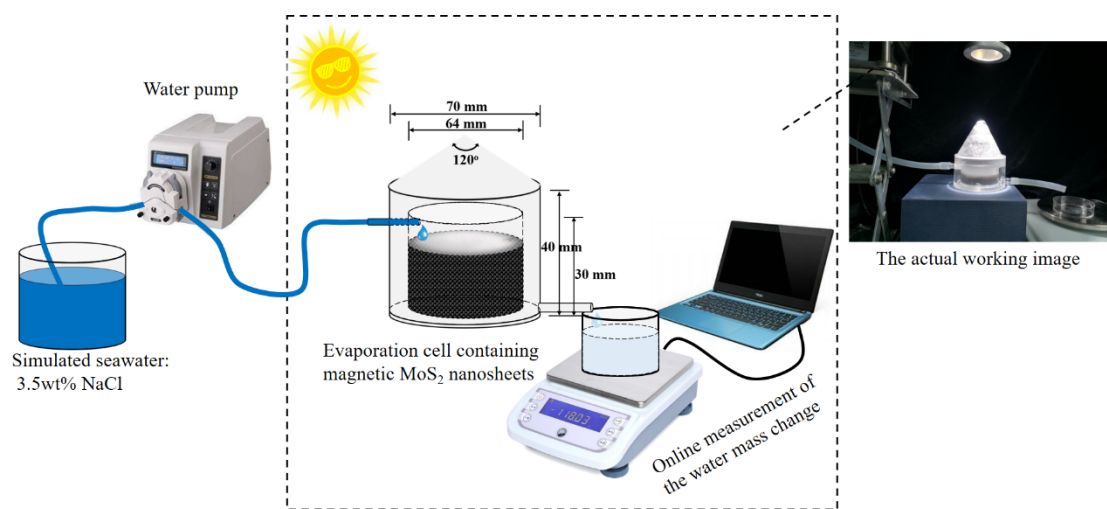


Fig. 3.1. Schematic diagram of the experimental set-up.

### 3.3. Results and discussion.

#### 3.3.1. Preparation and characterization

At first, MoS<sub>2</sub> nanoflowers prepared by the solvothermal method [15] was treated by the ultrasonic method to obtain the exfoliated MoS<sub>2</sub> nanosheets. As illustrated in Fig. 3.2, MoS<sub>2</sub> nanosheets were then added into the dopamine solution to form a thin PDA coating layer outside the surface of MoS<sub>2</sub> nanosheets [16]. It's

known that a PDA coating derived from the self-polymerization of dopamine monomers could be easily formed on almost all solid substrates due to its strong adhesion [17]. Note that the PDA coating was rich in functional groups including -COOH and -OH [17], ensuring that the functionalized MoS<sub>2</sub> nanosheets were capable of immobilizing positively charged iron ions (Fe<sup>3+</sup>/Fe<sup>2+</sup>) in solutions. The in-situ growth of Fe<sup>3+</sup>/Fe<sup>2+</sup> into nano Fe<sub>3</sub>O<sub>4</sub> would occur after the addition of citric acid and ammonia, resulting in the deposition of nano Fe<sub>3</sub>O<sub>4</sub> on the surface of MoS<sub>2</sub> nanosheets. At last, the magnetic MoS<sub>2</sub> was obtained from the resultant black solutions by the magnetic separation.

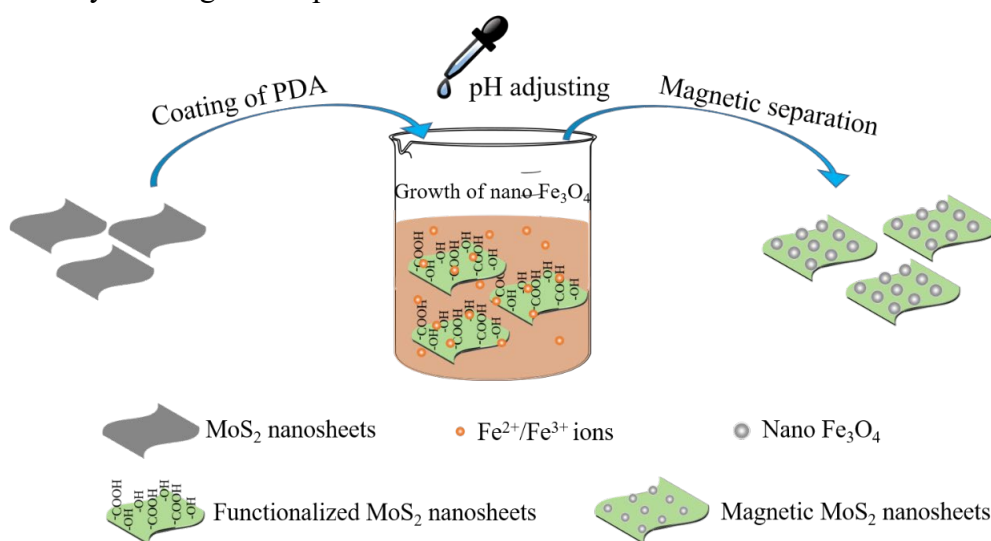


Fig. 3.2 Schematic diagram of the preparation procedure of magnetic MoS<sub>2</sub> nanosheets.

The structural characterization of pristine MoS<sub>2</sub>, nano Fe<sub>3</sub>O<sub>4</sub> and magnetic MoS<sub>2</sub> were carried out by X-ray diffraction spectra (XRD). As shown in Fig. 3.3(a), the characteristic peaks of both nanoflower-like MoS<sub>2</sub> and nanocrystalline Fe<sub>3</sub>O<sub>4</sub> were simultaneously indexed in the magnetic MoS<sub>2</sub> nanocomposites [5,16], suggesting the successful incorporation of nano Fe<sub>3</sub>O<sub>4</sub> onto MoS<sub>2</sub> nanosheets. No impurity peak was found, demonstrating the great purity of magnetic MoS<sub>2</sub>. Besides, based on the estimate from characteristic (311) peak via Bragg diffraction and the Scherrer formula, the particle sizes of the stand-alone Fe<sub>3</sub>O<sub>4</sub> nanospheres and the Fe<sub>3</sub>O<sub>4</sub> nanospheres in the magnetic MoS<sub>2</sub> nanosheets were calculated to be around 11 and 16 nm, respectively [5]. The SEM morphologies of the synthesized MoS<sub>2</sub> and magnetic MoS<sub>2</sub> nanosheets were displayed in Fig. 3.3(b) and Fig. 3.3(c), respectively. It was obvious that the synthesized MoS<sub>2</sub> was of the nano petal-like architectures with the lateral dimension of around 200 nm. Nano Fe<sub>3</sub>O<sub>4</sub> nanospheres were naturally attached to MoS<sub>2</sub> nanosheets and uniformly scattered on the surface of nanosheets, resulting in

the rough surfaces. Such surfaces would contribute to the high solar absorption because of the poor light reflects on the rough surface [1,18]. The EDS analysis based on Fig. 3.3(c) was further performed to identify the chemical composition of magnetic MoS<sub>2</sub> nanosheets, as showed in Fig. 3.3(d) and Table 3.1. Due to its high purity, the main chemical composition of magnetic MoS<sub>2</sub> nanocomposite could be roughly written as MoS<sub>2</sub>•xPDA•1.58Fe<sub>3</sub>O<sub>4</sub>, further confirming the successful attachment of nano Fe<sub>3</sub>O<sub>4</sub> onto the PDA-functionalized MoS<sub>2</sub> nanosheets.

Note that because of the introduction of hydrophilic PDA, magnetic MoS<sub>2</sub> nanosheets exhibited a well stable and homogeneous dispersion in solutions as displayed in Fig. 3.4, which was conducive to continuously receiving sunlight on the top area and maintaining the efficient solar steam generation.

The magnetic property of magnetic MoS<sub>2</sub> nanosheets played a critical role in its recycling by the easy magnetic separation. Shown in Fig. 3.3(e) were the magnetic property of both the stand-alone nano Fe<sub>3</sub>O<sub>4</sub> and magnetic MoS<sub>2</sub> nanosheets. The saturation magnetization of the stand-alone Fe<sub>3</sub>O<sub>4</sub> and magnetic MoS<sub>2</sub> nanosheets were 54.56 emu g<sup>-1</sup> and 45.38 emug<sup>-1</sup>, respectively. Although a reduced saturation magnetization was found for magnetic MoS<sub>2</sub> nanosheets compared to the stand-alone Fe<sub>3</sub>O<sub>4</sub>, such saturation magnetization of the magnetic MoS<sub>2</sub> nanosheets was still larger than that of most reported magnetic composites (28.7–43.0 emu g<sup>-1</sup>) [7,19,20], guaranteeing its great potential in practical application. In addition, no hysteresis loop was found on the curves of magnetic MoS<sub>2</sub> nanosheets, suggesting its superparamagnetism. Thereby, both the high magnetization and the superparamagnetic property ensured magnetic MoS<sub>2</sub> nanosheets be readily attracted and separated by an external magnetic field within a few seconds.

As displayed in Fig. 3.3(f), the solar absorption capacity of the magnetic MoS<sub>2</sub> nanosheets was analyzed based on the UV–vis–NIR absorption spectroscopy. In order to accurately calculate the solar absorption of the magnetic MoS<sub>2</sub> nanosheets, the proportion of solar absorption in different spectrum regions from UV light to NIR light was calculated according to Eq. 3.2 [1,21]:

$$A = \frac{\int (1-R) S d\lambda}{\int S d\lambda} \quad 3.2$$

where  $A$  is the solar absorption,  $\lambda$  is the wavelength (nm),  $S$  is the solar spectral irradiance ( $W m^{-2} nm^{-1}$ ),  $R$  is the reflectance of the sample. By calculation, the solar absorption of the magnetic MoS<sub>2</sub> nanosheets was  $96.15 \pm 0.53\%$ . Such solar absorption capacity of the magnetic MoS<sub>2</sub> nanosheets was as good as that of the recently reported

excellent solar absorbers [1,14]. Note that this high solar absorption capacity was ascribed to not only the MoS<sub>2</sub> nanosheets but also the PDA coating and the Fe<sub>3</sub>O<sub>4</sub> nanospheres since the latter two materials had also proven to be solar absorbers in other works [5,22]. These results suggested the magnetic MoS<sub>2</sub> nanosheets had an excellent light absorption in the broad wavelength ranging from 200 to 2400 nm, which included the ultraviolet, visible and near-infrared light, laying the foundation for its highly efficient photothermal conversion and high-performance solar steam generation.

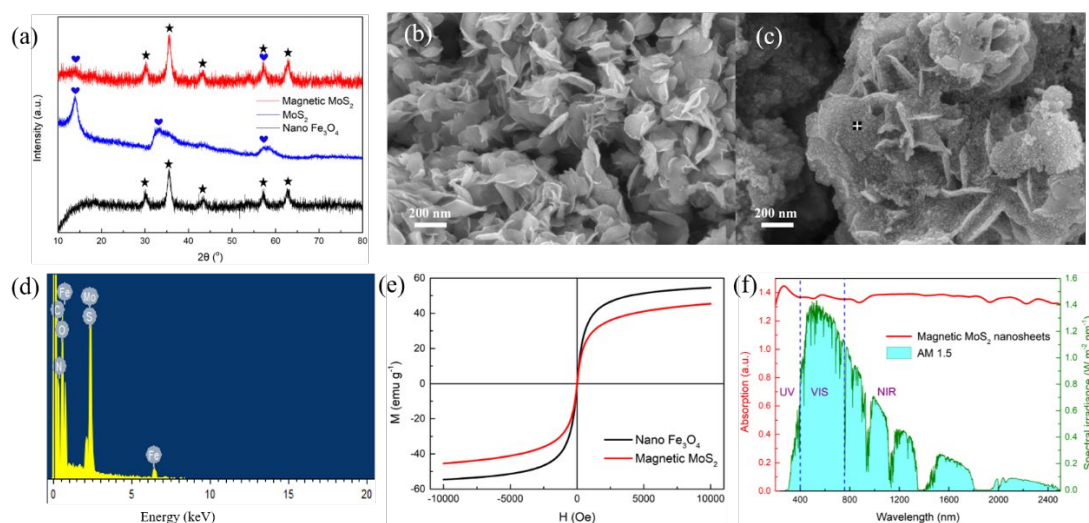
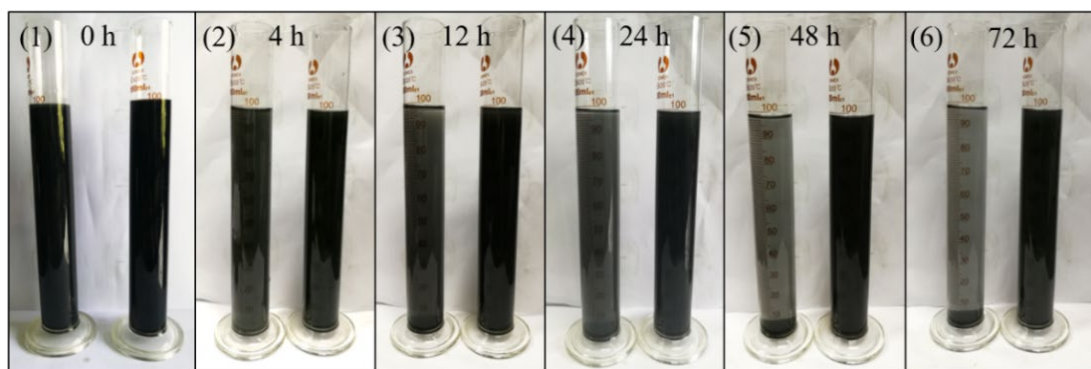


Fig. 3.3 (a) XRD patterns of the pristine MoS<sub>2</sub> nanosheets, nano Fe<sub>3</sub>O<sub>4</sub> and the magnetic MoS<sub>2</sub> nanosheets. SEM images of (b) the pristine MoS<sub>2</sub> nanosheets and (c) the magnetic MoS<sub>2</sub> nanosheets. (d) EDS analysis of the magnetic MoS<sub>2</sub> nanosheets according to (c). (e) The magnetic property of nano Fe<sub>3</sub>O<sub>4</sub> and magnetic MoS<sub>2</sub> nanosheets. (f) UV–Vis–NIR absorption spectroscopy of the magnetic MoS<sub>2</sub> nanosheets.



Left measuring cylinders: **pristine MoS<sub>2</sub> dispersion**; Right measuring cylinders: **magnetic MoS<sub>2</sub> dispersion**

Fig. 3.4. Stability of pristine MoS<sub>2</sub> dispersion and magnetic MoS<sub>2</sub> dispersion for different time.



Table 3.1 Element ratio in magnetic MoS<sub>2</sub> nanosheets

| Element | Weight percentage | Atomic percentage |
|---------|-------------------|-------------------|
| Mo      | 13.25             | 3.46              |
| S       | 9.71              | 7.59              |
| C       | 16.38             | 34.12             |
| N       | 4.25              | 7.59              |
| O       | 19.71             | 30.82             |
| Fe      | 36.69             | 16.44             |
| Total   | 100%              | 100%              |

In which, the atomic molar ratios: Mo : 2S : 3Fe  $\approx$  1 : 1.09 : 1.58. Note that polydopamine (PDA) consists of C, H, N, O, but there are no accurate chemical formulas for PDA, so far. H element cannot be detected by the SEM-EDS.

### 3.3.2. Evaluation of evaporation performances

In a typical volumetric system for solar steam generation, besides the inherent photothermal conversion property of solar absorbers, there were two additional factors which played the critical role in controlling the evaporation process with the ignorance of the heat loss: (1) the concentration of solar absorbers in the working fluids, and (2) the temperature of the working fluids [7].

As displayed in Fig. 3.5(a), the mass changes of the produced water over time under illumination of 1.0 kW m<sup>-2</sup> by using the magnetic MoS<sub>2</sub> nanosheets with different concentrations as the solar absorbers were recorded. The mass change increased with the increase of mass concentration of solar absorbers from 0 to 1.0 g L<sup>-1</sup>, and came to the plateau from 1.0 g L<sup>-1</sup> to 2.0 g L<sup>-1</sup>. As shown in Fig. 3.5(b), after illumination for ~20 min, the temperature of the brine solutions raised from 31°C to 55°C, as the concentration of the magnetic MoS<sub>2</sub> dispersions increased from 0 to 1.0 g L<sup>-1</sup> and maintained at 55°C from 1.0 to 2.0 g L<sup>-1</sup>. The similar tendency between the mass change and the temperature variation demonstrated that the temperature of working fluids indeed controlled the evaporation process. As a conclusion, the working fluids with increasing solar absorbers within certain concentration range greatly enhanced the formation of the high-temperature area for evaporation because of the increasing solar absorption, and beyond the concentration range it hardly further contributed to a higher temperature area because of the negligible improvement of the solar absorption [5,7]. To directly evaluate the evaporation performances, the thermal efficiency (also named as the light-to-heat conversion

efficiency) which was written as Eq. 3.3 and the evaporation efficiency (also named as the light-to-steam conversion efficiency) which was defined as Eq. 3.4 [7], were simultaneously analyzed:

$$\eta_h = \frac{m_v c_{p,1} \Delta T + m_w h_{LV}}{P_{in} A t} \quad 3.3$$

$$\eta_s = \dot{m} h_{LV} / P_{in} \quad 3.4$$

where  $\eta_h$  (%) and  $\eta_s$  (%) are the light-to-heat conversion efficiency and the light-to-steam conversion efficiency, respectively.  $m_v$  (kg) is the weight of bulk water, and  $m_w$  (kg) is the total mass of evaporated water during the evaporation time  $t$  (S).  $C_{p,1}$  is the specific heat of water at 1 atm, which is 4.2 kJ kg<sup>-1</sup> K<sup>-1</sup>.  $\Delta T$  is the temperature rise of the bulk water.  $A$  is the effective area for receiving solar energy, which is  $1.81 \times 10^{-3}$  m<sup>2</sup> in this work.  $\dot{m}$  is the stable evaporation rates, of which the value is equal to the absolute value of the straight-line gradient of the mass change over the illumination time in the range of 20–60 min.  $h_{LV}$  is the latent heat of water vaporization, normally taken to be 2.257 kJ g<sup>-1</sup>.  $P_{in}$  means the total incoming solar power, kW m<sup>-2</sup>.

The values of stable evaporation rates were originated from the slope of those aforementioned curves after subtracting the initial transition period of ~20 min (Fig. 3.6). Based on the evaporation rates and the temperature rises of the working fluids as given in Table 3.2 and Fig. 3.5(c), both the thermal efficiencies and evaporation efficiencies were obtained. The evaporation efficiencies were almost equal to the thermal efficiencies as shown in Fig. 3.6, suggesting that the vast majority of the converted heat had been used for steam production. This was ascribed to the negligible sensible heat resulted from the little amount of bulk water (0.040 kg) used in this designed evaporation system. Displayed in Fig. 3.5(c) were the calculated evaporation rates and evaporation efficiencies for various magnetic MoS<sub>2</sub> dispersions under the illumination of 1.0 kW m<sup>-2</sup>. With the concentration of magnetic MoS<sub>2</sub> dispersions increased from 0, 0.5, 1.0 to 2.0 g L<sup>-1</sup>, the evaporation rates increased from 0.25 kg m<sup>-2</sup> h<sup>-1</sup> to 1.0 kg m<sup>-2</sup> h<sup>-1</sup> and leveled off at around 1.0 kg m<sup>-2</sup> h<sup>-1</sup>, while the evaporation efficiency increased from 15.8% to 68.1% and reached a plateau of ~68%. Thereby, nanofluid containing 1.0 g L<sup>-1</sup> of magnetic MoS<sub>2</sub> nanosheets was chosen as the concentration of the working nanofluids in order to obtain the best evaporation performance with the least consumption of solar absorber.

The mass changes and the temperature variations of water over illumination time

under various illumination of 0, 1.0, 1.5, 2.0 and 2.5  $\text{kW m}^{-2}$  were displayed in Fig. 3.5(d) (based on Fig. 3.7) and Fig. 3.5(e), respectively. As expected, higher solar density was conducive to generating higher temperatures on the top area of the working fluids as displayed in Fig. 3.5(f). Namely, with the solar illumination increasing from 1.0  $\text{kW m}^{-2}$  to 2.5  $\text{kW m}^{-2}$ , the evaporation rates increased from  $\sim 1.0 \text{ kg m}^{-2} \text{ h}^{-1}$  at 1.0  $\text{kW m}^{-2}$  to  $\sim 3.2 \text{ kg m}^{-2} \text{ h}^{-1}$  at 2.5  $\text{kW m}^{-2}$ , and the corresponding evaporation efficiency increased from  $\sim 62.5\%$  at 1.0  $\text{kW m}^{-2}$  to 79.2% at 2.5  $\text{kW m}^{-2}$ . Although the work mainly paid attention to the low solar density range of 0-2.5  $\text{kW m}^{-2}$ , the evaporation performance of magnetic  $\text{MoS}_2$  nanosheets outstood most of the reported solar absorbers in the volumetric systems as shown in Table 3.3. These results demonstrated the magnetic  $\text{MoS}_2$  nanosheets an excellent solar absorber for high-performance solar steam generation in the volumetric evaporation system.

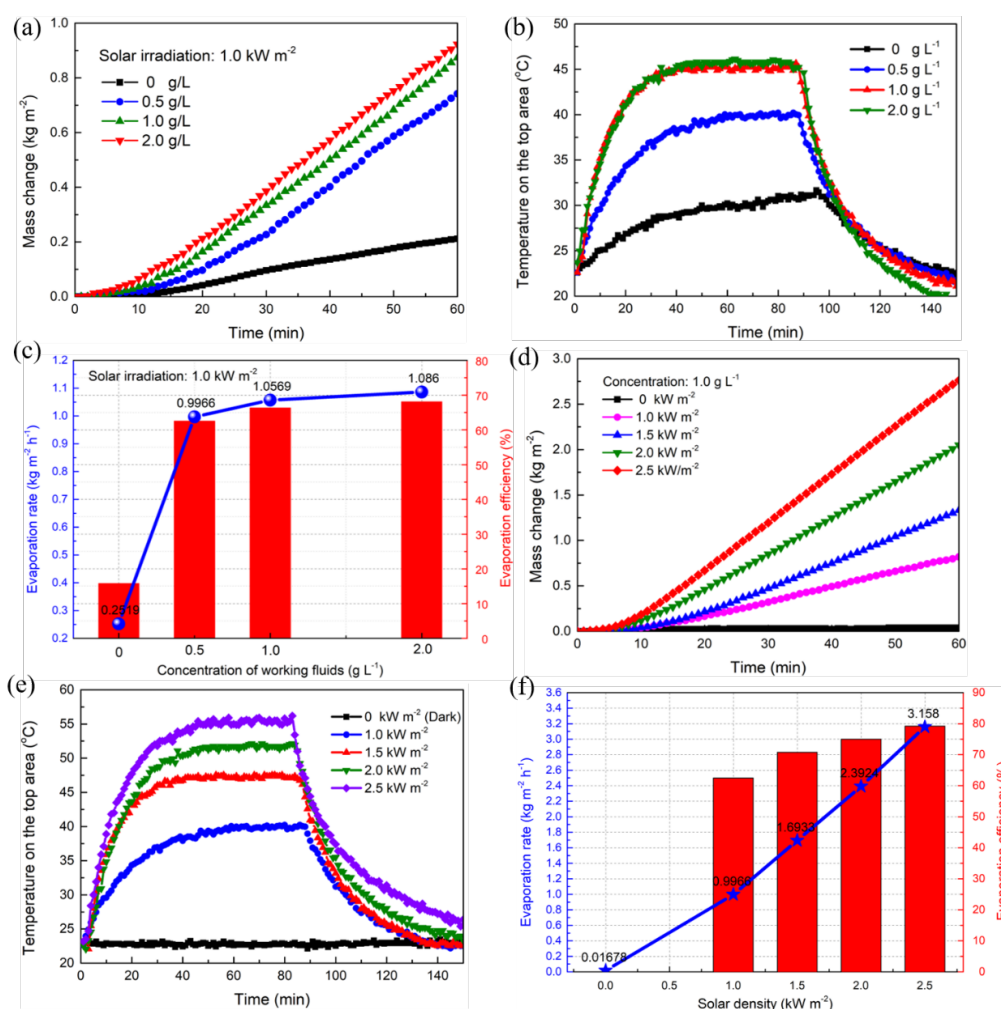


Fig. 3.5 (a) Mass change of water over illumination time for different concentrations of magnetic  $\text{MoS}_2$  dispersions under illumination of 1.0  $\text{kW m}^{-2}$ , and (b) temperature variations for various magnetic  $\text{MoS}_2$  dispersions with concentration of 0, 0.5, 1.0, and 2.0  $\text{g L}^{-1}$  under

illumination of  $1.0 \text{ kW m}^{-2}$ . (c) The corresponding evaporation rates and evaporation efficiency. (d)

Mass change of water over illumination time for  $1.0 \text{ g L}^{-1}$  magnetic  $\text{MoS}_2$  dispersions under various illumination of 0, 1.0, 1.5, 2.0 and  $2.5 \text{ kW m}^{-2}$ , and (e) temperature variations for magnetic  $\text{MoS}_2$  dispersions with concentration of  $1.0 \text{ g L}^{-1}$  under various illuminations of 0, 1.0, 1.5, 2.0 and  $2.5 \text{ kW m}^{-2}$ . (f) The corresponding evaporation rates and evaporation efficiency.

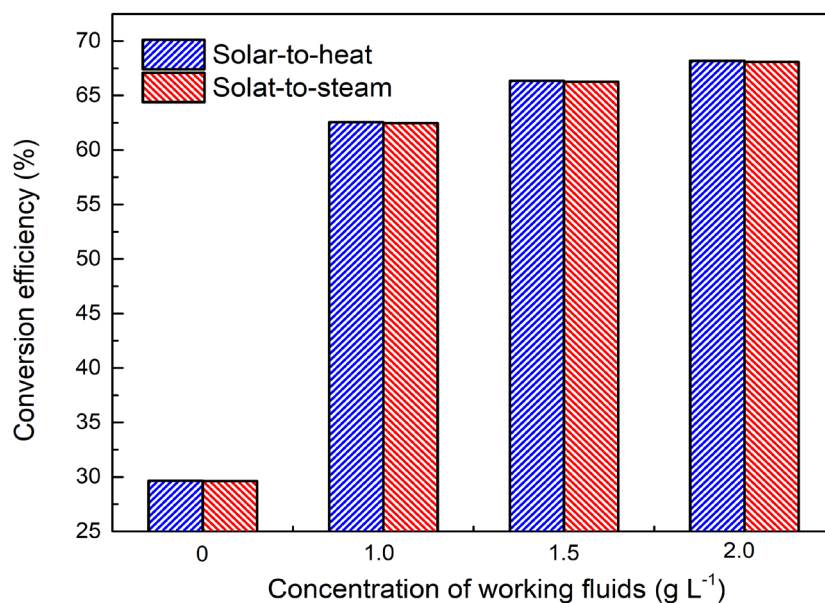


Fig. 3.6. The solar-to-heat efficiency and solar-to-steam efficiency of magnetic  $\text{MoS}_2$  dispersions with various concentration under solar irradiation of  $1.0 \text{ kW m}^{-2}$ .

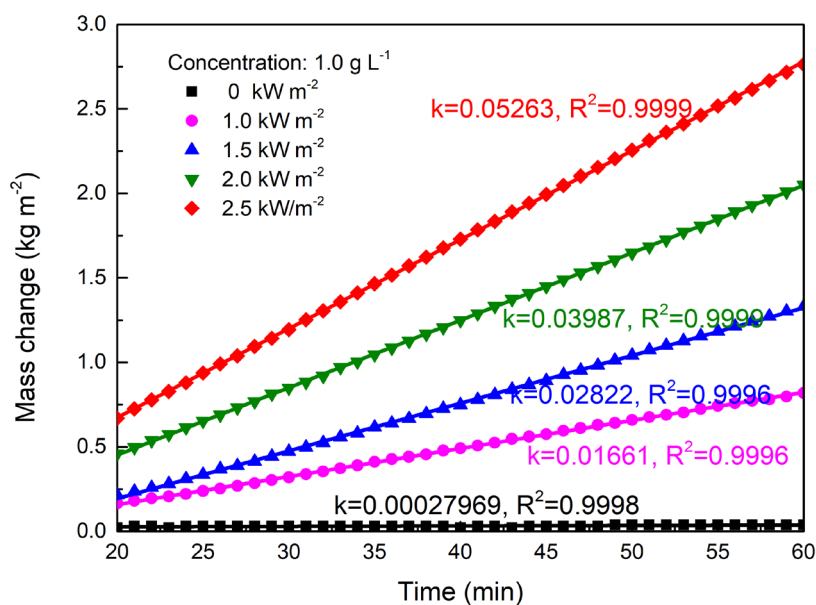


Fig. 3.7. Calculating the evaporation rates of magnetic  $\text{MoS}_2$  dispersions under various solar irradiation.

Table 3.2. The calculation of the thermal efficiency and the evaporation efficiency of working fluids with various concentrations under irradiation of  $1.0 \text{ kW m}^{-2}$ .

| Concentration (g L <sup>-1</sup> ) | Bulk water (kg) | Temperature rise, $\Delta T$ (K) | Time, $\Delta t$ (S) | Thermal efficiency (%) | Evaporation rates (kg m <sup>-2</sup> h <sup>-1</sup> ) | Latent heat (kJ g <sup>-1</sup> ) | Evaporation efficiency (%) |
|------------------------------------|-----------------|----------------------------------|----------------------|------------------------|---|-----------------------------------|----------------------------|
| 0                                  | 0.04            | 7.0                              | 2400                 | <b>29.63</b>           | 0.4724  | 2.257                             | <b>29.61</b>               |
| 0.5                                | 0.04            | 17.1                             | 2400                 | <b>62.56</b>           | 0.9966  | 2.257                             | <b>62.48</b>               |
| 1.0                                | 0.04            | 22.2                             | 2400                 | <b>66.37</b>           | 1.0569  | 2.257                             | <b>66.26</b>               |
| 2.0                                | 0.04            | 23                               | 2400                 | <b>68.20</b>           | 1.0860  | 2.257                             | <b>68.08</b>               |

Table 3.3. Comparison of various solar absorbers in the volumetric systems.

| Solar absorbers                      | Solar density (kW m <sup>-2</sup> ) | Absorber density (g L <sup>-1</sup> ) | Evaporation rates (kg m <sup>-2</sup> h <sup>-1</sup> ) | Evaporation efficiency (%) | Refs      |
|--------------------------------------|-------------------------------------|---------------------------------------|---|----------------------------|-----------|
| rGO-Fe <sub>3</sub> O <sub>4</sub>   | 1.0                                 | 1.0                                   | 1.12  | 66                         | [5]       |
|                                      | 2.0                                 |                                       | 2.25  | ~67                        |           |
| Fe <sub>3</sub> O <sub>4</sub> @CNT  | 1.0                                 | 0.5                                   | -   | 43.8                       | [7]       |
|                                      | 3.0                                 |                                       | -   | 23.3                       |           |
|                                      | 5.0                                 |                                       | -   | ~46                        |           |
|                                      | 7.0                                 |                                       | -   | ~55                        |           |
|                                      | 10.0                                |                                       | -   | 60.3                       |           |
| CNT nanofluids                       | 10                                  | $19.04 \times 10^{-4}$ vol%           | 8.5   | 46.8                       | [8]       |
| GO-Au                                | 1.0                                 | 0.5                                   | 1.58  | 59.2                       | [23]      |
|                                      | 1.0                                 |                                       | ~1.0  | ~63                        |           |
| rGO-Fe <sub>3</sub> O <sub>4</sub>   | 2.0                                 | 0.5                                   | ~2.2  | ~68                        | [24]      |
|                                      | 3.0                                 |                                       | ~3.4  | ~71                        |           |
|                                      | 4.0                                 |                                       | ~4.8  | ~75                        |           |
|                                      | 5.0                                 |                                       | ~6.2  | ~77                        |           |
| Magnetic MoS <sub>2</sub> nanosheets | 1.0                                 | 1.0                                   | 1.00  | 62.48                      | This work |
|                                      | 1.5                                 |                                       | 1.69  | 70.77                      |           |
|                                      | 2.0                                 |                                       | 2.39  | 75.00                      |           |
|                                      | 2.5                                 |                                       | 3.16  | 79.20                      |           |

### 3.3.3. Recyclability

Excellent recyclability of solar absorber was critical for its practical applications in industry. To obtain the quantitative separation process, the concentration variations of magnetic MoS<sub>2</sub> dispersions (initial concentration: 1.0 g L<sup>-1</sup>) as a function of the separation time was shown in Fig. 3.8(a). Note that the concentration of magnetic MoS<sub>2</sub> dispersions was determined based on the Beer–Lambert law, which declared that the absorbance of a dilute solution was proportional to its solute concentration. Because of excellent magnetic characteristics as aforementioned in Fig. 3.3(e), the magnetic MoS<sub>2</sub> nanosheets exhibited a very effective and fast separation from the aqueous solutions within a few minutes, laying the foundation for its recyclability and reusability. With the progress of evaporation and the addition of new saline water, the saline solution gradually became supersaturated due to the continued segregation of freshwater from the system, resulting in more and more nucleation and crystallization of salt ions in the solutions. In a typical cycle, the stable evaporation rates and evaporation efficiency were recorded by using 0.1 g L<sup>-1</sup> magnetic MoS<sub>2</sub> nanosheets as the solar absorbers under illumination of 1.0 kW m<sup>-2</sup> for 90 min, and then the used magnetic MoS<sub>2</sub> nanosheets were separated and washed with the help of a permanent magnet (PC-0127, N33 nickel-plated NdFeB). Afterwards, the magnetic MoS<sub>2</sub> nanosheets were redispersed in saline water to begin the next evaporation. Fig. 3.8(b) showed their recyclable performance as a function of the cycle numbers. No manifest change was found in the evaporation performance of magnetic MoS<sub>2</sub> nanosheets during its successive ten cycles, demonstrating that magnetic MoS<sub>2</sub> nanosheets had good recyclability and reusability.

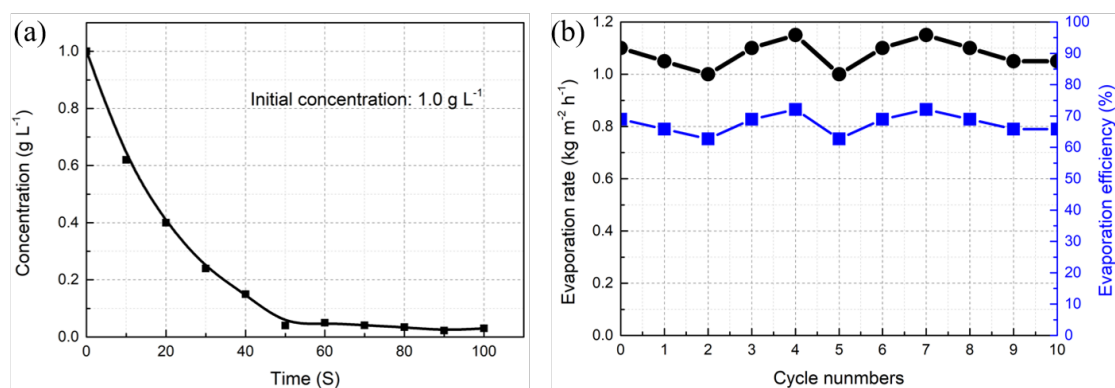


Fig. 3.8 (a) Concentration of magnetic MoS<sub>2</sub> dispersions as a function of the separation time by an external magnet. (b). The stable evaporation rates and evaporation efficiency of 1.0 g L<sup>-1</sup> magnetic MoS<sub>2</sub> nanosheets for 10 successive cycles (Each cycle: 1.0 kW m<sup>-2</sup>, 60 min illumination).

### 3.4. Conclusions.

In summary, magnetic MoS<sub>2</sub>-based solar absorbers with excellent light absorption had been successfully fabricated by the in-situ growth of nano Fe<sub>3</sub>O<sub>4</sub> on the PDA-functionalized MoS<sub>2</sub> nanosheets. The main chemical composition of the magnetic MoS<sub>2</sub> nanocomposite could be roughly written as MoS<sub>2</sub>•xPDA•1.58Fe<sub>3</sub>O<sub>4</sub>. Because of the introduction of hydrophilic PDA, the as-prepared magnetic MoS<sub>2</sub> nanosheets showed a long-term well dispersion in aqueous solution. Impressively, the high evaporation rate (3.16 kg m<sup>-2</sup> h<sup>-1</sup>) and high evaporation efficiency (79.2%) was achieved with the nanofluids containing 1.0 g L<sup>-1</sup> magnetic MoS<sub>2</sub> nanosheets as the solar absorber under a low solar illumination power of 2.5 kW m<sup>-2</sup>. Moreover, with the help of the decorating nano Fe<sub>3</sub>O<sub>4</sub>, the magnetic MoS<sub>2</sub> nanosheets exhibited a fast and effective separation from aqueous solution, laying the foundation for its well recyclability and reusability. This MoS<sub>2</sub>-based nanomaterial also offers the opportunity to develop other solar-based applications such as power generation and photocatalytic degradation of pollutants, etc.

### REFERENCES.

- [1] R. Chen, X. Wang, Q. Gan, T. Zhang, K. Zhu, M. Ye, A bifunctional MoS<sub>2</sub> -based solar evaporator for both efficient water evaporation and clean freshwater collection, *Journal of Materials Chemistry A*. 7 (2019) 11177–11185. doi:10.1039/c9ta02002k.
- [2] H. Yi, W. Zhan, Y. Zhao, S. Qu, W. Wang, P. Chen, S. Song, A novel core-shell structural montmorillonite nanosheets/stearic acid composite PCM for great promotion of thermal energy storage properties, *Solar Energy Materials and Solar Cells*. 192 (2019) 57–64. doi:10.1016/j.solmat.2018.12.015.
- [3] H. Yi, W. Zhan, Y. Zhao, X. Zhang, F. Jia, W. Wang, Z. Ai, S. Song, Design of MtNS/SA microencapsulated phase change materials for enhancement of thermal energy storage performances: Effect of shell thickness, *Solar Energy Materials and Solar Cells*. 200 (2019) 109935. doi:10.1016/j.solmat.2019.109935.
- [4] M. Gao, L. Zhu, C.K. Peh, G.W. Ho, Solar absorber material and system designs for photothermal water vaporization towards clean water and energy production, *Energy & Environmental Science*. 12 (2019) 841–864. doi:10.1039/C8EE01146J.
- [5] X. Wang, G. Ou, N. Wang, H. Wu, Graphene-based Recyclable Photo-Absorbers for High-Efficiency Seawater Desalination, *ACS Applied Materials and Interfaces*. 8 (2016) 9194–9199. doi:10.1021/acsami.6b02071.
- [6] G. Ni, N. Miljkovic, H. Ghasemi, X. Huang, S. V. Boriskina, C. Te Lin, J. Wang, Y. Xu,

- M.M. Rahman, T.J. Zhang, G. Chen, Volumetric solar heating of nanofluids for direct vapor generation, *Nano Energy*. 17 (2015) 290–301. doi:10.1016/j.nanoen.2015.08.021.
- [7] L. Shi, Y. He, Y. Huang, B. Jiang, Recyclable Fe<sub>3</sub>O<sub>4</sub>@CNT nanoparticles for high-efficiency solar vapor generation, *Energy Conversion and Management*. 149 (2017) 401–408. doi:10.1016/j.enconman.2017.07.044.
- [8] X. Wang, Y. He, G. Cheng, L. Shi, X. Liu, J. Zhu, Direct vapor generation through localized solar heating via carbon-nanotube nanofluid, *Energy Conversion and Management*. 130 (2016) 176–183. doi:10.1016/j.enconman.2016.10.049.
- [9] M. Gao, P.K.N. Connor, G.W. Ho, Plasmonic photothermic directed broadband sunlight harnessing for seawater catalysis and desalination, *Energy and Environmental Science*. 9 (2016) 3151–3160. doi:10.1039/c6ee00971a.
- [10] Z. Guo, G. Wang, X. Ming, T. Mei, J. Wang, J. Li, J. Qian, X. Wang, PEGylated Self-Growth MoS<sub>2</sub> on a Cotton Cloth Substrate for High-Efficiency Solar Energy Utilization, *ACS Applied Materials & Interfaces*. 10 (2018) 24583–24589. doi:10.1021/acsami.8b08019.
- [11] D. Ghim, Q. Jiang, S. Cao, S. Singamaneni, Y.-S. Jun, Mechanically interlocked 1T/2H phases of MoS<sub>2</sub> nanosheets for solar thermal water purification, *Nano Energy*. 53 (2018) 949–957. doi:10.1016/j.nanoen.2018.09.038.
- [12] Y. Gao, C. Chen, X. Tan, H. Xu, K. Zhu, Polyaniline-modified 3D-flower-like molybdenum disulfide composite for efficient adsorption/photocatalytic reduction of Cr(VI), *Journal of Colloid and Interface Science*. 476 (2016) 62–70. doi:10.1016/j.jcis.2016.05.022.
- [13] Q. Wang, L. Yang, F. Jia, Y. Li, S. Song, Removal of Cd (II) from water by using nano-scale molybdenum disulphide sheets as adsorbents, *Journal of Molecular Liquids*. 263 (2018) 526–533. doi:10.1016/j.molliq.2018.04.149.
- [14] W. Xu, X. Hu, S. Zhuang, Y. Wang, X. Li, L. Zhou, S. Zhu, J. Zhu, Flexible and Salt Resistant Janus Absorbers by Electrospinning for Stable and Efficient Solar Desalination, *Advanced Energy Materials*. 8 (2018) 1–7. doi:10.1002/aenm.201702884.
- [15] F. Jia, K. Sun, B. Yang, X. Zhang, Q. Wang, S. Song, Defect-rich molybdenum disulfide as electrode for enhanced capacitive deionization from water, *Desalination*. 446 (2018) 21–30. doi:10.1016/j.desal.2018.08.024.
- [16] Q. Wang, L. Peng, Y. Gong, F. Jia, S. Song, Y. Li, Mussel-inspired Fe<sub>3</sub>O<sub>4</sub>@Polydopamine(PDA)-MoS<sub>2</sub> core-shell nanosphere as a promising adsorbent for removal of Pb<sup>2+</sup> from water, *Journal of Molecular Liquids*. 282 (2019) 598–605. doi:10.1016/j.molliq.2019.03.052.



- [17] Y. Liu, K. Ai, L. Lu, Polydopamine and Its Derivative Materials: Synthesis and Promising Applications in Energy, Environmental, and Biomedical Fields, *Chemical Reviews*. 114 (2014) 5057–5115. doi:10.1021/cr400407a.
- [18] Y. Wang, C. Wang, X. Song, S.K. Megarajan, H. Jiang, A facile nanocomposite strategy to fabricate a rGO–MWCNT photothermal layer for efficient water evaporation, *Journal of Materials Chemistry A*. 6 (2018) 963–971. doi:10.1039/C7TA08972D.
- [19] S. Zhang, Y. Zhang, G. Bi, J. Liu, Z. Wang, Q. Xu, H. Xu, X. Li, Mussel-inspired polydopamine biopolymer decorated with magnetic nanoparticles for multiple pollutants removal, *Journal of Hazardous Materials*. 270 (2014) 27–34. doi:10.1016/j.jhazmat.2014.01.039.
- [20] L. Feng, M. Cao, X. Ma, Y. Zhu, C. Hu, Superparamagnetic high-surface-area Fe<sub>3</sub>O<sub>4</sub> nanoparticles as adsorbents for arsenic removal, *Journal of Hazardous Materials*. 217–218 (2012) 439–446. doi:10.1016/j.jhazmat.2012.03.073.
- [21] T. Lin, C. Yang, Z. Wang, H. Yin, X. Lü, F. Huang, J. Lin, X. Xie, M. Jiang, Effective nonmetal incorporation in black titania with enhanced solar energy utilization, *Energy and Environmental Science*. 7 (2014) 967–972. doi:10.1039/c3ee42708k.
- [22] X. Wu, G.Y. Chen, W. Zhang, X. Liu, H. Xu, A Plant-Transpiration-Process-Inspired Strategy for Highly Efficient Solar Evaporation, *Advanced Sustainable Systems*. 1 (2017) 1700046. doi:10.1002/adsu.201700046.
- [23] Y. Fu, T. Mei, G. Wang, A. Guo, G. Dai, S. Wang, J. Wang, J. Li, X. Wang, Investigation on enhancing effects of Au nanoparticles on solar steam generation in graphene oxide nanofluids, *Applied Thermal Engineering*. 114 (2017) 961–968. doi:10.1016/j.applthermaleng.2016.12.054.
- [24] Y. Liu, X. Wang, H. Wu, High-performance wastewater treatment based on reusable functional photo-absorbers, *Chemical Engineering Journal*. 309 (2017) 787–794. doi:10.1016/j.cej.2016.10.033.

The main content of this chapter was published on “*Renewable Energy*”.

## CHAPTER IV

### **Nanoscale MoS<sub>2</sub> nanosheets embed in 3D double layer structure (DLS) for high-efficiency solar desalination**

#### **4.1. Introduction**

To deal with the terrible freshwater shortage facing the globe, numerous technologies, such as thermal-based [1,2], membrane-based [3,4], electrochemistry-based [5,6] and solid-liquid extraction-based methods [7–9], etc. have been applied to produce clean freshwater from seawater/brackish water or industrial wastewater. However, these conventional technologies may more or less suffer from the same weaknesses such as the high energy consumption, the potential environmental pollution and the high capital cost of infrastructure construction [10]. Recently, solar desalination has been widely regarded as one of the most promising technologies to produce freshwater because of its use of inexhaustible sunlight to heat/evaporate water and its minimum greenhouse gas emissions [11,12]. Evaporator with double layer structure (DLS), which usually consisted of a top layer for photothermal conversion and a bottom layer for water supply and thermal insulator, is one of the most effective designs for solar desalination due to its excellent thermal management and efficient heat utilization [13]. The mostly considered materials for DLS-based photothermal conversions have been carbon-based materials, such as exfoliated graphite,[13] graphene oxide (GO) [14], reduced-graphene oxide (rGO) [15], polymer nanogels [16], and carbon nanotubes (CNT) [17]. Unfortunately, these carbon-based DLSs usually required high-temperature procedures and complex synthesis steps in their preparations, rising wide concerns about their cost and feasibility in their practical applications [18]. Recently, nanoscale MoS<sub>2</sub> was believed to be one of the most promising materials for solar desalination because of its excellent light-absorbing properties, easy composite processing and earth-abundant reserves [19–21]. For instance, the strong absorption (>70%) in atomically thin MoS<sub>2</sub> films ( $\leq 4$  layers) for narrowband incidence with arbitrarily prespecified wavelengths or broadband incidence like solar radiation was realized by leveraging on resonant photonic structures [22]. The single-walled nanotube–MoS<sub>2</sub> hybrid two-dimensional membrane with thickness of 120 nm exhibited an light-absorbing capacity of over 82% in the whole range of solar spectrum, which accounted for its high evaporation of 91.5% at the power density of 5 kW m<sup>-2</sup> [21]. However, the potential application of

MoS<sub>2</sub> as light absorbers especially for solar desalination has not been efficiently investigated, since some progress still should be made: (1) increasing the solar evaporation efficiency to enable MoS<sub>2</sub>-based evaporators more competitive with other advanced materials, (2) developing efficient system designs for MoS<sub>2</sub>-based evaporators that can efficiently utilize lower solar power (<3 kW m<sup>-2</sup>), and (3) developing high-efficiency and recyclable MoS<sub>2</sub>-based evaporators to meet its commercial application.

Herein, this work demonstrated the use of a novel MoS<sub>2</sub>-based 3D evaporator with DLS for solar desalination. The nanoscale MoS<sub>2</sub> embed in the top layer of the DLSs played the critical role of the solar-to heat conversion, while the bottom layer with highly enhanced fluid transport ability worked as the water pump. Besides its mechanical stability and recyclability, the solar desalination performance of the MPU-PPU evaporator and the working mechanisms have been investigated in detail. This work provided a novel strategy for constructing the solar evaporators with DLS that could be applied in desalination or water purification, which might contribute to mitigating the terrible water scarcity.

## 4.2. Experimental sections

### 4.2.1. Materials

Thiourea (CN<sub>2</sub>H<sub>4</sub>S), tris(hydroxymethyl)aminomethane (C<sub>4</sub>H<sub>11</sub>NO<sub>3</sub>, Tris), hexaammonium heptamolybdate tetrahydrate ((NH<sub>4</sub>)<sub>6</sub>Mo<sub>7</sub>O<sub>24</sub>·4H<sub>2</sub>O), ethanol (C<sub>2</sub>H<sub>6</sub>O), dopamine hydrochloride (C<sub>8</sub>H<sub>11</sub>NO<sub>2</sub>·HCl) was supplied by Shanghai Aladdin Bio-Chem Technology Co., Ltd. Hydrochloric acid (HCl) was purchased from Merck Pty. Ltd. Ordinary PU sponge (pore diameter: ~150 μm, density: 30 kg/m<sup>3</sup>) was purchased from Golden Rabbit Fabrics in Suqian city, China. Cloth special glue (Yingligu, YLG-B30) was bought from Dongguan Huigu Adhesive Products Co., Ltd. All chemicals were of analytical purity. Deionized Milli-Q water (18.2 MΩ cm, Millipore Corporation, France) was used in all the experiments.

### 4.2.2. Fabrication of MPU-PPU evaporator

**Synthesis of MoS<sub>2</sub>.** MoS<sub>2</sub> was prepared based on the reported works [23,24]. In detail, 2.48 g of (NH<sub>4</sub>)<sub>6</sub>Mo<sub>7</sub>O<sub>24</sub>·4H<sub>2</sub>O and 4.56 g of CN<sub>2</sub>H<sub>4</sub>S was dissolved in 72 mL of pure water. The mixture was then heated at 220°C for 6 h in a 100 mL Teflon-lined stainless-steel autoclave and finally naturally cooled to room temperature. The resultant black samples were washed with ultrapure water and ethanol for three times,

and then dried by vacuum freeze-drying.

**Fabrication of nanoscale MoS<sub>2</sub> embedded on PU sponge (MPU).** Firstly, the as-prepared MoS<sub>2</sub> (0.1 g) was dispersed into water solution (200 mL) and then treated by ultrasonic method at 150 W for 30 min to exfoliate MoS<sub>2</sub> and form the homogeneously dispersions. Secondly, the cylindrical PU sponges (diameter: 5.0, thicknesses: 0.2, 0.5, 1.0 and 2.0 cm), which had been immersed in ethanol solution for approximately 8 h to remove the inside organic purities and then dried in air oven at 80°C for 2 h, were then entirely immersed in the MoS<sub>2</sub> dispersions and repeatedly pressed with three abreast fingers for 50 times. Note that this procedure was extremely critical to the efficient immobilization of nanoscale MoS<sub>2</sub> on the frameworks of the sponge as shown in Fig. 4.1, which suggested that no press or inefficient press would lead to the inefficient immobilization of nanoscale MoS<sub>2</sub> on PU sponge. Thirdly, after being shaken at 150 rpm for different hours, the black and wet sponge was taken out without any press and then dried at 60°C for 12 h in an air oven. At last, the dried sponge was placed in the palms and rinsed with deionized water while being repeatedly pressed until there was not any shedding items in the discharged solutions, and then dried again in an air oven at 80°C for another 12 h.

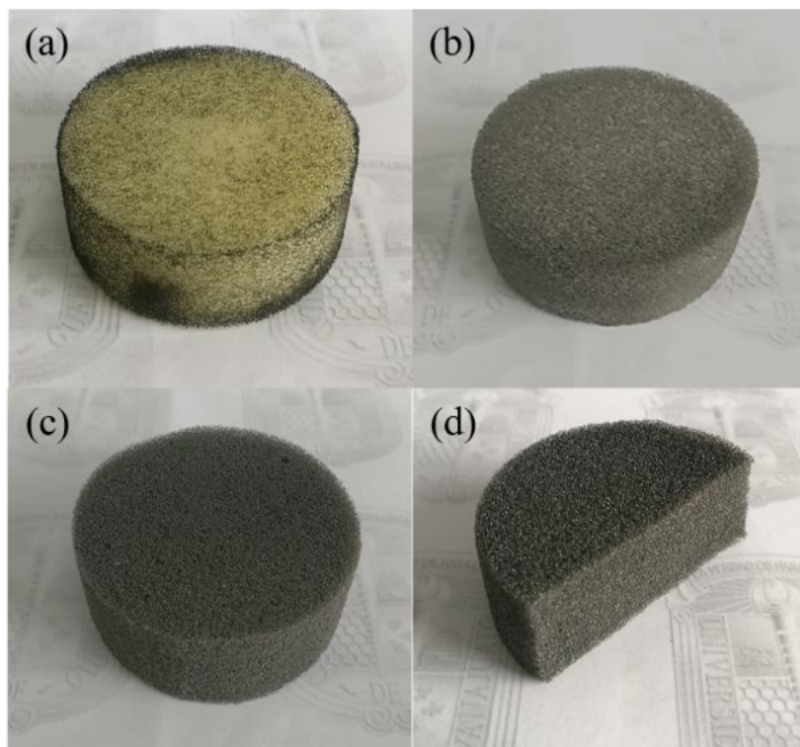


Fig. 4.1. Optical images of PU sponge immersed in MoS<sub>2</sub> dispersions for 6 h (a) without being pressed, (b) with being repeatedly pressed for 20 times, and (c) with being repeatedly pressed for 50 times. (d) the cross-section image of (c).

**Fabrication of polydopamine modified PU sponge (PPU).** Firstly, the washed sponge was immersed in a beaker containing 200 mL, 2 g/L dopamine buffers (10 mM Tris, pH 8.5), and repeatedly pressed with three abreast fingers for 50 times. Secondly, the beaker was transferred into room-temperature water base and shaken at 150 rpm for different time. The beaker mouth kept open to ensure its sufficient exposure to oxygen. The black sponge was then dried in an air oven at 80°C for 12 h. Finally, the sponge was rinsed with deionized water until there was not any shedding items in the discharged solutions, then dried in an air oven at 80°C for 12 h.

**Construction of MPU-PPU evaporator.** A piece of MPU (diameter: 5.0 cm, various thickness: 0.2, 0.5, 1.0 and 1.5 cm) and PPU (diameter: 5.0 cm, thickness: 1.0 cm) were glued together by the cloth glue and dried at 60°C for around 30 min, to form evaporators with DLSs. PU-PU and MPU-PU evaporators (top layer: 0.5 cm) were also prepared by the similar way for comparative experiments.

#### 4.2.3. Characterization methods

The structure of MoS<sub>2</sub> was analyzed by powder X-ray diffraction measurement (XRD, PIXcel-Empyrean). The morphology of samples was obtained from scanning electron microscopy (SEM; Hitachi S-4700). The X-ray photoelectron spectroscopy was recorded on an X-ray photoelectron spectrometer (Escalab 250Xi, Thermo Fisher Scientific). The contact angles were measured with intravenous drip method on a standard contact angle analyzer (JC2000A). The solar absorption of samples was measured by an ultraviolet-visible-near infrared diffuser reflectance spectrophotometer (LAMBDA950). An ion chromatography (Dionex Aquion) and an inductively coupled plasma atomic emission spectroscopy (ICP-AES, Prodigy 7) were applied to determine the concentrations of anions and cations in solutions, respectively.

#### 4.2.4. Experiments of solar desalination

The broadband illumination was supplied by the solar simulator (Perfectsolar M300) and controlled to be low solar density of 0-2.5 kW m<sup>-2</sup>. The solar intensity was measured by the Perfectsolar PL-MW2000 photoradiometer. A beaker containing the floating evaporator and saline water was placed on an electronic balance (Shanghai Yueping, YP6002, accuracy: 0.01 g) for real-time measurements of water mass changes. The probe of an electronic temperature logger (Jingchuang GSP-6) was inserted into the top layer of the evaporators to record the temperature vibration. An

ion chromatography (Dionex Aquion) and an inductively coupled plasma atomic emission spectroscopy (ICP-AES, Prodigy 7) were applied to determine the concentrations of anions and cations in aqueous solutions before and after solar desalination, respectively. All experiments of solar desalination were finished under the condition that the ambient temperature had been kept at  $23 \pm 2^\circ\text{C}$  by the air conditioner and the ambient humidity had been  $30 \pm 5\%$ .

### **4.3. Results and discussion**

#### **4.3.1. Preparation and characterization**

Fig. 4.2(a) illustrated the constructing strategy of MPU-PPU evaporator with DLS, which worked as a self-floating interfacial solar evaporating system. The washed PU sponge was immersed in 200 mL,  $0.5 \text{ g L}^{-1}$  MoS<sub>2</sub> dispersions. In this case, nanoscale MoS<sub>2</sub> in solutions would be immobilized onto the frameworks of the sponge because of the formation of the interlocked structure and the existence of electrostatic attraction, acquiring the nanoscale MoS<sub>2</sub> supported on PU sponge. Another piece of PU sponge was modified by polydopamine to change the poor fluid transport caused by its super hydrophobicity of the PU sponge, and the resultant sponge was noted as PPU. MPU and PPU were then assembled together with the appropriate glue to form the evaporator with DLS. Such an evaporator possessed the excellent self-floating property because of its lower inherent density than that of water. In the solar desalination system as illustrated in Fig. 4.2(b), the MPU-PPU evaporator, which could float on the saltwater's surface because of its low density, was placed in the internal container of the system to harvest solar energy and evaporate water, while the generated vapors were condensed and collected by a clean glass plate. The wall of the inner container was filled with cotton, which could work as an insulation layer to minimize the heat loss. In detail, the sunlight could be absorbed and then converted into heat by the MoS<sub>2</sub> to evaporate water inside the upper layer, while the unheated water was transferred to the upper layer from the bottom layer via the internal capillary force.

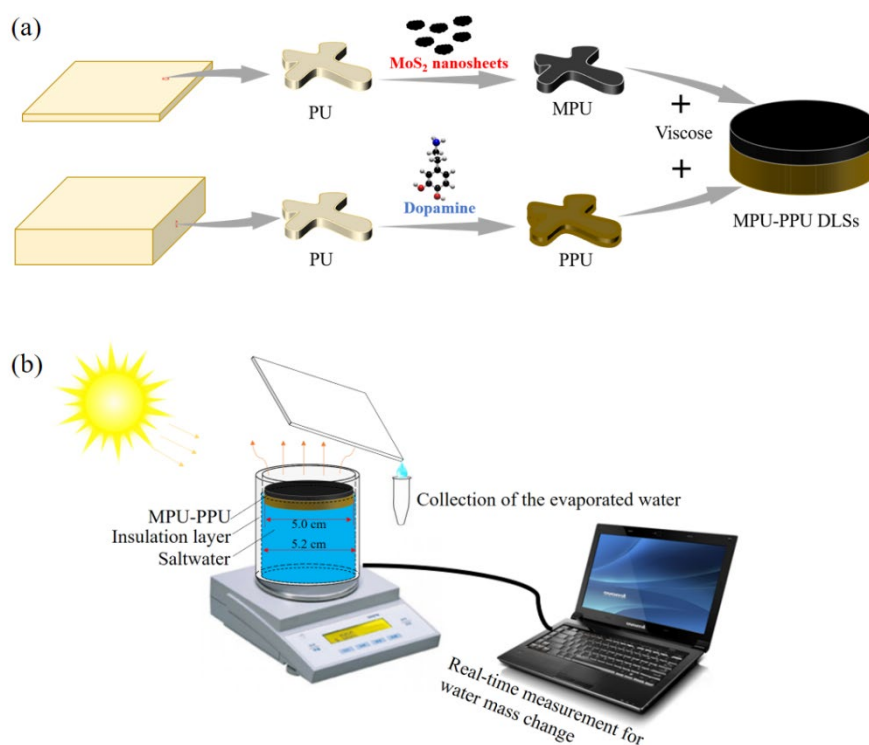


Fig. 4.2. (a) Illustration of constructing the MPU-PPU evaporator with DLSs. (b) Schematic illustration of solar desalination system by MPU-PPU evaporator.

The structure and morphology of the fabricated MPU-PPU evaporator were characterized by XRD and SEM. Fig. 4.3(a) displays the XRD pattern of the as-synthesized MoS<sub>2</sub>. The synthesized MoS<sub>2</sub> displayed five typical diffraction peaks at 13.8°, 32.3°, 35.5°, 43.0° and 57.6°, which were attributed to the (002), (100), (103), (105) and (110) crystal planes of the hexagonal phase MoS<sub>2</sub>, respectively [25]. The (002) reflection peak was found to be shifted a lot from its expected  $2\theta=14^\circ$ , indicating that the treated MoS<sub>2</sub> was five or less layered graphene-like MoS<sub>2</sub> [19]. It could be observed from Fig. 4.3(b) that the nanoscale MoS<sub>2</sub> was in their petal-shapes with lateral dimension of  $\sim 200$  nm. Interestingly, one side of nanoscale MoS<sub>2</sub> was open while the other side were linked together, forming the flower-like architectures as reported before [26]. It was also found that the pore sizes of the porous PU sponges ranged from 100  $\mu\text{m}$  to 400  $\mu\text{m}$ , and nanoscale MoS<sub>2</sub> was only deposited on the frameworks of the sponge without blocking the pores as displayed in Fig. 4.4. These large pores could contribute to the vapor escape [13], which consequently contributed to the vapor generation. To investigate the maximum capacity of nanoscale MoS<sub>2</sub> loaded on the PU sponge, the sponges (dry weight:  $\sim 1.0$  g) were immersed in 200 mL suspension solutions containing 0.1 g treated MoS<sub>2</sub> for various time and their mass changes were recorded. As displayed in Fig. 4.3(c), the mass of nanoscale MoS<sub>2</sub>

loaded on sponges increased with the prolongation of immersion time, and then leveled off when the immersing time was over 6 h. The maximum capacity of nanoscale MoS<sub>2</sub> loaded on PU sponge was calculated to be 66.2 mg g<sup>-1</sup>, suggesting more than 66wt% of the nanoscale MoS<sub>2</sub> in the suspensions could be immobilized onto the frameworks of the sponges.

Fig. 4.3(d) and Fig. 4.3(e) showed the surface morphology of PU sponges before and after the immobilization of nanoscale MoS<sub>2</sub>, respectively. It was found that the framework of the raw sponge has clean surface with wrinkles, and after the immobilization of MoS<sub>2</sub>, a great amount of nanoscale MoS<sub>2</sub> was embedded into these wrinkles, forming the interlocked architectures, which was confirmed by the insert image of Fig. 4.3(e) with higher magnification. In addition, nanoscale MoS<sub>2</sub> could be immobilized on the surfaces of these frameworks because of the existence of electrostatic attraction [27]. Thus, both the interlocked structure and the electrostatic attraction mainly accounted for the high capacity and tough immobilization of nanoscale MoS<sub>2</sub> on the frameworks of the PU sponge. Note that the assembling of nanoscale MoS<sub>2</sub> also altered the surface of PU sponge from solar yellow and relatively smooth into deep black and highly rough, which was beneficial for the solar absorption capability and low solar reflectance, respectively [11]. Fig. 4.3(f) displayed the photographs of the evaporators under front and back folds, demonstrating its excellent mechanical stability and great flexibility.

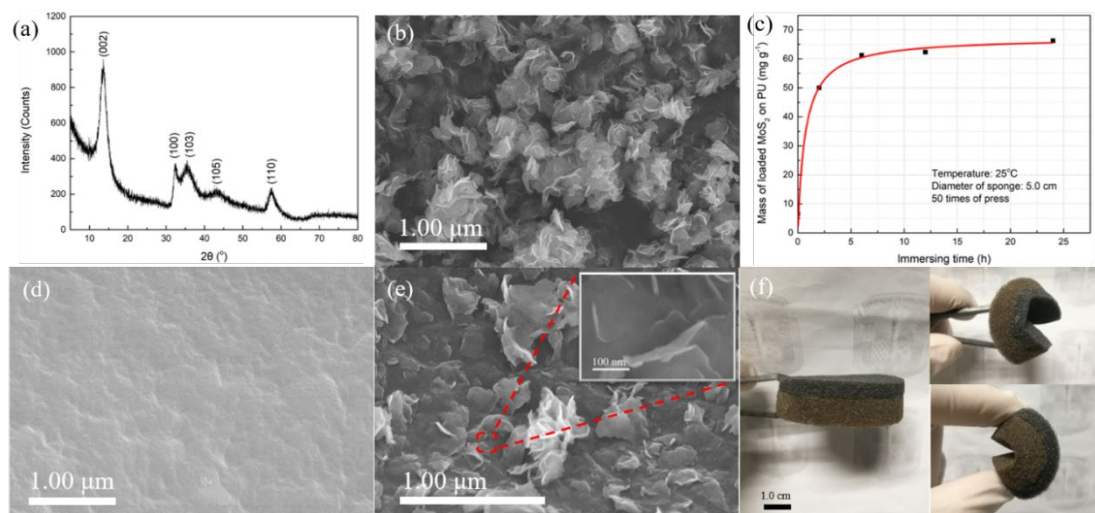


Fig. 4.3 (a) XRD spectrum and (b) SEM images of the synthesized MoS<sub>2</sub>. (c) Mass of MoS<sub>2</sub> loaded on PU over immersing time. (d) SEM images of raw PU sponge and (e) MoS<sub>2</sub> supported on PU sponge. (f) Optical image of the flexible evaporators (Layer thickness: top: 0.5 cm, bottom: 1.0 cm).



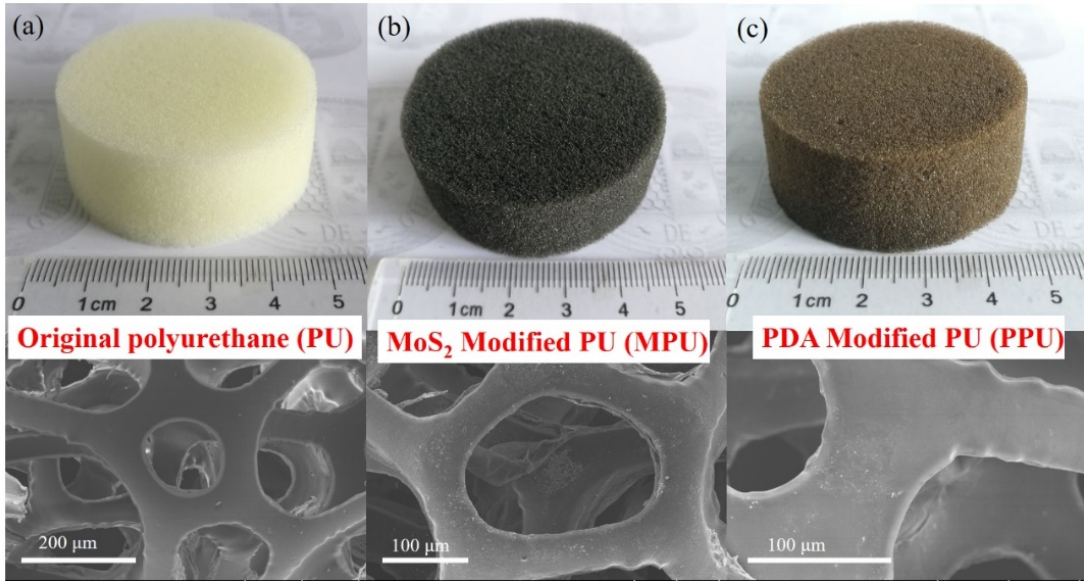


Fig. 4.4 Optical images and SEM images of (a) raw PU, (b) MoS<sub>2</sub> supported on PU (MPU) and (c) PDA modified PU (PPU). (Diameter: 5.0 cm, thickness: 2.0 cm).

#### 4.3.2. Solar desalination performance

Fig. 4.5(a) displayed that an obvious and visible vapor stream was generated under 1.0 kW m<sup>-2</sup> at around 20 min with the MPU-PPU (thickness: top layer, 0.5 cm, bottom layer 1.0 cm) serving as the evaporator. The working glass-cup contained 150 mL, 3.5wt% NaCl solution, which was often used as an alternative to the real seawater [28,29]. The water mass changes as a function of time were given in Fig. 4.5(b). In general, the cumulative water mass loss was increased slowly at the initial several minutes and then increased linearly with the illumination time. The transition period at the initial several minutes was related to the energy consumption required to initialize the evaporation process [26]. The values of stable evaporation rates were obtained from the slope of these curves after subtracting the initial transition period of ~10 min (Fig. 4.6). The performance of solar evaporation was further assessed by calculating their evaporation efficiency ( $\eta$ ), which was defined as Eq. 4.1):[19]

$$\eta = \dot{m}h_{LV}/q_i C_{opt} \quad 4.1$$

where  $\eta$  is the solar energy conversion efficiency, %;  $\dot{m}$  is the stable evaporation rates, kg m<sup>-2</sup> h<sup>-1</sup>;  $h_{LV}$  represents the liquid-vapor phase conversion enthalpy which consists of sensible heat and phase change enthalpy, 2.257 kJ g<sup>-1</sup>;  $q_i$  means the normalized solar intensity, 1.0 kW m<sup>-2</sup>;  $C_{opt}$  is the multiple of 1.0 kW m<sup>-2</sup>.

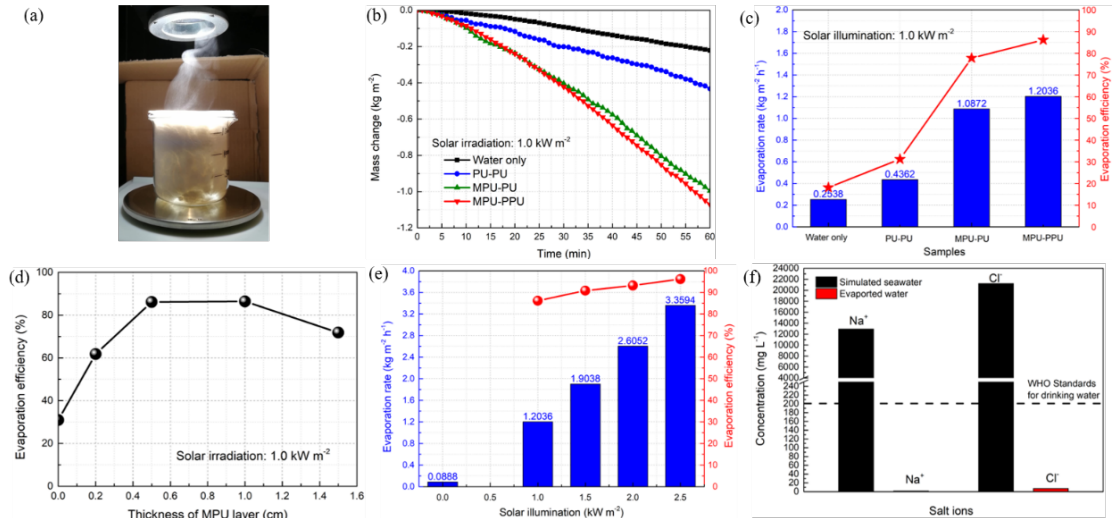


Fig. 4.5. (a) The optic image of solar steam generation derived from MPU-PPU evaporator under illumination of  $1.0 \text{ kW m}^{-2}$  at  $\sim 20$  min. (b) Mass change over time of various evaporators under illumination of  $1.0 \text{ kW m}^{-2}$ . (c) Evaporation rates and the corresponding evaporation efficiency of various evaporators. (d) Effect of the thickness of top MPU layer on the evaporation efficiency of MPU-PPU evaporators. (e) Evaporation rates and corresponding efficiency of under illumination of 0, 1.0, 1.5, 2.0 and  $2.5 \text{ kW m}^{-2}$ . (f) Comparison of the ion concentrations in aqueous solutions before and after solar desalination by MPU-PPU evaporator.

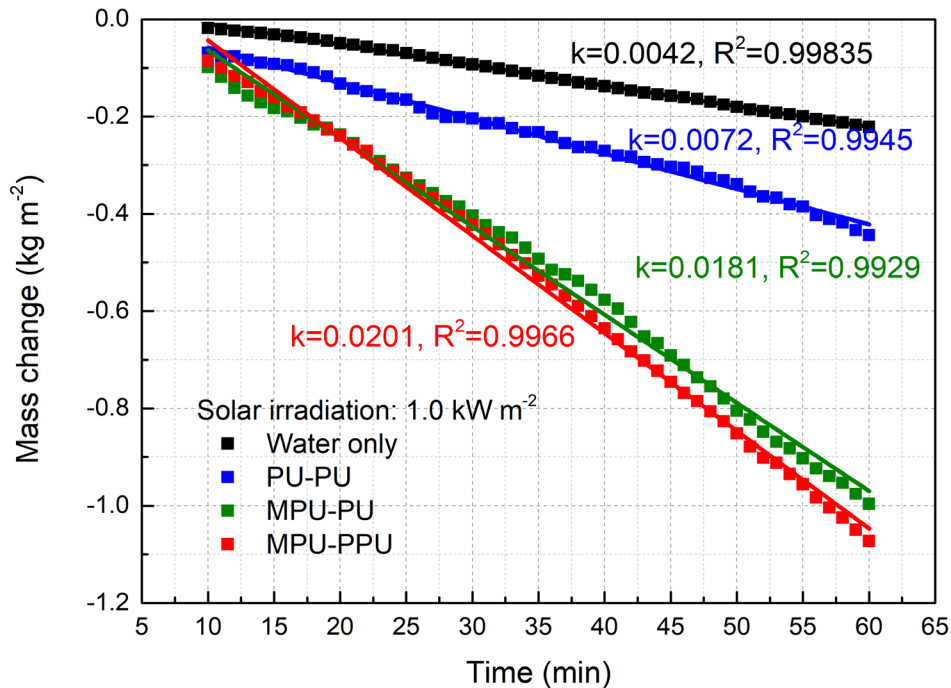


Fig. 4.6. Linear fitting results of the mass change curves of various evaporators under solar irradiation of  $1.0 \text{ kW m}^{-2}$ .

The stable water evaporation rates and the corresponding evaporation efficiency of various evaporators under illumination of  $1.0 \text{ kW m}^{-2}$  were displayed in Fig. 4.5(c). The evaporation rate was  $0.436 \text{ kg m}^{-2} \text{ h}^{-1}$  after the addition of PU-PU evaporator and further increased to  $1.087 \text{ kg m}^{-2} \text{ h}^{-1}$  after the introduction of MPU-PU evaporator. Impressively, the highest evaporation rate of  $1.204 \text{ kg m}^{-2} \text{ h}^{-1}$  was achieved by the introduction of MPU-PPU evaporator, indicating that the evaporation performance of MPU-PU evaporator was much superior to that of the other two evaporators. In addition, the evaporation efficiency of water with MPU-PPU evaporator reached a high level of 86.2% even under a low illumination of  $1.0 \text{ kW m}^{-2}$ , which was not only higher than that of MPU-PU (77.8%) but also most of reported works with evaporation efficiency of typically 50-70% under one-sun illumination (Table 4.1).

Table 4.1. Recent works of solar steam generation systems.

| Materials                | Power density<br>( $\text{kW m}^{-2}$ ) | Evaporation rate<br>( $\text{kg m}^{-2} \text{ h}^{-1}$ ) | Evaporation<br>efficiency (%) | Refs      |
|--------------------------|---|---|-------------------------------|-----------|
| F-Wood/CNTs              | 1                                       | 0.95  | 65                            | [17]      |
| H-G foam                 | 1                                       | 1.4   | 90                            | [31]      |
| PDA                      | 1                                       | 1.13  | 78                            | [32]      |
| Wood-PDA                 | 1                                       | 1.38  | 87                            | [33]      |
| rGO film                 | 1                                       | 1.14  | 89.2                          | [34]      |
| HNG3                     | 1                                       | 3.2   | 94                            | [16]      |
| SM-BPU sponge            | 1                                       | 0.83  | $52.2 \pm 2.5$                | [35]      |
|                          | 5                                       | 4.24  |                               |           |
| PEG/MoS <sub>2</sub> -CC | 1                                       | 1.3   | 80.1                          | [19]      |
|                          | 5                                       | 7.03  | 90.3                          |           |
| SWNT-MoS <sub>2</sub>    | 0.8                                     | 0.9   | 81                            | [36]      |
|                          | 5                                       | 6.6   | 91.5                          |           |
| ce-MoS <sub>2</sub>      | 0.76                                    | 0.81  | 75.7                          | [37]      |
|                          | 5.35                                    | 6.15  | 81.4                          |           |
| MPU-PPU                  | 1                                       | 1.20  | 86.2                          | This work |
|                          | 1.5                                     | 1.90  | 90.9                          |           |
|                          | 2.0                                     | 2.60  | 93.2                          |           |
|                          | 2.5                                     | 3.36  | 96.2                          |           |

To investigate the influence of MPU layer's thickness on the evaporating

performance, various MPU-PPU evaporators consisted of MPU (thickness: 0, 0.2, 0.5, 1.0 and 1.5 cm) and PPU (thickness: 1.0 cm) were fabricated. Their evaporation performance was then displayed in Fig. 4.5(d) and Fig. 4.7. With the thickness of MPU layer increasing from 0 cm to 1.0 cm, the evaporation efficiency increased from 30.1% to 86.4% and then leveled off, indicating the necessary existence of MoS<sub>2</sub> layer and the benefits of thicker MPU layer. The MPU layer with thickness of 0.2 cm failed to work as the most effective solar absorber since a great deal of solar illumination had been penetrated, while MPU layer with thickness of 0.5 cm and 1.0 cm exhibited the best solar absorption (Fig. 4.8). Thus, the increasing evaporation rates was derived from the thicker MPU layer with the enhanced solar adsorption. Nevertheless, the evaporation efficiency would decrease to 71.8% if the thickness further increased to 1.5 cm, which might be attributed to the unfavorable long-distance water transport as well as the poor hydrophilicity of MoS<sub>2</sub> inside the much thicker MPU layer.

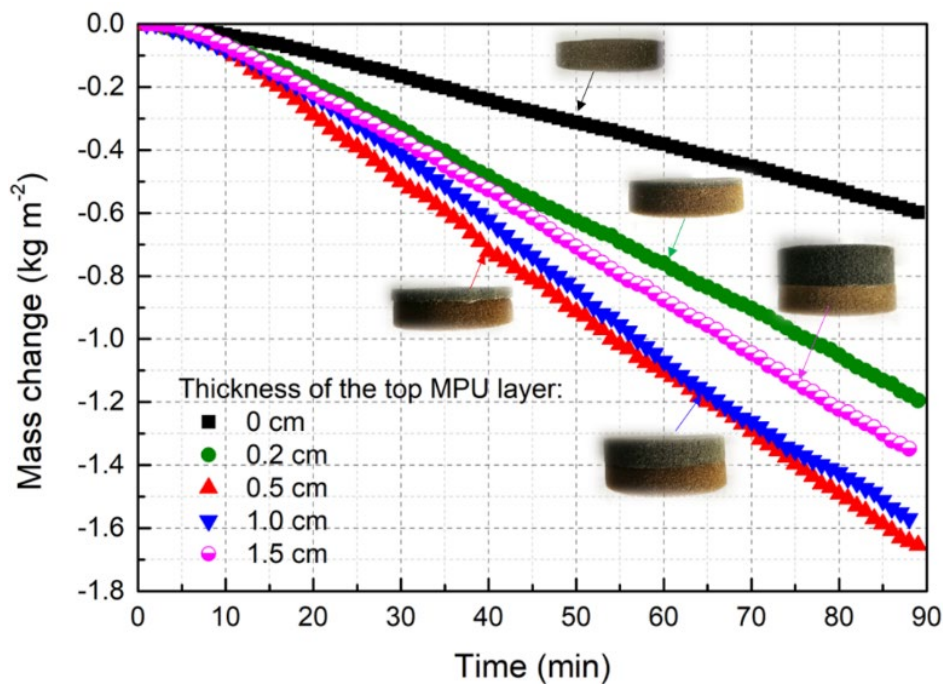


Fig. 4.7. Effect of the thickness of top MPU layer inside the DLSs on their evaporation rates.

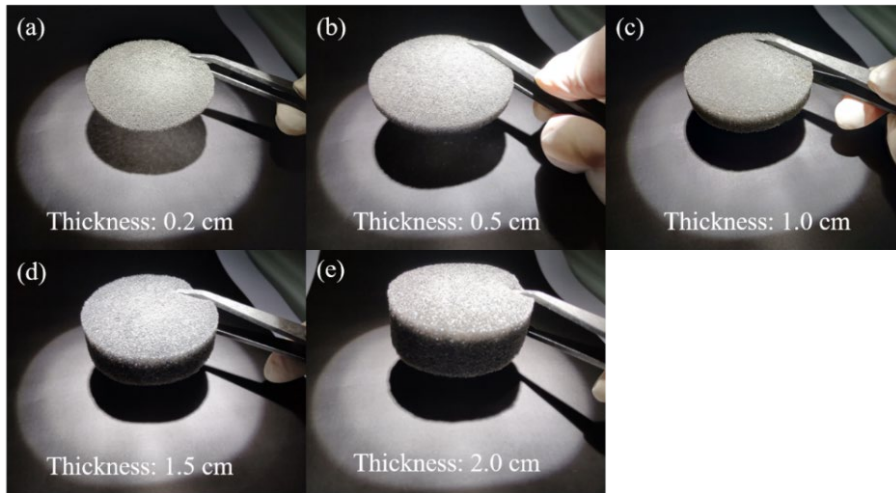


Fig. 4.8. Optical images of MPU layer with different thickness (0.2, 0.5, 1.0 and 1.5 cm) under illumination of  $1.0 \text{ kW m}^{-2}$ .

As shown in Fig. 4.5(e) and Fig. 4.9, under irradiation of 1.0, 1.5, 2.0 and 2.5  $\text{kW m}^{-2}$ , the evaporation rates of water with MPU-PPU evaporator were 1.20, 1.90, 2.61 and 3.36  $\text{kg m}^{-2} \text{ h}^{-1}$ , which was 13.6, 21.4, 29.3 and 37.8 times of natural evaporation rate of seawater in dark conditions ( $0.089 \text{ kg m}^{-2} \text{ h}^{-1}$ ), respectively. The corresponding evaporation efficiency of the MPU-PPU evaporator reached a high level of 86.2% at a low illumination of  $1.0 \text{ kW m}^{-2}$  and superhigh level over 90% at higher solar illumination ( $1.5\text{-}2.5 \text{ kW m}^{-2}$ ).

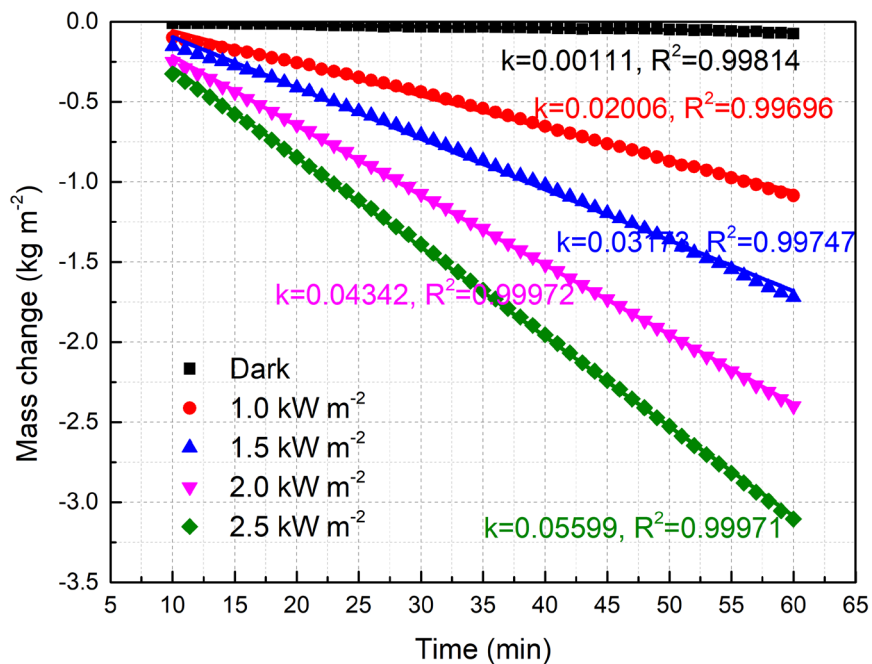


Fig. 4.9. Mass change over time of the MPU-PPU evaporator under illuminations of 0, 1.0, 1.5, 2.0 and 2.5  $\text{kW m}^{-2}$ .

As displayed in Fig. 4.5(f), the concentrations of  $\text{Na}^+$  and  $\text{Cl}^-$  ions after solar desalination had been reduced to an extremely low level of  $1.3 \text{ mg L}^{-1}$  and  $6.9 \text{ mg L}^{-1}$ , which was far below the World Health Organization (WHO) standards for drinking water with limits of  $200 \text{ mg L}^{-1}$  [30], demonstrating the MPU-PPU evaporator an effective device for solar desalination. The recyclability of the MPU-PPU evaporator was also one of the most vital parameters for its practical application. The MPU-PPU evaporator exhibited the similar evaporation performances even after being tested for ten cycles under 1-h illumination of  $1.0 \text{ kW m}^{-2}$  (Fig. 4.10), indicating its excellent recyclability. As shown in Fig. 4.11, no obvious change was found on the top surface of MPU-PPU evaporator after ten cycles of use, directly suggesting the stable immobilization of  $\text{MoS}_2$  in the DLS. Thus, this DLS provided great possibility in its commercial use because of its high desalination efficiency and well durability. Besides the outstanding performance for solar desalination, the MPU-PPU evaporator held the promising application prospects in other related fields such as photocatalysis fields and the water pollution treatments because of its excellent capacity of solar harvesting and its 3D network structures for free-separation.

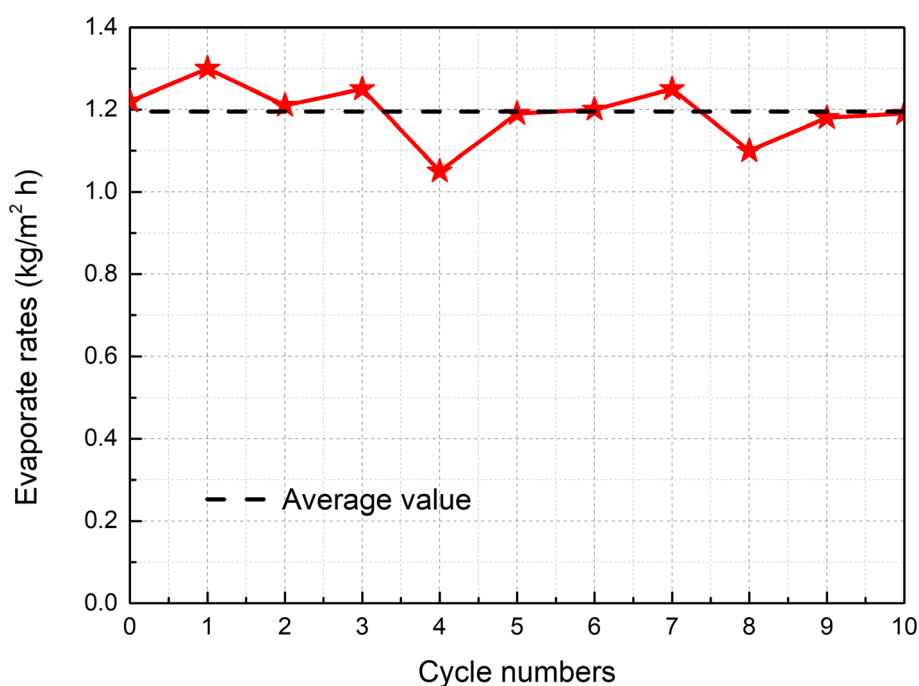


Fig. 4.10. Concentration of  $\text{Na}^+$  and  $\text{Cl}^-$  in the simulated seawater and evaporated water.

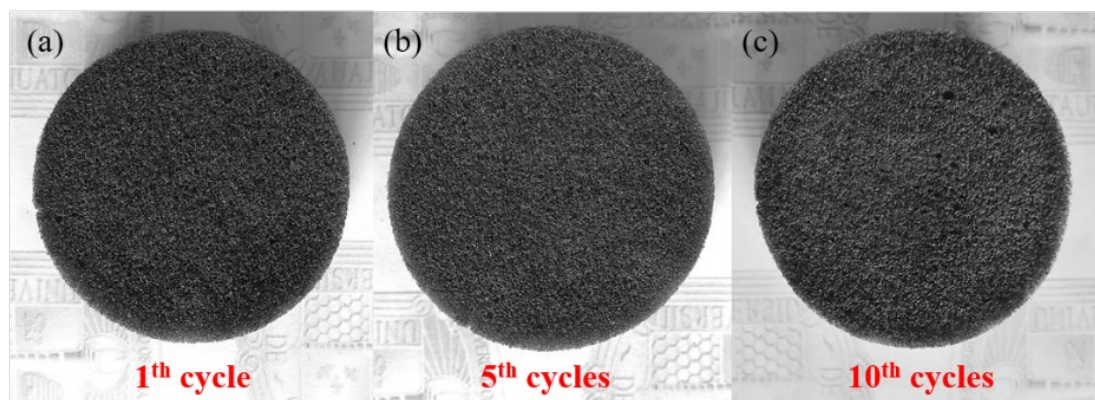


Fig. 4.11. Optical images of the top surface of MPU-PPU after 1<sup>th</sup>, 5<sup>th</sup> and 10<sup>th</sup> cycles.

### 4.3.3. Working mechanisms of high-efficiency solar desalination

As shown in Fig. 4.12(a), nanoscale MoS<sub>2</sub> synthesized by the hydrothermal methods had a superhigh solar absorption (>95.0%) within a broadband wavelength from 400 to 1800 nm and a high solar absorption (>85%) between 1800 and 2500 nm, indicating the sufficient solar harvesting of nanoscale MoS<sub>2</sub> in the whole range of sunlight [19]. The high-performance solar absorption capacity of the synthesized nanoscale MoS<sub>2</sub> was mainly attributed to the following factors: (1) the highly enhanced surface area of MoS<sub>2</sub> for solar absorption due to its nano-petal shapes; (2) the enhanced internal electronic vibration caused by the nanocrystal size of MoS<sub>2</sub> sample; (3) the multiple internal reflection of the achieved solar derived from the hierarchical nanoflower layers of MoS<sub>2</sub> [36,38]. Such a high solar absorption laid foundations for a high-performance solar energy conversion. If the heat loss was negligible, the surface temperature of the evaporators was critical to the evaporation process.[39]As displayed in Fig. 4.12(b), the surface temperatures of single seawater, PU-PU, MPU-PU and MPU-PPU evaporators were recorded over time under illumination of 1.0 kW m<sup>-2</sup>. High temperatures (~55°C) could be maintained on top surfaces of both MPU-PU evaporator and MPU-PPU evaporator, suggesting the high photothermal conversion capacity of nanoscale MoS<sub>2</sub>. As shown in Fig. 4.12(c), both the PU layer and the PPU layer exhibited the extremely low thermal conductivity, which could act as the thermal isolators inside the MPU-PU and MPU-PPU evaporators for restraining the thermal energy from diffusing into the unheated water. Namely, low thermal conductivity of bottom layer inside the evaporators with DLS contributed to suppressing heat dissipation into the bulk water, forming the heat localization on the top layer. Moreover, the wetting property of the bottom layer was also characterized by measuring the water contact angle. As illustrated in Fig. 4.12(d),

the contact angles on the top surfaces gradually decreased from  $132^\circ$  to  $76^\circ$  with the increase of the PDA-modification time, indicating the change of bottom layer from superhydrophobic into hydrophilic. Therefore, the hydrophilic property of water transport path would be improved because water was more effectively transported into the air-water interface through the porous transport channels. This was also responsible for higher the evaporating performance of MPU-PPU than that of MPU-PU. In addition, the inherent porous networks inside the upper MPU layer as aforementioned also offered the evaporator with abundant channels for vapor escape. As concludingly illustrated in Fig. 4.12(e), the four factors: (1) high photothermal efficiency, (2) localized heating effect, (3) hydrophilic bottom layer to leverage capillary forces and promote fluid flow to the hot region, together with (4) the porous structure which enabled efficient water supply and vapor channel, guaranteed the MPU-PPU with DLS an ideal evaporator for high-performance solar desalination.

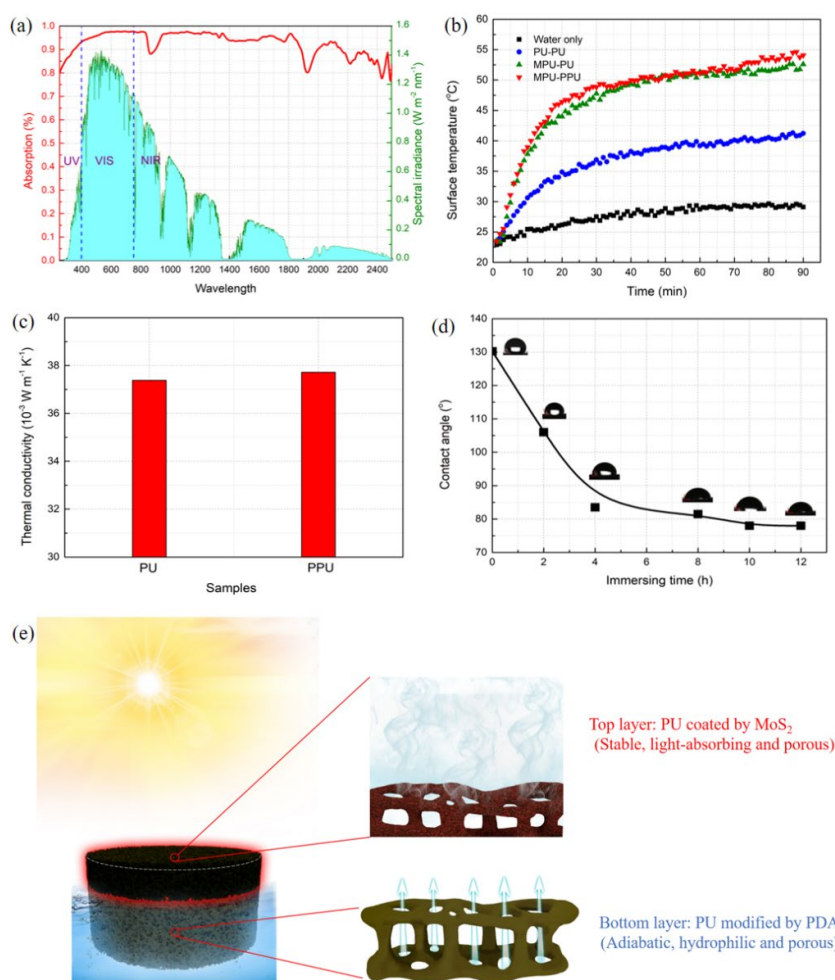


Fig. 4.12. (a) Solar absorption property of the synthesized nanoscale MoS<sub>2</sub>. (b) Temperature variations on the top surfaces of seawater, PU-PU, MPU-PU and MPU-PPU evaporators as a



function of time under illumination of  $1.0 \text{ kW m}^{-2}$ . (c) The thermal conductivity of the bottom layers of the evaporators. (d) Contact angles of PPU as a function of treated time in PDA solution. (e) Schematic diagram of working mechanisms of the MPU-PPU evaporator for solar desalination.

#### 4.4. Conclusions

In summary, a simple, available, low-cost evaporator with DLS had been successfully developed for high-efficiency solar desalination. High solar evaporation efficiency of 86.2 % even under a low illumination of  $1.0 \text{ kW m}^{-2}$  and superhigh evaporation efficiency over 90% under solar illumination of  $1.5\text{-}2.5 \text{ kW m}^{-2}$  were achieved, which outperformed many other reported advanced materials for solar desalination. The MPU-PPU evaporator provided great possibility in its commercial use because of its high desalination efficiency and well durability.

#### REFERENCES

- [1] A. Gambler, E. Badreddin, Dynamic modelling of MSF plants for automatic control and simulation purposes: A survey, *Desalination*. 166 (2004) 191–204. doi:10.1016/j.desal.2004.06.073.
- [2] H. Sayyaadi, A. Saffari, Thermoeconomic optimization of multi effect distillation desalination systems, *Applied Energy*. 87 (2010) 1122–1133. doi:10.1016/j.apenergy.2009.05.023.
- [3] W. Suwaileh, D. Johnson, S. Khodabakhshi, N. Hilal, Superior cross-linking assisted layer by layer modification of forward osmosis membranes for brackish water desalination, *Desalination*. 463 (2019) 1–12. doi:10.1016/j.desal.2019.04.009.
- [4] G. Amy, N. Ghaffour, Z. Li, L. Francis, R.V. Linares, T. Missimer, S. Lattemann, Membrane-based seawater desalination: Present and future prospects, *Desalination*. 401 (2017) 16–21. doi:10.1016/j.desal.2016.10.002.
- [5] Y. Oren, Capacitive deionization (CDI) for desalination and water treatment - past, present and future (a review), *Desalination*. 228 (2008) 10–29. doi:10.1016/j.desal.2007.08.005.
- [6] S. Al-Amshawee, M.Y.B.M. Yunus, A.A.M. Azodein, D.G. Hassell, I.H. Dakhil, H.A. Hasan, Electrodialysis desalination for water and wastewater: A review, *Chemical Engineering Journal*. 380 (2020) 122231. doi:10.1016/j.cej.2019.122231.
- [7] Q. Wang, L. Yang, F. Jia, Y. Li, S. Song, Removal of Cd (II) from water by using nano-scale molybdenum disulphide sheets as adsorbents, *Journal of Molecular Liquids*. 263 (2018) 526–533. doi:10.1016/j.molliq.2018.04.149.
- [8] F. Jia, Q. Wang, J. Wu, Y. Li, S. Song, Two-Dimensional Molybdenum Disulfide as a

- Superb Adsorbent for Removing Hg<sup>2+</sup> from Water, *ACS Sustainable Chemistry & Engineering*. 5 (2017) 7410–7419. doi:10.1021/acssuschemeng.7b01880.
- [9] Q. Wang, L. Peng, Y. Gong, F. Jia, S. Song, Y. Li, Mussel-inspired Fe<sub>3</sub>O<sub>4</sub>@Polydopamine(PDA)-MoS<sub>2</sub> core-shell nanosphere as a promising adsorbent for removal of Pb<sup>2+</sup> from water, *Journal of Molecular Liquids*. 282 (2019) 598–605. doi:10.1016/j.molliq.2019.03.052.
- [10] L. Zhu, M. Gao, C.K.N. Peh, G.W. Ho, Recent progress in solar-driven interfacial water evaporation: Advanced designs and applications, *Nano Energy*. 57 (2019) 507–518. doi:10.1016/j.nanoen.2018.12.046.
- [11] Y. Wang, C. Wang, X. Song, S.K. Megarajan, H. Jiang, A facile nanocomposite strategy to fabricate a rGO-MWCNT photothermal layer for efficient water evaporation, *Journal of Materials Chemistry A*. 6 (2018) 963–971. doi:10.1039/C7TA08972D.
- [12] F.E. Ahmed, R. Hashaikeh, N. Hilal, Solar powered desalination – Technology, energy and future outlook, *Desalination*. 453 (2019) 54–76. doi:10.1016/j.desal.2018.12.002.
- [13] H. Ghasemi, G. Ni, A.M. Marconnet, J. Loomis, S. Yerci, N. Miljkovic, G. Chen, Solar steam generation by heat localization, *Nature Communications*. 5 (2014) 1–7. doi:10.1038/ncomms5449.
- [14] Y. Li, T. Gao, Z. Yang, C. Chen, Y. Kuang, J. Song, C. Jia, E.M. Hitz, B. Yang, L. Hu, Graphene oxide-based evaporator with one-dimensional water transport enabling high-efficiency solar desalination, *Nano Energy*. 41 (2017) 201–209. doi:10.1016/j.nanoen.2017.09.034.
- [15] G. Wang, Y. Fu, X. Ma, W. Pi, D. Liu, X. Wang, Reusable reduced graphene oxide based double-layer system modified by polyethylenimine for solar steam generation, *Carbon*. 114 (2017) 117–124. doi:10.1016/j.carbon.2016.11.071.
- [16] F. Zhao, X. Zhou, Y. Shi, X. Qian, M. Alexander, X. Zhao, S. Mendez, R. Yang, L. Qu, G. Yu, Highly efficient solar vapour generation via hierarchically nanostructured gels, *Nature Nanotechnology*. 13 (2018) 489–495. doi:10.1038/s41565-018-0097-z.
- [17] C. Chen, Y. Li, J. Song, Z. Yang, Y. Kuang, E. Hitz, C. Jia, A. Gong, F. Jiang, J.Y. Zhu, B. Yang, J. Xie, L. Hu, Highly Flexible and Efficient Solar Steam Generation Device, *Advanced Materials*. 29 (2017) 1701756. doi:10.1002/adma.201701756.
- [18] D. Ghim, Q. Jiang, S.S. Cao, S. Singamaneni, Y.S. Jun, Mechanically interlocked 1T/2H phases of MoS<sub>2</sub> nanosheets for solar thermal water purification, *Nano Energy*. 53 (2018) 949–957. doi:10.1016/j.nanoen.2018.09.038.
- [19] Z. Guo, G. Wang, X. Ming, T. Mei, J. Wang, J. Li, J. Qian, X. Wang, PEGylated Self-Growth MoS<sub>2</sub> on a Cotton Cloth Substrate for High-Efficiency Solar Energy

- Utilization, *ACS Applied Materials & Interfaces*. 10 (2018) 24583–24589. doi:10.1021/acsami.8b08019.
- [20] R. Chen, X. Wang, Q. Gan, T. Zhang, K. Zhu, M. Ye, A bifunctional MoS<sub>2</sub> -based solar evaporator for both efficient water evaporation and clean freshwater collection, *Journal of Materials Chemistry A*. 7 (2019) 11177–11185. doi:10.1039/c9ta02002k.
- [21] X. Yang, Y. Yang, L. Fu, M. Zou, Z. Li, A. Cao, Q. Yuan, An Ultrathin Flexible 2D Membrane Based on Single-Walled Nanotube-MoS<sub>2</sub> Hybrid Film for High-Performance Solar Steam Generation, *Advanced Functional Materials*. 28 (2018) 1704505. doi:10.1002/adfm.201704505.
- [22] L. Huang, G. Li, A. Gurarslan, Y. Yu, R. Kirste, W. Guo, J. Zhao, R. Collazo, Z. Sitar, G.N. Parsons, M. Kudenov, L. Cao, Atomically Thin MoS<sub>2</sub> Narrowband and Broadband Light Superabsorbers, *ACS Nano*. 10 (2016) 7493–7499. doi:10.1021/acs.nano.6b02195.
- [23] Y. Gao, C. Chen, X. Tan, H. Xu, K. Zhu, Polyaniline-modified 3D-flower-like molybdenum disulfide composite for efficient adsorption/photocatalytic reduction of Cr(VI), *Journal of Colloid and Interface Science*. 476 (2016) 62–70. doi:10.1016/j.jcis.2016.05.022.
- [24] Q. Wang, F. Jia, S. Song, Y. Li, Hydrophilic MoS<sub>2</sub>/polydopamine (PDA) nanocomposites as the electrode for enhanced capacitive deionization, *Separation and Purification Technology*. 236 (2020) 116298. doi:10.1016/j.seppur.2019.116298.
- [25] Y. Gao, C. Chen, X. Tan, H. Xu, K. Zhu, Polyaniline-modified 3D-flower-like molybdenum disulfide composite for efficient adsorption/photocatalytic reduction of Cr(VI), *Journal of Colloid and Interface Science*. 476 (2016) 62–70. doi:10.1016/j.jcis.2016.05.022.
- [26] F. Jia, K. Sun, B. Yang, X. Zhang, Q. Wang, S. Song, Defect-rich molybdenum disulfide as electrode for enhanced capacitive deionization from water, *Desalination*. 446 (2018) 21–30. doi:10.1016/j.desal.2018.08.024.
- [27] W. Li, M.C. Tekell, Y. Huang, K. Bertelsmann, M. Lau, D. Fan, Synergistic High-Rate Solar Steaming and Mercury Removal with MoS<sub>2</sub>/C @ Polyurethane Composite Sponges, *Advanced Energy Materials*. 8 (2018) 1–11. doi:10.1002/aenm.201802108.
- [28] W. Xu, X. Hu, S. Zhuang, Y. Wang, X. Li, L. Zhou, S. Zhu, J. Zhu, Flexible and Salt Resistant Janus Absorbers by Electrospinning for Stable and Efficient Solar Desalination, *Advanced Energy Materials*. 8 (2018) 1–7. doi:10.1002/aenm.201702884.
- [29] L. Sun, J. Liu, Y. Zhao, J. Xu, Y. Li, Highly efficient solar steam generation via mass-produced carbon nanosheet frameworks, *Carbon*. 145 (2019) 352–358. doi:10.1016/j.carbon.2019.01.040.

- [30] World Health Organization, Safe Drinking-water from Desalination, World Health Organization. WHO/HSE/WS (2011).
- [31] K. Wang, J. Yang, D. Wei, H. Ren, F. Wang, M. Tang, Z. Chen, M. Wang, J. Shan, H. Peng, B. Guan, Z. Liu, Hierarchical Graphene Foam for Efficient Omnidirectional Solar-Thermal Energy Conversion, *Advanced Materials*. 29 (2017) 1702590. doi:10.1002/adma.201702590.
- [32] S. Cao, H. Gholami Derami, S. Singamaneni, Q. Jiang, D. Ghim, Y.-S. Jun, Polydopamine-filled bacterial nanocellulose as a biodegradable interfacial photothermal evaporator for highly efficient solar steam generation, *Journal of Materials Chemistry A*. 5 (2017) 18397–18402. doi:10.1039/c7ta04834c.
- [33] X. Wu, G.Y. Chen, W. Zhang, X. Liu, H. Xu, A Plant-Transpiration-Process-Inspired Strategy for Highly Efficient Solar Evaporation, *Advanced Sustainable Systems*. 1 (2017) 1700046. doi:10.1002/adsu.201700046.
- [34] A. Guo, X. Ming, Y. Fu, G. Wang, X. Wang, Fiber-Based, Double-Sided, Reduced Graphene Oxide Films for Efficient Solar Vapor Generation, *ACS Applied Materials and Interfaces*. 9 (2017) 29958–29964. doi:10.1021/acsami.7b07759.
- [35] S. Ma, C.P. Chiu, Y. Zhu, C.Y. Tang, H. Long, W. Qarony, X. Zhao, X. Zhang, W.H. Lo, Y.H. Tsang, Recycled waste black polyurethane sponges for solar vapor generation and distillation, *Applied Energy*. 206 (2017) 63–69. doi:10.1016/j.apenergy.2017.08.169.
- [36] Q. Yuan, Z. Li, X. Yang, Y. Yang, M. Zou, L. Fu, A. Cao, An Ultrathin Flexible 2D Membrane Based on Single-Walled Nanotube-MoS<sub>2</sub> Hybrid Film for High-Performance Solar Steam Generation, *Advanced Functional Materials*. 28 (2017) 1704505. doi:10.1002/adfm.201704505.
- [37] D. Ghim, Q. Jiang, S. Cao, S. Singamaneni, Y.-S. Jun, Mechanically interlocked 1T/2H phases of MoS<sub>2</sub> nanosheets for solar thermal water purification, *Nano Energy*. 53 (2018) 949–957. doi:10.1016/j.nanoen.2018.09.038.
- [38] H. Ren, M. Tang, B. Guan, K. Wang, J. Yang, F. Wang, M. Wang, J. Shan, Z. Chen, D. Wei, H. Peng, Z. Liu, Hierarchical Graphene Foam for Efficient Omnidirectional Solar-Thermal Energy Conversion, *Advanced Materials*. 29 (2017) 1–7. doi:10.1002/adma.201702590.
- [39] X. Wang, G. Ou, N. Wang, H. Wu, Graphene-based Recyclable Photo-Absorbers for High-Efficiency Seawater Desalination, *ACS Applied Materials and Interfaces*. 8 (2016) 9194–9199. doi:10.1021/acsami.6b02071.

The main content of this chapter was published as “*Desalination 481 (2020): 114359.*”

## CHAPTER V

# Facile preparation of high-quality 3D MoS<sub>2</sub> aerogel for highly efficient solar desalination

### 5.1. Introduction

Solar driven desalination has received tremendous attention in vapor generation, desalination and sterilization,[1] because of its use of the inexhaustible solar energy and few environmental footprints. Quite a few milestone-works, such as plasmonic structures,[2] two-dimensional water path,[3] artificial transpiration,[4] water-lily structures[5] and Janus membranes,[6] etc., provide tremendous and rational designs for solar desalination systems, significantly improving the flexibility, scalability and economics of this technology. Besides, since graphene oxide (GO) aerogels were used for solar steam generation,[7] a plenty of aerogel-based evaporators, including metal aerogels,[8] carbon nanotube (CNT) aerogels[9,10] and graphene-based aerogels,[11–13] etc., have been fabricated to harvest solar energy for water desalination or purification. These aerogels are proved useful for solar desalination because of their well solar-absorbing capacity, high porosity, large surface area and low thermal conductivity.[14] However, it also should be pointed out that many aerogels share the similar weakness of complex preparation process and high capital loss to some extent, limiting their practical applicant and promoting the need of expanding aerogels' material-pools. As one of the most attractive advanced materials in electronics, catalysis, biomedical, environmental and energy-related fields in recent years,[15–18] MoS<sub>2</sub> nanosheets are also expected to have new applications in solar desalination because of its excellent solar absorbance and conversion properties.[19,20] Unfortunately, MoS<sub>2</sub> nanosheets fail to be a star material like GO or CNTs in terms of fabricating aerogels for the advanced applications. Namely, till now only one MoS<sub>2</sub>-based aerogel prepared by two-step sulfur treatment has been used as sensor for NO<sub>2</sub> detection,[21] and several MoS<sub>2</sub>/graphene hybrid aerogels fabricated with the indispensable help of graphene for energy generation or pollutant detection,[22,23] have been found, indicating the insufficient investigation of MoS<sub>2</sub>-based aerogels. The difficulties faced by MoS<sub>2</sub> nanosheets in the manufacture of aerogels can mainly be attributed to the fact: MoS<sub>2</sub> nanosheets are usually free or lack of the strong connecting/bonding sites-the functional groups which however play the critical role in the construction of high-quality aerogels. Based on our previous

works, the use of functionalized MoS<sub>2</sub> nanosheets might be an effective solution to overcome this problem.[24] That is, inspired by the mussel-chemistry, MoS<sub>2</sub> nanosheets can be facilely functionalized by polydopamine (PDA) via the self-polymerization of dopamine monomers,[25] rendering the resultant functionalized MoS<sub>2</sub> nanosheets rich in functional groups such as catechol, amine and imine.[26,27] Moreover, chitosan, often serves as the basic frameworks of various aerogels with the help of cross-linkers,[28] can be also expected to work as the frameworks in aerogels to prepare MoS<sub>2</sub> aerogels because of its rich hydroxyl and amino groups.[29]

For the first time, this work demonstrates the facile preparation of a high-quality MoS<sub>2</sub> aerogel with three-dimensional (3D) architectures and its application as solar absorber in solar desalination. The mechanical quality and light-absorbing capacity of MoS<sub>2</sub> aerogels are also highlighted. With broad light absorption, open channel structure, high specific surface area and heat localization caused by its low thermal conductivity, this aerogels exhibit high solar evaporation efficiencies of 88.0%-95.3% under low solar irradiation of 1.0-3.0 kW m<sup>-2</sup> as well as the excellent desalination performance, holding the great potentials as high-performance solar absorber for solar desalination or water purification. All details are carefully examined as below.

## 5.2. Experimental section

**Preparation of the 3D MoS<sub>2</sub> aerogels:** Firstly, the starting MoS<sub>2</sub> is prepared based on the reported works.[30,31] Secondly, to prepared functionalized MoS<sub>2</sub> nanosheets, 100 mg as-synthesized MoS<sub>2</sub> samples are dispersed in Tris-buffer aqueous solution (75 mL, 10 mM; pH 8.5) and treated at 150 W for 10 min with a sonicator to exfoliate the MoS<sub>2</sub>. Afterwards, dopamine hydrochloride (150 mg, Sigma-Aldrich) is added into the mixture which is then stirred (500 rpm) at ambient temperature for 4.0 h. The resulting powders are washed several times using deionized water and finally dried in a vacuum freeze dryer. Thirdly, 200 mg of the functionalized MoS<sub>2</sub> nanosheets, 150 mg of chitosan (dissolved in 1% acetic acid solutions) are adequately mixed together for 1 h, and then 15 mg of glutaraldehyde (25wt%) is added and mechanical stirred for 2 h. The mixture is then dried in a vacuum freeze dryer at -50°C for at least 24 h.

**Characterizations:** The morphologies of samples are obtained from scanning electron microscopy (SEM; Hitachi S-4700). The light-absorbing property of samples is measured by an UV-Vis-NIR spectrophotometer (LAMBDA950). The FTIR spectra of samples are obtained from the Nexus Thermo Nicolet spectrometer. An ion

chromatography (Dionex Aquion) and an inductively coupled plasma atomic emission spectroscopy (ICP-AES, Prodigy 7) are applied to determine the concentrations of anions and cations in solutions, respectively. The compressive stress-strain curves are obtained from the microcomputer-controlled electronic universal testing machine (SHT4106, MTS System Corporation) with a loading speed of  $10 \text{ mm min}^{-1}$ . Thermal conductivity coefficient of the 3D MoS<sub>2</sub> aerogel is tested on the Hot Disk thermal constants analyzer (TPS 2500, Uppsala, Sweden) using the transient plane source (TPS) method according to ISO 22007-2, and the residual diagram is displayed in Fig. 5.1. Contact angle is obtained from a standard contact angle analyzer (JC2000A).

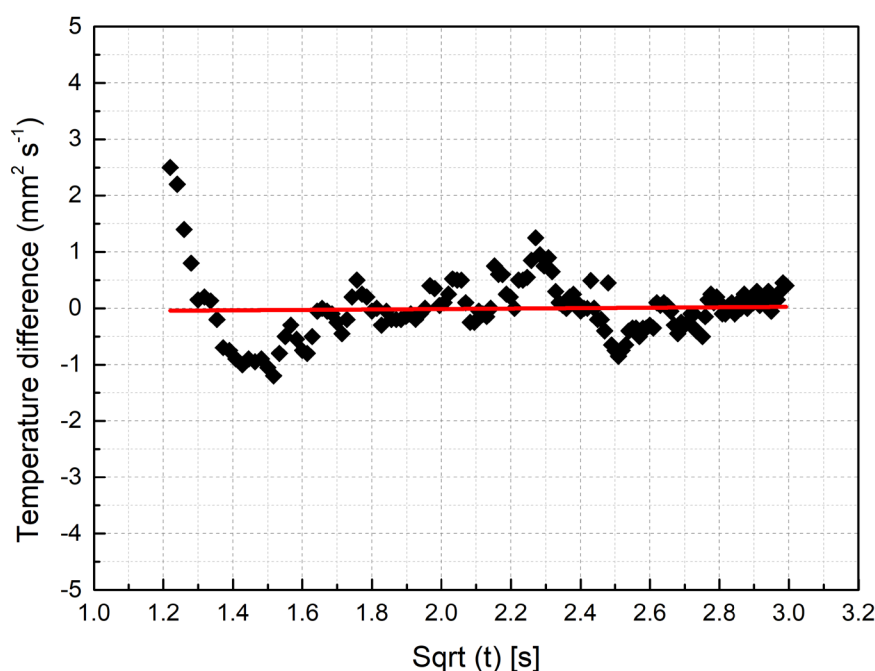


Fig. 5.1 Residual plot of the thermal conductivity of the 3D MoS<sub>2</sub> aerogel based on the transient plane source method.

**Solar desalination test:** The broadband illumination is supplied by the solar simulator (Beijing Perfectlight, Microsolar 300) with the controllable solar density. Solar density is measured by a photoradiometer (Perfectsolar PL-MW2000). A beaker containing the floating evaporator and saline water is placed on an electronic balance (Shanghai Yueping, YP6002, accuracy: 0.01 g) for real-time measurements of water mass. The probe of an electronic temperature logger (Jingchuang, GSP-6) is inserted into the top layer of the evaporators and an IR camera (FORTRIC 220s) is used to record the temperature vibrations. All experiments of solar evaporation and desalination have been finished under the below conditions: the ambient temperatures are  $23 \pm 2^\circ\text{C}$  controlled by the air conditioner and the ambient humidity is  $30 \pm 5\%$ .

### 5.3. Results and Discussion

Fig. 5.2 displays the typical fabrication strategy of 3D MoS<sub>2</sub> aerogels (which are originated from the functionalized MoS<sub>2</sub> nanosheets in throughout text if there is no special description). The functionalized MoS<sub>2</sub> nanosheets with abundant functional groups, chitosan and glutaraldehyde are adequately mixed in water by mechanical stirring. The mixture is then dried by a vacuum freeze dryer at -50°C. During the freezing process, the ice crystals grow along the axis of mode due to the temperature gradient generated by the cold trap, and finally form one piece of frozen materials consisting of ice crystals surrounded by the walls formed by chitosan molecules and functionalized MoS<sub>2</sub> nanosheets.[7] Subsequently, the negative pressure of vacuum in the cold trap contributes to the removal of the ice crystals via the sublimation of ice into vapor, leaving the undestroyed porous frameworks. The resultant MoS<sub>2</sub> aerogel can be placed on a flexible cedar leaf without changing the original shape of the cedar leaf because of its high porosity and ultralight property (see the optical image in Fig. 8.1). The formation of Schiff-base (-C=N-), hydrogen-bond interactions (-O•••H or -N•••H) and the electrostatic interactions between the negatively charged functionalized MoS<sub>2</sub> nanosheets and the positively charged chitosan molecules, simultaneously account for the formation of MoS<sub>2</sub> aerogels with high porosity and excellent machinal stability.

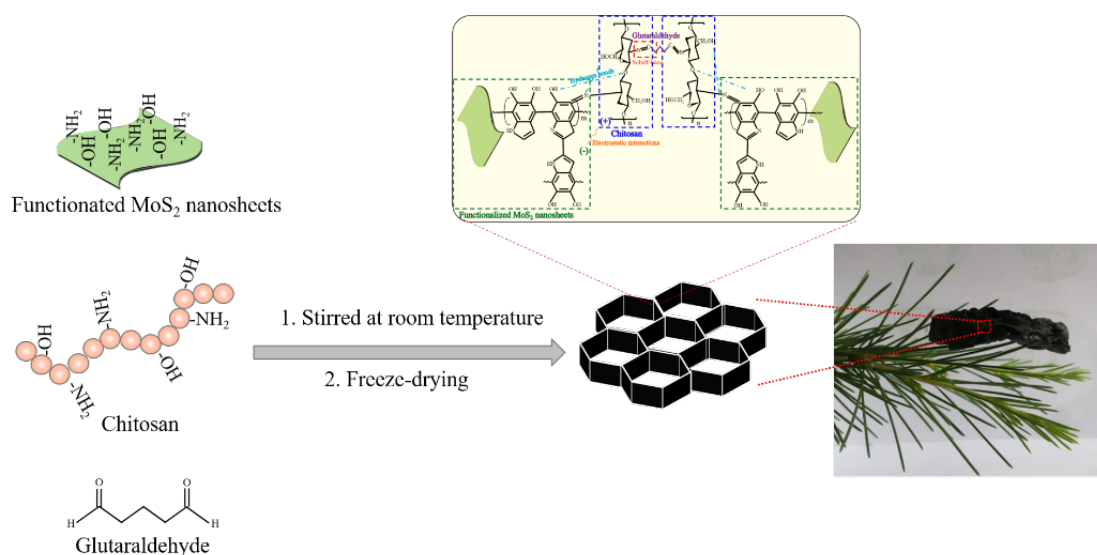


Fig. 5.2. Schematic diagram of preparation strategy of 3D MoS<sub>2</sub> aerogels.

Fig. 5.3 shows the SEM and optical morphology of the single MoS<sub>2</sub> nanosheets and MoS<sub>2</sub>-based aerogels. In Fig. 5.3(a), the scanning electron microscopy (SEM)



image displays the as-prepared MoS<sub>2</sub> is in the nanosheet-like architecture with an average lateral size of approximately 200 nm. Fig. 5.3(b) shows the interconnected 3D porous networks of the MoS<sub>2</sub> aerogels with the pore size of 20–50 μm, which benefits to the escape of the generating vapors. The functionalized MoS<sub>2</sub> nanosheets in MoS<sub>2</sub> aerogels are stably embed between the chitosan molecules, according to the high-resolution SEM morphology as displayed in Fig. 5.4. According to the measurement of N<sub>2</sub> adsorption/desorption isotherm as displayed in Fig. 5.5, the Brunauer-Emmett-Teller (BET) surface area of MoS<sub>2</sub> aerogels reaches a high level of ~155 m<sup>2</sup> g<sup>-1</sup>, which is superior to that of graphene-based aerogels (~125 m<sup>2</sup> g<sup>-1</sup>). [7] The density of MoS<sub>2</sub> aerogels is measured to be ~ 8 kg m<sup>-3</sup>, which is far below the density of saline water (1.03×10<sup>3</sup>-1.33×10<sup>3</sup> kg m<sup>-3</sup>), thus ensuring the free self-floating of MoS<sub>2</sub> aerogel on saline water's surface.

The optical images in Fig. 5.3(c) and (d) display the morphology of MoS<sub>2</sub>-based aerogels prepared by functionalized MoS<sub>2</sub> nanosheets and single MoS<sub>2</sub> nanosheets, respectively. MoS<sub>2</sub> aerogels prepared by the functionalized MoS<sub>2</sub> nanosheets show the stable and regular geometric shapes with diameter of 5.0 cm and thickness of 1.0 cm after being repeatedly pressed, while the MoS<sub>2</sub> aerogels originated from single MoS<sub>2</sub> nanosheets are crunchy and turned out to be powders after being pressed.

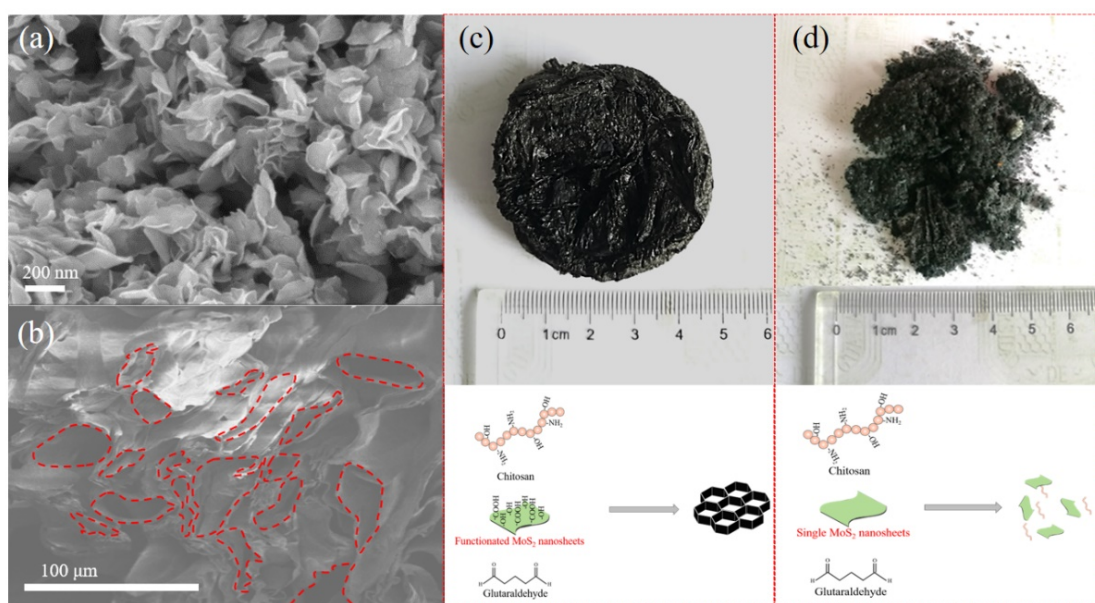


Fig. 5.3. SEM images of (a) single MoS<sub>2</sub> nanosheets and (b) MoS<sub>2</sub> aerogels. Optical images of MoS<sub>2</sub>-based aerogels prepared by (c) functionalized MoS<sub>2</sub> nanosheets and (d) single MoS<sub>2</sub> nanosheets after being pressed.

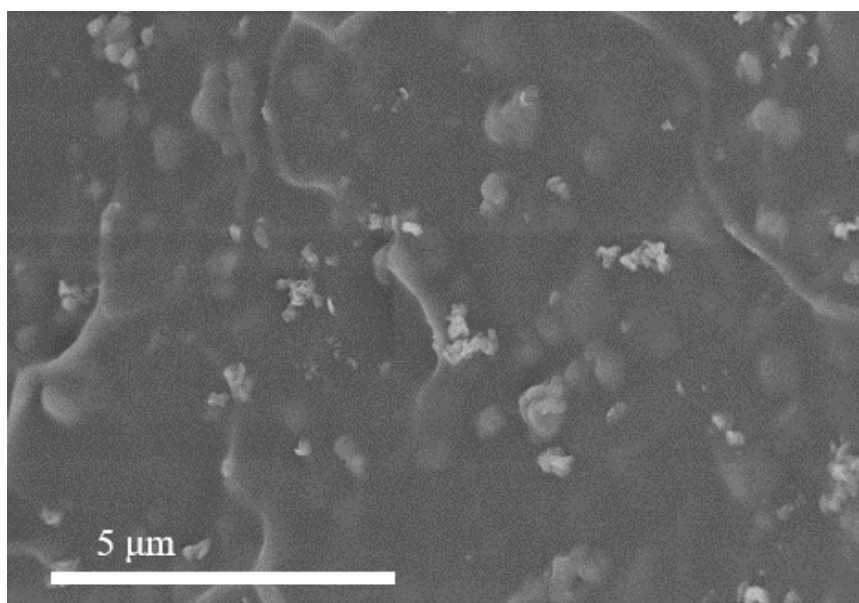


Fig. 5.4. The location of functionalized MoS<sub>2</sub> nanosheets in the 3D MoS<sub>2</sub> aerogels.

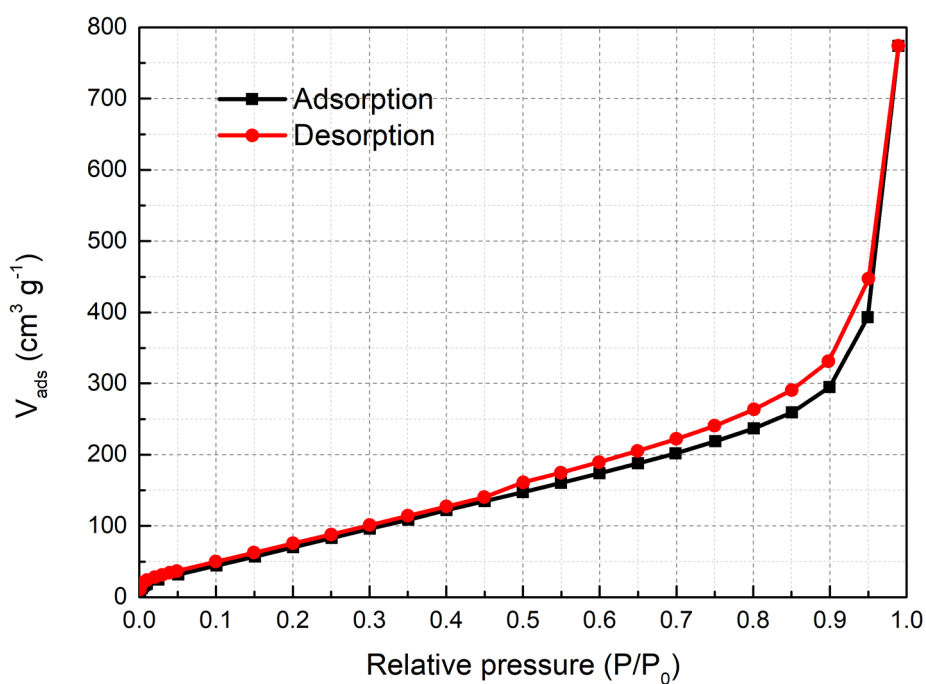


Fig. 5.5. N<sub>2</sub> adsorption/desorption isotherm of MoS<sub>2</sub> aerogels prepared from the functionalized MoS<sub>2</sub> nanosheets.

As displayed in Fig. 5.6(a), the mechanical performance of MoS<sub>2</sub> aerogels derived from functionalized MoS<sub>2</sub> nanosheets is further confirmed by the mechanical tests. The first linear region up to ~40% strain is ascribed to the elastic deformation, and the second region of 40%-60% strain is attributed to a plastic deformation caused

by the breaks of the cross-links,[28] and finally a steep increase in the stress is found in the strain region over 60%. Accordingly, the compressive elastic strain of the 3D MoS<sub>2</sub> aerogel prepared by the functionalized MoS<sub>2</sub> nanosheets reaches up to ~60%. The tensile stress-strain curve as shown Fig. 5.7 shows that the 3D MoS<sub>2</sub> aerogel has a tensile strength of around 520 kPa and a fracture strain of 59%, further demonstrating its excellent mechanical stability. This difference can be ascribed to the existence or lack of strong connecting/binding interactions between the MoS<sub>2</sub> nanosheets and chitosan molecules, suggesting the necessary functionalization of MoS<sub>2</sub> nanosheets in preparing MoS<sub>2</sub> aerogels with high mechanical stability.

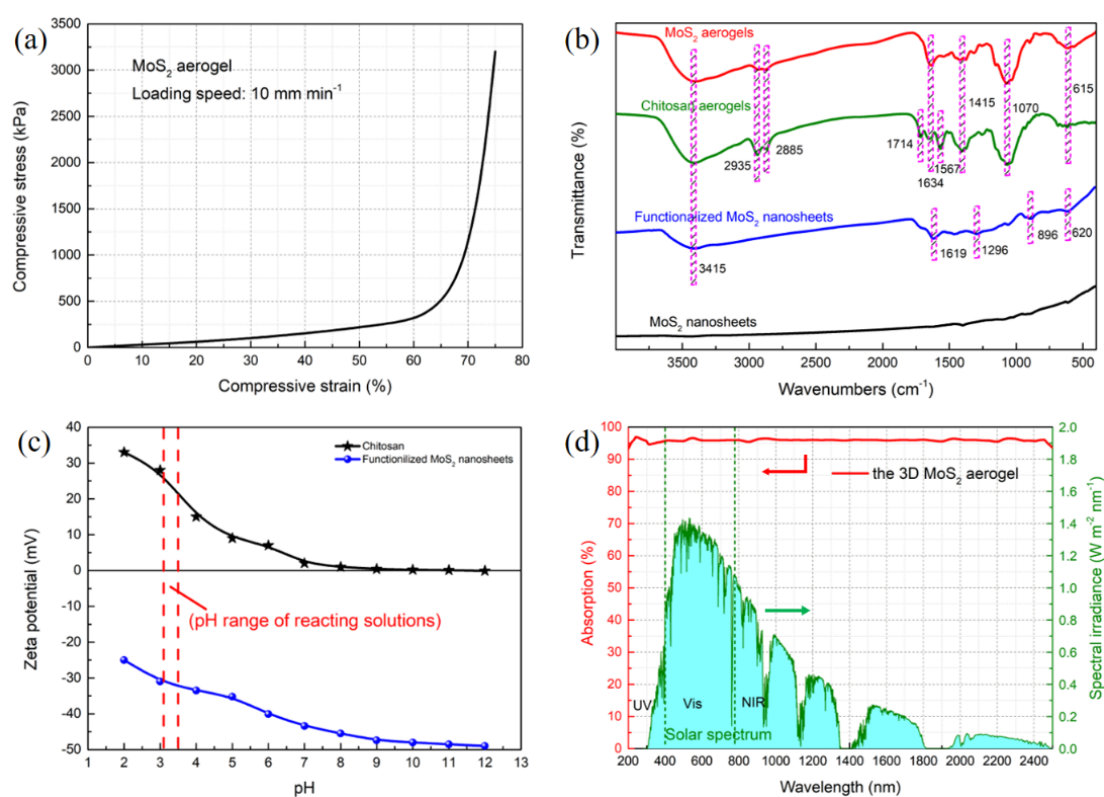


Fig. 5.6. (a) Compression stress-strain curves of MoS<sub>2</sub> aerogels prepared by the functionalized MoS<sub>2</sub> nanosheets. (b) FTIR spectra of chitosan, single MoS<sub>2</sub> nanosheets, functionalized MoS<sub>2</sub> nanosheets and MoS<sub>2</sub> aerogels. (c) Zeta potentials of chitosan and functionalized MoS<sub>2</sub> nanosheets. (d) Light absorption spectra of pure chitosan, single MoS<sub>2</sub> nanosheets, functionalized MoS<sub>2</sub> nanosheets and MoS<sub>2</sub> aerogels.

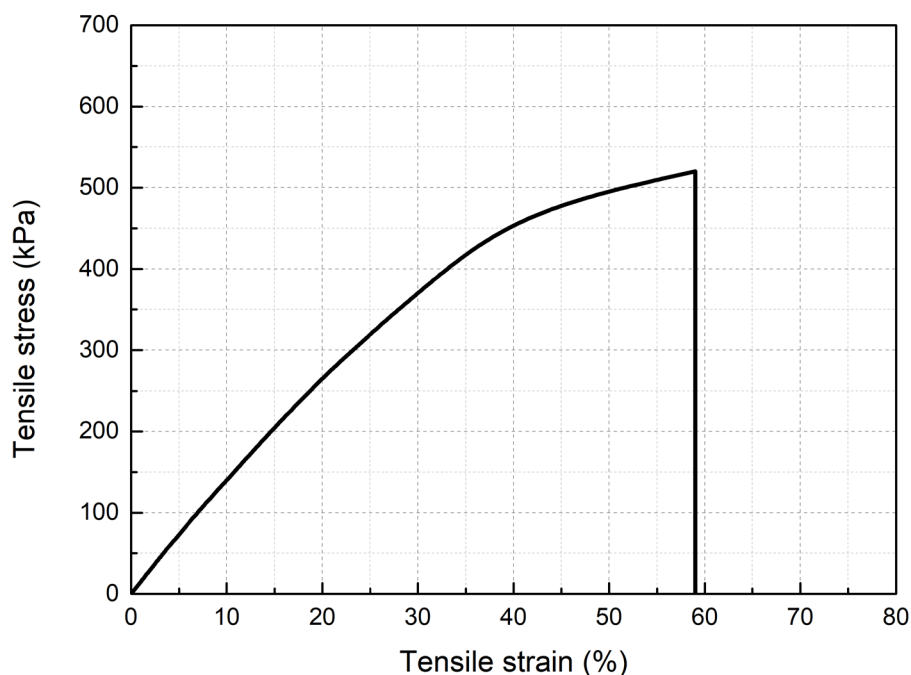


Fig. 5.7. Tensile stress-strain curve of the 3D MoS<sub>2</sub> aerogel.

The intrinsic mechanisms of MoS<sub>2</sub> aerogel with high stability are investigated. The Fourier transform infrared (FTIR) spectra of single MoS<sub>2</sub> nanosheets, functionalized MoS<sub>2</sub> nanosheets, chitosan aerogel and the 3D MoS<sub>2</sub> aerogels are displayed in Fig. 5.6(b). No obvious adsorption peak is found in the single MoS<sub>2</sub> nanosheets, demonstrating that the surfaces of MoS<sub>2</sub> nanosheets are free/lack of functional groups. In comparison, the functionalized MoS<sub>2</sub> nanosheets exhibited the characteristic adsorption peaks at 3415 cm<sup>-1</sup> (stretching vibration of phenolic O-H),[32] 1619 cm<sup>-1</sup> (stretching vibration of aromatic ring and bending vibration of N-H) and 1296 cm<sup>-1</sup> (stretching phenolic C-O),[33] and 620–929 cm<sup>-1</sup> (the vibrations of C-H bonds in benzene rings),[34] and these emerging peaks can be attributed to the introduction of PDA, demonstrating the successful introduction of functional groups (mainly amines and phenolic hydroxyls) onto the MoS<sub>2</sub> nanosheets. For chitosan aerogels, the peaks at 3415 cm<sup>-1</sup> (stretching vibration of O-H), 2935 cm<sup>-1</sup> and 2885 cm<sup>-1</sup> (alkane group of C-H),[35], 1714 cm<sup>-1</sup> (stretching C=O),[36] 1567 cm<sup>-1</sup> (amino groups on the chitosan chain),[37] 1415 cm<sup>-1</sup> (stretching vibration of N-H) and 1070 cm<sup>-1</sup> (stretching vibration of C-O),[38] can be clearly observed, revealing the typical composition of chitosan aerogels with hydroxyl, amino and N-acetyl amino. Notably, compared to chitosan aerogels, the adsorption peak at 1567 cm<sup>-1</sup> in MoS<sub>2</sub> aerogels is disappeared, indicating that the amino groups on the chitosan chains are involved in the interaction between chitosan and functionalized MoS<sub>2</sub>

nanosheets.[39,40] In addition, the characteristic peaks at  $1634\text{ cm}^{-1}$  are found in both chitosan aerogels and  $\text{MoS}_2$  aerogels, which can be assigned to the formation of Schiff-base (stretching vibration of  $-\text{C}=\text{N}-$ ) produced by the cross-linking reactions between the amino group of chitosan and aldehyde group of glutaraldehyde.[28,39,41] Also, hydrogen bonds play a role in formation of stable  $\text{MoS}_2$  aerogels due to the existence of abundant hydroxyl and amino groups inside the 3D  $\text{MoS}_2$  aerogels.

Fig. 5.6(c) shows the surface charges of chitosan and functionalized  $\text{MoS}_2$  nanosheets. It is found that chitosan and functionalized  $\text{MoS}_2$  nanosheets are positively and negatively charged within the wide pH range of 2.0-12.0, respectively. Therefore, electrostatic attraction also plays an important role in the interaction between chitosan and functionalized  $\text{MoS}_2$  nanosheets at the narrow pH range (3.25-3.50). Note that although single  $\text{MoS}_2$  nanosheets are also negatively charged as displayed in Fig. 5.8 within the reacting pH range, the mere existence of electrostatic attraction is unable to prepare  $\text{MoS}_2$  aerogels with high stability due to the crumbly structure of  $\text{MoS}_2$  aerogels originated from single  $\text{MoS}_2$  nanosheets as aforementioned in Fig. 5.3.

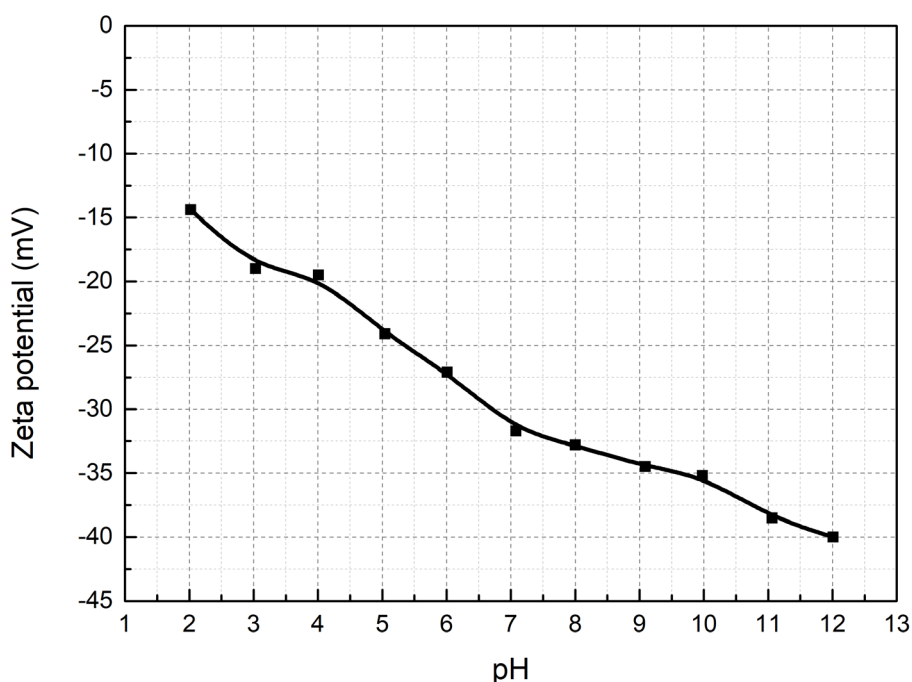


Fig. 5.8. Zeta potentials of single  $\text{MoS}_2$  nanosheets within the wide pH range of 2.0-12.0.

The light-absorbing capacity of  $\text{MoS}_2$  aerogels is recorded on an ultraviolet visible-near-infrared (UV-Vis-NIR) spectrophotometer equipped with an integrating sphere. As displayed in Fig. 5.6(d), a superhigh light-absorbing capacity of 95% is achieved by  $\text{MoS}_2$  aerogels (weighted by AM1.5G solar spectrum) within the wide

light wavelength of 200–2500 nm, laying foundations for its highly efficient solar-to-heat conversion as well as solar desalination. In addition, the hydrophilicity of solar absorbers also can play a significant role in solar desalination since the continuous vapor generations usually require the efficient water supply through their inside networks. Note that the 3D MoS<sub>2</sub> aerogels possess good hydrophilicity (as displayed in Fig. 5.9) due to the introduced PDA and chitosan molecules with various hydrophilic functional groups as aforementioned before.[24] As a result, water can easily and rapidly penetrate through the interconnected pores of aerogels, ensuring the efficient water supply from bottom cold bulk water to the top hot regions during the vapor generation.

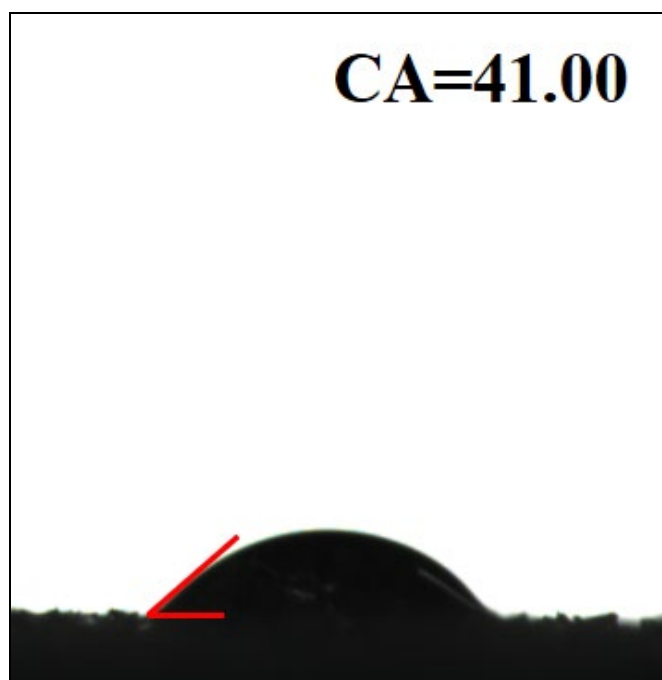


Fig. 5.9. Contact angle of the 3D MoS<sub>2</sub> aerogel.

These results demonstrate that MoS<sub>2</sub> aerogels hold excellent mechanical stability, high porosity, outstanding light-harvesting capability and high hydrophilicity, which can contribute to its application as the effective solar-absorber for solar desalination.

To reduce costs and enhance commercial applicability, this work mainly pays attention to the solar desalination performance of the 3D MoS<sub>2</sub> aerogels under the low solar irradiation of 1.0-3.0 kW m<sup>-2</sup>. Since the purification effects of solar desalination are almost completely independent on salt concentration,[4,42] the 3.5wt% NaCl aqueous solutions, which serve as an alternative to the real seawater or other types of saline water,[6,43] are often used to determine the desalination performance. The

typical curves of time-dependent mass change of water due to the vapor generation are displayed in Fig. 5.10(a), based on which the corresponding evaporation rates can be calculated according to their slopes as shown in Fig. 5.11. With MoS<sub>2</sub> aerogels as solar absorbers under the solar irradiation of 1.0 kW m<sup>-2</sup>, the evaporation rate is up to 1.27 kg m<sup>-2</sup> h<sup>-1</sup>, which is around 5.0 times that of pure water (0.2538 kg m<sup>-2</sup> h<sup>-1</sup>).

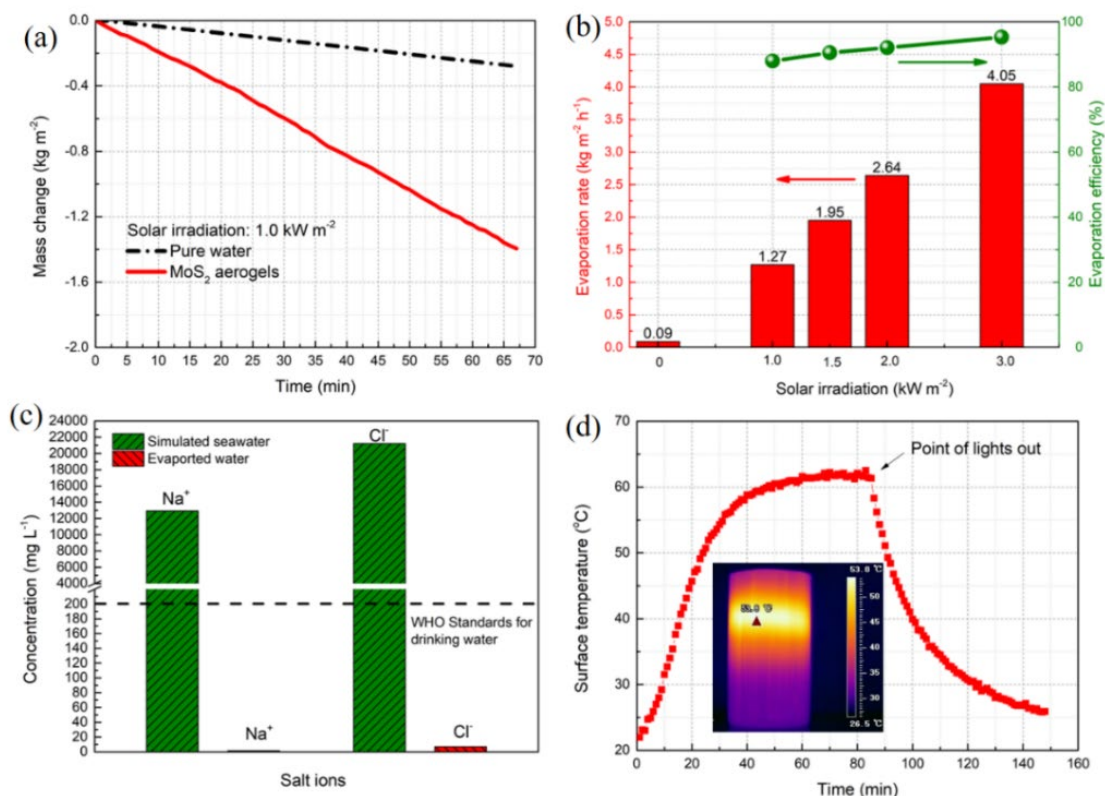


Fig. 5.10. (a) Mass change of water over time under solar irradiation of 1.0 kW m<sup>-2</sup> with MoS<sub>2</sub> aerogels as solar absorbers. (b) Evaporation performance of water with the MoS<sub>2</sub> aerogels under solar irradiation of 1.0-3.0 kW m<sup>-2</sup>. (c) Desalination performance achieved by MoS<sub>2</sub> aerogels. (d) Temperature variations on the top surface of MoS<sub>2</sub> aerogels during the solar desalination (under solar irradiation of 3.0 kW m<sup>-2</sup>), the inset image is the temperature distribution of the device during evaporation recorded by an IR camera.

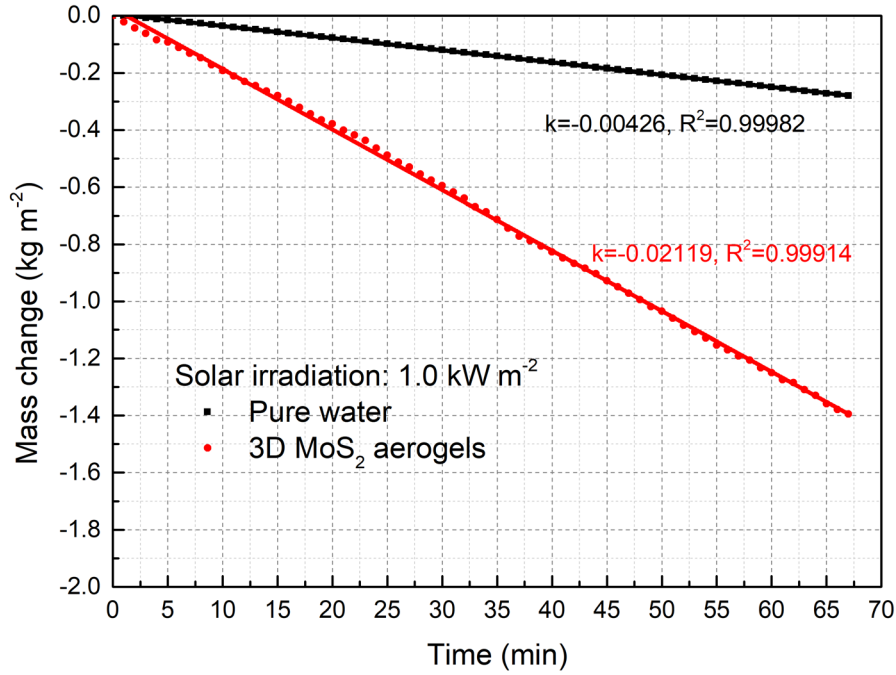


Fig. 5.11. Linear fitting results of the time-dependent mass change of water with the 3D MoS<sub>2</sub> aerogels and pure water under solar irradiation of 1.0 kW m<sup>-2</sup>.

The evaporation efficiency, which is defined as  $\eta = \dot{m} (L_v + Q) / P_{in}$  (where  $\dot{m}$  is the mass flux after subtracting the evaporation rate in the dark ( $\dot{m} = \dot{m}_{light} - \dot{m}_{dark}$ ), kg m<sup>-2</sup> h<sup>-1</sup>;  $L_v$  is the latent heat of vaporization of water,  $L_v(T) = 1.91846 \times 10^6 [T / (T - 33.91)]^2$  J/kg;  $Q$  is the sensible heat of water of unit mass,  $Q = c (T - T_0)$  J/kg, in which  $c$  is the specific heat of water (4.2 J/gK),  $T$  is the temperature of vaporization and  $T_0$  is the initial temperature of the water;  $P_{in}$  is the incident solar energy on the absorber surface, respectively), [4,44] is further used to evaluate the evaporation performance. Based on the results in Fig. 5.12 and Table 5.1, the evaporation rates and evaporation efficiencies are calculated and displayed in Fig. 5.10(b). Impressively, high evaporation efficiency of 88.0% under the low solar density of 1.0 kW m<sup>-2</sup> and superhigh evaporation efficiencies over 90% under the slightly enhanced solar density of 1.5-3.0 kW m<sup>-2</sup> can be achieved by the 3D MoS<sub>2</sub> aerogels, suggesting that higher solar irradiation can contribute to the higher evaporation efficiency. These evaporation efficiencies are much superior to that of most other advanced solar absorbers under the similar conditions (as shown in Table 5.2).



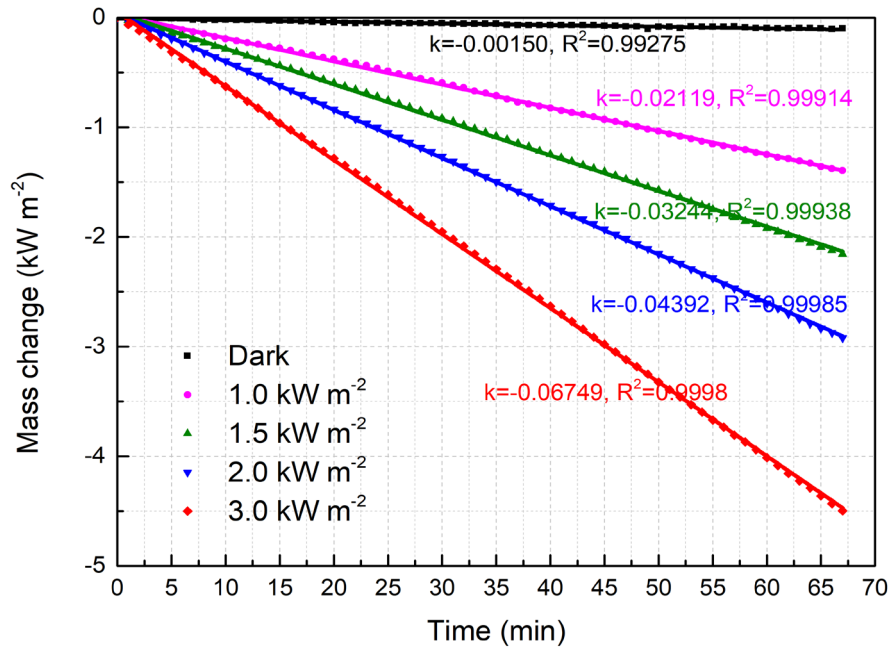


Fig. 5.12. Linear fitting results of the time-dependent mass change of water with the 3D MoS<sub>2</sub> aerogels under solar irradiations of 0, 1.0, 1.5, 2.0 and 3.0 kW/m<sup>2</sup>.

Table 5.1 Calculation details of the evaporation efficacies under 1.0-3.0 kW m<sup>-2</sup>.

| P <sub>in</sub><br>(Incident solar power, kW m <sup>-2</sup> ) | T <sub>0</sub> (Initial temperature, K) | T<br>(Temperature of vaporization, K) | L <sub>v</sub> (latent heat of vaporization, ×10 <sup>6</sup> J kg <sup>-1</sup> ) | Q (Sensible heat of water, ×10 <sup>6</sup> J kg <sup>-1</sup> ) | ṁ (Evaporation rate, kg m <sup>-2</sup> h <sup>-1</sup> ) | η (Evaporation efficiency, %) |
|--|---|---------------------------------------|--|--|--|-------------------------------|
| 1.0  | 295                                     | 315                                   | 2.409  | 0.0836   | 1.27   | 88.0                          |
| 1.5  | 295                                     | 322                                   | 2.397  | 0.1129   | 1.95   | 90.5                          |
| 2.0  | 295                                     | 325                                   | 2.391  | 0.1254   | 2.64   | 92.1                          |
| 3.0  | 295                                     | 335                                   | 2.375  | 0.1672   | 4.05   | 95.3                          |

Table 5.2 The evaporation performance of various advanced materials in recent works.

| Materials                          | Power density (kW m <sup>-2</sup> ) | Evaporation rate (kg m <sup>-2</sup> h <sup>-1</sup> ) | Evaporation efficiency (%) | Refs |
|------------------------------------|-------------------------------------|--|----------------------------|------|
| RGO-SA-CNT aerogels                | 1                                   | 1.622  | 83                         | [7]  |
| CNT-modified Wood Membrane         | 1                                   | 0.95   | 65                         | [45] |
| PDA-filled Bacterial Nanocellulose | 1                                   | 1.13   | 78                         | [46] |
| CNT-modified flexible wood         | 10                                  | 11.22  | 81                         | [47] |

|  |      |      |            |           |
|--|------|------|------------|-----------|
| Black Polyurethane Sponges                                     | 1    | 0.83 | 52.2 ± 2.5 | [48]      |
|  | 5    | 4.24 |            |           |
| PEGylated MoS <sub>2</sub> - Cotton Cloth                      | 1    | 1.3  | 80.1       | [19]      |
|  | 5    | 7.03 | 90.3       |           |
| Single Walled Nanotube-MoS <sub>2</sub> Hybrid Films           | 0.8  | 0.9  | 81         | [49]      |
|  | 5    | 6.6  | 91.5       |           |
| Chemical Exfoliated MoS <sub>2</sub> - Bacterial Nanocellulose | 0.76 | 0.81 | 75.7       | [50]      |
|  | 5.35 | 6.15 | 81.4       |           |
| MoS <sub>2</sub> aerogels                                      | 1    | 1.27 | 88.0       | This work |
|  | 1.5  | 1.95 | 90.5       |           |
|  | 2.0  | 2.64 | 92.1       |           |
|  | 3.0  | 4.05 | 95.3       |           |

As displayed in Fig. 5.10(c), the concentrations of Na<sup>+</sup> and Cl<sup>-</sup> ions in the collected distillates reach extremely low level of 1.3 mg L<sup>-1</sup> and 6.9 mg L<sup>-1</sup>, respectively, which are far below the World Health Organization (WHO) standards for drinking water with limits,[51] suggesting the excellent desalination performance of the 3D MoS<sub>2</sub> aerogels. In addition, due to its excellent mechanical stability, this 3D MoS<sub>2</sub> aerogel can be reused for at least 10 cycles (each cycle lasts for around 90 min) with stable freshwater productivity as displayed in Fig. 5.13, suggesting its promising perspective in commercial application.

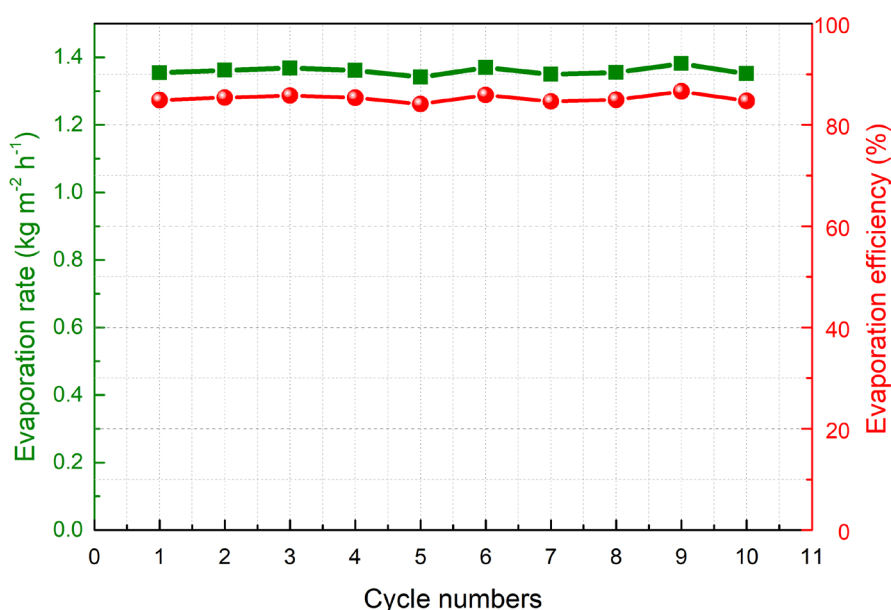


Fig. 5.13. Cycling performance of MoS<sub>2</sub> aerogels under solar irradiation of 1.0 kW m<sup>-2</sup>.

To further investigate the working mechanisms of highly efficient vapor generation provided by the 3D MoS<sub>2</sub> aerogels, the temperature variations on the top surfaces of the solar absorbers and temperature distributions across the work beaker are captured (Fig. 5.10(d)). The temperature on the top surface of the 3D MoS<sub>2</sub> aerogels can increase from ~22°C to ~62°C, indicating that MoS<sub>2</sub> aerogels can effectively transfer the harvested solar energy into thermal energy to heat the water on the top surface. Note that a heat localization can be expected because of the low thermal conductivity of the 3D MoS<sub>2</sub> aerogels (~0.37 W m<sup>-1</sup> K<sup>-1</sup> at room temperature). As shown in the inset image of Fig. 5.10(d), a sharp temperature gradient along the beaker can be clearly observed, directly confirming the formation of the heat localization inside beakers during the evaporation process.

Therefore, the efficient and broadband light-absorbing capacity, the effective heat localization without compromising water supply, and the effective vapor escape derived from its porous structure, synchronously account for the highly efficient solar evaporation of the 3D MoS<sub>2</sub> aerogels.

## 5.4. Conclusion

A novel 3D MoS<sub>2</sub> aerogel with high porosity and high mechanical stability is successfully fabricated. The excellent mechanical performance of MoS<sub>2</sub> aerogels can be attributed to the formation of cross-linking bonds, hydrogen bonds as well as electrostatic attraction between functionalized MoS<sub>2</sub> nanosheets and chitosan frameworks. This MoS<sub>2</sub> aerogels meet all the requirement of solar absorbers for solar desalination: excellent solar-to-heat conversion, porous networks for vapor escape, good hydrophilicity for continuous water supply and low thermal conductivity for effective heat localization, resulting in the excellent evaporation efficiency. With 3D architectures for easy separation and facile preparation, this MoS<sub>2</sub> aerogels provide promising applications not only in solar-assisted desalination but also in many other fields such as solar energy harvesting and storage, liquid-phase separation, electrochemical applications and photocatalytic oxidation, etc.

## REFERENCES

- [1] N. Xu, X. Hu, W. Xu, X. Li, L. Zhou, S. Zhu, J. Zhu, Mushrooms as Efficient Solar Steam-Generation Devices, *Advanced Materials*. 29 (2017) 1606762. doi:10.1002/adma.201606762.
- [2] L. Zhou, Y. Tan, J. Wang, W. Xu, Y. Yuan, W. Cai, S. Zhu, J. Zhu, 3D self-assembly of

- aluminium nanoparticles for plasmon-enhanced solar desalination, *Nature Photonics*. 10 (2016) 393–398. doi:10.1038/nphoton.2016.75.
- [3] X. Li, W. Xu, M. Tang, L. Zhou, B. Zhu, S. Zhu, J. Zhu, Graphene oxide-based efficient and scalable solar desalination under one sun with a confined 2D water path, *Proceedings of the National Academy of Sciences of the United States of America*. 113 (2016) 13953–13958. doi:10.1073/pnas.1613031113.
- [4] X. Li, R. Lin, G. Ni, N. Xu, X. Hu, B. Zhu, G. Lv, J. Li, S. Zhu, J. Zhu, Three-dimensional artificial transpiration for efficient solar waste-water treatment, *National Science Review*. 5 (2018) 70–77. doi:10.1093/nsr/nwx051.
- [5] N. Xu, J. Li, Y. Wang, C. Fang, X. Li, Y. Wang, L. Zhou, B. Zhu, Z. Wu, S. Zhu, J. Zhu, A water lily-inspired hierarchical design for stable and efficient solar evaporation of high-salinity brine, *Science Advances*. 5 (2019) 1–8. doi:10.1126/sciadv.aaw7013.
- [6] W. Xu, X. Hu, S. Zhuang, Y. Wang, X. Li, L. Zhou, S. Zhu, J. Zhu, Flexible and Salt Resistant Janus Absorbers by Electrospinning for Stable and Efficient Solar Desalination, *Advanced Energy Materials*. 8 (2018) 1–7. doi:10.1002/aenm.201702884.
- [7] X. Hu, W. Xu, L. Zhou, Y. Tan, Y. Wang, S. Zhu, J. Zhu, Tailoring Graphene Oxide-Based Aerogels for Efficient Solar Steam Generation under One Sun, *Advanced Materials*. 29 (2017) 1604031. doi:10.1002/adma.201604031.
- [8] X. Wu, M.E. Robson, J.L. Phelps, J.S. Tan, B. Shao, G. Owens, H. Xu, A flexible photothermal cotton-CuS nanocage-agarose aerogel towards portable solar steam generation, *Nano Energy*. 56 (2019) 708–715. doi:10.1016/j.nanoen.2018.12.008.
- [9] F. Jiang, H. Liu, Y. Li, Y. Kuang, X. Xu, C. Chen, H. Huang, C. Jia, X. Zhao, E. Hitz, Y. Zhou, R. Yang, L. Cui, L. Hu, Lightweight, Mesoporous, and Highly Absorptive All-Nanofiber Aerogel for Efficient Solar Steam Generation, *ACS Applied Materials & Interfaces*. 10 (2018) 1104–1112. doi:10.1021/acsami.7b15125.
- [10] P. Mu, Z. Zhang, W. Bai, J. He, H. Sun, Z. Zhu, W. Liang, A. Li, Superwetting Monolithic Hollow-Carbon-Nanotubes Aerogels with Hierarchically Nanoporous Structure for Efficient Solar Steam Generation, *Advanced Energy Materials*. 9 (2019) 1–9. doi:10.1002/aenm.201802158.
- [11] Y. Fu, G. Wang, T. Mei, J. Li, J. Wang, X. Wang, Accessible Graphene Aerogel for Efficiently Harvesting Solar Energy, *ACS Sustainable Chemistry & Engineering*. 5 (2017) 4665–4671. doi:10.1021/acssuschemeng.6b03207.
- [12] B. Huo, D. Jiang, X. Cao, H. Liang, Z. Liu, C. Li, J. Liu, N-doped graphene /carbon hybrid aerogels for efficient solar steam generation, *Carbon*. 142 (2019) 13–19. doi:10.1016/j.carbon.2018.10.008.

- [13] P. Iamprasertkun, A. Krittayavathananon, M. Sawangphruk, N-doped reduced graphene oxide aerogel coated on carboxyl-modified carbon fiber paper for high-performance ionic-liquid supercapacitors, *Carbon*. 102 (2016) 455–461. doi:10.1016/j.carbon.2015.12.092.
- [14] K. McEnaney, L. Weinstein, D. Kraemer, H. Ghasemi, G. Chen, Aerogel-based solar thermal receivers, *Nano Energy*. 40 (2017) 180–186. doi:10.1016/j.nanoen.2017.08.006.
- [15] D. Voiry, M. Salehi, R. Silva, T. Fujita, M. Chen, T. Asefa, V.B. Shenoy, G. Eda, M. Chhowalla, Conducting MoS<sub>2</sub> nanosheets as catalysts for hydrogen evolution reaction, *Nano Letters*. 13 (2013) 6222–6227. doi:10.1021/nl403661s.
- [16] C. Liu, Q. Wang, F. Jia, S. Song, Adsorption of heavy metals on molybdenum disulfide in water: A critical review, *Journal of Molecular Liquids*. 292 (2019) 111390. doi:10.1016/j.molliq.2019.111390.
- [17] Z. Wang, B. Mi, Environmental Applications of 2D Molybdenum Disulfide (MoS<sub>2</sub>) Nanosheets, *Environmental Science and Technology*. 51 (2017) 8229–8244. doi:10.1021/acs.est.7b01466.
- [18] Q. Wang, L. Yang, F. Jia, Y. Li, S. Song, Removal of Cd (II) from water by using nano-scale molybdenum disulphide sheets as adsorbents, *Journal of Molecular Liquids*. 263 (2018) 526–533. doi:10.1016/j.molliq.2018.04.149.
- [19] Z. Guo, G. Wang, X. Ming, T. Mei, J. Wang, J. Li, J. Qian, X. Wang, PEGylated Self-Growth MoS<sub>2</sub> on a Cotton Cloth Substrate for High-Efficiency Solar Energy Utilization, *ACS Applied Materials & Interfaces*. 10 (2018) 24583–24589. doi:10.1021/acsami.8b08019.
- [20] Q. Wang, F. Jia, A. Huang, Y. Qin, S. Song, Y. Li, M.A.C. Arroyo, MoS<sub>2</sub>@sponge with double layer structure for high-efficiency solar desalination, *Desalination*. 481 (2020) 114359. doi:10.1016/j.desal.2020.114359.
- [21] H. Long, L. Chan, A. Harley-Trochimczyk, L.E. Luna, Z. Tang, T. Shi, A. Zettl, C. Carraro, M.A. Worsley, R. Maboudian, 3D MoS<sub>2</sub> Aerogel for Ultrasensitive NO<sub>2</sub> Detection and Its Tunable Sensing Behavior, *Advanced Materials Interfaces*. 4 (2017) 1–8. doi:10.1002/admi.201700217.
- [22] L. Jiang, B. Lin, X. Li, X. Song, H. Xia, L. Li, H. Zeng, Monolayer MoS<sub>2</sub>-Graphene Hybrid Aerogels with Controllable Porosity for Lithium-Ion Batteries with High Reversible Capacity, *ACS Applied Materials and Interfaces*. 8 (2016) 2680–2687. doi:10.1021/acsami.5b10692.
- [23] H. Long, A. Harley-Trochimczyk, T. Pham, Z. Tang, T. Shi, A. Zettl, C. Carraro, M.A. Worsley, R. Maboudian, High Surface Area MoS<sub>2</sub>/Graphene Hybrid Aerogel for

- Ultrasensitive NO<sub>2</sub> Detection, *Advanced Functional Materials*. 26 (2016) 5158–5165. doi:10.1002/adfm.201601562.
- [24] Q. Wang, F. Jia, S. Song, Y. Li, Hydrophilic MoS<sub>2</sub>/polydopamine (PDA) nanocomposites as the electrode for enhanced capacitive deionization, *Separation and Purification Technology*. 236 (2020) 116298. doi:10.1016/j.seppur.2019.116298.
- [25] H. Lee, S.M. Dellatore, W.M. Miller, P.B. Messersmith, Mussel-Inspired Surface Chemistry for Multifunctional Coatings, *Science*. 318 (2007) 426–430. doi:10.1126/science.1147241.
- [26] Y. Liu, K. Ai, L. Lu, Polydopamine and Its Derivative Materials: Synthesis and Promising Applications in Energy, Environmental, and Biomedical Fields, *Chemical Reviews*. 114 (2014) 5057–5115. doi:10.1021/cr400407a.
- [27] Q. Wang, L. Peng, Y. Gong, F. Jia, S. Song, Y. Li, Mussel-inspired Fe<sub>3</sub>O<sub>4</sub>@Polydopamine(PDA)-MoS<sub>2</sub> core-shell nanosphere as a promising adsorbent for removal of Pb<sup>2+</sup> from water, *Journal of Molecular Liquids*. 282 (2019) 598–605. doi:10.1016/j.molliq.2019.03.052.
- [28] S. Takeshita, S. Yoda, Chitosan Aerogels: Transparent, Flexible Thermal Insulators, *Chemistry of Materials*. 27 (2015) 7569–7572. doi:10.1021/acs.chemmater.5b03610.
- [29] K.A.S. Meraz, S.M.P. Vargas, J.T.L. Maldonado, J.M.C. Bravo, M.T.O. Guzman, E.A.L. Maldonado, Eco-friendly innovation for nejayote coagulation-flocculation process using chitosan: Evaluation through zeta potential measurements, *Chemical Engineering Journal*. 284 (2016) 536–542. doi:10.1016/j.ccej.2015.09.026.
- [30] Y. Gao, C. Chen, X. Tan, H. Xu, K. Zhu, Polyaniline-modified 3D-flower-like molybdenum disulfide composite for efficient adsorption/photocatalytic reduction of Cr(VI), *Journal of Colloid and Interface Science*. 476 (2016) 62–70. doi:10.1016/j.jcis.2016.05.022.
- [31] F. Jia, K. Sun, B. Yang, X. Zhang, Q. Wang, S. Song, Defect-rich molybdenum disulfide as electrode for enhanced capacitive deionization from water, *Desalination*. 446 (2018) 21–30. doi:10.1016/j.desal.2018.08.024.
- [32] W. Wang, Y. Zhao, H. Bai, T. Zhang, V. Ibarra-Galvan, S. Song, Methylene blue removal from water using the hydrogel beads of poly(vinyl alcohol)-sodium alginate-chitosan-montmorillonite, *Carbohydrate Polymers*. 198 (2018) 518–528. doi:10.1016/j.carbpol.2018.06.124.
- [33] X. Liu, J. Cao, H. Li, J. Li, Q. Jin, K. Ren, J. Ji, Mussel-Inspired Polydopamine: A Biocompatible and Ultrastable Coating for Nanoparticles in Vivo, *ACS Nano*. 7 (2013) 9384–9395. doi:10.1021/nn404117j.

- [34] M. Wu, G. Chen, P. Liu, W. Zhou, Q. Jia, Polydopamine-based immobilization of a hydrazone covalent organic framework for headspace solid-phase microextraction of pyrethroids in vegetables and fruits, *Journal of Chromatography A*. 1456 (2016) 34–41. doi:10.1016/j.chroma.2016.05.100.
- [35] L. Jaiswal, S. Shankar, J.-W. Rhim, Carrageenan-based functional hydrogel film reinforced with sulfur nanoparticles and grapefruit seed extract for wound healing application, *Carbohydrate Polymers*. 224 (2019) 115191. doi:10.1016/j.carbpol.2019.115191.
- [36] P. Bösigler, G. Tegl, I.M.T. Richard, L. Le Gat, L. Huber, V. Stagl, A. Mensah, G.M. Guebitz, R.M. Rossi, G. Fortunato, Enzyme functionalized electrospun chitosan mats for antimicrobial treatment, *Carbohydrate Polymers*. 181 (2018) 551–559. doi:10.1016/j.carbpol.2017.12.002.
- [37] Z. Yu, B. Li, J. Chu, P. Zhang, Silica in situ enhanced PVA/chitosan biodegradable films for food packages, *Carbohydrate Polymers*. 184 (2018) 214–220. doi:10.1016/j.carbpol.2017.12.043.
- [38] S. Kheirandish, M. Ghaedi, K. Dashtian, F. Heidari, F. Pourebrahim, S. Wang, Chitosan extraction from lobster shells and its grafted with functionalized MWCNT for simultaneous removal of Pb<sup>2+</sup> ions and eriochrome cyanine R dye after their complexation, *International Journal of Biological Macromolecules*. 102 (2017) 181–191. doi:10.1016/j.ijbiomac.2017.03.035.
- [39] Y. Wang, Y. Zhang, C. Hou, M. Liu, Mussel-inspired synthesis of magnetic polydopamine-chitosan nanoparticles as biosorbent for dyes and metals removal, *Journal of the Taiwan Institute of Chemical Engineers*. 61 (2016) 292–298. doi:10.1016/j.jtice.2016.01.008.
- [40] D.-M. Guo, Q.-D. An, Z.-Y. Xiao, S.-R. Zhai, D.-J. Yang, Efficient removal of Pb(II), Cr(VI) and organic dyes by polydopamine modified chitosan aerogels, *Carbohydrate Polymers*. 202 (2018) 306–314. doi:10.1016/j.carbpol.2018.08.140.
- [41] R.R. Gadkari, S. Suwalka, M.R. Yogi, W. Ali, A. Das, R. Alagirusamy, Green synthesis of chitosan-cinnamaldehyde cross-linked nanoparticles: Characterization and antibacterial activity, *Carbohydrate Polymers*. 226 (2019) 115298. doi:10.1016/j.carbpol.2019.115298.
- [42] X. Li, B. Zhu, J. Zhu, Graphene oxide based materials for desalination, *Carbon*. 146 (2019) 320–328. doi:10.1016/j.carbon.2019.02.007.
- [43] X. Wang, G. Ou, N. Wang, H. Wu, Graphene-based Recyclable Photo-Absorbers for High-Efficiency Seawater Desalination, *ACS Applied Materials and Interfaces*. 8 (2016) 9194–9199. doi:10.1021/acsami.6b02071.

- [44] X. Li, G. Ni, T. Cooper, N. Xu, J. Li, L. Zhou, X. Hu, B. Zhu, P. Yao, J. Zhu, Measuring Conversion Efficiency of Solar Vapor Generation, *Joule*. 3 (2019) 1798–1803. doi:10.1016/j.joule.2019.06.009.
- [45] C. Chen, Y. Li, J. Song, Z. Yang, Y. Kuang, E. Hitz, C. Jia, A. Gong, F. Jiang, J.Y. Zhu, B. Yang, J. Xie, L. Hu, Highly Flexible and Efficient Solar Steam Generation Device, *Advanced Materials*. 29 (2017) 1701756. doi:10.1002/adma.201701756.
- [46] Q. Jiang, H. Gholami Derami, D. Ghim, S. Cao, Y.-S. Jun, S. Singamaneni, Polydopamine-filled bacterial nanocellulose as a biodegradable interfacial photothermal evaporator for highly efficient solar steam generation, *Journal of Materials Chemistry A*. 5 (2017) 18397–18402. doi:10.1039/C7TA04834C.
- [47] C. Chen, Y. Li, J. Song, Z. Yang, Y. Kuang, E. Hitz, C. Jia, A. Gong, F. Jiang, J.Y. Zhu, B. Yang, J. Xie, L. Hu, Highly Flexible and Efficient Solar Steam Generation Device, *Advanced Materials*. 29 (2017) 1–8. doi:org/10.1002/adma.201701756.
- [48] S. Ma, C.P. Chiu, Y. Zhu, C.Y. Tang, H. Long, W. Qarony, X. Zhao, X. Zhang, W.H. Lo, Y.H. Tsang, Recycled waste black polyurethane sponges for solar vapor generation and distillation, *Applied Energy*. 206 (2017) 63–69. doi:10.1016/j.apenergy.2017.08.169.
- [49] Q. Yuan, Z. Li, X. Yang, Y. Yang, M. Zou, L. Fu, A. Cao, An Ultrathin Flexible 2D Membrane Based on Single-Walled Nanotube-MoS<sub>2</sub> Hybrid Film for High-Performance Solar Steam Generation, *Advanced Functional Materials*. 28 (2017) 1704505. doi:10.1002/adfm.201704505.
- [50] D. Ghim, Q. Jiang, S. Cao, S. Singamaneni, Y.-S. Jun, Mechanically interlocked 1T/2H phases of MoS<sub>2</sub> nanosheets for solar thermal water purification, *Nano Energy*. 53 (2018) 949–957. doi:10.1016/j.nanoen.2018.09.038.
- [51] World Health Organization, Safe Drinking-water from Desalination, World Health Organization. WHO/HSE/WS (2011).

The main content of this chapter was published on “*ACS Applied Materials & Interfaces*”.



## CHAPTER VI

### Hydrophilic MoS<sub>2</sub>/polydopamine nanocomposites as the electrode for enhanced capacitive deionization

#### 6.1. Introduction

At present, the deficits of clean freshwater have been terribly aggravated because of the increasing population and urbanization as well as the deterioration of water quality. A great quantity of methods, such as multi-stage flash distillation, reverse osmosis and capacitive deionization (CDI), etc., have been applied in scale to produce freshwater from sea or brackish water [1]. Among these methods, CDI has been regarded as a promising technology with low-cost and easy-operation because of its non-necessity of heat-treatment, high pressure or membrane process [2]. With a low direct voltage (0.8-1.2 V) loaded to the CDI cell, salt ions in aqueous solution will be transferred into electric double layers (EDLs) at electrode/solution interfaces by electrostatic forces, subsequently stored inside the EDLs, resulting in the desalinated water in the CDI cell [3]. If the electric field is removed, the trapped ions are released back into the aqueous solution, revealing the recoverability and low-cost property of CDI techniques. Recently, besides the carbon-based materials and metal oxides [1,4,5], MoS<sub>2</sub> has been applied as an electrode material in the CDI system due to its ideal platform and outstanding electrochemical property. For instance, when acted as the electrode materials for CDI device, the chemical exfoliated MoS<sub>2</sub> nanosheets exhibited a high specific capacitance of 109.7 F/g and high ion quality removal capacity of 8.81 mg/g, which was mainly because of their unique two-dimensional (2D) thin sheet structure of 1T phase [6]. It was reported that the defect-rich MoS<sub>2</sub> originated from the general thermal treatment possessed a highly promoted electrosorption capacity of 35 mg/g, compared to that of original MoS<sub>2</sub> (12.8 mg/g), since the defects could provide MoS<sub>2</sub> with abundant negative charges [7]. Unfortunately, the poor water wettability of MoS<sub>2</sub> still remained one of the primary weaknesses facing MoS<sub>2</sub> for its CDI application. The poor water wettability of MoS<sub>2</sub> was detrimental to the access of electrolyte to its surfaces, resulting in not only the high transfer resistance at the solid-liquid interfaces but also the inefficient utilization of the electrochemical surfaces, which might bring about a restricted CDI performance. In this case, one consideration of us is to modify MoS<sub>2</sub> with polydopamine (PDA) which possesses the great surface adhesion, outstanding

hydrophilicity and electroactive property [8]. Up to till now, MoS<sub>2</sub>/PDA composites have never been applied in any capacitive deionization devices.

In this work, attempts were made to promote the CDI performances of MoS<sub>2</sub> with the direct modification of PDA. To begin with, by the facile immersion of MoS<sub>2</sub> in dopamine solution at room temperature, MoS<sub>2</sub>/PDA nanocomposites were successfully prepared, and the amounts of deposited PDA could be controlled via tuning the soak time. Afterwards, the property of as-synthesized materials, such as the chemical composition, water contact angles, morphology and electrochemical property, etc., were determined. At last, the CDI performances of MoS<sub>2</sub>/PDA-4 electrodes were investigated along with the desalination assesses compared to original MoS<sub>2</sub> as well as other electrode materials. With the soak time being carefully adjusted, MoS<sub>2</sub> modified by PDA for 4 h (MoS<sub>2</sub>/PDA-4) could exhibit not only lower inner resistance due to its better wettability, but also much higher specific capacitance because of the incorporation of electroactive PDA compared to original MoS<sub>2</sub>, which rendered the MoS<sub>2</sub>/PDA nanocomposites a much more enhanced CDI performance.

## 6.2. Experimental

### 6.2.1. Materials

Ammonium molybdate tetrahydrate ((NH<sub>4</sub>)<sub>6</sub>Mo<sub>7</sub>O<sub>24</sub>·4H<sub>2</sub>O), thiourea (CN<sub>2</sub>H<sub>4</sub>S), dopamine hydrochloride (C<sub>8</sub>H<sub>11</sub>NO<sub>2</sub>·HC), ethanol (C<sub>2</sub>H<sub>6</sub>O), sodium nitrate (NaCl) and conductive carbon black were supplied by Shanghai Sinopharm Chemical Reagent Co., Ltd. Polytetrafluoroethylene (PTFE; 60 wt% water solution) and tris(hydroxymethyl) aminomethane (Tris, C<sub>4</sub>H<sub>11</sub>NO<sub>3</sub>) were purchased from Shanghai Aladdin Bio-Chem Technology Co., LTD. Hydrochloric acid (HCl) was purchased from Merck Pty. Ltd. All reagents were of analytical purity. Deionized water (18.2 MΩ cm) was originated from Milli-Q instrument (Millipore Corporation, France).

### 6.2.2. Synthesis of MoS<sub>2</sub>

Firstly, 72 mL homogeneous aqueous solution containing 2.48 g (NH<sub>4</sub>)<sub>6</sub>Mo<sub>7</sub>O<sub>24</sub>·4H<sub>2</sub>O and 4.56 g CN<sub>2</sub>H<sub>4</sub>S were obtained by being sonicated for 30 min in water base. Then, the mixture was transferred into a Teflon-lined stainless-steel autoclave and thermally treated at 220°C for 6 h [9]. After being naturally cooled down to ambient temperature, the black precipitates were collected by the vacuum filtration through the micropore membranes (Average pore size of 0.22 μm), washed with deionized water for three times, and finally dried by vacuum freeze-drying.

### 6.2.3. Synthesis of MoS<sub>2</sub>/PDA nanocomposites

Typically, 100 mg as-synthesized MoS<sub>2</sub> was added into 100 mL Tris-buffer aqueous solution (10 mM, pH 8.5) and then sonicated at 150 W for 30 min to obtain exfoliated MoS<sub>2</sub>. Afterwards, 100 mg dopamine hydrochloride was added. The mixtures were shaken at 150 rpm and kept for various time (2, 4, 8, 12, 16 and 24 h) in a water base at room temperature (25°C). Once dopamine hydrochloride was added, the polymerization of dopamine occurred immediately, accompanied by the solution's color changed from colorless to light brown and eventually to dark brown. Finally, the black powders were washed with deionized water for four times by the aforementioned vacuum filtration and dried by vacuum freeze-drying. The resultant samples were denoted as MoS<sub>2</sub>/PDA-t, where t represented the soak time, for instance, if MoS<sub>2</sub> was soaked in the dopamine solution for 4 h, the resulted sample was named as MoS<sub>2</sub>/PDA-4. Though the exact polymerization mechanisms of dopamine by using O<sub>2</sub> as the oxidant in alkaline medium have not been well understood yet, one of the possible pathways in this work (Fig. 6.1) due to the same reaction conditions could be [8,10]:

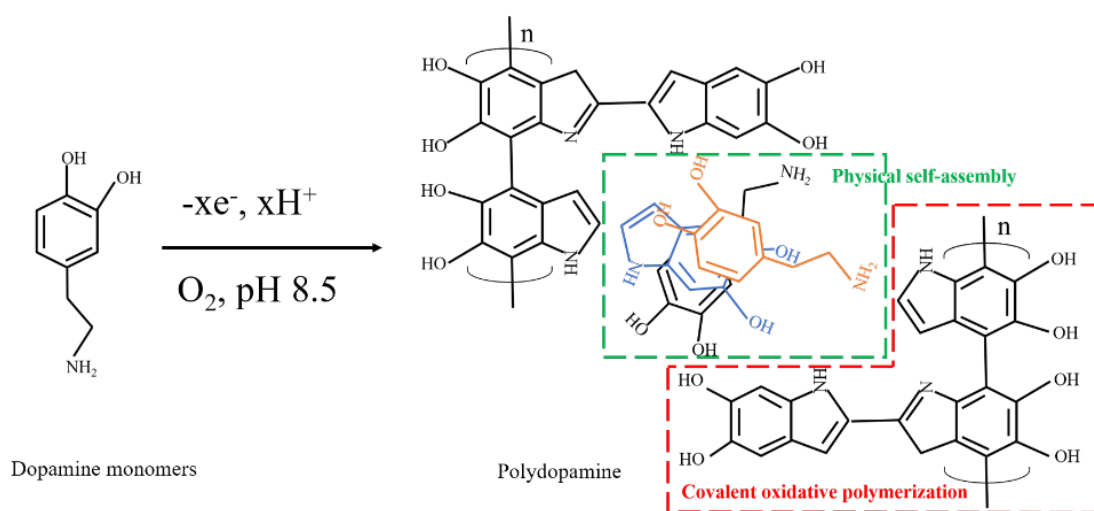


Fig. 6.1. Sketch of the possible polymerization process of dopamine in this work (25°C, pH 8.5).

### 6.2.4. Characterizations

The morphology of samples was observed using scanning electron microscopy (SEM, SU8010, Hitachi). Powder X-ray diffraction patterns (XRD) of the samples was obtained from the PIXcel-Empyrean instrument. The samples were mixed with KBr powders and mounted on a Nexus Thermo Nicolet spectrometer for the Fourier transform infrared spectroscopy (FTIR) measurement at room temperature. The

hydrophilicity was determined by measuring the contact angle using a goniometer (JC2000A). The surface charges of materials were obtained from the Malvern Zeta sizer Nano ZS90. The chemical analysis of materials was conducted using an X-ray photoelectron spectroscopy (XPS, ESCALAB 250XI, Thermo Fisher Scientific).

### 6.2.5. Electrochemical measurement

To fabricate the electrodes for electrochemical measurement, 1 ml ethanol/water (V:V=1:1) solvent was added into 40 mg mixtures which contained the as-synthesized materials, acetylene carbon black and polytetrafluoroethylene (PTFE) with a mass ratio of 8:1:1, to form a black slurry. Afterwards, the slurry was ground and evenly coated onto the stainless-steel cloth (1.0 cm×1.0 cm), dried at 60°C in vacuum for 8 h, and pressed under 10 MPa for 10 min. Finally, the cyclic voltammetry (CV) and electrochemical impedance spectroscopy (EIS) measurements were carried out on an electrochemical workstation (AMETEK VersaSTAT 4) with the Pt foil (1.0 cm×1.0 cm), Ag/AgCl electrode (saturated KCl, 3.5 mol/L) and 100 mL, 1 mol/L NaCl solution working as the counter electrodes, the reference electrodes and electrolyte, respectively. The specific capacitance  $C$  (F/g) of the materials were originated from Eq. 6.1 [11]:

$$C = \int I \times dE / (2\nu \times m \times \Delta E) \quad 6.1$$

where  $I$  and  $\Delta E$  represent the instantaneous current (A) and potential window (V), respectively.  $m$  is the mass of the active material (g). And  $\nu$  means the scan rate (mV/s).

### 6.2.6. CDI test

The CDI test was performed in a self-made device (Fig. 6.2(a)), in which the key unit for desalination was illustrated in Fig. 6.2(b). The titanium plate coated with active carbon (the positive electrodes) and another titanium plate coated with MoS<sub>2</sub> or MoS<sub>2</sub>/PDA nanocomposites (the negative electrodes) were parallelly set in the CDI unit. The titanium plates were separated by a silicone rubber gasket with thickness of 2 mm, of which the center possessed a square channel with size of 6 cm × 6 cm.

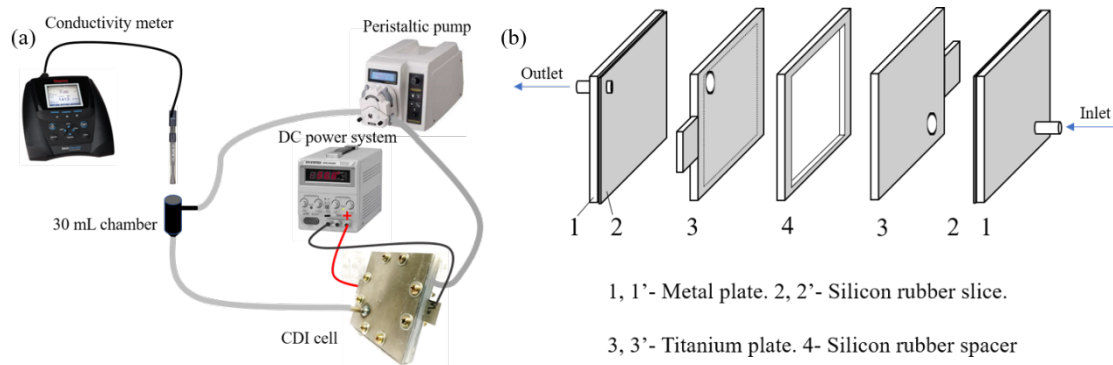


Fig. 6.2. (a) Sketch of the self-made CDI unit. (b) Diagram of the CDI device in this work.

In a typical CDI test, 40 mL of NaCl solution with a desired concentration was circularly flowed in the CDI unit at a speed of 25 mL/min, accompanied by a 1.2 V (DC voltage) loading on two current collectors. The continuous conductivity detection of aqueous solution containing NaCl was performed by the Thermo Scientific Orion Star A215 conductivity meter equipped with an Orion 013005 MD conductivity electrode. The concentration of salt solution was positively correlated to the conductivity (see in Fig. 6.3). The electrosorption capacity  $Q$  (mg/g) was calculated using Eq. 6.2:

$$Q = \frac{(C_0 - C_t)}{m} \times V \quad 6.2$$

where  $C_0$  (mg/L) and  $C_t$  (mg/L) are the concentration of NaCl at initial time and time  $t$ , respectively.  $V$  (L) is the total volume of the electrolyte.  $m$  (g) is the mass of active materials on electrodes, which was 0.064 g in this work.

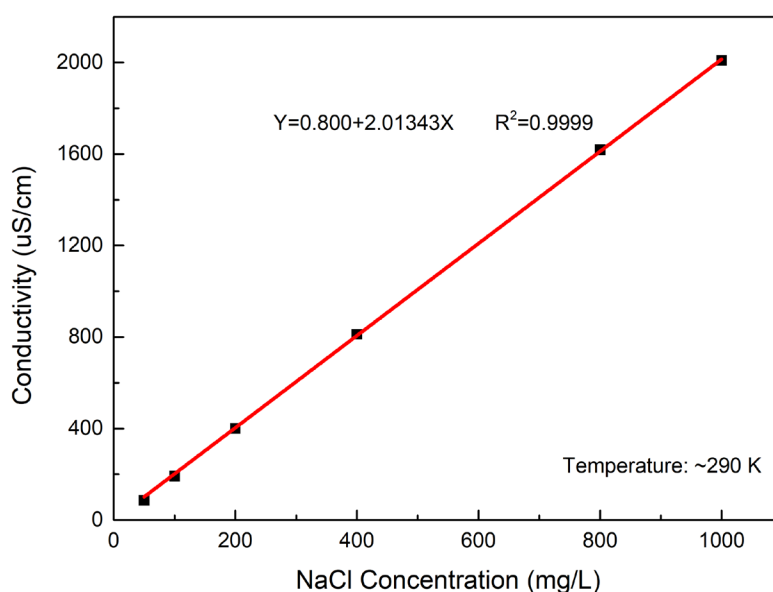


Fig. 6.3. The relationship between the concentration and conductivity of NaCl aqueous solution.

## 6.3. Results and discussion

### 6.3.1. Characterizations

To investigate the main composition of the as-synthesized materials, the XRD spectrum of MoS<sub>2</sub> modified by PDA for 0, 4, 12 and 24 h are displayed in Fig. 6.4(a). Five characteristic peaks at 13.20°, 32.80°, 35.26°, 41.66° and 57.70° were attributed to the typical (002), (100), (103), (105) and (110) planes of MoS<sub>2</sub> [9,12], respectively, demonstrating that the as-synthesized composites was mainly composited with MoS<sub>2</sub>. Comparing to original MoS<sub>2</sub>, MoS<sub>2</sub>/PDA composites possessed much lower crystallinity based on their much weaker reflections, revealing that a large number of PDA/MoS<sub>2</sub> sheets were of its loose structure and high exfoliation [13].

FTIR measurements were further conducted to investigate the chemical structure of PDA/MoS<sub>2</sub> composites. As shown in Fig. 6.4(b), the peaks at ~3441 cm<sup>-1</sup> and ~1624 cm<sup>-1</sup> derived from the characteristic O-H vibrations of adsorbed water molecules (H<sub>2</sub>O) [14,15]. The negligible O-H vibrations of H<sub>2</sub>O in original MoS<sub>2</sub> was attributed to the little water contents due to its hydrophobicity, while the great quantity of O-H vibrations of H<sub>2</sub>O in MoS<sub>2</sub>/PDA composites were originated from the large water contents because of their great hydrophilicity. The enhancements of O-H vibrations of H<sub>2</sub>O from original MoS<sub>2</sub> to MoS<sub>2</sub>/PDA-24 might be attributed to reason that the amount of deposited PDA on the surfaces of MoS<sub>2</sub> would increase with the prolongation of immersion time. What is more, the newly emerging peaks at 1504, 1271 and 1057 cm<sup>-1</sup> were attributed to the main vibrational modes of C=N, C-N and -OH of PDA [15], and their enhancing vibrational signals with the increase of soak time directly confirmed the increased amount of deposited PDA film on the surface of MoS<sub>2</sub>. The tiny peak at 1400 cm<sup>-1</sup> for original MoS<sub>2</sub> was mainly assigned to the hydrogen bonds of S···H [16]. Another tiny peaks at ~613 cm<sup>-1</sup> were assigned to C-S and found in all samples, which might because of the existence of impurities (by-products) during the formation of MoS<sub>2</sub>.

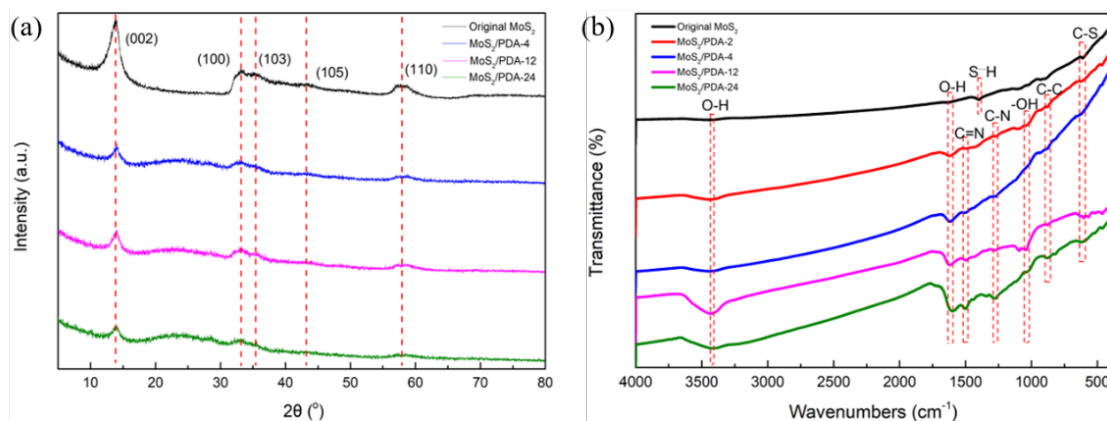


Fig. 6.4. (a) XRD and (b) FTIR spectra of the original MoS<sub>2</sub> and various MoS<sub>2</sub>/PDA nanocomposites.

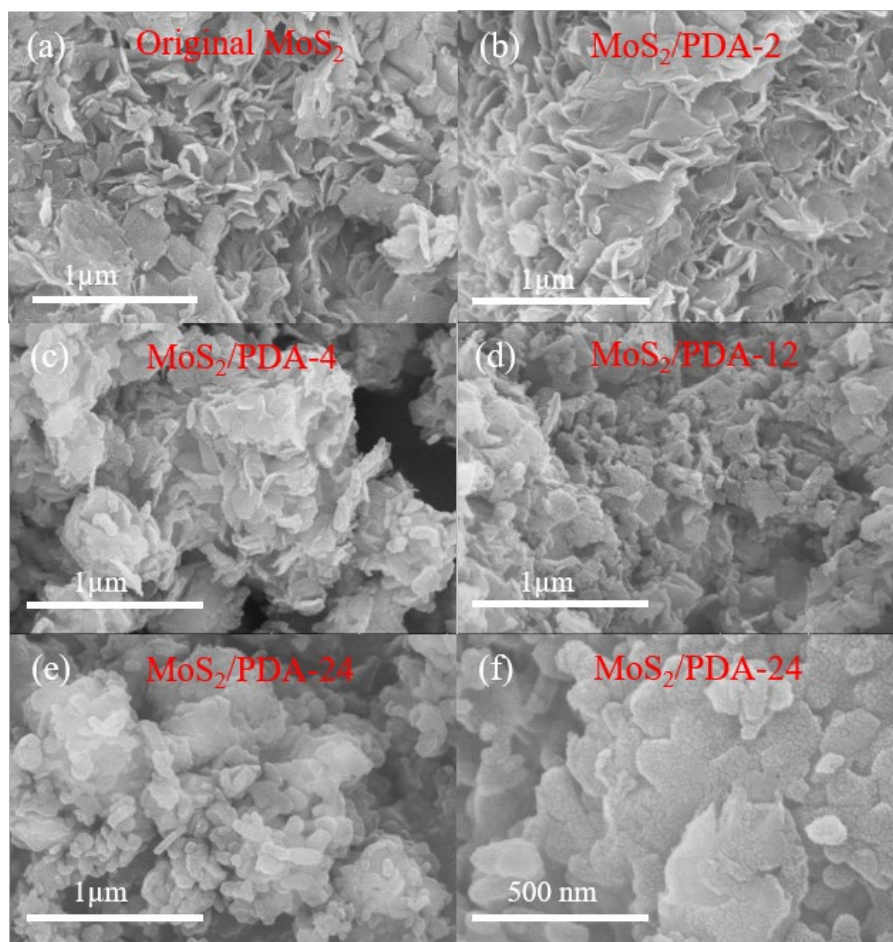


Fig. 6.5. SEM images of (a) original MoS<sub>2</sub>, (b) MoS<sub>2</sub>/PDA-2, (c) MoS<sub>2</sub>/PDA-4, (d) MoS<sub>2</sub>/PDA-12 and (e, f) MoS<sub>2</sub>/PDA-24.

Fig. 6.5 showed the SEM images of original MoS<sub>2</sub> and various MoS<sub>2</sub>/PDA nanocomposites. As displayed in Fig. 6.5(a), original MoS<sub>2</sub> was around 450 nm in size and was of its flower-like architectures. Fig. 6.5(b)-(f) shows the morphologies of

MoS<sub>2</sub> encapsulated by PDA with different levels. It was prone to figure out the loose petal-like architectures of MoS<sub>2</sub> in the MoS<sub>2</sub>/PDA nanocomposites, which were originated ultrasonic exfoliation of original MoS<sub>2</sub>. As illustrated in Fig4(b)-(f), it could be directly observed that more and more PDA were deposited on the surface of MoS<sub>2</sub> with the prolongation of immersion time. Namely, the amount of deposited PDA on MoS<sub>2</sub> could be finely controlled via tuning the soak time.

The water wettability of original MoS<sub>2</sub> and various MoS<sub>2</sub>/PDA nanocomposites were characterized by the water contact angle measurement. As displayed in Fig. 6.6(a), the contact angle of original MoS<sub>2</sub> was 71.0°, revealing a typical surface hydrophobicity of original MoS<sub>2</sub>. Impressively, with the coating of PDA, MoS<sub>2</sub>/PDA-4, MoS<sub>2</sub>/PDA-12 and MoS<sub>2</sub>/PDA-24 showed highly improved water wettability with the contact angle of 60.50°, 52.00° and 42.50°, respectively (see Fig. 6.6(b)–(d)). The tendency of descending contact angles from original MoS<sub>2</sub>, MoS<sub>2</sub>/PDA-4, MoS<sub>2</sub>/PDA-12 and MoS<sub>2</sub>/PDA-24 directly suggested that the hydrophilicity of MoS<sub>2</sub>/PDA nanocomposites increased with the increase of soak time. Such enhanced hydrophilicity was favorable for the diffusion of salt ions from/into the surface of MoS<sub>2</sub>/PDA electrodes, and then contributed to its desalination process in CDI device. These results demonstrated the necessity of the PDA coating on the surface improvement of MoS<sub>2</sub>.

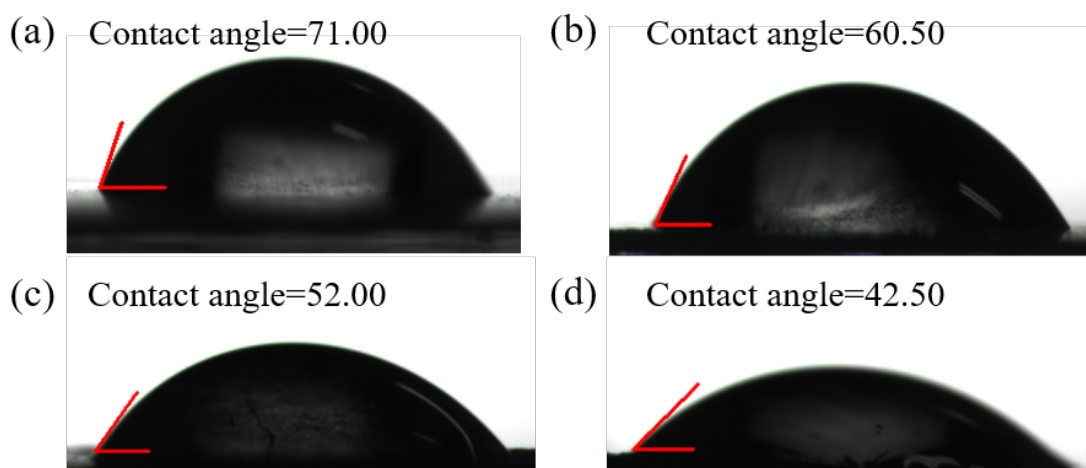


Fig. 6.6. Water contact angles of (a) original MoS<sub>2</sub>, (b) MoS<sub>2</sub>/PDA-4, (c) MoS<sub>2</sub>/PDA-12 and (d) MoS<sub>2</sub>/PDA-24.

The change of elements in various MoS<sub>2</sub>/PDA nanocomposites were investigated by XPS spectra and the results were shown in Fig. 6.7. In Fig. 6.7(a), it was figured



out that the as-prepared samples mainly consisted of Mo, S, C, N and O elements, which agreed well with the chemical composition of MoS<sub>2</sub>/PDA hybrids. In addition, the relative intensity of C, N and O were enhanced as the polymerization time increased, demonstrating the increased relative content of PDA in corresponding MoS<sub>2</sub>/PDA nanocomposites. It was also found that all characteristic peaks of MoS<sub>2</sub>, such as Mo 3p, Mo 3d, Mo 3s and S 2p were decreased as the polymerization time prolonged [17]. In Fig. 6.7(b), the spectrum of Mo 3s with single peak at 505.9 eV decreased from original MoS<sub>2</sub> to MoS<sub>2</sub>/PDA-24, directly confirming the decreasing relative content of Mo element. This change might originate from the results: (1) The increasing amounts of the coating PDA as time resulted in the reduction of the relative content of MoS<sub>2</sub>; (2) Partial architectures of MoS<sub>2</sub> crystalline were destroyed because of the redox capacity of dopamine during its polymerization [10] and then caused the loss of Mo and S atoms.

In Fig. 6.7(c), the peaks at 285.0 eV, 286.4 eV and 288.8 eV were assigned to C-C, C-O and O-C=O species [18], respectively, further demonstrating the existence of PDA with abundant functional groups. The additional tiny peak at 287.2 eV in original MoS<sub>2</sub> was related to C-N species, which derived from the residual precursors during the formation of MoS<sub>2</sub>. In the N 1s spectrum as displayed in Fig. 6.7(d), the peaks at 395.6 eV, 398.6 eV and 400.8 eV were ascribed to Mo 3p [19], pyridinic N [20] and graphitic N [21], respectively. Notably, the relative content of graphitic N in MoS<sub>2</sub>/PDA nanocomposites increased when the polymerization time increased and almost leveled off when the polymerization time was more than 4 h. High-level electroactive graphitic N and pyridinic N could greatly contribute to the increase of the limiting current density and the improvement of onset potential [22], thus resulting in an enhanced conductivity and specific capacitance of MoS<sub>2</sub>/PDA compared to original MoS<sub>2</sub>. In order to get a larger amount of graphitic N and pyridinic N with least time consuming, 4 h was expected the best polymerization time for obtaining MoS<sub>2</sub>/PDA nanocomposites with excellent electrochemical property at room temperatures in this work.

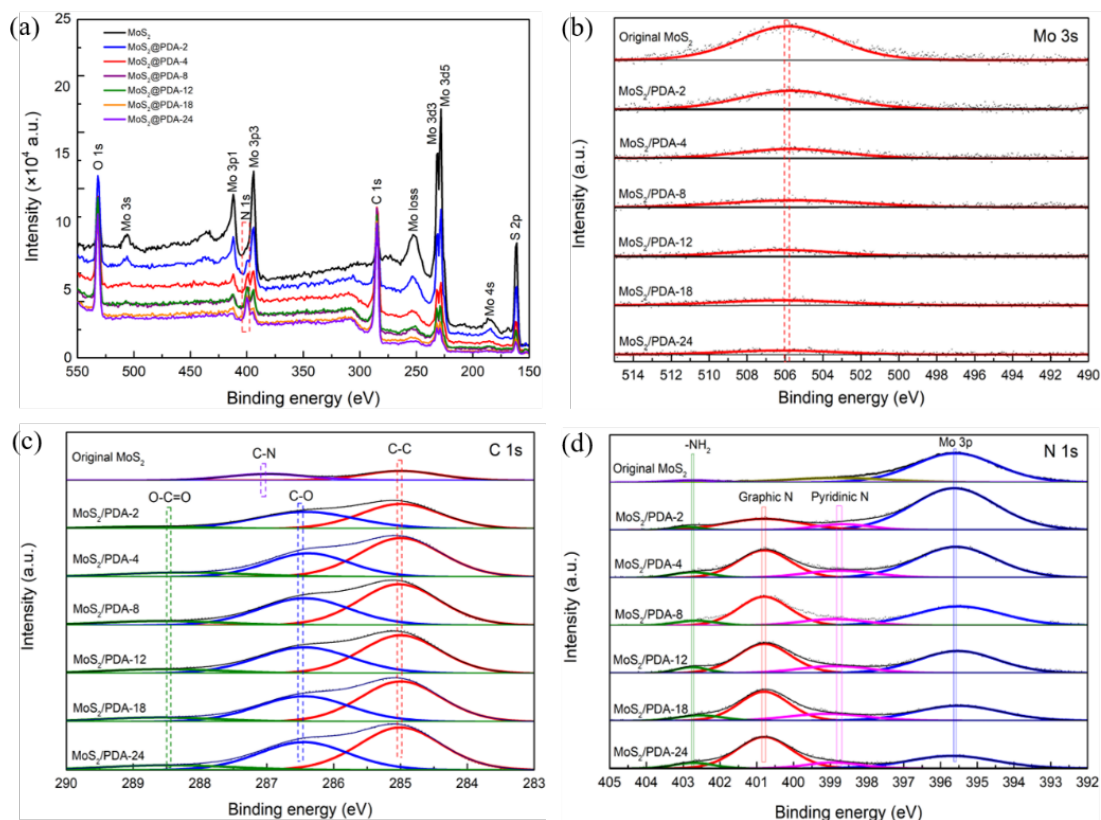


Fig. 6.7 (a) XPS survey scans of various MoS<sub>2</sub>/PDA nanocomposites. High-resolution spectra of (b) Mo 3s, (c) C 1s and (d) N 1s of various MoS<sub>2</sub>/PDA nanocomposites.

The cyclic voltammetry (CV) measurements are usually applied to investigate the electrochemical behavior of electrode materials thus predict their performance in the CDI process [1,4,5,7]. For a detailed investigation of time-dependent modification, the CV curves of MoS<sub>2</sub> modified by PDA for 0, 2, 4, 8, 12, 18, 24 h at a scanning rate of 20 mV/s was displayed in Fig. 6.8(a). Compared to original MoS<sub>2</sub>, MoS<sub>2</sub>/PDA nanocomposites showed nearly symmetric rectangular shapes without Faradaic reactions, suggesting the typical double layer capacitor behavior contributed to the current response [4]. It was found that the integrated area of CV curves of MoS<sub>2</sub>/PDA nanocomposites gradually increased with the polymerization time increased but declined when the polymerization time was longer than 4 h, demonstrating 4 h turned out to be the suitable polymerization time for fabricating PDA-based nanocomposites with the best electrochemical performance [10]. In addition, the CV curves' integrated area of MoS<sub>2</sub>/PDA nanocomposites would further decline to be less than that of original MoS<sub>2</sub> if the soak time was over 8 h, which was believed to involve with the increasing thickness of PDA films and the structural changes of MoS<sub>2</sub>/PDA nanocomposites, which would be further discussed in next sections. In other words,

MoS<sub>2</sub>/PDA-4 possessed the highest specific capacitance among the MoS<sub>2</sub>/PDA nanocomposites.

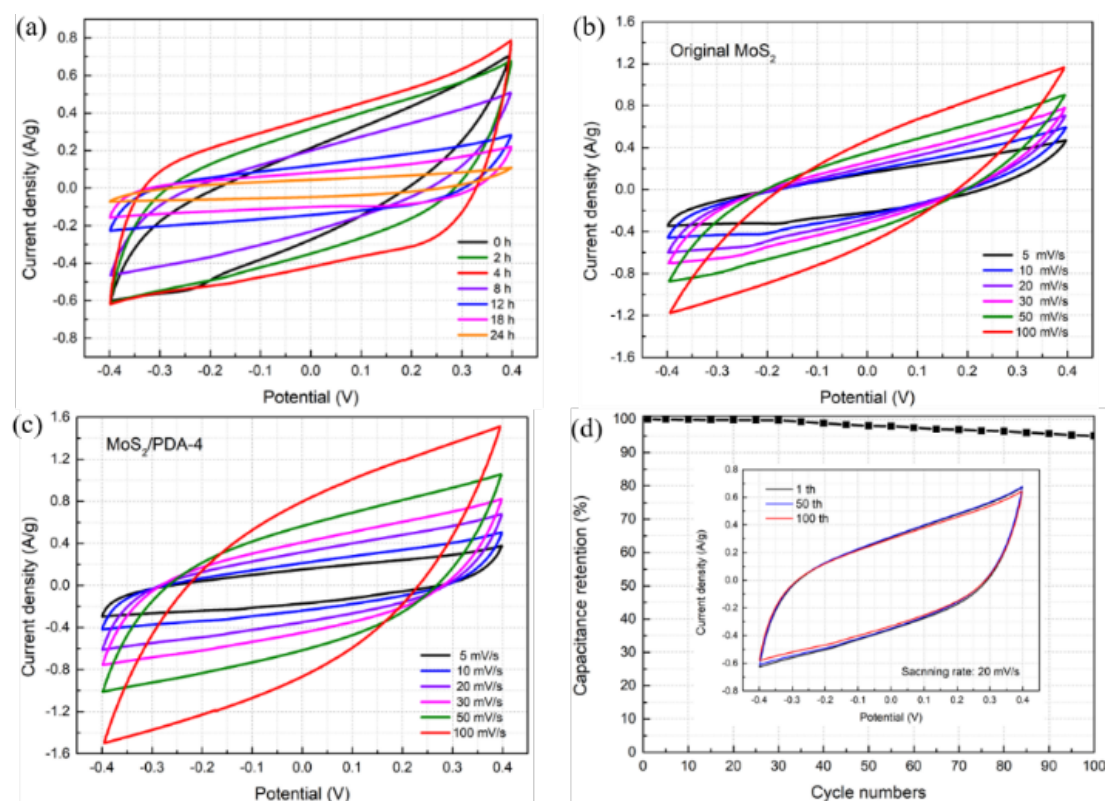


Fig. 6.8. CV curves of (a) MoS<sub>2</sub> modified by PDA for 0, 2, 4, 8, 12, 18, 24 h at 20 mV/s, (b) original MoS<sub>2</sub> and (c) MoS<sub>2</sub>/PDA-4 with scanning rates ranging from 5 mV/s to 100mV/s. (d) Cycling performance of MoS<sub>2</sub>/PDA-4 at 20 mV/s (Inset: CV curves in 1<sup>th</sup>, 50<sup>th</sup> and 100<sup>th</sup> cycles).

All measurements were performed in 1.0 M NaCl solution.

In Fig. 6.8(b) and (c), CV curves of both original MoS<sub>2</sub> and MoS<sub>2</sub>/PDA-4 exhibited obvious distortions from the typical rectangle shape to the foliate shape when the scanning rates increased from 5 mV/s to 100 mV/s, disclosing the sluggish ion diffusion through the thick double layer [5]. The superior electrochemical properties of MoS<sub>2</sub>/PDA-4 were also highlighted by the excellent cyclic stability. As shown in Fig. 6.8(d), the CV curves remained its original shapes which was accompanied by the specific capacitance remained basically unchanged level of 95% even after 100 successive cycles, revealing the impressive electrochemical stability and cyclic stability of MoS<sub>2</sub>/PDA-4 electrodes. These results implied that MoS<sub>2</sub>/PDA-4 should be superior to both original MoS<sub>2</sub> and other MoS<sub>2</sub>/PDA nanocomposites for CDI applications.

### 6.3.2. CDI performance

Displayed in Fig. 6.9 were the CDI performances of original MoS<sub>2</sub> and MoS<sub>2</sub>/PDA-4 at 1.2 V in NaCl solution.

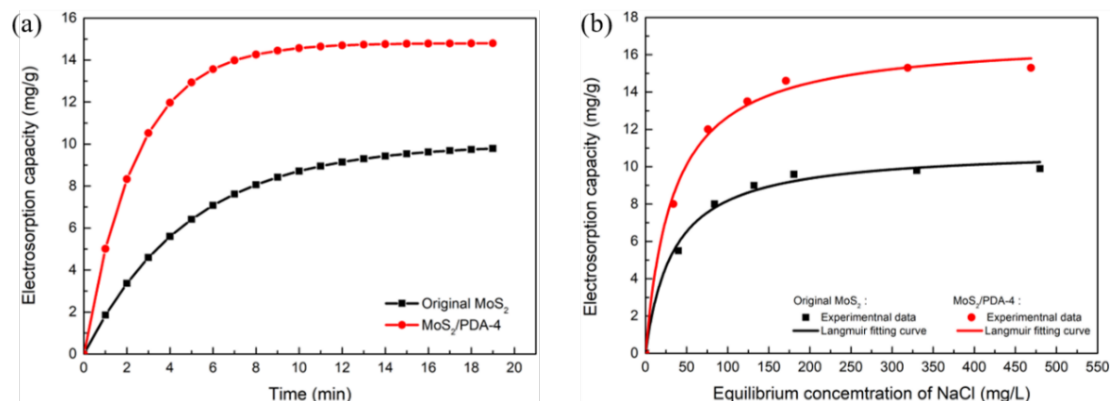


Fig. 6.9. (a) Electro sorption capacity of origin MoS<sub>2</sub> and MoS<sub>2</sub>/PDA-4 in 200 mg/L NaCl solution at different times. (b) Electro sorption capacity of original MoS<sub>2</sub> and MoS<sub>2</sub>/PDA-4 in NaCl solutions with various concentrations and their corresponding Langmuir fitting curves.

The time-evolved desalination behaviors of original MoS<sub>2</sub> and MoS<sub>2</sub>/PDA-4 in 200 mg/L NaCl solution was given in Fig. 6.9(a). Evidently, the electro sorption process of NaCl on MoS<sub>2</sub>/PDA-4 nanocomposites could reach an equilibrium quickly within ~9 min. Such an electro sorption rate was much rapider than that of original MoS<sub>2</sub> (~16 min) as well as most of the previously reported materials in CDI cell (15-80 min) [1,4,6,23]. A rapid electro sorption rate was one of the favorable indicators to assess the CDI electrode materials in their practical applications [6]. The improvement of adsorption rate was believed to involve with the incorporation of the hydrophilic PDA coating on the surface of MoS<sub>2</sub> [10]. Fig. 6.9(b) displayed the NaCl electro sorption capacity of original MoS<sub>2</sub> and MoS<sub>2</sub>/PDA-4 in various feeding concentrations. Impressively, MoS<sub>2</sub>/PDA-4 nanocomposites exhibited a saturated electro sorption capacity of ~14.80 mg/g, which was 1.51 times of that of original MoS<sub>2</sub> (9.79 mg/g). To further evaluate the improved desalination capacity of MoS<sub>2</sub>/PDA-4, the electro sorption data was then fitted according to the Langmuir equation (Eq 6.3) [24,25]:

$$Q_e = \frac{Q_m \times K_L \times C_e}{1 + Q_m \times C_e} \quad 6.3$$

where  $C_e$  (mg/L),  $Q_e$  (mg/g),  $Q_m$  (mg/g) and  $K_L$ (mg/L) were the equilibrium concentration of NaCl, electro sorption capacity at equilibrium, the maximum

electrosorption capacity and the Langmuir constant, respectively.

The fitting results were displayed in Fig. 6.9(b) as well as Table 5.1. It was concluded that the Langmuir isotherm curves fitted well with the experiment data due to their high correlating coefficient over 95%. Thus, the maximum electrosorption capacity ( $Q_m$ ) of original MoS<sub>2</sub> and MoS<sub>2</sub>/PDA-4 were calculated to be 10.97 mg/g and 16.94 mg/g, respectively. Notably, MoS<sub>2</sub>/PDA-4 outperformed not only original MoS<sub>2</sub> but also the previously reported materials (As displayed in Table 5.2) in terms of the desalination capacity. In conclusion, it was of great significance to modify MoS<sub>2</sub> by PDA to obtain a novel electrode with enhanced desalination performance.

Table 5.1 Parameters of Langmuir fitting models for the electrosorption of NaCl on original MoS<sub>2</sub> and MoS<sub>2</sub>/PDA-4.

| Parameters                | $Q_m$ | $K_L$   | $R^2$ |
|---------------------------|-------|---------|-------|
| Original MoS <sub>2</sub> | 10.97 | 0.02923 | 0.951 |
| MoS <sub>2</sub> /DPA-4   | 16.94 | 0.02954 | 0.974 |

Table 5.2 Comparisons of CDI performances between the electrode materials in this work and other recently reported electrode materials.

| Materials  | Applied Voltage (V) | Capacity (F/g)                 | $Q_m$ (mg/g) | Refs |
|--|---------------------|--------------------------------|--------------|------|
| Graphene/<br>Mesoporous Carbon                       | 2.0                 | 52.12<br>(0.5 M NaCl, 5 mV/s)  | 0.731        | [1]  |
| Holey Graphene<br>Hydrogel                           | 1.2                 | 148<br>(0.5 M NaCl, 5 mV/s)    | 26.8         | [4]  |
| Graphene Aerogel                                     | 1.2                 | 53.1<br>(0.1 M NaCl, 100 mV/s) | 15.8         | [5]  |
| Chemically Exfoliated<br>MoS <sub>2</sub> Nanosheets | 1.2                 | 109.7<br>(1 M NaCl, 10 mV/s)   | 8.81         | [6]  |
| Polydopamine/Active<br>Carbon                        | 1.2                 | 131.4<br>(1 M NaCl, 1 mV/s)    | 11.9         | [10] |
| N-Activated<br>Carbon/SnO <sub>2</sub>               | 1.2                 | 408.8<br>(0.1 M NaCl, 50 mV/s) | 3.42         | [26] |
| Graphene/CNT   | 2.0                 | 69<br>(0.5 M NaCl, 10 mV/s)    | 1.41         | [27] |

|  |     |                               |       |           |
|--|-----|-------------------------------|-------|-----------|
| MnO <sub>2</sub> /Activated Carbon Composite | 1.0 | 77.6<br>(1 M NaCl, 5 mV/s)    | 9.26  | [28]      |
| Functional Graphene Nanocomposite            | 2.0 | 42.5<br>(1 M NaCl, 100 mV/s)  | 2.36  | [29]      |
| Nitrogen Doped Graphene                      | 1.8 | 64.52<br>(1 M NaCl, 100 mV/s) | 4.81  | [30]      |
| ZrO <sub>2</sub> /Activated Carbon           | 1.2 | 282.8<br>(1 M, 20 mV/s)       | 4.79  | [31]      |
| Original MoS <sub>2</sub>                    | 1.2 | 75<br>(1 M NaCl, 20 mV/s)     | 10.97 | This work |
| MoS <sub>2</sub> /PDA-4                      | 1.2 | 99.9<br>(1 M NaCl, 20 mV/s)   | 16.94 | This work |

### 6.3.3. The origins of the enhanced CDI performance

#### (1) Change of electrochemical property

The vital role played by polydopamine in enhancing electrochemical performance in capacitive fields was to improve the conductivity of active materials [8]. Fig. 6.10(a) exhibited the specific capacitance of various MoS<sub>2</sub>/PDA nanocomposites based on the results in Fig. 6.8(a). As expected, MoS<sub>2</sub>/PDA-4 possessed the highest specific capacitance of 99.17 F/g, which was 1.3 time as that of original MoS<sub>2</sub> (75.52 F/g). However, the specific capacitance of MoS<sub>2</sub>/PDA nanocomposites would decline to be less than that of original MoS<sub>2</sub> when the polymerization time was over 8 h. This phenomenon was believed to involve with the two factors: (1) The partial architectures of MoS<sub>2</sub> crystalline were destroyed by the deposition of PDA as mentioned before, (2) The much thicker PDA layer was detrimental to the access of electrolyte to the surfaces of MoS<sub>2</sub> thus leading a reduced current response. Thereby, the coating process of PDA on the surface of MoS<sub>2</sub> ought to be carefully adjusted by time.

Fig. 6.10(b) shows the Nyquist plots of original MoS<sub>2</sub> and various MoS<sub>2</sub>/PDA nanocomposites, in which the inset exhibits an equivalent electrical circuit for the analysis of the EIS data. In detail,  $R_s$ ,  $R_c$ ,  $C_c$  and  $Z_D$  represented the solution resistance, the interfacial contact resistance, capacitance of electrode materials, the diffusion impedance at solid/solution interface, respectively [4].  $R_s$  was related to numerous factors such as the contact between the current collectors and the electrode materials and the resistance of the electrolyte inside electrodes, etc [10].  $R_c$  was

positively correlated to the diameter of the semicircle in middle frequency regions, while  $Z_D$  was reflected by the slopes of the graph in low frequency regions [10]. In comparison with original  $\text{MoS}_2$ , all of various  $\text{MoS}_2/\text{PDA}$  electrodes exhibited smaller diameters of the semicircles and more vertical slopes due to their good hydrophilicity, correspondingly revealing their lower contact resistances ( $R_c$ ) and lower ion diffusion resistance ( $R_D$ ). The lower inner resistances might also be responsible for the rapid ion migration occurred at  $\text{MoS}_2/\text{PDA}$  electrodes as well as the fast electrosorption rate for salt ions.

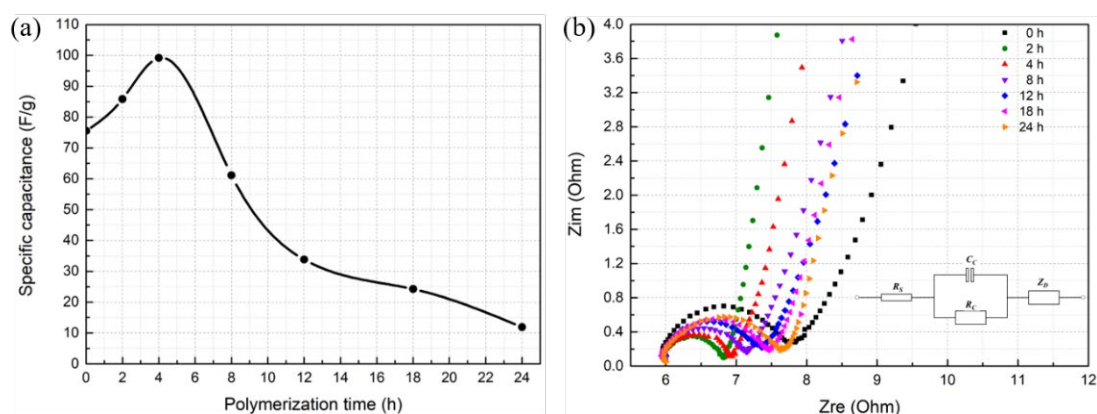


Fig. 6.10. (a) Specific capacitance of various  $\text{MoS}_2/\text{PDA}$  nanocomposites obtained at scanning rate of 20 mV/s in 1.0 M NaCl solution. (b) Nyquist plots of various  $\text{MoS}_2/\text{PDA}$  nanocomposites. (Inset: Equivalent electrical circuit).

These results directly demonstrated that the coating of polydopamine contributed to promoting the capacitive response as well as ion transport within  $\text{MoS}_2/\text{PDA}$  nanocomposites. It should also be pointed out that with the increase of the polymerization time, the diameters of the semicircle in middle frequency regions of  $\text{MoS}_2/\text{PDA}$  nanocomposites gradually increased and slopes of the graph in low frequency regions slightly decreased, which might derived from the fact that the thicker PDA layer would block the access of ions to electrodes' surfaces and result in the increased inner resistances.

It was believed that a typical CDI process mainly consists of the following four steps: (1) mass transfer of salt ions at the solid-liquid interfaces, (2) energy storage accompanied by ion electrosorption inside the EDLs, (3) mass transfer of salt ions between electrodes and brine, and (4) ion diffusion within brine [5,6,32]. Therefore, a high-performance CDI electrode material ought to possess both high capacitances and the proper property boosting the ion transfer processes [6]. In this work, the much

higher specific capacitance because of the incorporation of electroactive PDA and the lower inner resistances due to its better water wettability compared to original MoS<sub>2</sub>, should be responsible for the results that MoS<sub>2</sub>/PDA-4 electrodes possessed significantly enhanced desalination performance in light of desalination capacity and electroadsorption rate.

## (2) Change of surface charge

It was also suspected that the coating of PDA on MoS<sub>2</sub> not only provided more hydrophilicity and electroactivity, but also introduced negative charge on the surface of the composite electrode materials [8]. Considering the electroneutrality during the hydrolysis of the salt ions, the surface charge of MoS<sub>2</sub> and MoS<sub>2</sub>/PDA-4 were investigated with the solution pH ranging from 4.0 to 8.0. As displayed in Fig. 6.11, both the surfaces of MoS<sub>2</sub> and MoS<sub>2</sub>/PDA-4 were negatively charged, and the surface turned more negatively charged with the increase of the solution pH. Such property was beneficial to electrodes in holding the positively charged salt ions [7,28]. What is more, compared to original MoS<sub>2</sub>, the coating of PDA on the surface of MoS<sub>2</sub> offered more abundant negative charges and therefore resulted in the increased amount of Na<sup>+</sup> ions trapped in the thicker EDLs because of the electrostatic interaction [7].

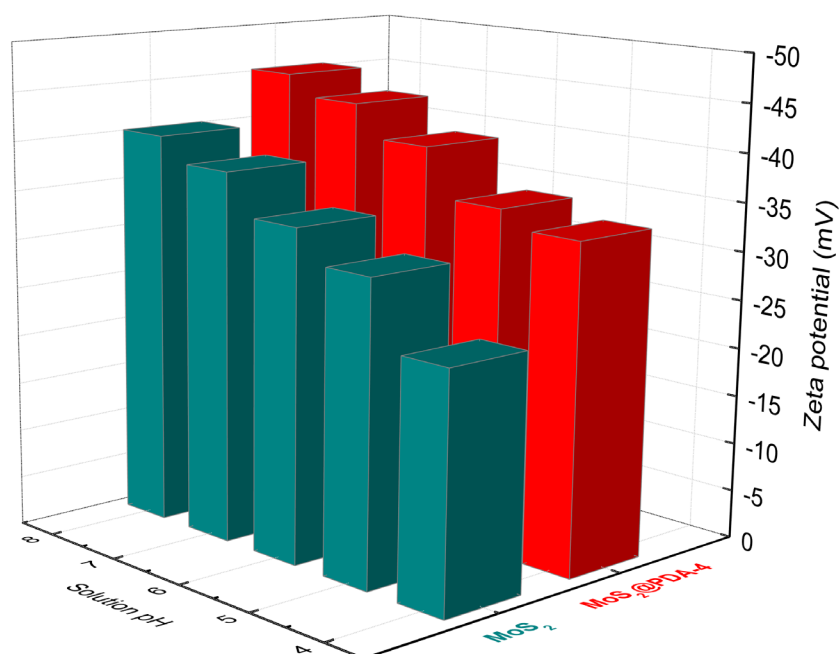


Fig. 6.11. Surface charge of MoS<sub>2</sub> and MoS<sub>2</sub>/PDA-4.

### 6.3.4. Cycling performance

As displayed in Fig. 6.12(a), desalination cycling was finally conducted to assess



the cycling performances of MoS<sub>2</sub>/PDA-4 nanocomposites. Due to its high electrochemical stability as aforementioned before, MoS<sub>2</sub>/PDA-4 electrodes presented a relatively high and stable desalination capacity even for 10 successive cycles, demonstrating the well regeneration and recyclability of MoS<sub>2</sub>/PDA-4. Furthermore, the stability of PDA in the electrode materials was investigated since it was suspected to be washed out during the continuous operation of CDI. The dissolution of PDA into the solution was detected by the ultraviolet-visible (UV-Vis) absorption spectrometry because of the characteristic adsorption peak of PDA at 420 nm. As displayed in Fig. 6.12(b) and (Table 6.3), it was found that the amount of PDA in the MoS<sub>2</sub>/PDA-4 electrodes released into the solution was extremely negligible (<0.20wt%) even after the 10 successive cycles, suggesting its excellent stability in the electrode materials during the continuous operation of CDI. Such stable and excellent recyclability of MoS<sub>2</sub>/PDA-4 demonstrated its good prospects in not only practical capacitive deionization but also in other capacitive fields such as supercapacitors.

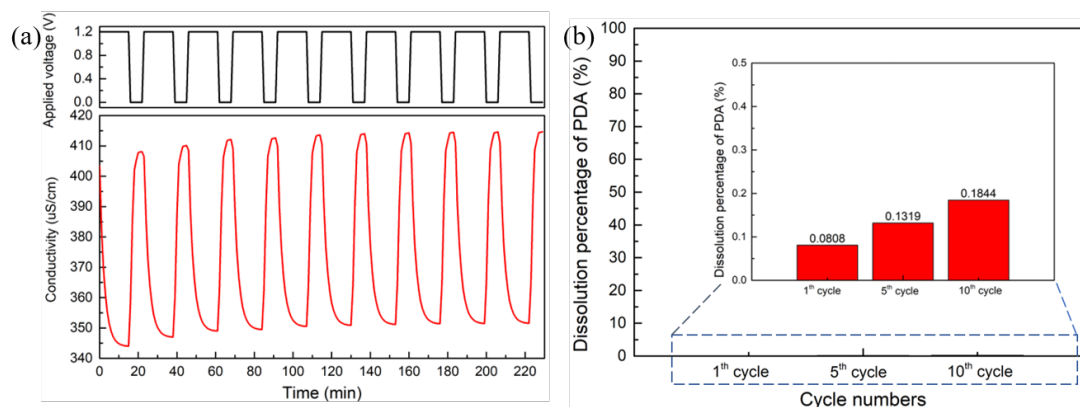


Fig. 6.12. (a) Cycling performances of MoS<sub>2</sub>/PDA-4 electrodes in 200 mg/L NaCl solution. (b) Dissolution results of the PDA in MoS<sub>2</sub>/PDA-4 electrodes during the continuous CDI operation.

Table 6.3. Dissolution results of the PDA in MoS<sub>2</sub>/PDA-4 electrodes during the continuous CDI operation.

| Cycles  | 1 <sup>st</sup> cycle | 5 <sup>th</sup> cycles | 10 <sup>th</sup> cycle |
|---|-----------------------|------------------------|------------------------|
| Concentration of PDA in solutions, C <sub>PDA</sub><br>(mg/L) | 1.2923                | 2.1097                 | 2.951                  |
| Dissolution percentage of PDA*, (%)                           | 0.0808                | 0.1319                 | 0.1844                 |

\*Dissolution percentage of PDA =  $(C_{PDA} \times \text{volume of solutions}) \times 100 / (\text{Mass of MoS}_2/\text{PDA-4 in electrode materials}) = (C_{PDA} \times 0.04 \text{ L}) \times 100 / (64 \text{ mg})$ .

## 6.4. Conclusions

Based on the above results, the main conclusions of this study were as follows:

(1) A series of MoS<sub>2</sub>/PDA nanocomposites with improved wettability were successfully prepared by the facial self-polymerization of dopamine on the surface of MoS<sub>2</sub>.

(2) With polymerization time being finely controlled, the incorporation of hydrophilic and electroactive PDA could promote the specific capacitance, reduce the inner resistances and turned the surface charge of original MoS<sub>2</sub>, resulting in an outstandingly enhanced desalination performance of MoS<sub>2</sub>/PDA-4 based cells compared to that of original MoS<sub>2</sub>.

(3) Moreover, the cycling tests of MoS<sub>2</sub>/PDA-4 based electrodes manifested its good stability and regeneration ability.

(4) It is expected that this work will not only offer a promising method to enhance the desalination performance of CDI electrode materials, but also hold the potential to be applied in other capacitive property-related fields such as batteries, supercapacitors and catalysis, etc.

## REFERENCES

- [1] D. Zhang, X. Wen, L. Shi, T. Yan, J. Zhang, Enhanced capacitive deionization of graphene/mesoporous carbon composites, *Nanoscale*. 4 (2012) 5440–5446. doi:10.1039/c2nr31154b.
- [2] X. Liu, H. Liu, M. Mi, W. Kong, Y. Ge, J. Hu, Nitrogen-doped hierarchical porous carbon aerogel for high-performance capacitive deionization, *Separation and Purification Technology*. 224 (2019) 44–50. doi:10.1016/j.seppur.2019.05.010.
- [3] Y. Oren, Capacitive deionization (CDI) for desalination and water treatment - past, present and future (a review), *Desalination*. 228 (2008) 10–29. doi:10.1016/j.desal.2007.08.005.
- [4] W. Kong, X. Duan, Y. Ge, H. Liu, J. Hu, X. Duan, Holey graphene hydrogel with in-plane pores for high-performance capacitive desalination, *Nano Research*. 9 (2016) 2458–2466. doi:10.1007/s12274-016-1132-8.
- [5] H. Yin, S. Zhao, J. Wan, H. Tang, L. Chang, L. He, H. Zhao, Y. Gao, Z. Tang, Three-Dimensional Graphene/Metal Oxide Nanoparticle Hybrids for High-Performance Capacitive Deionization of Saline Water, *Advanced Materials*. 25 (2013) 6270–6276. doi:10.1002/adma.201302223.
- [6] F. Xing, T. Li, J. Li, H. Zhu, N. Wang, X. Cao, Chemically exfoliated MoS<sub>2</sub> for capacitive deionization of saline water, *Nano Energy*. 31 (2017) 590–595.

- doi:10.1016/j.nanoen.2016.12.012.
- [7] F. Jia, K. Sun, B. Yang, X. Zhang, Q. Wang, S. Song, Defect-rich molybdenum disulfide as electrode for enhanced capacitive deionization from water, *Desalination*. 446 (2018) 21–30. doi:10.1016/j.desal.2018.08.024.
- [8] Y. Liu, K. Ai, L. Lu, Polydopamine and Its Derivative Materials: Synthesis and Promising Applications in Energy, Environmental, and Biomedical Fields, *Chemical Reviews*. 114 (2014) 5057–5115. doi:10.1021/cr400407a.
- [9] Y. Gao, C. Chen, X. Tan, H. Xu, K. Zhu, Polyaniline-modified 3D-flower-like molybdenum disulfide composite for efficient adsorption/photocatalytic reduction of Cr(VI), *Journal of Colloid and Interface Science*. 476 (2016) 62–70. doi:10.1016/j.jcis.2016.05.022.
- [10] Z. Xie, J. Cheng, J. Yan, W. Cai, P. Nie, H.T.H. Chan, J. Liu, Polydopamine Modified Activated Carbon for Capacitive Desalination, *Journal of The Electrochemical Society*. 164 (2017) A2636–A2643. doi:10.1149/2.1391712jes.
- [11] W. Peng, H. Li, S. Song, Synthesis of Fluorinated Graphene/CoAl-Layered Double Hydroxide Composites as Electrode Materials for Supercapacitors, *ACS Applied Materials and Interfaces*. 9 (2017) 5204–5212. doi:10.1021/acsami.6b11316.
- [12] J. Zhou, H. Xiao, B. Zhou, F. Huang, S. Zhou, W. Xiao, D. Wang, Hierarchical MoS<sub>2</sub>-rGO nanosheets with high MoS<sub>2</sub> loading with enhanced electro-catalytic performance, *Applied Surface Science*. 358 (2015) 152–158. doi:10.1016/j.apsusc.2015.07.187.
- [13] H. Liu, F. Zhang, W. Li, X. Zhang, C.-S. Lee, W. Wang, Y. Tang, Porous tremella-like MoS<sub>2</sub>/polyaniline hybrid composite with enhanced performance for lithium-ion battery anodes, *Electrochimica Acta*. 167 (2015) 132–138. doi:10.1016/j.electacta.2015.03.151.
- [14] W. Wang, Y. Zhao, H. Bai, T. Zhang, V. Ibarra-Galvan, S. Song, Methylene blue removal from water using the hydrogel beads of poly(vinyl alcohol)-sodium alginate-chitosan-montmorillonite, *Carbohydrate Polymers*. 198 (2018) 518–528. doi:10.1016/j.carbpol.2018.06.124.
- [15] N. Cao, B. Yang, A. Barras, S. Szunerits, R. Boukherroub, Polyurethane sponge functionalized with superhydrophobic nanodiamond particles for efficient oil/water separation, *Chemical Engineering Journal*. 307 (2017) 319–325. doi:10.1016/j.cej.2016.08.105.
- [16] D. Liu, Z. Li, Q. Sun, X. Kong, A. Zhao, Z. Wang, In situ FT-IR study of thiophene adsorbed on the surface of sulfided Mo catalysts, *Fuel*. 92 (2012) 77–83. doi:10.1016/j.fuel.2011.07.043.

- [17] F. Jia, Q. Wang, J. Wu, Y. Li, S. Song, Two-Dimensional Molybdenum Disulfide as a Superb Adsorbent for Removing  $\text{Hg}^{2+}$  from Water, *ACS Sustainable Chemistry & Engineering*. 5 (2017) 7410–7419. doi:10.1021/acssuschemeng.7b01880.
- [18] N. Li, J. Zhou, Z. Sheng, W. Xiao, Molten salt-mediated formation of g-C<sub>3</sub>N<sub>4</sub>-MoS<sub>2</sub> for visible-light-driven photocatalytic hydrogen evolution, *Applied Surface Science*. 430 (2018) 218–224. doi:10.1016/j.apsusc.2017.08.086.
- [19] G. Yang, X. Li, Y. Wang, Q. Li, Z. Yan, L. Cui, S. Sun, Y. Qu, H. Wang, Three-dimensional interconnected network few-layered MoS<sub>2</sub>/N, S co-doped graphene as anodes for enhanced reversible lithium and sodium storage, *Electrochimica Acta*. 293 (2019) 47–59. doi:S0013468618322515.
- [20] J. Sen Li, Y. Wang, C.H. Liu, S.L. Li, Y.G. Wang, L.Z. Dong, Z.H. Dai, Y.F. Li, Y.Q. Lan, Coupled molybdenum carbide and reduced graphene oxide electrocatalysts for efficient hydrogen evolution, *Nature Communications*. 7 (2016) 1–8. doi:10.1038/ncomms11204.
- [21] K. Qu, Y. Zheng, S. Dai, S.Z. Qiao, Polydopamine-graphene oxide derived mesoporous carbon nanosheets for enhanced oxygen reduction, *Nanoscale*. 7 (2015) 12598–12605. doi:10.1039/c5nr03089g.
- [22] Y. Su, Y. Zhu, H. Jiang, J. Shen, X. Yang, W. Zou, J. Chen, C. Li, Cobalt nanoparticles embedded in N-doped carbon as an efficient bifunctional electrocatalyst for oxygen reduction and evolution reactions, *Nanoscale*. 6 (2014) 15080–15089. doi:10.1039/c4nr04357j.
- [23] M. Haro, G. Rasines, C. MacÍas, C.O. Ania, Stability of a carbon gel electrode when used for the electro-assisted removal of ions from brackish water, *Carbon*. 49 (2011) 3723–3730. doi:10.1016/j.carbon.2011.05.001.
- [24] Q. Wang, L. Yang, F. Jia, Y. Li, S. Song, Removal of Cd (II) from water by using nano-scale molybdenum disulphide sheets as adsorbents, *Journal of Molecular Liquids*. 263 (2018) 526–533. doi:10.1016/j.molliq.2018.04.149.
- [25] Q. Wang, L. Peng, Y. Gong, F. Jia, S. Song, Y. Li, Mussel-inspired Fe<sub>3</sub>O<sub>4</sub>@Polydopamine(PDA)-MoS<sub>2</sub> core-shell nanosphere as a promising adsorbent for removal of Pb<sup>2+</sup> from water, *Journal of Molecular Liquids*. 282 (2019) 598–605. doi:10.1016/j.molliq.2019.03.052.
- [26] A.S. Yasin, J. Jeong, I.M.A. Mohamed, C.H. Park, C.S. Kim, Fabrication of N-doped & SnO<sub>2</sub> -incorporated activated carbon to enhance desalination and bio-decontamination performance for capacitive deionization, *Journal of Alloys and Compounds*. 729 (2017) 764–775. doi:10.1016/j.jallcom.2017.09.185.
- [27] D. Zhang, T. Yan, L. Shi, Z. Peng, X. Wen, J. Zhang, Enhanced capacitive deionization

- performance of graphene/carbon nanotube composites, *Journal of Materials Chemistry*. 22 (2012) 14696. doi:10.1039/c2jm31393f.
- [28] Y.H. Liu, H.C. Hsi, K.C. Li, C.H. Hou, Electrodeposited manganese dioxide/activated carbon composite as a high-performance electrode material for capacitive deionization, *ACS Sustainable Chemistry and Engineering*. 4 (2016) 4762–4770. doi:10.1021/acssuschemeng.6b00974.
- [29] Z. Wang, L. Yue, Z.T. Liu, Z.H. Liu, Z. Hao, Functional graphene nanocomposite as an electrode for the capacitive removal of FeCl<sub>3</sub> from water, *Journal of Materials Chemistry*. 22 (2012) 14101–14107. doi:10.1039/c2jm32175k.
- [30] X. Xu, L. Pan, Y. Liu, T. Lu, Z. Sun, Enhanced capacitive deionization performance of graphene by nitrogen doping, *Journal of Colloid and Interface Science*. 445 (2015) 143–150. doi:10.1016/j.jcis.2015.01.003.
- [31] A.S. Yasin, I.M.A. Mohamed, M.T. Amen, N.A.M. Barakat, C.H. Park, C.S. Kim, Incorporating zirconia nanoparticles into activated carbon as electrode material for capacitive deionization, *Journal of Alloys and Compounds*. 772 (2019) 1079–1087. doi:10.1016/j.jallcom.2018.09.057.
- [32] P.M. Biesheuvel, M.Z. Bazant, Nonlinear dynamics of capacitive charging and desalination by porous electrodes, *Physical Review E*. 81 (2010) 1–12. doi:10.1103/PhysRevE.81.031502.

The main content of this chapter was published as “*Separation and Purification Technology* 236 (2020): 116298.”

## CHAPTER VII

### Removal of Cd (II) from water by using nanoscale MoS<sub>2</sub> sheets as adsorbents

#### 7.1. Introduction

Heavy metal contamination in water has been a severe public health issue due to the significant toxic effects on the environment and human beings. Cadmium, as well as mercury and lead, belong to a harmful heavy metal group, which are of high concern among environmentalists. Typically, exposure to cadmium (Cd<sup>2+</sup>) can cause bone and kidney damage, renal disturbance, lung insufficiency, cancer, and hypertension in human beings [1], necessitating the removal of cadmium ions from water systems.

Among the current technologies to remove cadmium ions, adsorption is considered as one of the most low-cost, effective, and technically feasible methods [2]. However, conventional adsorbents usually suffer from limitations of low uptake capacity and poor selectivity, which lead to a disadvantage during their application. As a result, a significant branch of current research is aimed at developing novel materials because the adsorption performance highly depends on the types of adsorbent. Molybdenum disulphide (MoS<sub>2</sub>) has recently been attracting increasing attention in electronics-[3,4], catalysts-[5], biomedicine-[6,7], desalination-[8], and energy-related fields [9]. With its sulphur planes being intrinsically rich and negatively charged, molybdenum disulphide might serve as a novel and efficient adsorbent for removing heavy metal ions due to the strong interactions between soft acid and soft base, based on the principle of hard and soft acids and bases (the HSAB principle) [10]. MoS<sub>2</sub> nanosheets with widened interlayer spacing have proved to be excellent scavengers for Hg<sup>2+</sup> and Pb<sup>2+</sup> due to the significant affinity between molybdenum disulphide and metal ions [11–15]. The multifunctional magnetic ferrite–MoS<sub>2</sub>–carbon dot nano hybrids also exhibited high adsorption performance for Pb<sup>2+</sup> in aqueous solutions, showing 588.24 mg/g for MnFe<sub>2</sub>O<sub>4</sub>–MoS<sub>2</sub>–carbon dot, and 660.67 mg/g for as-synthesized CoFe<sub>2</sub>O<sub>4</sub>–MoS<sub>2</sub>–carbon dot, respectively [16]. The adsorption capacity of molybdenum disulphide/reduced graphene oxide were found to be 322 and 294 mg/g for Pb (II) and Ni (II) ions [17], respectively, while the adsorption capacity of Fe<sub>3</sub>O<sub>4</sub>/MoS<sub>2</sub> was found to be 172.41 and 46.51 mg/g for Ag (I) and Pb (II) ions [18], respectively. The dahlia-like molybdenum disulphide

nanosheets, synthesised by hydrothermal treatment, exhibited an appropriate capacity (80 mg/g) for  $\text{Co}^{2+}$  from food and water samples due to its abundant sulphur groups on the edges and surfaces of the nanosheets [19]. In addition, the  $\text{CaFe}_2\text{O}_4/\text{MoS}_2$  hybrid showed a good solid-phase extraction capacity for paclitaxel chemotherapy medication in injection vials and water samples [20]. Moreover, porous 3D  $\text{MoS}_2$  composite aerogel-supported Au nanoparticles have been fabricated to remove  $\text{Hg}^{2+}$  from contaminated water, which can also decrease the  $\text{Hg}^{2+}$  levels from 10 ppm to 0.11 ppb within some minutes [21]. Despite possessing a strong affinity to remove mercury and lead, it is suspected that  $\text{MoS}_2$  could be used to remove less soft ions in aqueous solutions. Therefore, the high-toxicity cadmium ion was selected as the targeted adsorbate. So far, the performance of molybdenum disulphide nanosheets in the decontamination of cadmium ions from aqueous solutions remains unknown.

In this work, attempts were made to investigate the possible adsorption behaviour, as well as the immobilization mechanism of cadmium ions in an aqueous solution by using nano-scale molybdenum disulphide sheets prepared from natural molybdenite bulks as the adsorbent. Firstly, Raman spectra, high resolution transmission microscope (HRTEM), and atomic force microscope (AFM) were conducted to characterise nano-scale molybdenum disulphide sheets prepared in this work. Secondly, a set of experiments involving the solution pH, contact time, and cadmium ion concentration were conducted to understand the adsorption behaviour of cadmium on nano-scale molybdenum disulphide sheets. Finally, the possible mechanisms of adsorption were investigated by X-ray photoelectron spectroscopy (XPS).

## 7.2. Materials and methods

### 7.2.1. Materials

Natural molybdenite bulks collected from the Wuzhou Mine, Guangxi Province, China, were used in the preparation of nano-scale molybdenum disulphide sheets. The content of molybdenum disulphide in the natural sample was  $\sim 97.45\%$ , based on the X-ray fluorescence (XRF) analysis.

Cadmium nitrate ( $\text{Cd}(\text{NO}_3)_2 \cdot 4\text{H}_2\text{O}$ ), nitric acid ( $\text{HNO}_3$ ), sodium hydroxide ( $\text{NaOH}$ ), and sodium sulphate ( $\text{Na}_2\text{SO}_4$ ) were purchased from Sinopharm Chemical Reagent Co., Ltd. (China). All of the reagents were of analytical grade. The ultra-pure water used in this work was collected from a Milli-Q meter (Millipore, Bedford, MA), with a resistivity of 18.2  $\text{M}\Omega$  cm.

## 7.2.2. Methods

### Preparation of nano-scale molybdenum disulphide sheets

Nano-scale molybdenum disulphide sheets were prepared from natural molybdenite bulks. Firstly, the bulk molybdenite was treated with an electrochemical process. In this process, the molybdenite bulks were used as the positive electrode, with an initial voltage of 1.0 V for 15 min, followed by an increased voltage of 10 V for 24 h to produce O<sub>2</sub>, which tended to escape from the system, causing the expansion of interlayers. Secondly, further exfoliation of the molybdenite was achieved by the ultra-sonication process in deionized water at 150 W for 20 min with a Sonic Vibracell. Finally, the exfoliated molybdenum disulphide was washed for four times through 0.1 µm filters.

### *Batch adsorption tests*

Batch experiments were carried out to study the effects of solution pH, contact time, and initial ion concentration on the adsorption behaviour of cadmium ions on nanoscale molybdenite sheets. Adsorption experiments were carried out at various pH levels, using 50 ml Erlenmeyer flasks containing 20 ml cadmium solution with an initial concentration of 50 mg/L. The solution pH was adjusted to the range of 1.0 to 7.0, followed by the addition of 1 mL suspension containing 1.9 mg of nano-scale molybdenum disulphide sheets. Subsequently, the mixtures were shaken for 60 min at 20°C. The effect of contact time was determined by adding 5.0 mL suspension of nano-scale molybdenum disulphide sheets into a 500 mL solution contained 100 mg/L of cadmium ions, subsequently storing it for regular intervals of time, up to 120 min (pH: 6.0). For the equilibrium adsorption isotherms, 1.0 mL suspension of nano-scale molybdenum disulphide sheets was added into 20 ml solutions with varying concentrations of cadmium, from 0 to 600 mg/L (pH: 6.0). Each data point was obtained from an individual Erlenmeyer flask. The pH for all the solutions was adjusted by using 0.1 and 1.0 mol/L NaOH or HNO<sub>3</sub>. It should be noted that, to avoid the effects of filters on the detection of the residual concentration of ions, 5 mL of the mixture was filtered after adsorption with a 0.1 µm filter membrane, with the initial 2 mL of filtrate being discarded, while the subsequent 3 mL was collected in a clean tube and used for testing.

All batch adsorption experiments were performed in duplicates. The amount of bound cadmium per gram of nano-scale molybdenum disulphide sheets,  $q_e$  (mg/g), was calculated based on Eq. 7.1:



$$q_e = (C_0 \times V_0 - C_t \times V_t) / m \quad 7.1$$

where  $q_e$  is the amount of metal ions adsorbed on nano-scale molybdenum disulphide sheets, mg/g;  $V_0$  and  $V_t$  are the volumes of the solution before and after adsorption, L;  $C_0$  and  $C_t$  are the concentrations of metal ions in the solution before and after adsorption, mg/L; and  $m$  is the mass of nano-scale molybdenum disulphide sheets used in the test, g.

### **Measurements**

X-ray diffraction (XRD) powder patterns were recorded using a D8 Avance system, with a 0.15406-nm Cu  $K\alpha$  radiation (Bruker AXS, Germany). Raman spectra were obtained from an InVia Raman system, combined with a confocal microprobe (Renishaw, UK) using a 514-nm Ar laser. The morphologies of the materials were recorded on a JEM-2100F (JEOL, Japan) high-resolution transmission microscope (HRTEM), with an acceleration voltage of 200 kV. X-ray photoelectron spectroscopy (XPS) studies were conducted on an ESCALAB 250Xi (Thermo Fisher Scientific, USA), using an Al  $K\alpha$  with an energy resolution of 0.45 eV. An atomic force microscope (AFM) in peak force mode with a Bruker Multimode 8 system (Bruker, USA) was used to obtain the thickness distribution of the prepared materials. The pH of the solutions was noted accurately with a pH/ion meter (Thermo Fisher Scientific, USA). Atomic absorption spectrometry (GBC Avanta M, Australia) was used to detect the concentration of cadmium ions in aqueous solutions.

## **7.3. Results and discussion**

### **7.3.1. Characterization**

The XRD patterns and Raman spectra of molybdenite before and after exfoliation are shown in Fig. 7.1. In Fig. 7.1(a), seven typical peaks were observed, which correspond to (002), (004), (100), (103), (006), (105), and (008) peaks of molybdenum disulphide, respectively, according to the JCPDS No. 37-1492. The absence of obvious impurity peaks further confirmed the high purity of molybdenum disulphide. When compared with molybdenite before exfoliation, the (002) reflection of molybdenite after exfoliation decreased significantly, usually accompanied by the conclusion of a large number of molybdenum disulphide bulks being highly exfoliated [22,23]. The Raman spectrum of molybdenite before and after exfoliation is shown in Fig. 7.1(b). The peaks at  $381 \text{ cm}^{-1}$  and  $406 \text{ cm}^{-1}$  were assigned to the typical  $E_{2g}^1$  and  $A_{1g}$  modes, which were derived from the in-plane vibration and the

out-of-plane vibration of Mo and S atoms, respectively [24]. It was believed that the blue-shift of the  $E_{2g}^1$  mode and the red-shift of  $A_{1g}$  mode in Fig. 7.1(b) demonstrated the decrease of the thickness of pristine molybdenum disulphide [24,25], which further confirmed the effective exfoliation of molybdenum disulphide.

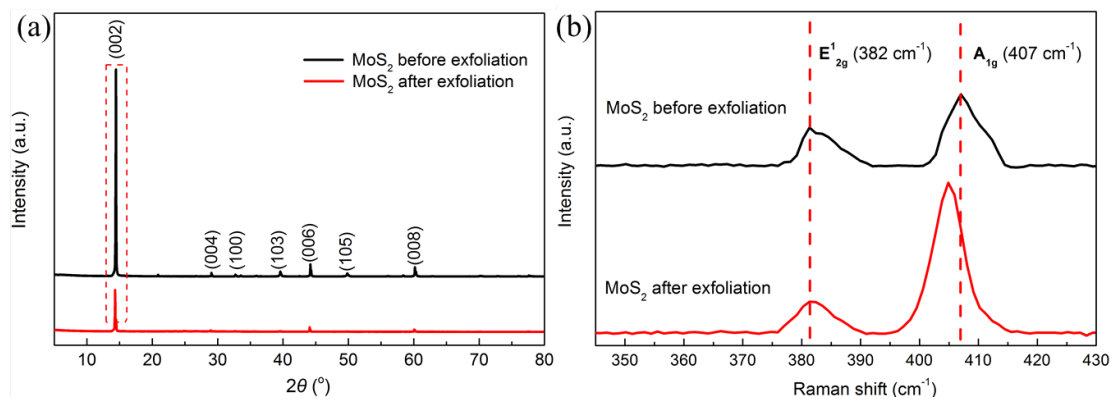


Fig. 7.1. (a) XRD patterns and (b) Raman spectra of molybdenite before and after exfoliation.

The morphology of nano-scale molybdenum disulphide sheets obtained from transmission electron microscopy (TEM) is shown in Fig. 7.2. As shown in Fig. 7.2(a), the TEM image with lower magnification demonstrated that the typical diameter of as-prepared nano-scale molybdenum disulphide sheets ranged from hundreds of nanometres to several micrometres. Fig. 7.2(b) shows an image with a higher magnification of folded edges on nano-scale molybdenum disulphide sheets, with a thickness of approximately 1.7 nm, which belonged to the thickness range of the bilayer molybdenum disulphide nanosheets [23]. An HRTEM image of the basal plane is shown in Fig. 7.2(c), in which the blurs on the surface of nanosheets probably were defects. In Fig. 7.2(d), the selected area electron diffraction (SAED) pattern showed typical lattice fringes and a hexagonal symmetrical structure [23,27], which indicated that the molybdenum and sulphur atoms were still arranged in hexagonal sheets, namely the molybdenum disulphide after exfoliation remained its 2H phase.

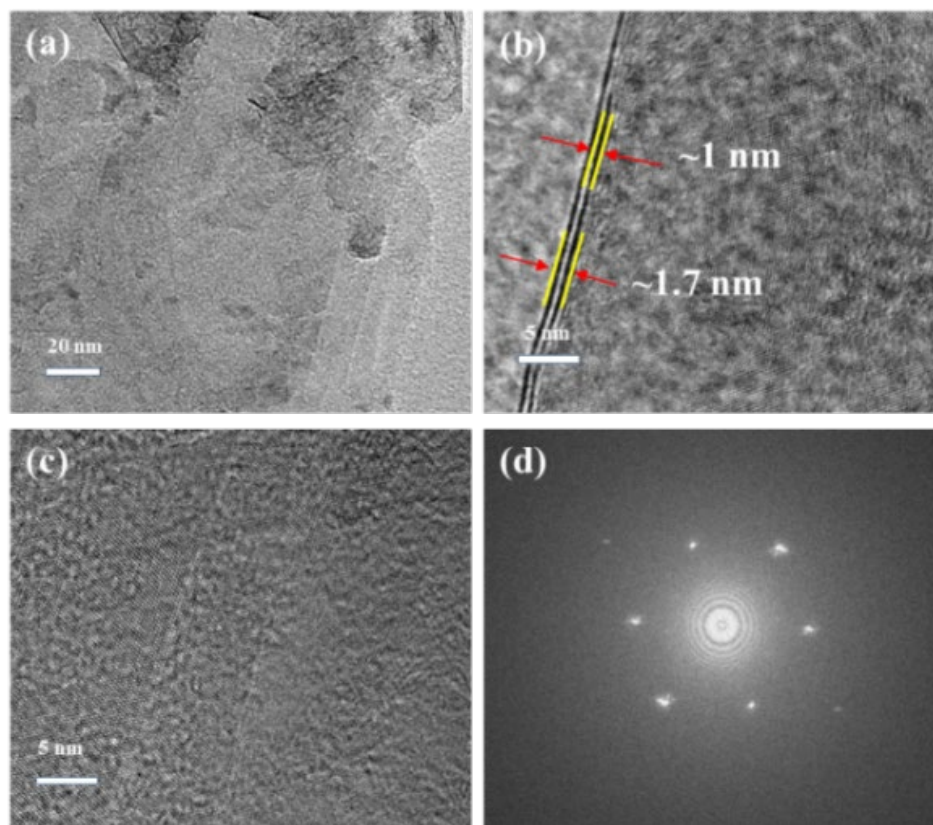


Fig. 7.2. (a) TEM images of nano-scale molybdenum disulphide sheets; (b) HRTEM image of bilayer molybdenum disulphide with folded edges; (c) HRTEM image of the basal plane; (d) SAED pattern with a typical hexagonal structure of molybdenum disulphide nanosheets.

To understand the thickness distribution of nano-scale molybdenum disulphide sheets prepared in this work, the samples were deposited on the surface of the mica substrate, subsequently being observed with an AFM. For statistical purposes, 500 samples were randomly selected for observation, with the results shown in Fig. 7.3. As shown in Fig. 7.3(a), the representative AFM image of the nano-scale molybdenum disulphide sheets with fewer nanometres demonstrated that most molybdenum disulphide nanosheets were of low thickness. Fig. 7.3(b) exhibited the corresponding height ( $\sim 1.0$  nm) of the cross-section in Fig. 7.3(a), which was believed to be the thickness of the monolayer molybdenum disulphide nanosheets [28]. In Fig. 7.3(c), the molybdenum disulphide nanosheets, with their height ranging from 1.0 nm to 2.0 nm, were believed to be the bilayer molybdenum disulphide nanosheets [11,24,29]. The bilayer molybdenum disulphide nanosheets accounted for the highest ratio, of over 41.1%, which meant the majority of molybdenum disulphide nanosheets were bilayer. Meanwhile, the molybdenum disulphide nanosheets with single three, four, and five layers accounted for approximately 16.6%, 13.2%, 7.3%, and 4%,

respectively. Besides, nano-scale molybdenum disulphide sheets with a thickness of over 5.0 nm accounted for 17.8%, which indicated that 82.2% of the molybdenum disulphide nanosheets had less than five layers. Thus, the AFM results well illustrated a typical two-dimensional size for nano-scale molybdenum disulphide sheets prepared in this work.

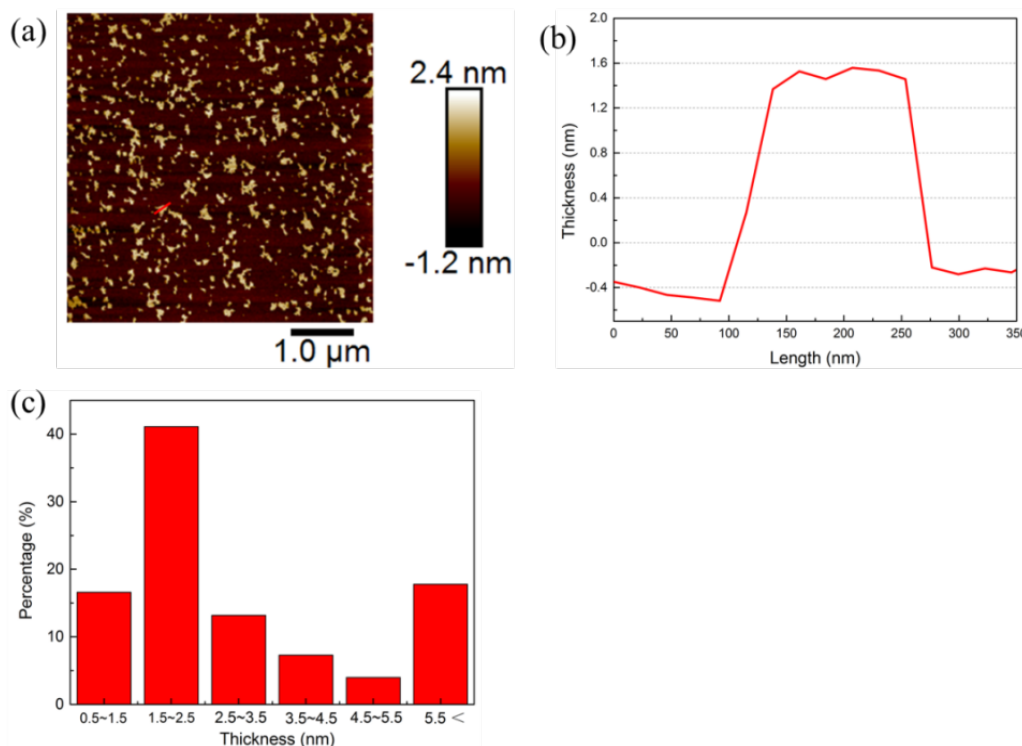


Fig. 7.3. AFM characterisation of molybdenum disulphide nanosheets: (a) typical AFM image of molybdenum disulphide nanosheets, (b) corresponding cross-sectional profile of the molybdenum disulphide nanosheets marked in panel (a), and (c) histogram of the thickness distribution of molybdenum disulphide nanosheets.

### 7.3.2. Effect of pH on cadmium ion adsorption on nano-scale molybdenum disulphide sheets

Cadmium adsorption on nano-scale molybdenum disulphide sheets, as a function of pH at 20°C, is displayed in Fig. 7.4. As shown in Fig. 7.4(a), the adsorption amount of cadmium increased with the increase of solution pH, indicating that the sorption process was highly pH-dependent. It was noticed that the adsorption capacity increased with increasing pH at a lower range of 1.0 to 4.0, reaching a plateau value at higher pH values of 4.0–7.0. At low solution pH ranging from 1.0–4.0, the surface of the nano-scale molybdenum disulphide sheets turned more negatively charged as the solution pH increased [11], resulting in increasing electrostatic attraction between the

ions and the adsorbent. What's more, as the concentration of  $\text{H}_3\text{O}^+$  decreased, the negatively charged sulphide plane became weaker in protonation, resulting in an increase in the available binding sites for cadmium ions on the sulphide surface, along with an increase in the adsorption capacity. Despite the surface of molybdenum disulphide being more negative with the increase in pH from 4.0 to 7.0, the electrostatic attraction between the saturated surface and cadmium ions was no longer strong for immobilizing more cadmium ions.

Fig. 7.4(b) shows the distribution of various hydrolysed Cd (II) species in solution ( $20^\circ\text{C}$ ) at various pH values, according to the hydrolytic equilibria and their respective stability constants [30]. It is clear that the Cd (II) ion was the primary specie presented in the aqueous medium with pH less than 6.0, while the precipitation of cadmium hydroxide began at pH 8.5. Considering the adsorption capacity of cadmium ions was similar at a higher pH, a pH of 6.0 was used in the remaining studies to keep Cd (II) ions being the main adsorbate.

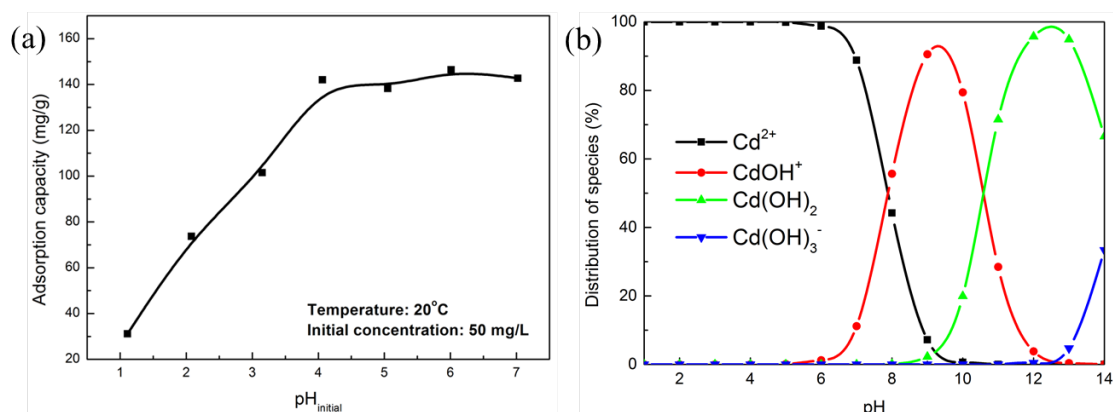


Fig. 7.4. (a) Effect of solution pH on cadmium adsorption with nano-scale molybdenum disulphide sheets. (b) Plot of % distribution of ionic species against solution pH ( $20^\circ\text{C}$ ).

### 7.3.3. Adsorption kinetics of cadmium on nano-scale molybdenum disulphide sheets

To understand the adsorption kinetics of cadmium on nano-scale molybdenum disulphide sheets, the adsorption capacity as a function of time is shown in Fig. 7.5. It is obvious that the equilibrium reached at a short time—approximately 30 min—at room temperature with an initial cadmium concentration of 50 mg/L. In Fig. 7.5(a), the experimental data were fitted with the pseudo-first-order kinetics model (Eq. 7.2) and the pseudo-second-order kinetics model (Eq. 7.3). In order to further investigate

the diffusion mechanism, the Weber-Morris intraparticle diffusion model (Eq. 7.4) was also applied. The fitting parameters are provided in Table 3.1.

$$q_t = q_e \times [1 - \exp(-k_1 \times t)] \tag{7.2}$$

$$q_t = \frac{t}{t/q_e + 1/(k_2 \times q_e^2)} \tag{7.3}$$

$$q_t = k_i \times t^{1/2} + C \tag{7.4}$$

where  $q_e$  and  $q_t$  are the amounts of metal ions adsorbed at equilibrium time and at different intervals, respectively, mg/g;  $k_1$  ( $\text{min}^{-1}$ ),  $k_2$  ( $\text{g}/(\text{mg} \cdot \text{min})$ ) and  $k_i$  ( $\text{mg}/(\text{g} \cdot \text{min}^{1/2})$ ) are rate constants of the pseudo-first-order kinetics, pseudo-second-order kinetics, and intraparticle diffusion model, respectively;  $C$  is the thickness of the boundary layer, mg/L.

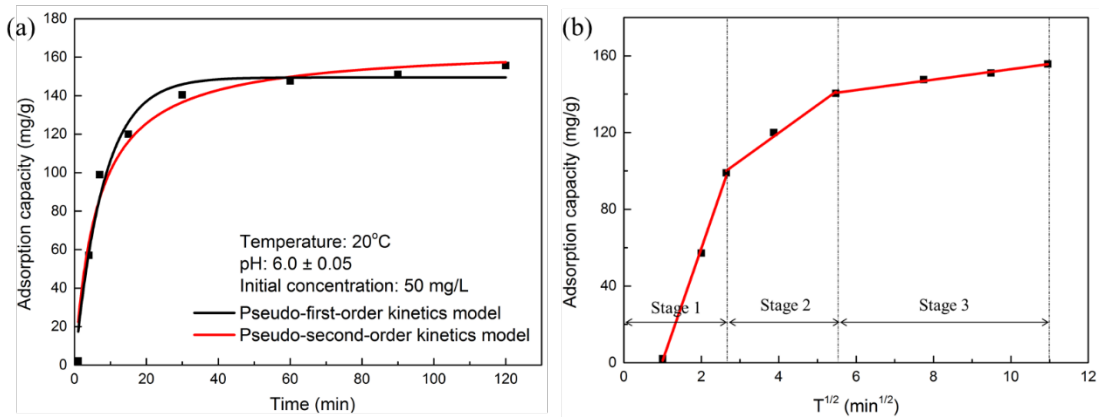


Fig. 7.5. (a) Adsorption kinetics of cadmium ions on nano-scale molybdenum disulphide sheets. (b) Intraparticle diffusion plot for the adsorption of cadmium ions onto nano-scale molybdenum disulphide sheets.

Table 3.1. Kinetic parameters of cadmium ion adsorption on nano-scale molybdenum disulphide sheets.

| Pseudo first-order kinetic model |        |       | Pseudo-second-order kinetic model           |        |       | Intraparticle diffusion model                     |        |       |
|----------------------------------|--------|-------|---|--------|-------|---|--------|-------|
| $k_1$                            | $q_e$  | $R^2$ | $k_2$                                       | $q_e$  | $R^2$ | $k_{i2}$  | $C$    | $R^2$ |
| ( $\text{min}^{-1}$ )            | (mg/g) |       | ( $\text{g}/(\text{mg} \cdot \text{min})$ ) | (mg/g) |       | ( $\text{mg}/(\text{g} \cdot \text{min}^{1/2})$ ) | (mg/L) |       |
| 0.124                            | 149.52 | 0.989 | $9.42 \times 10^{-4}$                       | 165.78 | 0.995 | 14.55   | 61.60  | 0.985 |

As shown in Table 3.1, the current adsorption system predominantly follows the pseudo-second-order rate model because of its higher correlation ( $R^2$ ) with the experimental data. Considering that the pseudo-second-order rate model was based on the assumption that the rate-limiting step might be the chemical sorption or chemisorption [31], the overall immobilized process of cadmium ions on nano-scale molybdenum disulphide sheets might be attributed to chemisorption. In Fig. 7.5(b), it was obvious that the plots were multi-linear, which could be divided into different stages, suggesting the presence of three adsorption processes. To explain further, stage 1 was attributed to bulk diffusion, stage 2 was attributed to the intraparticle diffusion, while stage 3 was the final equilibrium stage, where intraparticle diffusion started to slow down because of the low concentration cadmium ions in the solution. The values of  $k_{i2}$  and  $C$  in Table 3.1 were obtained from the second linear portion. The value of  $R^2$  for this model was 0.985, indicating that the adsorption followed the intraparticle diffusion model after 7 min. Based on the facts that the lines did not pass through the origin and the parameter of  $C$  reached a high level of 61.60 mg/L, it can be concluded that the intraparticle diffusion was not the only rate-limiting step, with boundary layer control also potentially being involved in this process [18,32].

#### 7.3.4. Adsorption isotherms of cadmium ions on nano-scale molybdenum disulphide sheets

The experimental data of the adsorption capacity of cadmium ions with respect to the equilibrium concentration is shown in Fig. 7.6. The experimental data were subsequently fitted with Langmuir isotherm, Freundlich isotherm, and Langmuir-Freundlich isotherm in the nonlinear model, which are described in Eqs. 7.5-7.7, respectively, while the fitting parameters are shown in Table 3.2.

$$q_e = \frac{Q_{\max} \times K_L \times C_e}{1 + K_L \times C_e} \quad 7.5$$

$$q_e = K_F \times C_e^{1/n} \quad 7.6$$

$$q_e = \frac{Q_{\max} \times K_{LF} \times C_e^{1/n}}{1 + K_{LF} \times C_e^{1/n}} \quad 7.7$$

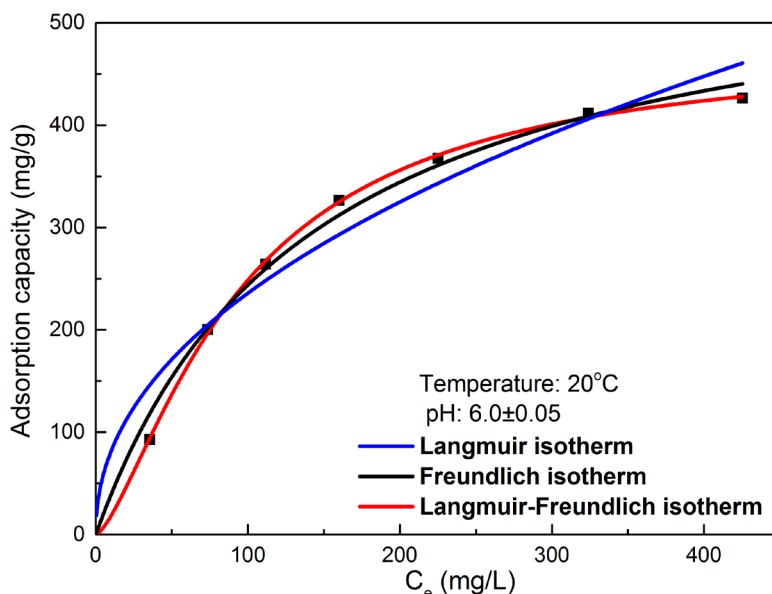


Fig. 7.6. Adsorption isotherms of cadmium ions on nano-scale molybdenum disulphide sheets.

Table 3.2. Parameters of Langmuir, Freundlich, and Langmuir-Freundlich isotherm models for cadmium ion adsorption on nano-scale molybdenum disulphide sheets.

|           | Langmuir isotherm |        |         | Freundlich isotherm |        |         | Langmuir-Freundlich isotherm |            |          |         |
|-----------|-------------------|--------|---------|---------------------|--------|---------|------------------------------|------------|----------|---------|
|           | model             |        |         | model               |        |         | model                        |            |          |         |
|           | $Q_{\max}$        | $K_L$  | $R_1^2$ | $1/n$               | $K_F$  | $R_2^2$ | $1/n$                        | $Q_{\max}$ | $K_{LF}$ | $R_3^2$ |
|           | (mg/g)            | (L/mg) |         |                     | (mg/g) |         |                              | (mg/g)     | (L/g)    |         |
| $Cd^{2+}$ | 585.4             | 0.0071 | 0.984   | 0.46                | 28.03  | 0.917   | 1.43                         | 477        | 1.5E-3   | 0.999   |

As the adsorption isotherms shown in Fig. 7.6, the LF isotherm provided a better fit for the experimental data than either the Langmuir or the Freundlich isotherm, which could also be analytically confirmed by comparing their corresponding  $R^2$  values (shown in Table 3.2). It should be pointed out that even though the LF isotherm possessed the best overall fit, the adsorption isotherm of cadmium ions also showed relatively good fit to both Langmuir and Freundlich isotherms, with high correlations of 0.984 and 0.917, respectively. In fact, this was because the LF isotherm combined both Langmuir and Freundlich models. The superior fitting to the LF empirical isotherm demonstrated the heterogeneity of the surfaces based on the corresponding theoretical models [33]. Meanwhile, the surfaces of nano-scale molybdenum disulphide sheets were initially suspected homogeneous due to the regular and uniform distribution of S atoms in their crystals [34]. The heterogeneous surface of nano-scale molybdenum disulphide sheets might derive from the fact that



defects, partial oxidation, and overlapping layers were generated during the combined mechanical and electrochemical preparation [35].

Impressively, the saturated adsorption capacity of cadmium ions on nano-scale molybdenum disulphide sheets as adsorbent was found to be around 477 mg/g, which was significantly higher than those of most the reported adsorbents (shown in Table 3). For instance, the maximum  $\text{Cd}^{2+}$  adsorption capacity of nano-scale molybdenum disulphide sheets was 11.5 and 4.3 times higher than those of the oxidized nanoporous activated carbon and the functionalized metal-organic framework, respectively. It should be pointed out that  $\text{MoS}_2$  before exfoliation showed a very poor saturated adsorption capacity of 6.24 mg/g for cadmium ions. This was due to the fact that the gallery height between two neighbouring layers of pristine  $\text{MoS}_2$  was 0.298 nm, which is too narrow for hydrated metal ions to enter the interior spaces, where the majority of potential binding sites were located.

Table 3.3. Comparison of cadmium adsorption performances by various adsorbents.

| Adsorbents  | Saturated adsorption capacity (mg/g) | Best fitting isotherm model | Refs |
|---|--------------------------------------|-----------------------------|------|
| Polyacrylamide-grafted Iron (III) Oxide                           | 147.2                                | Langmuir                    | [36] |
| Oxidized Nanoporous Activated Carbon                              | 38.2                                 | Langmuir                    | [37] |
| Hydrous Manganese Dioxide   | 111.0                                | Langmuir                    | [38] |
| Fe-Montmorillonite  | 25.7                                 | Langmuir-Freundlich         | [39] |
| Ground Wheat Stems  | 11.6                                 | Langmuir                    | [40] |
| Carboxyl-Terminated Superparamagnetic Iron Oxide Nanoparticles    | 20.0                                 | -                           | [41] |
| EGTA-modified Chitosan  | 83.2                                 | BiLangmuir                  | [42] |
| Magnetic $\text{Fe}_3\text{O}_4$ @Carbon Nanoparticles            | 39.7                                 | -                           | [43] |
| Sodium Acrylate and Acrylamide Copolymer/Graphene Oxide Hydrogels | 196.4                                | Langmuir                    | [44] |
| Functionalized metal-organic framework                            | 88.7                                 | -                           | [45] |
| Pristine molybdenum disulphide                                    | 6.24                                 | -                           | This |

|   |       |                     |      |
|---|-------|---------------------|------|
| Nano-scale molybdenum disulphide sheets | 477.0 | Langmuir-Freundlich | work |
|---|-------|---------------------|------|

### 7.3.5. Mechanism analysis of adsorption

XPS analysis was conducted to understand the mechanisms of cadmium ions immobilized on nano-scale molybdenum disulphide sheets. The results are shown in Fig. 7.7. The all surveys of nano-scale molybdenum disulphide sheets, with and without cadmium ions, are shown in Fig. 7.7(a). The typical peak of Cd 3d could be observed, which demonstrated successful cadmium uptake by the nano-scale molybdenum disulphide sheets. The Cd 3d spectra are shown in Fig. 7.7(b), in which the doublet peaks at 405.4 eV and 412.4 eV were assigned to the Cd 3d<sub>5/2</sub> and 3d<sub>3/2</sub> of CdS [46]. The formation of Cd–S demonstrated the affinity between cadmium ions and the sulphur of nano-scale molybdenum disulphide sheets. The other doublet peaks at 415.8 eV corresponded to Mo 3p<sub>3/2</sub> of MoO<sub>3</sub> [47], which might mainly derive from the oxidation of molybdenum located on the surface or edges of nano-scale molybdenum disulphide sheets [48]. As the S 2p spectra shown in Fig. 7.7(c), the peak at 161.5 eV was indicative of Cd–S[49], further confirming that cadmium ions were strongly bonded with the sulphur in nano-scale molybdenum disulphide sheets, forming the Cd–S species. The two peaks at 161.9 eV and 163.2 eV were assigned to S 2p<sub>3/2</sub> and 2p<sub>1/2</sub> of molybdenum disulphide [26,50]. In addition, a typical peak at 164.7 eV was assigned to S 2p of MoS<sub>3</sub> [51], which might derive from the slight oxidation of the sulphide in the crystals of nano-scale molybdenum disulphide sheets [52]. In Fig. 7.7(d), the peaks at 530.9 eV corresponded to the O 1s in MoO<sub>3</sub> [53], which further confirmed the existence of MoO<sub>3</sub>. The last peak at 533.0 eV was associated with the water adsorbed at the surface of the sample [47]. Despite the existence of the negatively charged MoO<sub>3</sub>, no corresponding peak of Cd–O species was found in the Cd 3d and O 1s spectra, which indicated that there was few/no combination between the O and cadmium ions. Thereby, S provided the main active binding sites for cadmium ions on nano-scale molybdenum disulphide sheets. Once attracted to the negatively charged surfaces of the nano-scale molybdenum disulphide sheets by electrostatic adsorption, the cadmium ions would be strongly adsorbed on the sulphur plates by forming the relatively stable Cd–S complexation species. In addition, the LF-model-fitted adsorption isotherm indicated that the multilayer immobilisation of cadmium ions might occur on the nano-scale molybdenum disulphide sheets because LF serves as an indicator of multilayer adsorption.

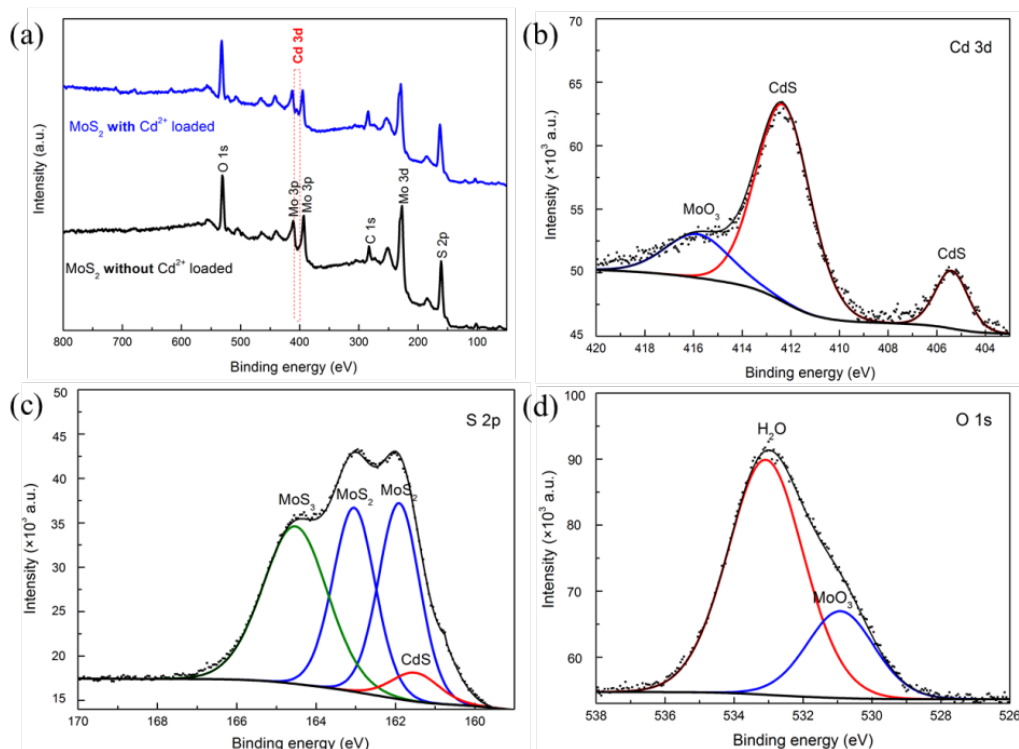


Fig. 7.7. XPS of nano-scale molybdenum disulphide sheets, with and without Cd<sup>2+</sup> ions loaded. (a) All surveys, with and without Cd<sup>2+</sup> loaded, (b) Cd 3d spectra, (c) S 2p spectra, (d) O 1s spectra (the points are the original data, while the outermost black lines are the fitting curves).

## 7.4. Conclusions

The as-prepared nano-scale molybdenum disulphide sheets in this work exhibited good uptake capacity for cadmium ions from an aqueous solution. The adsorption fitted well with the pseudo-second-order kinetic model and the Langmuir-Freundlich isotherm. The good fitting to the Langmuir-Freundlich isotherm demonstrated potential multilayer adsorption and the heterogeneous surface of the nano-scale molybdenum disulphide sheets. The formation of –S–Cd species derived from the soft and soft interaction between the sulphide planes and cadmium ions mainly accounted for the high adsorption capacity of cadmium ions on nano-scale molybdenum disulphide.

## REFERENCES

- [1] H. Shir Khanloo, M. Ghazaghi, H.Z. Mousavi, Cadmium determination in human biological samples based on trioctylmethyl ammonium thiosalicylate as a task-specific ionic liquid by dispersive liquid-liquid microextraction method, *Journal of Molecular Liquids*. 218 (2016) 478–483. doi:10.1016/j.molliq.2016.02.035.

- [2] G. Bhanjana, N. Dilbaghi, K.-H. Kim, S. Kumar, Carbon nanotubes as sorbent material for removal of cadmium, *Journal of Molecular Liquids*. 242 (2017) 966–970. doi:10.1016/j.molliq.2017.07.072.
- [3] D. Lembke, S. Bertolazzi, A. Kis, Single-layer MoS<sub>2</sub> electronics, *Accounts of Chemical Research*. 48 (2015) 100–110. doi:10.1021/ar500274q.
- [4] R.S. Sundaram, M. Engel, A. Lombardo, R. Krupke, A.C. Ferrari, P. Avouris, M. Steiner, Electroluminescence in single layer MoS<sub>2</sub>, *Nano Letters*. 13 (2013) 1416–1421. doi:10.1021/nl400516a.
- [5] S. Agarwal, I. Tyagi, V.K. Gupta, A. Fakhri, S. Shahidi, Sonocatalytic, sonophotocatalytic and photocatalytic degradation of morphine using molybdenum trioxide and molybdenum disulfide nanoparticles photocatalyst, *Journal of Molecular Liquids*. 225 (2017) 95–100. doi:10.1016/j.molliq.2016.11.029.
- [6] W. Yin, J. Yu, F. Lv, L. Yan, L.R. Zheng, Z. Gu, Y. Zhao, Functionalized Nano-MoS<sub>2</sub> with Peroxidase Catalytic and Near-Infrared Photothermal Activities for Safe and Synergetic Wound Antibacterial Applications, *ACS Nano*. 10 (2016) 11000–11011. doi:10.1021/acsnano.6b05810.
- [7] T. Liu, C. Wang, X. Gu, H. Gong, L. Cheng, X. Shi, L. Feng, B. Sun, Z. Liu, Drug delivery with PEGylated MoS<sub>2</sub> nano-sheets for combined photothermal and chemotherapy of cancer, *Advanced Materials*. 26 (2014) 3433–3440. doi:10.1002/adma.201305256.
- [8] F. Xing, T. Li, J. Li, H. Zhu, N. Wang, X. Cao, Chemically exfoliated MoS<sub>2</sub> for capacitive deionization of saline water, *Nano Energy*. 31 (2017) 590–595. doi:10.1016/j.nanoen.2016.12.012.
- [9] J. Feng, M. Graf, K. Liu, D. Ovchinnikov, D. Dumcenco, M. Heiranian, V. Nandigana, N.R. Aluru, A. Kis, A. Radenovic, Single-layer MoS<sub>2</sub> nanopores as nanopower generators, *Nature*. 536 (2016) 197–200. doi:10.1038/nature18593.
- [10] R.G. Pearson, Hard and Soft Acids and Bases, *Journal of Chemical Education*. 45 (1968) 581–587. doi:10.1021/ja00905a001.
- [11] F. Jia, Q. Wang, J. Wu, Y. Li, S. Song, Two-Dimensional Molybdenum Disulfide as a Superb Adsorbent for Removing Hg<sup>2+</sup> from Water, *ACS Sustainable Chemistry & Engineering*. 5 (2017) 7410–7419. doi:10.1021/acssuschemeng.7b01880.
- [12] K. Ai, C. Ruan, M. Shen, L. Lu, MoS<sub>2</sub> Nanosheets with Widened Interlayer Spacing for High-Efficiency Removal of Mercury in Aquatic Systems, *Advanced Functional Materials*. 26 (2016) 5542–5549. doi:10.1002/adfm.201601338.
- [13] F. Jia, X. Zhang, S. Song, AFM study on the adsorption of Hg<sup>2+</sup> on natural molybdenum disulfide in aqueous solutions, *Phys. Chem. Chem. Phys.* 19 (2017) 3837–3844.

- doi:10.1039/C6CP07302F.
- [14] X. Zhang, F. Jia, B. Yang, S. Song, Oxidation of Molybdenum Disulfide Sheet in Water under in Situ Atomic Force Microscopy Observation, *The Journal of Physical Chemistry C*. 121 (2017) 9938–9943. doi:10.1021/acs.jpcc.7b01863.
- [15] C. Liu, F. Jia, Q. Wang, B. Yang, S. Song, Two-dimensional molybdenum disulfide as adsorbent for high-efficient Pb(II) removal from water, *Applied Materials Today*. 9 (2017) 220–228. doi:10.1016/j.apmt.2017.07.009.
- [16] J. Wang, W. Zhang, X. Yue, Q. Yang, F. Liu, Y. Wang, D. Zhang, Z. Li, J. Wang, One-pot synthesis of multifunctional magnetic ferrite–MoS<sub>2</sub>–carbon dot nanohybrid adsorbent for efficient Pb(II) removal, *J. Mater. Chem. A*. 4 (2016) 3893–3900. doi:10.1039/C6TA00269B.
- [17] M.J. Aghagoli, F. Shemirani, Hybrid nanosheets composed of molybdenum disulfide and reduced graphene oxide for enhanced solid phase extraction of Pb (II) and Ni (II), *Microchimica Acta*. (2016). doi:10.1007/s00604-016-2000-7.
- [18] M.J. Aghagoli, M.H. Beyki, F. Shemirani, Facile synthesis of Fe<sub>3</sub>O<sub>4</sub>/MoS<sub>2</sub> nanohybrid for solid phase extraction of Ag(I) and Pb(II): kinetic, isotherm and thermodynamic studies, *International Journal of Environmental Analytical Chemistry*. (2017) 1–24. doi:10.1080/03067319.2017.1414204.
- [19] M.J. Aghagoli, M. Hossein Beyki, F. Shemirani, Application of dahlia-like molybdenum disulfide nanosheets for solid phase extraction of Co(II) in vegetable and water samples, *Food Chemistry*. 223 (2017) 8–15. doi:10.1016/j.foodchem.2016.12.023.
- [20] M.J. Aghagoli, M.H. Beyki, F. Shemirani, Fabrication of CaFe<sub>2</sub>O<sub>4</sub>/MoS<sub>2</sub> hybrid and its application for adsorption of paclitaxel chemotherapy medication in injection vial and water samples, *Journal of the Iranian Chemical Society*. 15 (2018) 499–510. doi:10.1007/s13738-017-1250-6.
- [21] L. Zhi, W. Zuo, F. Chen, B. Wang, 3D MoS<sub>2</sub> Composition Aerogels as Chemosensors and Adsorbents for Colorimetric Detection and High-Capacity Adsorption of Hg<sup>2+</sup>, *ACS Sustainable Chemistry and Engineering*. 4 (2016) 3398–3408. doi:10.1021/acssuschemeng.6b00409.
- [22] Y. Liang, R. Feng, S. Yang, H. Ma, J. Liang, J. Chen, Rechargeable Mg batteries with graphene-like MoS<sub>2</sub> cathode and ultrasmall Mg nanoparticle anode, *Advanced Materials*. 23 (2011) 640–643. doi:10.1002/adma.201003560.
- [23] N. Liu, P. Kim, J.H. Kim, J.H. Ye, S. Kim, C.J. Lee, Large-area atomically thin MoS<sub>2</sub> nanosheets prepared using electrochemical exfoliation, *ACS Nano*. 8 (2014) 6902–6910. doi:10.1021/nn5016242.

- [24] C. Lee, H. Yan, L. Brus, T. Heinz, J. Hone, S. Ryu, Anomalous lattice vibrations of single- and few-layer MoS<sub>2</sub>, *ACS Nano*. 4 (2010) 2695–700. doi:10.1021/nn1003937.
- [25] S. Najmaei, Z. Liu, P.M. Ajayan, J. Lou, Thermal effects on the characteristic Raman spectrum of molybdenum disulfide (MoS<sub>2</sub>) of varying thicknesses, *Applied Physics Letters*. 100 (2012). doi:10.1063/1.3673907.
- [26] H. Li, Y. Wang, G. Chen, Y. Sang, H. Jiang, J. He, X. Li, H. Liu, Few-layered MoS<sub>2</sub> nanosheets wrapped ultrafine TiO<sub>2</sub> nanobelts with enhanced photocatalytic property, *Nanoscale*. 8 (2016) 6101–6109. doi:10.1039/C5NR08796A.
- [27] G. Eda, H. Yamaguchi, D. Voiry, T. Fujita, M. Chen, M. Chhowalla, Photoluminescence from chemically exfoliated MoS<sub>2</sub>, *Nano Letters*. 11 (2011) 5111–5116. doi:10.1021/nl201874w.
- [28] A. Splendiani, L. Sun, Y. Zhang, T. Li, J. Kim, C.Y. Chim, G. Galli, F. Wang, Emerging photoluminescence in monolayer MoS<sub>2</sub>, *Nano Letters*. 10 (2010) 1271–1275. doi:10.1021/nl903868w.
- [29] H. Wang, L. Yu, Y.H. Lee, Y. Shi, A. Hsu, M.L. Chin, L.J. Li, M. Dubey, J. Kong, T. Palacios, Integrated circuits based on bilayer MoS<sub>2</sub> transistors, *Nano Letters*. 12 (2012) 4674–4680. doi:10.1021/nl302015v.
- [30] D. Borah, K. Senapati, Adsorption of Cd(II) from aqueous solution onto pyrite, *Fuel*. 85 (2006) 1929–1934. doi:10.1016/j.fuel.2006.01.012.
- [31] Y.S. Ho, G. McKay, The kinetics of sorption of divalent metal ions onto sphagnum moss peat, *Water Research*. 34 (2000) 735–742. doi:10.1016/S0043-1354(99)00232-8.
- [32] J. Zhang, Y. Li, C. Zhang, Y. Jing, Adsorption of malachite green from aqueous solution onto carbon prepared from *Arundo donax* root, *Journal of Hazardous Materials*. 150 (2008) 774–782. doi:10.1016/j.jhazmat.2007.05.036.
- [33] R.J. Umpleby, S.C. Baxter, Y. Chen, R.N. Shah, K.D. Shimizu, Characterization of molecularly imprinted polymers with the Langmuir - Freundlich isotherm, *Analytical Chemistry*. 73 (2001) 4584–4591. doi:10.1021/ac0105686.
- [34] J. Xie, H. Zhang, S. Li, R. Wang, X. Sun, M. Zhou, J. Zhou, X. Wen, D. Lou, Y. Xie, Defect-Rich MoS<sub>2</sub> Ultrathin Nanosheets with Additional Active Edge Sites for Enhanced Electrocatalytic Hydrogen Evolution, *Advanced Materials*. 25 (2013) 5807–5813. doi:10.1002/adma.201302685.
- [35] Z. Liu, M. Amani, S. Najmaei, Q. Xu, X. Zou, W. Zhou, T. Yu, C. Qiu, A.G. Birdwell, F.J. Crowne, R. Vajtai, B.I. Yakobson, Z. Xia, M. Dubey, P.M. Ajayan, J. Lou, Strain and structure heterogeneity in MoS<sub>2</sub> atomic layers grown by chemical vapour deposition, *Nature Communications*. 5 (2014) 5246. doi:10.1038/ncomms6246.

- [36] G.N. Manju, K. Anoop Krishnan, V.P. Vinod, T.S. Anirudhan, An investigation into the sorption of heavy metals from wastewaters by polyacrylamide-grafted iron(III) oxide, *Journal of Hazardous Materials*. 91 (2002) 221–238. doi:10.1016/S0304-3894(01)00392-2.
- [37] B.K.M.T. Xiao, Competitive Adsorption of Aqueous Metal Ions on an Oxidized Nanoporous Activated Carbon Competitive Adsorption of Aqueous Metal Ions on an, *Langmuir*. 20 (2004) 4566–4578. doi:10.1021/la049712j.
- [38] S.S. Tripathy, J.L. Bersillon, K. Gopal, Adsorption of Cd<sup>2+</sup> on hydrous manganese dioxide from aqueous solutions, *Desalination*. 194 (2006) 11–21. doi:10.1016/j.desal.2005.10.023.
- [39] P. Wu, W. Wu, S. Li, N. Xing, N. Zhu, P. Li, J. Wu, C. Yang, Z. Dang, Removal of Cd<sup>2+</sup> from aqueous solution by adsorption using Fe-montmorillonite, *Journal of Hazardous Materials*. 169 (2009) 824–830. doi:10.1016/j.jhazmat.2009.04.022.
- [40] G. Tan, D. Xiao, Adsorption of cadmium ion from aqueous solution by ground wheat stems, *Journal of Hazardous Materials*. 164 (2009) 1359–1363. doi:10.1016/j.jhazmat.2008.09.082.
- [41] Z. Feng, S. Zhu, D.R. Martins De Godoi, A.C.S. Samia, D. Scherson, Adsorption of Cd<sup>2+</sup> on carboxyl-terminated superparamagnetic iron oxide nanoparticles, *Analytical Chemistry*. 84 (2012) 3764–3770. doi:10.1021/ac300392k.
- [42] F. Zhao, E. Repo, D. Yin, M.E.T. Sillanpää, Adsorption of Cd(II) and Pb(II) by a novel EGTA-modified chitosan material: Kinetics and isotherms, *Journal of Colloid and Interface Science*. 409 (2013) 174–182. doi:10.1016/j.jcis.2013.07.062.
- [43] Z. Chen, Z. Geng, Z. Zhang, L. Ren, T. Tao, R. Yang, Z. Guo, Synthesis of Magnetic Fe<sub>3</sub>O<sub>4</sub>@C Nanoparticles Modified with -SO<sub>3</sub>H and -COOH Groups for Fast Removal of Pb<sup>2+</sup>, Hg<sup>2+</sup>, and Cd<sup>2+</sup> Ions, *European Journal of Inorganic Chemistry*. 2014 (2014) 3172–3177. doi:10.1002/ejic.201301500.
- [44] S. He, F. Zhang, S. Cheng, W. Wang, Synthesis of sodium acrylate and acrylamide copolymer/GO hydrogels and their effective adsorption for Pb<sup>2+</sup> and Cd<sup>2+</sup>, *ACS Sustainable Chemistry and Engineering*. 4 (2016) 3948–3959. doi:10.1021/acssuschemeng.6b00796.
- [45] Y. Wang, G. Ye, H. Chen, X. Hu, Z. Niu, S. Ma, Functionalized metal–organic framework as a new platform for efficient and selective removal of cadmium(  $\text{Cd}^{2+}$  ) from aqueous solution, *J. Mater. Chem. A*. 3 (2015) 15292–15298. doi:10.1039/C5TA03201F.
- [46] G. Hota, S.B. Idage, K.C. Khilar, Characterization of nano-sized CdS-Ag<sub>2</sub>S core-shell nanoparticles using XPS technique, *Colloids and Surfaces A: Physicochemical and Engineering Aspects*. 293 (2007) 5–12. doi:10.1016/j.colsurfa.2006.06.036.

- [47] R. Cárdenas, J. Torres, J.E. Alfonso, Optical characterization of MoO<sub>3</sub> thin films produced by continuous wave CO<sub>2</sub> laser-assisted evaporation, *Thin Solid Films*. 478 (2005) 146–151. doi:10.1016/j.tsf.2004.10.027.
- [48] X. Zheng, J. Xu, K. Yan, H. Wang, Z. Wang, S. Yang, Space-confined growth of MoS<sub>2</sub> nanosheets within graphite: The layered hybrid of MoS<sub>2</sub> and graphene as an active catalyst for hydrogen evolution reaction, *Chemistry of Materials*. 26 (2014) 2344–2353. doi:10.1021/cm500347r.
- [49] S. Rengaraj, S. Venkataraj, S.H. Jee, Y. Kim, C.W. Tai, E. Repo, A. Koistinen, A. Ferancova, M. Sillanpää, Cauliflower-like CdS microspheres composed of nanocrystals and their physicochemical properties, *Langmuir*. 27 (2011) 352–358. doi:10.1021/la1032288.
- [50] H.W. Wang, P. Skeldon, G.E. Thompson, XPS studies of MoS<sub>2</sub> formation from ammonium tetrathiomolybdate solutions, *Surface and Coatings Technology*. 91 (1997) 200–207. doi:10.1016/S0257-8972(96)03186-6.
- [51] H. Vrubel, D. Merki, X. Hu, Hydrogen evolution catalyzed by MoS<sub>3</sub> and MoS<sub>2</sub> particles, *Energy & Environmental Science*. 5 (2012) 6136. doi:10.1039/c2ee02835b.
- [52] T. Weber, J.C. Muijsers, J.W. Niemantsverdriet, The Structure of Amorphous MoS<sub>3</sub>, *The Journal of Physical Chemistry*. 99 (1995) 9194–9200. doi:10.1021/j100022a037.
- [53] C.L. Bianchi, M.G. Cattania, P. Villa, XPS characterization of Ni and Mo oxides before and after “in situ” treatments, *Applied Surface Science*. 70–71 (1993) 211–216. doi:10.1016/0169-4332(93)90429-F.

*The main content of this chapter was published as “Journal of Molecular Liquids 263 (2018): 526-533.”*



## CHAPTER VIII

# Mussel-inspired Fe<sub>3</sub>O<sub>4</sub>@polydopamine (PDA)- MoS<sub>2</sub> core–shell nanosphere as a promising adsorbent for removal of Pb<sup>2+</sup> from water

### 8.1. Introduction

As one of the most harmful heavy metal ions in aqueous solution, lead ions (Pb<sup>2+</sup>) is a longstanding environmental contaminant that can cause terrible damage, such as kidney disease and reduction in hemoglobin formation, mental retardation, infertility and abnormalities, to human beings [1]. Among numerous involved technologies to treat industry wastewater with high concentration of Pb<sup>2+</sup> (such as the effluents from production of batteries, alloys, gasoline additives and pigments) [2], adsorption is considered as one of the most versatile technique due to its property of easy operation, high efficiency and low cost [3]. In general, conventional adsorbents for Pb<sup>2+</sup> are porous clay-based or carbon-based [4,5], which unfortunately often share the similar limitations of low adsorption capacity and poor selectivity.

Thanks to the recent developments of nanotechnology, the application of nanoadsorbents are an emerging and efficient method to scavenge Pb<sup>2+</sup> from industry wastewater because of their particular structure and special properties [6]. Molybdenum disulfide (MoS<sub>2</sub>) in nanoscale structures, such as nanosheets, nanoflowers and nanorods [7–13], have recently attracted increasing attention because of their extremely high specific surface areas and abundant binding sites for metal ions. However, the difficulty of solid–liquid separation via traditional centrifugation and filtration terribly restricted the practical applications of nanoscale MoS<sub>2</sub>. To address this issue, one of the effective approaches is to prepare magnetic MoS<sub>2</sub> nanohybrids. Till now, only three papers reported removal of heavy metal ions using MoS<sub>2</sub>/Fe<sub>3</sub>O<sub>4</sub> nanocomposites [14–16]. For instance, MoS<sub>2</sub>/Fe<sub>3</sub>O<sub>4</sub> nanocomposites, prepared by the immobilization of Fe<sub>3</sub>O<sub>4</sub> particles to MoS<sub>2</sub> nanorods by physical adsorption/electrostatic interaction [14], or in situ growth of Fe<sub>3</sub>O<sub>4</sub> particles on the defects of MoS<sub>2</sub> nanosheets [16], exhibited adsorption capacity of 11.7 mg/g, 9.6 mg/g and 425.5 mg/g for Cu<sup>2+</sup>, Pb<sup>2+</sup> and Hg<sup>2+</sup>, respectively. Such limited adsorption capacity might derive from the occupation of binding sites by the formed nanoscale Fe<sub>3</sub>O<sub>4</sub>. In addition, these MoS<sub>2</sub>/Fe<sub>3</sub>O<sub>4</sub> nanocomposites suffered from the poor stability

in acidic solution due to their entire exposure of  $\text{Fe}_3\text{O}_4$  to  $\text{H}^+$ , which made it difficult to regenerate the used adsorbents by the general acid treatment to some extent. Inspired by mussel chemistry, polydopamine (PDA) might serve as a stable and efficient protective coating for  $\text{Fe}_3\text{O}_4$  nanospheres due to its strong adhesion properties [17]. The PDA coating also possesses abundant functional groups, which might be favorable to immobilize precursors for some in-situ reactions, for instance, in-situ growth of  $\text{MoS}_2$  to form a special core-shell architecture. To date, the synthesis of  $\text{Fe}_3\text{O}_4@\text{PDA}-\text{MoS}_2$  core-shell nanospheres and their detail adsorption performance towards heavy metal ions have never been found yet.

Herein, this thesis reported a facile synthetic method of in-situ hydrothermal growth of nanoscale  $\text{MoS}_2$  on PDA modified  $\text{Fe}_3\text{O}_4$  nanospheres ( $\text{Fe}_3\text{O}_4@\text{PDA}$ ) to prepare magnetic  $\text{Fe}_3\text{O}_4@\text{PDA}-\text{MoS}_2$  core-shell nanospheres, where polydopamine acted as both the protecting coating for core  $\text{Fe}_3\text{O}_4$  and the template for the in-situ growth of  $\text{MoS}_2$  nanoflowers. The architectures and properties of the nanocomposites were characterized. Afterwards, the adsorption performance of  $\text{Pb}^{2+}$  on the nanocomposites, including effect of solution pH, adsorption kinetics, isotherms, thermodynamic, mechanisms and regeneration performance were investigated. The as-synthesized magnetic  $\text{Fe}_3\text{O}_4@\text{PDA}-\text{MoS}_2$  core-shell nanospheres not only exhibited a long-term stability in acid solution and easy separation from aqueous solution, but also possessed a desirable adsorption performance for  $\text{Pb}^{2+}$ .

## 8.2. Materials and methods

### 8.2.1. Chemical Materials

Ammonium molybdate tetrahydrate ( $(\text{NH}_4)_6\text{Mo}_7\text{O}_{24}\cdot 4\text{H}_2\text{O}$ ), ethanol ( $\text{C}_2\text{H}_6\text{O}$ ), tris(hydroxymethyl) aminomethane ( $\text{C}_4\text{H}_{11}\text{NO}_3$ , Tris), thiourea ( $\text{CN}_2\text{H}_4\text{S}$ ), ferric chloride hexahydrate ( $\text{FeCl}_3\cdot 6\text{H}_2\text{O}$ ), nitric acid ( $\text{HNO}_3$ ), anhydrous sodium acetate ( $\text{CH}_3\text{COONa}$ ) and ethylene glycol ( $\text{C}_2\text{H}_6\text{O}_2$ , EG) were supplied by the Sinopharm Chemical Reagent Co., Ltd (Shanghai, China). Dopamine hydrochloride ( $\text{C}_8\text{H}_{11}\text{NO}_2\cdot\text{HCl}$ ) was purchased from Shanghai Aladdin Bio-Chem Technology Co., Ltd. Hydrochloric acid ( $\text{HCl}$ ) was bought from Merck Pty. Ltd. All chemicals were of analytical purity and used without further purification. Deionized water (18.2 M $\Omega$  cm) originated from Milli-Q instrument (Millipore Corporation, France) was used in all the experiments.

### 8.2.2. Fabrication of $\text{Fe}_3\text{O}_4@\text{PDA}-\text{MoS}_2$ nanocomposites

**Fabrication of Fe<sub>3</sub>O<sub>4</sub>.** A modified solvothermal method was used to prepare the Fe<sub>3</sub>O<sub>4</sub> microspheres[18,19]. In detail, 1.35 g FeCl<sub>3</sub>·6H<sub>2</sub>O and 3.60 g CH<sub>3</sub>COONa were added into 50 mL EG solution under magnetic stirring. Afterwards, the yellow solution was transferred into a Teflon-lined stainless-steel autoclave and then heated at 473 K for 8 h. After being naturally cooled down to room temperature (298 K), the obtained black products were separated by a magnet and washed alternately with deionized water and ethanol for at least three times, and finally dried in vacuum at 298 K overnight.

**Fabrication of Fe<sub>3</sub>O<sub>4</sub>@PDA.** Fe<sub>3</sub>O<sub>4</sub>@PDA nanoparticles were fabricated by a modified method[20]. At length, 160 mg Fe<sub>3</sub>O<sub>4</sub> nanoparticles and 160 mg dopamine hydrochloride were added into 80 mL, 10 mM (pH = 8.5) Tris-HCl buffer solution. The mixture was then shaken for 24 h at 298 K, and the resultants were separated by a magnet and washed alternately with deionized water and ethanol for at least three times.

**Fabrication of Fe<sub>3</sub>O<sub>4</sub>@PDA-MoS<sub>2</sub> nanocomposites.** 40 mL solution, which contained 1.24 g of (NH<sub>4</sub>)<sub>6</sub>Mo<sub>7</sub>O<sub>24</sub>·4H<sub>2</sub>O and 1.07 g of CN<sub>2</sub>H<sub>4</sub>S, was stirred to form a homogeneous solution, and then 80 mg Fe<sub>3</sub>O<sub>4</sub>@PDA nanospheres was added into the solution. The mixtures were treated by ultrasound at 150 W for ten minutes in a water bath to form a homogeneous solution, and then transferred into a 100 mL Teflon-lined stainless-steel autoclave and heated at 493 K for 6 h. In comparison, MoS<sub>2</sub> and Fe<sub>3</sub>O<sub>4</sub>@MoS<sub>2</sub> were synthesized in a similar way without the addition of Fe<sub>3</sub>O<sub>4</sub>@PDA and dopamine, respectively. After being naturally cooled down to room temperature, the precipitates were collected, washed alternately with deionized water and ethanol for at least three times, and finally dried by vacuum freeze-drying. The theoretical mass ratio of Fe<sub>3</sub>O<sub>4</sub>@PDA to MoS<sub>2</sub> was calculated to be 1:14.

### 8.2.3. Characterization

The morphologies of samples were observed using scanning electron microscopy (SEM, S-4700, Hitachi) and transmission electron microscopy (TEM, TF20, Jeol 2100F) operating at 200 kV. X-ray diffraction (XRD) measurements were performed via an Empyrean PRO diffractometer. Zeta potentials were used to determine surface potential using Malvern Zeta sizer Nano ZS90. The Brunauer–Emmett–Teller surface areas (BET) of the products were analyzed using a nitrogen adsorption apparatus (TriStar II 3020). The hysteresis loops of the samples were obtained from a VSM (PPMS-9T, Quantum Design). The concentration determination of Pb<sup>2+</sup> in aqueous

solutions were conducted with atomic absorption spectroscopy (AAS, CONTRAA-700). The concentration of samples was conducted by an inductively coupled plasma-optical emission spectrum (ICP-OES, Prodigy, Leeman Labs).

#### 8.2.4. Batch adsorption test

The effects of solution pH on adsorption were investigated in 100 mL conical flasks which contained 50 mL, 100 mg/L  $\text{Pb}^{2+}$  aqueous solution. The initial solution pH ranged from 1.0 to 7.0, which were adjusted by adding negligible volumes of 0.1 mol/L  $\text{HNO}_3$  or 0.01 mol/L  $\text{NaOH}$ . Afterwards, 20.0 mg of the as-prepared adsorbents are added and shaken for 180 min at 293 K. A magnet was used to separate the adsorbents and aqueous solution. In a similar way, adsorption isotherms (293 K, 303 K and 313 K) were obtained with initial  $\text{Pb}^{2+}$  concentration ranging from 10 to 1000 mg/L, respectively. To investigate the adsorption rate, 100 mg of the as-prepared adsorbents were added into a 1000 mL conical flask, which contained 800 mL aqueous solution with 200 mg/L  $\text{Pb}^{2+}$ . After being shaken at 180 rpm in water bath for 60 min at 293 K, 4 mL solution will be sucked out at preset time intervals, such as 0, 1, 5, 10, 20, 30, 60, 90, 120, 240 min. Considering that the adsorbent and solution needed to be separated in time, solid-liquid separation here was carried out by syringe filtration rather than a magnet [8]. To regenerate the adsorbents, the used adsorbents were immersed into 40 mL, 0.01 mol/L  $\text{HCl}$  solutions and shaken continuously for 30 min, and finally rinsed with deionized water.

At time  $t$  (min), the adsorption capacities of adsorbents,  $Q_t$  (mg/g), were originated from the following Eq 8.1:

$$Q_t = (C_0 - C_t) \times V/M \quad 8.1$$

where  $C_0$  (mg/L) is the initial concentration of  $\text{Pb}^{2+}$  in aqueous solution,  $C_t$  (mg/L) is the concentration of  $\text{Pb}^{2+}$  in aqueous solution at time  $t$  (min),  $M$  (g) is the total mass of adsorbent, and  $V$  (L) is the volume of aqueous solution, respectively.

#### 8.2.5. Stability test of adsorbents

To test the stability of the sample in acid solutions, 20 mg portions of  $\text{Fe}_3\text{O}_4@\text{PDA}-\text{MoS}_2$  (Seen in Fig. 8.1) were dispersed in seven 10-mL bottles with 0.01 mol/L  $\text{HNO}_3$  solution and shaken for 1, 2, 4, 8, 15, 24, 48 and 72 h at room temperature, respectively. Afterwards, a magnet was used to separate the adsorbent and solution. The concentrations of  $\text{Fe}^{2+}$  and  $\text{Fe}^{3+}$  in supernatant were measured by AAS, and the precipitates were dried by vacuum freeze-drying and weighted.

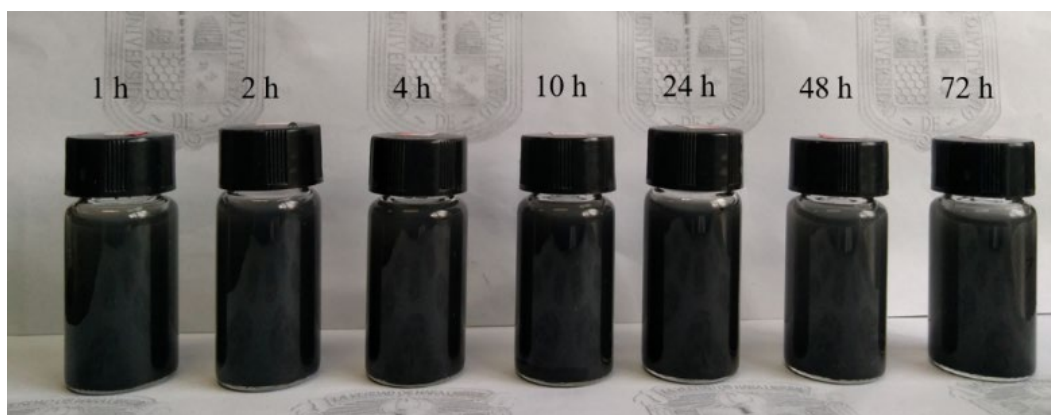


Fig. 8.1. Optical images of  $\text{Fe}_3\text{O}_4@\text{PDA}-\text{MoS}_2$  immersed in 10 mL, 0.01 mol/L  $\text{HNO}_3$  for different time.

### 8.3. Results and discussion

#### 8.3.1. Preparation and characterizations

As displayed in Fig. 8.2, using  $\text{FeCl}_3 \cdot \text{H}_2\text{O}$  as the single iron source,  $\text{Fe}_3\text{O}_4$  nanospheres were prepared via a solvothermal method in EG solutions. Subsequently, the as-prepared  $\text{Fe}_3\text{O}_4$  nanospheres were added into dopamine solution (10 mM Tris, pH 8.5), leading to the formation of uniform PDA coatings with thickness of around 40 nm outside the  $\text{Fe}_3\text{O}_4$  nanospheres. When mixed with solutions containing  $(\text{NH}_4)_6\text{Mo}_7\text{O}_{24}$  and  $\text{CN}_2\text{H}_4\text{S}$ ,  $\text{Fe}_3\text{O}_4@\text{PDA}$  nanospheres were then able to immobilize the precursors of  $\text{MoS}_2$  because of the existence of the abundant functional groups outside the surfaces of  $\text{Fe}_3\text{O}_4@\text{PDA}$  nanospheres. With  $\text{Fe}_3\text{O}_4@\text{PDA}$  nanospheres serving as templates,  $\text{MoS}_2$  was able to grow in situ on the surface of  $\text{Fe}_3\text{O}_4@\text{PDA}$  to construct  $\text{Fe}_3\text{O}_4@\text{PDA}-\text{MoS}_2$  nanocomposites with high specific surface area.

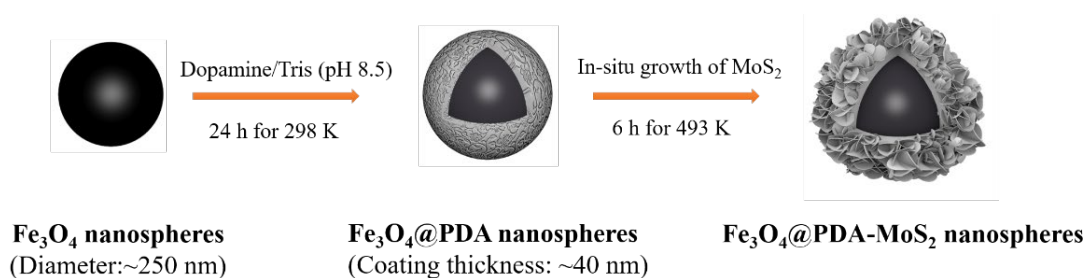


Fig. 8.2. Schematic diagram of the fabrication of  $\text{Fe}_3\text{O}_4@\text{PDA}-\text{MoS}_2$  nanocomposites.

The morphologies of  $\text{Fe}_3\text{O}_4$  nanospheres,  $\text{Fe}_3\text{O}_4@\text{PDA}$  nanospheres and  $\text{Fe}_3\text{O}_4@\text{PDA}-\text{MoS}_2$  nanospheres were shown in Fig. 8.2(a)-(e). As shown in Fig. 8.3(a) and (b), the synthesized  $\text{Fe}_3\text{O}_4$  appeared to be nanospheres with diameter of

around 250 nm. The thickness of PDA coating outside the  $\text{Fe}_3\text{O}_4$  nanospheres were around 40 nm, as displayed in Fig. 8.3(c) and (d). In Fig. 8.3(e) and (f), the in-situ grown  $\text{MoS}_2$  displayed a flower-like architecture with diameters of around 300 nm, and it was prone to find that the in-situ grown  $\text{MoS}_2$  possessed a more incompact architecture of  $\text{MoS}_2$  compared to the pure  $\text{MoS}_2$  (Morphology could be seen in Fig. 8.4).

To investigate the crystal structure and phase purity, XRD spectrum of  $\text{Fe}_3\text{O}_4$ ,  $\text{Fe}_3\text{O}_4$ @PDA nanospheres, pure  $\text{MoS}_2$  and  $\text{Fe}_3\text{O}_4$ @PDA- $\text{MoS}_2$  nanospheres were given in Fig. 8.3(g). It could be found that the diffraction peaks of  $\text{Fe}_3\text{O}_4$  corresponded well with the (220), (311), (400), (422), (511) and (440) reflections of the standard cubic phase of  $\text{Fe}_3\text{O}_4$  according to JCPDS Card no. 89-0691. Moreover, the crystal phase of  $\text{Fe}_3\text{O}_4$  was not altered after hybridization with PDA. The peaks of pure  $\text{MoS}_2$  corresponded well with the (002), (100), (103) and (110) reflections, which were the characteristic diffraction peaks of  $\text{MoS}_2$  according to JCPDS Card no.37-1492. As for the diffraction of  $\text{Fe}_3\text{O}_4$ @PDA- $\text{MoS}_2$  composites, it was prone to find the characteristic reflections of both  $\text{MoS}_2$  and  $\text{Fe}_3\text{O}_4$ , indicating the successful formation of  $\text{Fe}_3\text{O}_4$ @PDA- $\text{MoS}_2$  composites. No peaks corresponding to impurities were detected, indicating a purified phase of  $\text{Fe}_3\text{O}_4$ @PDA- $\text{MoS}_2$  nanocomposites by the solvothermal reaction.

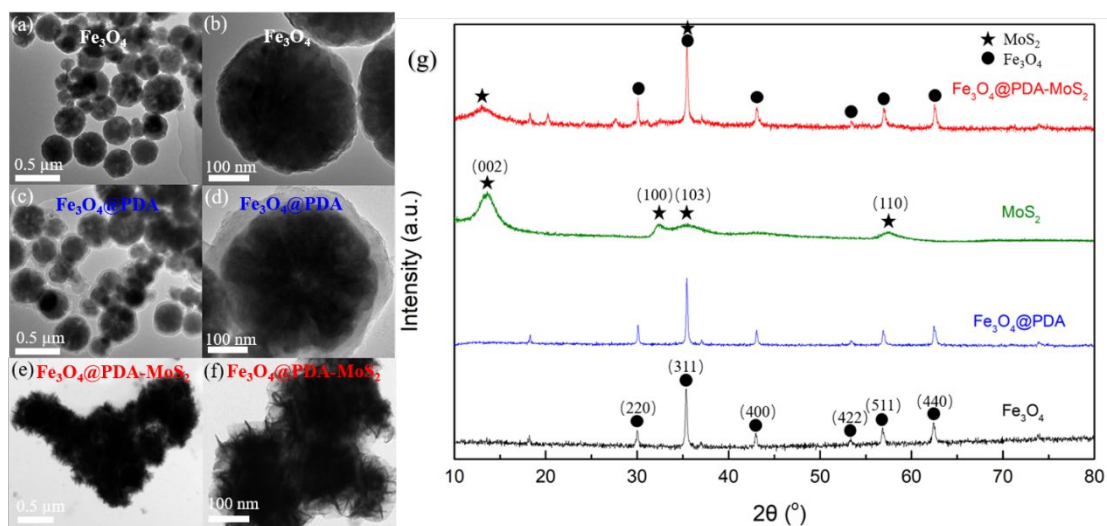
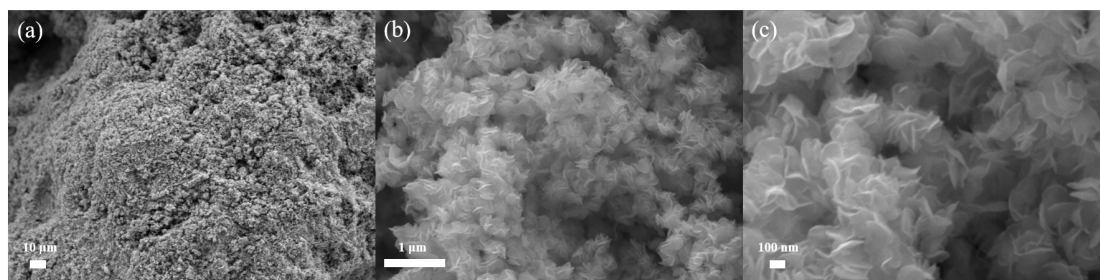


Fig. 8.3. TEM images of (a, b)  $\text{Fe}_3\text{O}_4$  nanospheres, (c, d)  $\text{Fe}_3\text{O}_4$ @PDA nanospheres and (e, f)  $\text{Fe}_3\text{O}_4$ @PDA- $\text{MoS}_2$  nanospheres. (g) XRD spectrum of  $\text{Fe}_3\text{O}_4$  nanospheres,  $\text{Fe}_3\text{O}_4$ @PDA, pure  $\text{MoS}_2$  and  $\text{Fe}_3\text{O}_4$ @PDA- $\text{MoS}_2$ .

Fig. 8.4. SEM image of pure MoS<sub>2</sub>.

Because of the existence of PDA, the precise concentration of MoS<sub>2</sub> in the compositions were unable to be detected by XRD spectrum, which requires the further determination of Fe<sub>3</sub>O<sub>4</sub>@PDA–MoS<sub>2</sub> nanocomposites. With the ICP results shown in Table 8.1 (only three main elements were given because of the instrument limitation), it was prone to figure out the mole ratio of Mo : S was 1 : 2.02, which was well consistent with the chemical composition of MoS<sub>2</sub>. Because of its purified phases, the mass ratio of Fe<sub>3</sub>O<sub>4</sub>, PDA and MoS<sub>2</sub> in Fe<sub>3</sub>O<sub>4</sub>@PDA–MoS<sub>2</sub> nanocomposites were calculated to be around 33.17%, 19.23% and 47.6%, respectively.

Table 8.1. ICP results of Fe<sub>3</sub>O<sub>4</sub>@PDA–MoS<sub>2</sub> nanocomposites

| Elements           | Fe    | Mo    | S     |
|--------------------|-------|-------|-------|
| Concentration, wt% | 24.00 | 28.27 | 19.09 |
| Mole ratio         | 1.46  | 1     | 2.02  |

The nitrogen adsorption–desorption isotherms were performed to investigate the BET surface areas of Fe<sub>3</sub>O<sub>4</sub> nanospheres, Fe<sub>3</sub>O<sub>4</sub>@PDA, pure MoS<sub>2</sub> and Fe<sub>3</sub>O<sub>4</sub>@PDA–MoS<sub>2</sub> nanospheres, as displayed in Fig. 8.5. Compared to the as-prepared Fe<sub>3</sub>O<sub>4</sub> nanospheres which had a BET specific surface area of 39.615 m<sup>2</sup>/g (Fig. 8.5(a)), Fe<sub>3</sub>O<sub>4</sub>@PDA core-shell nanospheres possessed a much smaller specific surface area of 7.292 m<sup>2</sup>/g (Fig. 8.5(b)). This was because that the pore size of the PDA was too small to be detected in present measurement [21]. Namely, the whole core Fe<sub>3</sub>O<sub>4</sub> nanospheres were encapsulated by the tight PDA coatings, which thus might work as an effective protective shell. In Fig. 8.5(c) and (d), the as-synthesized MoS<sub>2</sub> nanoflowers presented the typical IV type isotherm with a well-defined hysteresis loop while the Fe<sub>3</sub>O<sub>4</sub>@PDA–MoS<sub>2</sub> nanocomposites exhibited the typical II type isotherm almost without any hysteresis loop, respectively, indicating the presence of mesopores in the pure MoS<sub>2</sub> and macropores in the Fe<sub>3</sub>O<sub>4</sub>@PDA–MoS<sub>2</sub> nanospheres. Impressively, the pure MoS<sub>2</sub> only possessed a low specific surface area

of  $12.019 \text{ m}^2/\text{g}$ , while  $\text{Fe}_3\text{O}_4@\text{PDA}-\text{MoS}_2$  nanospheres exhibited the biggest BET specific surface area of  $43.383 \text{ m}^2/\text{g}$ . If the mass of the core  $\text{Fe}_3\text{O}_4@\text{PDA}$  inside the nanocomposites was subtracted, the specific surface area of  $\text{MoS}_2$  in-situ growth on  $\text{Fe}_3\text{O}_4@\text{PDA}$  was as 7.6 times as that of the pure  $\text{MoS}_2$  nanoflowers, which might derive from the advantage of the dopamine surfaces with abundant functional groups during its serving as the template. Such a property was favorable for the application of  $\text{MoS}_2$  to scavenge pollutants.

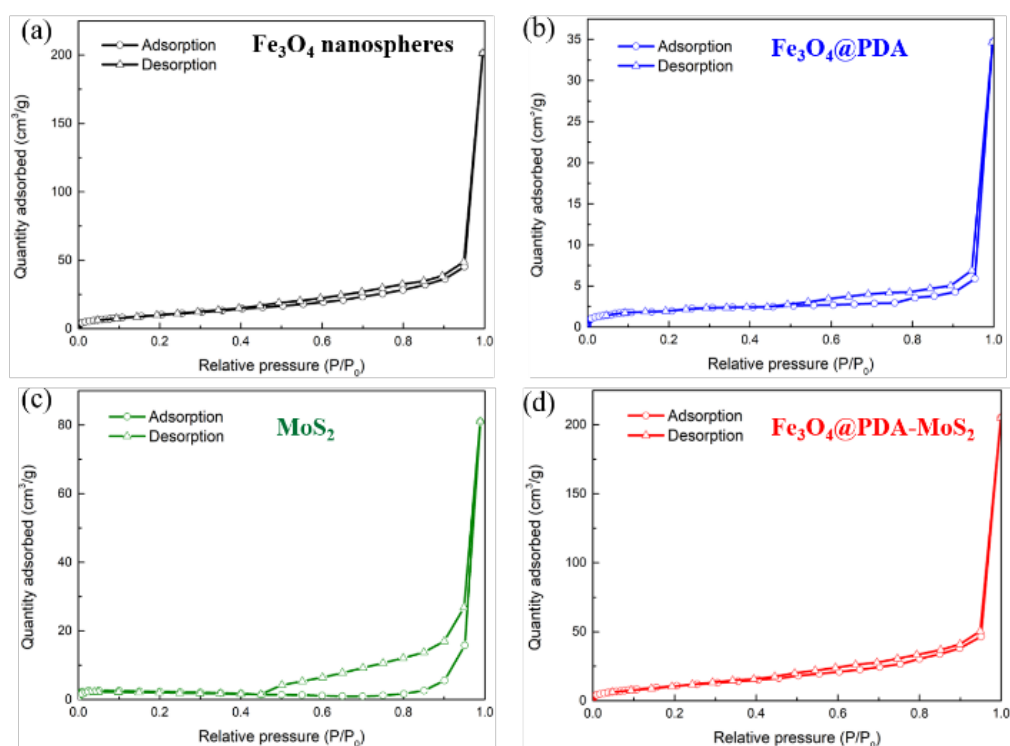


Fig. 8.5. Nitrogen adsorption–desorption isotherm plot of  $\text{Fe}_3\text{O}_4$ ,  $\text{Fe}_3\text{O}_4@\text{PDA}$ , pure  $\text{MoS}_2$  and  $\text{Fe}_3\text{O}_4@\text{PDA}-\text{MoS}_2$  nanospheres.

Fig. 8.6 shows the magnetic hysteresis loops of the original  $\text{Fe}_3\text{O}_4$  nanospheres,  $\text{Fe}_3\text{O}_4@\text{PDA}$  and  $\text{Fe}_3\text{O}_4@\text{PDA}-\text{MoS}_2$  nanospheres at 298 K. The saturated magnetization ( $M_s$ ) of the original  $\text{Fe}_3\text{O}_4$  nanospheres reached a high level of  $85.6 \text{ emu/g}$ , which decreased to  $65.6 \text{ emu/g}$  after the coating of PDA, and further decreased to  $53.2 \text{ emu/g}$  after the sequent assembly of  $\text{MoS}_2$ . Despite that the  $M_s$  of  $\text{Fe}_3\text{O}_4@\text{PDA}-\text{MoS}_2$  was lower than that of the other two materials, this value was larger than most of the reported magnetic composites ( $28.7\text{--}52.0 \text{ emu/g}$ ) [20–22], thus could meet the requirement for its practical application. Note that there were no hysteresis loops in the magnetization curve, demonstrating the superparamagnetism of  $\text{Fe}_3\text{O}_4@\text{PDA}-\text{MoS}_2$  nanospheres. Thanks to the high saturated magnetization as well



as the superparamagnetism, the magnetic nanocomposites were prone to be attracted together and separated by a nearby magnet within a few seconds, as illustrated in the inset photographs. Once the magnet was removed, the magnetic nanocomposites could be redispersed well in aqueous solutions, guaranteeing the nanocomposites economic and reusable properties for practical applications.

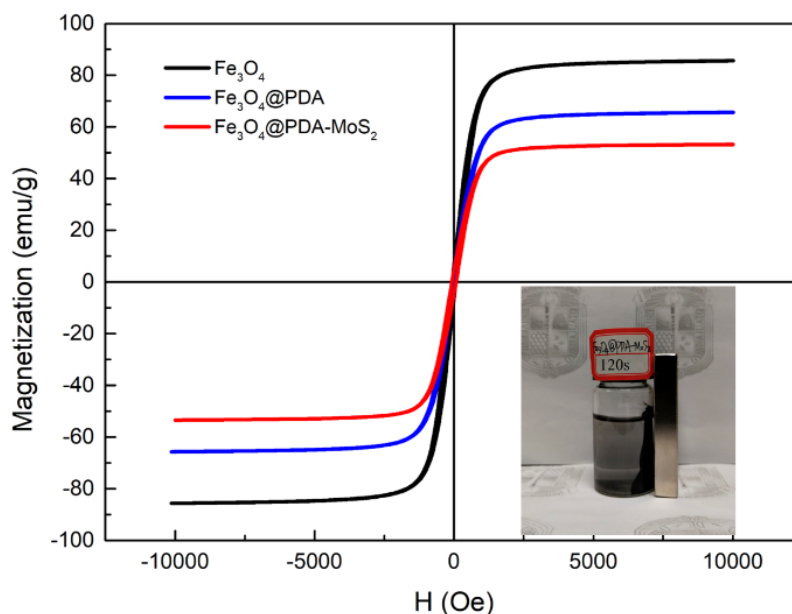


Fig. 8.6. Magnetic hysteresis loop of the original Fe<sub>3</sub>O<sub>4</sub>, Fe<sub>3</sub>O<sub>4</sub>@PDA and Fe<sub>3</sub>O<sub>4</sub>@PDA-MoS<sub>2</sub> nanospheres. (Inset photographs illustrated the magnetic separability of Fe<sub>3</sub>O<sub>4</sub>@PDA-MoS<sub>2</sub> nanospheres from aqueous solution in 120 s.)

### 8.3.2. Stability of adsorbents

The stability of Fe<sub>3</sub>O<sub>4</sub>@PDA-MoS<sub>2</sub> nanospheres played a critical role in its practical applications, considering that the regeneration of adsorbents was carried out efficiently and easily by exchanging the adsorbed metal ions with H<sup>+</sup> in concentrated acid aqueous solution. This work had detected the stability of Fe<sub>3</sub>O<sub>4</sub>@PDA-MoS<sub>2</sub> nanospheres in acid solution with extremely low pH. As shown in Fig. 8.7, even being entirely soaked after 72 h in 0.01 mol/L HNO<sub>3</sub> (pH~2.0), the mass loss of the Fe<sub>3</sub>O<sub>4</sub>@PDA-MoS<sub>2</sub> nanospheres came to a negligible level of 4.34%. In contrast, Fe<sub>3</sub>O<sub>4</sub>@MoS<sub>2</sub> without the PDA coating (The XRD pattern was given in Fig. 8.8) showed a high mass loss ratio of around 35.00%, demonstrating its instability of regeneration by general acid treatment.

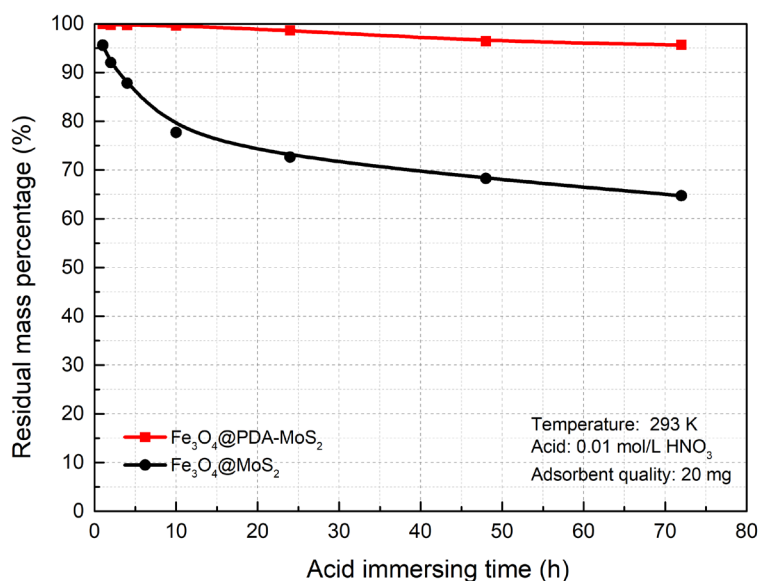


Fig. 8.7. Stability test of Fe<sub>3</sub>O<sub>4</sub>@MoS<sub>2</sub> and Fe<sub>3</sub>O<sub>4</sub>@PDA-MoS<sub>2</sub> nanospheres in strong acid solution.

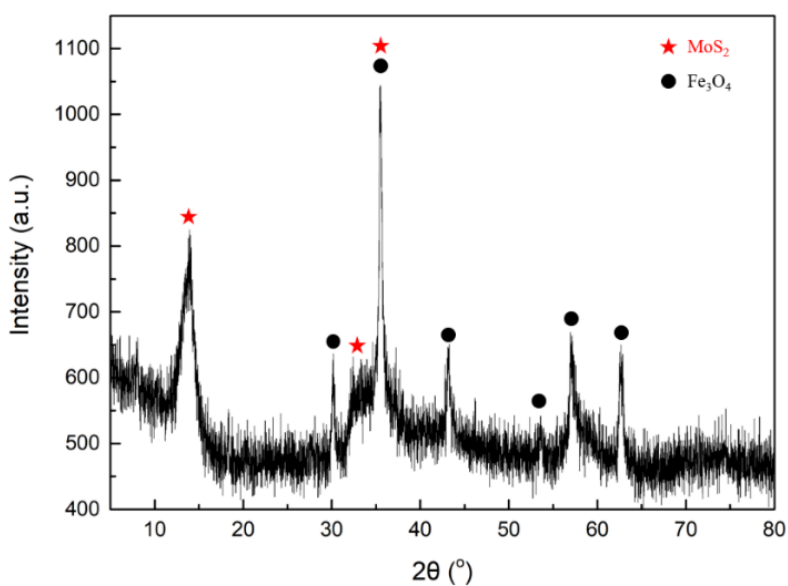


Fig. 8.8. XRD pattern of Fe<sub>3</sub>O<sub>4</sub>@MoS<sub>2</sub>.

Despite there was a tight PDA coating outside the Fe<sub>3</sub>O<sub>4</sub> nanosphere, there remained the speculations for H<sup>+</sup> to get access to core Fe<sub>3</sub>O<sub>4</sub> as time prolonged enough, considering the existence of pores in the polymers and the tiny sizes of H<sup>+</sup>. Thereby, the concentration of Fe<sup>2+</sup>/Fe<sup>3+</sup> in the supernatant solutions after extraction of the Fe<sub>3</sub>O<sub>4</sub>@PDA-MoS<sub>2</sub> nanospheres were further measured and the results were given in Table 8.2. According to Table 8.2, after being entirely immersed for 72 h, Fe<sub>3</sub>O<sub>4</sub>@PDA-MoS<sub>2</sub> nanospheres showed a leakage of Fe<sup>3+</sup>/Fe<sup>2+</sup> into the solution of only 2.09% (w/w), while Fe<sub>3</sub>O<sub>4</sub>@MoS<sub>2</sub> nanospheres showed a much higher one of

16.88% (w/w), further confirming the long-term stability of the Fe<sub>3</sub>O<sub>4</sub>@PDA-MoS<sub>2</sub> nanospheres under the strong acid condition.

Table 8.2. The Fe<sup>3+</sup>/Fe<sup>2+</sup> leakage of Fe<sub>3</sub>O<sub>4</sub>@MoS<sub>2</sub> and Fe<sub>3</sub>O<sub>4</sub>@PDA-MoS<sub>2</sub> nanospheres in acid solutions (pH=1.98).

| Samples  | Immersing time (h)                    | 1     | 2      | 4      | 7      | 24     | 48     | 72     |
|--|---------------------------------------|-------|--------|--------|--------|--------|--------|--------|
| Fe <sub>3</sub> O <sub>4</sub> @MoS <sub>2</sub>         | *C <sub>Fe</sub> (mg/L)               | 88.95 | 144.04 | 208.40 | 238.15 | 281.71 | 324.40 | 333.60 |
|  | *W <sub>Fe</sub> /W <sub>s</sub> (%)  | 4.45  | 7.20   | 10.42  | 11.91  | 14.09  | 16.22  | 16.88  |
| Fe <sub>3</sub> O <sub>4</sub> @PDA<br>-MoS <sub>2</sub> | C <sub>Fe</sub> * (mg/L)              | 7.65  | 9.519  | 11.14  | 15.91  | 30.94  | 39.50  | 41.70  |
|  | W <sub>Fe</sub> /W <sub>s</sub> * (%) | 0.33  | 0.48   | 0.56   | 0.80   | 1.55   | 1.98   | 2.09   |

\*C<sub>Fe</sub> - Concentration of Fe<sup>2+</sup>/Fe<sup>3+</sup> in supernatant; \*W<sub>Fe</sub>/W<sub>s</sub> - Mass ratio of lost Fe<sup>2+</sup>/Fe<sup>3+</sup> to sample.

### 8.3.3. Effect of solution pH

The solution pH was a very influential parameter in removal of heavy metal ions because it dominated the species of metal ions present in aqueous solution as well as influenced the surface charge of adsorbents. Shown in Fig. 8.9(a) was the adsorption capacity of Fe<sub>3</sub>O<sub>4</sub>@PDA-MoS<sub>2</sub> nanospheres varied with solution pH. The adsorption capacity increased with the increasing solution pH in range of 1.0-4.0, and then leveled off when solution pH continually increased from 4.0 to 7.0. Lead ions mainly exist as Pb<sup>2+</sup> or Pb(OH)<sup>+</sup> or both in aqueous solutions with pH<6.0, and then formed hydrolysis products when solution pH was over 7.0 [23]. The surface potential of Fe<sub>3</sub>O<sub>4</sub>@PDA-MoS<sub>2</sub> nanospheres varied with pH was shown in Fig. 8.9(b), in which the surfaces of Fe<sub>3</sub>O<sub>4</sub>@PDA-MoS<sub>2</sub> nanospheres were negatively charged during the whole pH range, and the surface of Fe<sub>3</sub>O<sub>4</sub>@PDA-MoS<sub>2</sub> nanospheres became more negatively charged as the pH increased. Accordingly, the low Pb<sup>2+</sup> ions uptake at low solution pH mainly derived from the competition between Pb<sup>2+</sup> and concentrated H<sup>+</sup> for binding sites [3]. While the pH increased to around 4.0, both the decreased competition between Pb<sup>2+</sup> and H<sup>+</sup> and the increased electrostatic attraction between Pb<sup>2+</sup> and the surface of nanocomposites might be responsible for the great improvement of Pb<sup>2+</sup> adsorption on the surface of Fe<sub>3</sub>O<sub>4</sub>@PDA-MoS<sub>2</sub> nanospheres. With solution pH sequentially increasing from 4.0 to 7.0, the electrostatic attraction between the saturated surface and Pb<sup>2+</sup> were no longer strong for immobilizing more Pb<sup>2+</sup> despite the surface of Fe<sub>3</sub>O<sub>4</sub>@PDA-MoS<sub>2</sub> core-shell nanospheres turned more and more negative, leading to minimum increases in adsorption. It should be noted that the two curves illustrated similar tendency as the pure MoS<sub>2</sub> did in our previous

works [9], which might derive from the special architecture of  $\text{Fe}_3\text{O}_4@\text{PDA}-\text{MoS}_2$  core-shell nanospheres that the nanoscale  $\text{MoS}_2$  was covered on the whole outside surface of  $\text{Fe}_3\text{O}_4@\text{PDA}$ .

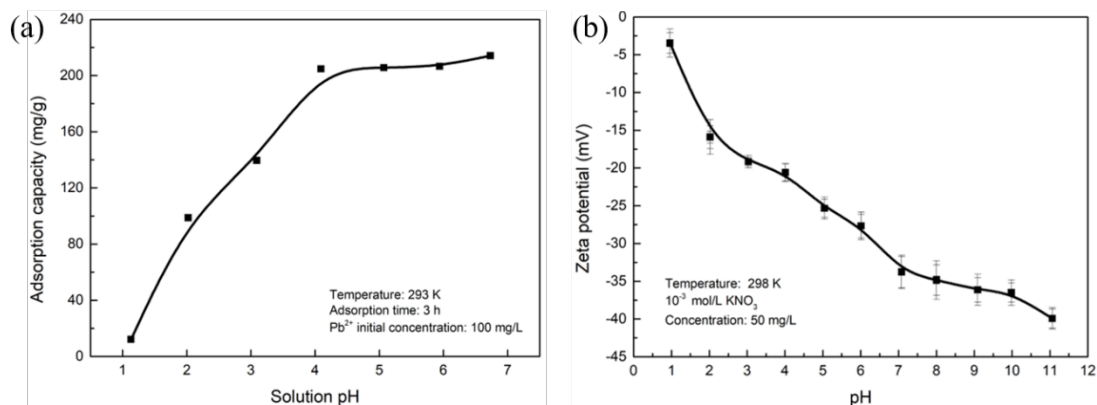


Fig. 8.9. (a) Effect of solution pH on  $\text{Pb}^{2+}$  adsorption with  $\text{Fe}_3\text{O}_4@\text{PDA}-\text{MoS}_2$  nanospheres. (b) Zeta potential of  $\text{Fe}_3\text{O}_4@\text{PDA}-\text{MoS}_2$  nanospheres.

### 8.3.4. Adsorption kinetics and isotherms

It was of great significance to study the adsorption kinetics and isotherms for a better understanding of adsorption process.

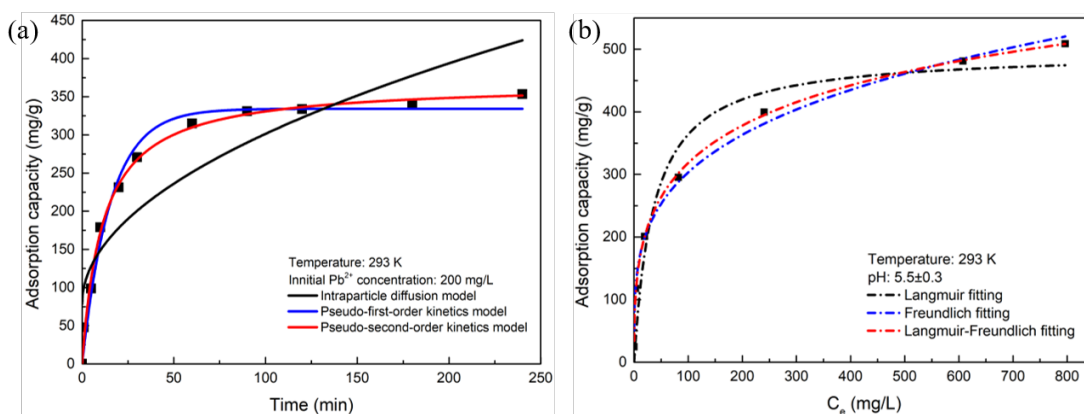


Fig. 8.10. (a) Adsorption kinetic of  $\text{Pb}^{2+}$  on  $\text{Fe}_3\text{O}_4@\text{PDA}-\text{MoS}_2$  nanospheres and the fitting results, (b) Adsorption isotherm of  $\text{Pb}^{2+}$  on  $\text{Fe}_3\text{O}_4@\text{PDA}-\text{MoS}_2$  nanospheres and the fitting results.

The results of the time-dependent adsorption experiments were given in Fig. 8.10(a), in which the adsorption equilibrium reached at approximately 60 min at 293 K with a high initial  $\text{Pb}^{2+}$  concentration of 200 mg/L, demonstrating a fast adsorption process of  $\text{Pb}^{2+}$  on  $\text{Fe}_3\text{O}_4@\text{PDA}-\text{MoS}_2$  core-shell nanospheres. In order to further analyze the adsorption process, the experimental data was fitted with the three

generally used kinetic models: the pseudo-first-order kinetic (Eq. 8.2), pseudo-second-order kinetic (Eq. 8.3 and intraparticle diffusion model (Eq. 8.4):[24,25]

$$Q_t = Q_e \times (1 - e^{-K_1 \times t}) \quad 8.2$$

$$Q_t = t / (t/Q_e + 1/(K_2 \times Q_e^2)) \quad 8.3$$

$$Q_t = K_3 \times t^{0.5} + C \quad 8.4$$

where  $Q_e$  (mg/g) and  $Q_t$  (mg/g) were the adsorption capacity at equilibrium time and at time  $t$  (min), respectively.  $K_1$  (/min),  $K_2$  (g/(mg min)) and  $K_3$  (mg/(g·min<sup>0.5</sup>)) were the rate constants of the pseudo-first-order kinetics, pseudo-second-order kinetics, and intraparticle diffusion model, respectively;  $C$  (mg/L) represented the thickness of the boundary layer [8].

According to the fitting results as given in Table S8.3, it could be concluded that the adsorption of  $Pb^{2+}$  on  $Fe_3O_4@PDA-MoS_2$  nanospheres followed the pseudo-second-order kinetics due to its highest fitting coefficient of 0.995 to the experimental data. As a consequence, the overall adsorption process of  $Pb^{2+}$  on  $Fe_3O_4@PDA-MoS_2$  nanospheres might be involved with a chemical process, in view of the assumption that the pseudo second-order kinetic model was a rate limiting step governed by the sharing or exchange of electrons between sorbent and sorbate [8]. What is more, the rate constant of the pseudo-second-order reached a high level of 2.4076 g/mg·min, which was much higher than that of graphene oxide (0.269-0.274 g/mg·min) and titanite/ $Fe_3O_4$  nanocomposites (1.48 g/mg·min) [3,26], demonstrating a fast adsorption process of  $Pb^{2+}$  on  $Fe_3O_4@PDA-MoS_2$  nanospheres.

Table 8.3. Parameters of the pseudo-first-kinetic, pseudo-second-kinetic and intraparticle diffusion models for  $Pb^{2+}$  adsorption on  $Fe_3O_4@PDA-MoS_2$  at 293 K.

| Pseudo-first-order kinetic model |          |        | Pseudo-second-order kinetic model |          |        | Intraparticle diffusion model |        |        |
|----------------------------------|----------|--------|-----------------------------------|----------|--------|-------------------------------|--------|--------|
| $K_1$                            | $Q_e$    | $R^2$  | $K_2$                             | $Q_e$    | $R^2$  | $K_3$                         | $C$    | $R^2$  |
| (/min)                           | (mg/g)   |        | (g/mg·min)                        | (mg/g)   |        | (g/mg·min <sup>0.5</sup> )    | (mg/L) |        |
| 0.0649                           | 334.2312 | 0.9858 | 2.4076                            | 368.1225 | 0.9953 | 22.3038                       | 78.365 | 0.7905 |

As shown in Fig. 8.10(b), the adsorbate distribution between the liquid phase and solid phase when the  $Pb^{2+}$  uptake had reached equilibrium at 293 K was assessed. The

Langmuir, Freundlich and Langmuir-Freundlich models (which was also called as Koble–Corrigan model [27]) were considered for the studies, of which the expressions could be written as Eqs. 8.5-8.7, respectively:

$$Q_e = \frac{Q_{max} \times K_L \times C_e}{1 + K_L \times C_e} \quad 8.5$$

$$Q_e = K_F \times C_e^{1/n} \quad 8.6$$

$$Q_e = \frac{Q_{max} \times K_{LF} \times C_e^{1/n}}{1 + K_{LF} \times C_e^{1/n}} \quad 8.7$$

where  $C_e$  (mg/L) was the equilibrium concentration of  $Pb^{2+}$  in aqueous solution,  $Q_{max}$  (mg/g) was the maximum adsorption capacity.  $K_L$ ,  $K_F$  and  $K_{LF}$  were the Langmuir adsorption constant, the Freundlich adsorption constant and the Langmuir-Freundlich adsorption constant, respectively. In addition,  $1/n$  was Freundlich constants related to the adsorption intensity.

The fitting results of different isotherm models were given in Table 8.4, in which the experimental data followed well with the Langmuir-Freundlich model most exactly because of the highest fitting coefficient of 0.998, demonstrating the surface heterogeneity of  $Fe_3O_4@PDA-MoS_2$  nanospheres based on the corresponding theoretical models [8,28]. The surface heterogeneity of  $Fe_3O_4@PDA-MoS_2$  nanospheres might mainly derive from special flower-like architecture of nanoscale  $MoS_2$  as well as the functional groups (such as the unsaturated sulfur atoms or the bridging  $S_2^{2-}$  [29]) on the surface [30]. Moreover,  $1/n$  was smaller than 1, indicating the favorable adsorption of  $Pb^{2+}$  on  $Fe_3O_4@PDA-MoS_2$  nanospheres.

Table 8.4. Langmuir, Freundlich and Langmuir-Freundlich isotherms parameters for  $Pb^{2+}$  adsorption on  $Fe_3O_4@PDA-MoS_2$  nanospheres at 293 K.

| Langmuir model      |                 |       | Freundlich model |                 |       | Langmuir-Freundlich model |                   |       |       |
|---------------------|-----------------|-------|------------------|-----------------|-------|---------------------------|-------------------|-------|-------|
| $Q_{max}$<br>(mg/g) | $K_L$<br>(L/mg) | $R^2$ | $1/n$            | $K_F$<br>(mg/g) | $R^2$ | $Q_{max}$<br>(mg/g)       | $K_{FL}$<br>(L/g) | $1/n$ | $R^2$ |
| 495.973             | 0.028           | 0.927 | 0.260            | 91.591          | 0.993 | 1028.087                  | 0.079             | 0.376 | 0.998 |

Note that the experimental adsorption capacity of  $Pb^{2+}$  on  $Fe_3O_4@PDA-MoS_2$  nanospheres at 293 K was around 508.9 mg/g, which is significantly higher than most of the recently reported adsorbents as shown in Table 8.5, although it did not come to its theoretical value of 1028.087 mg/g. Moreover, compared to some other

MoS<sub>2</sub>/Fe<sub>3</sub>O<sub>4</sub> compositions with different architectures, Fe<sub>3</sub>O<sub>4</sub>@PDA-MoS<sub>2</sub> nanospheres exhibited a such high adsorption capacity mainly due to the fact that the specific surface area of the in-situ grown MoS<sub>2</sub> on Fe<sub>3</sub>O<sub>4</sub>@PDA nanospheres had been substantially increased, and little occupation of binding sites for heavy metal ions on the surfaces of MoS<sub>2</sub>.

Table 8.5. Comparison of adsorption performances of Pb<sup>2+</sup> by various adsorbents.

| Adsorbents   | Conditions       | Maximum adsorption capacity (mg/g) | Refs      |
|--|------------------|------------------------------------|-----------|
| Powdered Active Carbon   | pH 5.0, T 303 K  | 26.9                               | [31]      |
| Celtek Clay  | pH 6.0, T 293 K  | 18.08                              | [32]      |
| EDTA-Graphene Oxide  | pH 6.8, T 298 K  | 479                                | [33]      |
| Graphene Oxide   | pH 5.5, T 298 K  | 125                                | [34]      |
| Biochar-rGO  | pH 6.0, T 298 K  | 26.10                              | [35]      |
| MoS <sub>2</sub> -Fe <sub>3</sub> O <sub>4</sub> Nanosheets      | pH 6.0           | 9.6                                | [14]      |
| Fe <sub>3</sub> O <sub>4</sub> /MoS <sub>2</sub> Nanohybrid      | pH 6.5           | 46.51                              | [15]      |
| Fe <sub>3</sub> O <sub>4</sub> @PDA-MoS <sub>2</sub> Nanospheres | pH ~5.5, T 293 K | 508.9                              | This work |

### 8.3.5. Adsorption thermodynamics and mechanisms

For the further investigation of adsorption mechanism, the experimental adsorption data of Pb<sup>2+</sup> on Fe<sub>3</sub>O<sub>4</sub>@PDA-MoS<sub>2</sub> nanospheres at 293, 303 and 313 K were fitted to the Langmuir-Freundlich isotherms, of which the results were shown in Fig. 8.11 and Table 8.6. The results further confirmed the experimental data at different adsorption temperature fitted well with Langmuir-Freundlich model with high correlations over 0.995. Subsequently, these experimental data from the batch adsorption experiment were analyzed using enthalpy change ( $\Delta H_0$ ), entropy change ( $\Delta S_0$ ) and Gibbs free energy change ( $\Delta G_0$ ), which could be determined by below Eq. 8.8 and Eq. 8.9:

$$\Delta G_0 = -RT \ln(K_0) \quad 8.8$$

$$\ln(K_0) = \Delta S_0/R - \Delta H_0/RT \quad 8.9$$

where  $K_0$  at different temperatures was determined by plotting  $\ln(Q_e/C_e)$  versus  $Q_e$  (Seen in Fig. 8.12) and extrapolating  $Q_e$  to zero [36], and the parameters at different temperature were given in Table 8.7.  $T$  (K) was the system temperature, and  $R$  (8.314 J/mol·K) was the universal gas constant.

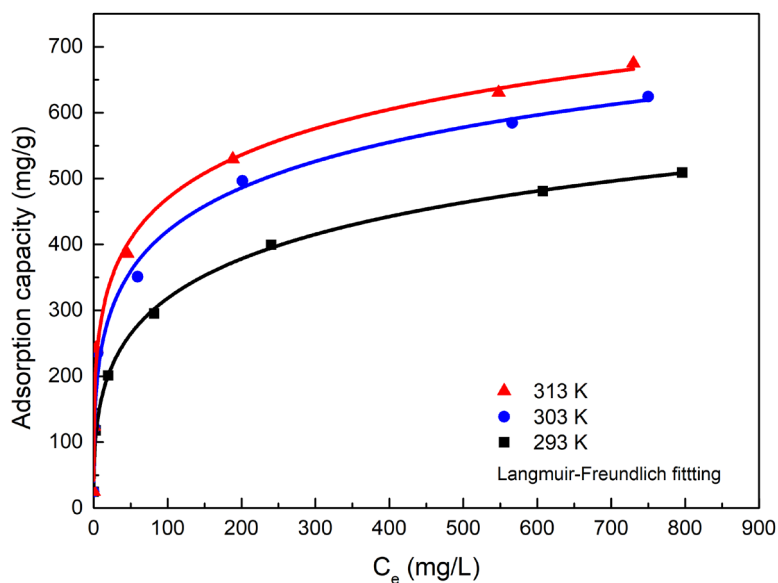


Fig. 8.11. Fitting results of Langmuir-Freundlich models for  $\text{Pb}^{2+}$  on  $\text{Fe}_3\text{O}_4@\text{PDA-MoS}_2$  nanospheres at 293 K, 303 K and 313 K.

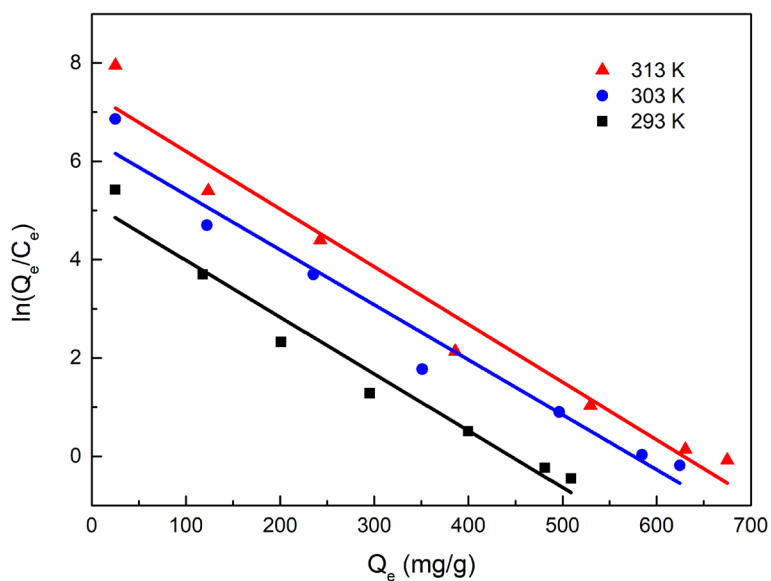


Fig. 8.12. Plots of  $\ln(Q_e/C_e)$  versus  $Q_e$  at various temperatures.

Table 8.6. Fitting results of  $\text{Pb}^{2+}$  on  $\text{Fe}_3\text{O}_4@\text{PDA-MoS}_2$  nanospheres at 293 K, 303 K and 313 K by Langmuir-Freundlich isotherm model

| Temperature (K) | Langmuir-Freundlich model |                |       |       |
|-----------------|---------------------------|----------------|-------|-------|
|                 | $Q_{max}$ (mg/g)          | $K_{FL}$ (L/g) | $1/n$ | $R^2$ |
| 293             | 735.27                    | 0.043          | 0.66  | 0.997 |
| 303             | 742.84                    | 0.046          | 0.72  | 0.995 |
| 313             | 759.38                    | 0.055          | 0.77  | 0.998 |



Table 8.7. Distribution coefficient ( $K_{\theta}$ ) values calculated for the adsorption of  $\text{Pb}^{2+}$  on  $\text{Fe}_3\text{O}_4@\text{PDA-MoS}_2$  nanospheres at different temperatures.

| Temperature | $K_{\theta}$ | $\ln K_{\theta}$ |
|-------------|--------------|------------------|
| 293 K       | 5.14         | 1.637            |
| 303 K       | 6.44         | 1.863            |
| 313 K       | 7.38         | 1.999            |

According to Eq (9),  $\Delta H_{\theta}$  and  $\Delta S_{\theta}$  could be calculated from the Van't Hoff equation by plotting  $\ln K_{\theta}$  versus  $1/T$ , and the results were shown in Fig. 8.13 and Table 8.8. A linear relationship with high correlation in the range of chosen temperature was found, demonstrating the correction of the Van't Hoff type equation for the evaluation of the thermodynamic parameters for the adsorption. Thereby, the values of  $\Delta G_{\theta}$ ,  $\Delta H_{\theta}$  and  $\Delta S_{\theta}$  were given in Table 8.9. The negative values of  $\Delta G_{\theta}$  and positive values of  $\Delta H_{\theta}$  demonstrated the adsorption of  $\text{Pb}^{2+}$  on  $\text{Fe}_3\text{O}_4@\text{PDA-MoS}_2$  nanospheres was spontaneous and endothermic. Namely, higher temperature was favorable for the adsorption of  $\text{Pb}^{2+}$  on  $\text{Fe}_3\text{O}_4@\text{PDA-MoS}_2$  nanospheres. It should be pointed out that the values of  $\Delta G_{\theta}$  ranged from -3.990 to -5.209 kJ/mol, which was below -20 kJ/mol, indicating a physical process was also involved in the immobilization of  $\text{Pb}^{2+}$  on  $\text{Fe}_3\text{O}_4@\text{PDA-MoS}_2$  nanospheres [32]. The  $\Delta S_{\theta}$  reached a positive value of 60.89 J/mol K, revealing the decreasing orderliness at the solid/liquid interface during the immobilization of  $\text{Pb}^{2+}$  on  $\text{Fe}_3\text{O}_4@\text{PDA-MoS}_2$  nanospheres [37].

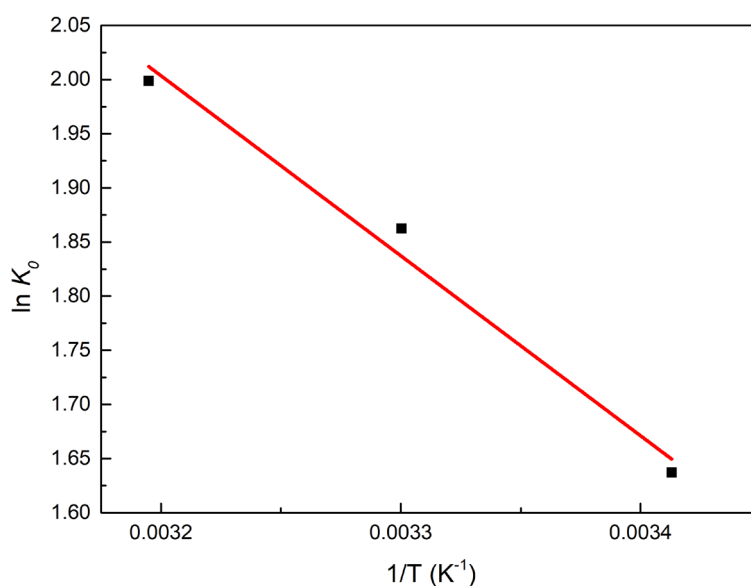


Fig. 8.13. Van't Hoff plot for  $\text{Pb}^{2+}$  on  $\text{Fe}_3\text{O}_4@\text{PDA-MoS}_2$  nanospheres.

Table 8.8. Parameters of Van't Hoff plot for  $\text{Pb}^{2+}$  on  $\text{Fe}_3\text{O}_4@\text{PDA}-\text{MoS}_2$  nanospheres.

| Parameters | Intercept | Slope    | $R^2$ |
|------------|-----------|----------|-------|
| Value      | 7.324     | -1662.55 | 0.970 |

Table 8.9. Thermodynamic constants for the adsorption of  $\text{Pb}^{2+}$  on  $\text{Fe}_3\text{O}_4@\text{PDA}-\text{MoS}_2$  nanospheres.

| Temperature (K) | $\Delta G_0$ (kJ/mol) | $\Delta H_0$ (kJ/mol) | $\Delta S_0$ (J/mol K) |
|-----------------|-----------------------|-----------------------|------------------------|
| 293             | -3.990                |                       |                        |
| 303             | -4.699                | +13.82                | +60.89                 |
| 313             | -5.209                |                       |                        |

Based on the results above as well as our previous works [8,38–40], the main mechanisms involved in the adsorption of  $\text{Pb}^{2+}$  on  $\text{Fe}_3\text{O}_4@\text{PDA}-\text{MoS}_2$  nanospheres might be: (1) ion exchange, which was assigned to the electrostatic nature of  $\text{Fe}_3\text{O}_4@\text{PDA}-\text{MoS}_2$  nanospheres, and (2) surface complexation, which derived from the soft and soft interaction between the sulfide planes of  $\text{MoS}_2$  and  $\text{Pb}^{2+}$ .

### 8.3.6. Cyclic stability and reusability

A promising and outstanding adsorbent should possess not only easy regeneration but also high regeneration capability. Due to the obviously declined adsorption capacity at low pH values and its long-term stability in acid solution,  $\text{Fe}_3\text{O}_4@\text{PDA}-\text{MoS}_2$  nanospheres could be regenerated by the general acid treatment. As shown in Fig. 8.14, compared to its adsorption capacity for first cycle, no obvious decrease of adsorption capacity of  $\text{Fe}_3\text{O}_4@\text{PDA}-\text{MoS}_2$  nanospheres was found even after ten cycles of regeneration and reuse, which further confirmed its good cyclic stability and demonstrated its reusability of practical application in removal of heavy metal ions. It also should be pointed out the strong surface complexation between  $\text{Pb}^{2+}$  and  $\text{MoS}_2$  might account for the tiny decrease of adsorption capacity for the reused adsorbents compared to the original adsorption capacity, and the ion exchange took the most significant part during the immobilization of  $\text{Pb}^{2+}$ .

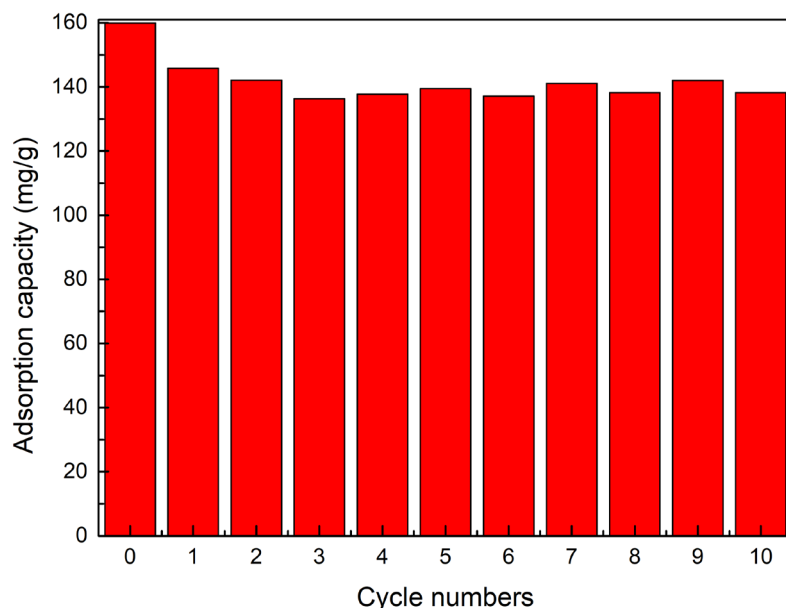


Fig. 8.14. Adsorption capacity of  $\text{Fe}_3\text{O}_4@\text{PDA-MoS}_2$  nanospheres in ten cycles of regeneration.

## 8.4. Conclusions

(1)  $\text{Fe}_3\text{O}_4@\text{PDA-MoS}_2$  nanocomposites with special nanosphere-architecture could be successfully prepared by in situ growth of  $\text{MoS}_2$  on the surface of  $\text{F}_3\text{O}_4@\text{PDA}$  nanospheres.

(2) The superparamagnetic properties of  $\text{F}_3\text{O}_4@\text{PDA-MoS}_2$  nanospheres guaranteed the nanocomposites being readily recycled by an external magnetic field.

(3) The existence of PDA coating outside  $\text{Fe}_3\text{O}_4$  nanospheres could not only significantly improve the specific surface area of  $\text{MoS}_2$  but also ensure the stability of the nanocomposites.

(4) Detailed adsorption study demonstrated  $\text{F}_3\text{O}_4@\text{PDA-MoS}_2$  nanospheres an outstanding adsorbent towards  $\text{Pb}^{2+}$ , and the experimental data followed well with the pseudo-second-order kinetic model and Langmuir-Freundlich isotherm, respectively. The adsorption of  $\text{Pb}^{2+}$  on  $\text{F}_3\text{O}_4@\text{PDA-MoS}_2$  nanospheres belonged to a spontaneous and endothermic process.

## REFERENCES

- [1] H. Li, J. Li, C. Xu, P. Yang, D.H.L. Ng, P. Song, M. Zuo, Hierarchically porous  $\text{MoS}_2/\text{CoAl-LDH/HCF}$  with synergistic adsorption-photocatalytic performance under visible light irradiation, *Journal of Alloys and Compounds*. 698 (2017) 852–862. doi:10.1016/j.jallcom.2016.12.310.
- [2] S.T. Akar, S. Arslan, T. Alp, D. Arslan, T. Akar, Biosorption potential of the waste

- biomaterial obtained from *Cucumis melo* for the removal of  $Pb^{2+}$  ions from aqueous media: Equilibrium, kinetic, thermodynamic and mechanism analysis, *Chemical Engineering Journal*. 185 (2012) 82–90. doi:10.1016/j.cej.2012.01.032.
- [3] W. Peng, H. Li, Y. Liu, S. Song, A review on heavy metal ions adsorption from water by graphene oxide and its composites, *Journal of Molecular Liquids*. 230 (2017) 496–504. doi:10.1016/j.molliq.2017.01.064.
- [4] M.K. Uddin, A review on the adsorption of heavy metals by clay minerals, with special focus on the past decade, *Chemical Engineering Journal*. 308 (2017) 438–462. doi:10.1016/j.cej.2016.09.029.
- [5] A.E. Burakov, E. V. Galunin, I. V. Burakova, A.E. Kucherova, S. Agarwal, A.G. Tkachev, V.K. Gupta, Adsorption of heavy metals on conventional and nanostructured materials for wastewater treatment purposes: A review, *Ecotoxicology and Environmental Safety*. 148 (2018) 702–712. doi:10.1016/j.ecoenv.2017.11.034.
- [6] Z. Cai, A.D. Dwivedi, W.N. Lee, X. Zhao, W. Liu, M. Sillanpää, D. Zhao, C.H. Huang, J. Fu, Application of nanotechnologies for removing pharmaceutically active compounds from water: Development and future trends, *Environmental Science: Nano*. 5 (2018) 27–47. doi:10.1039/c7en00644f.
- [7] Z. Wang, B. Mi, Environmental Applications of 2D Molybdenum Disulfide ( $MoS_2$ ) Nanosheets, *Environmental Science and Technology*. 51 (2017) 8229–8244. doi:10.1021/acs.est.7b01466.
- [8] Q. Wang, L. Yang, F. Jia, Y. Li, S. Song, Removal of Cd (II) from water by using nano-scale molybdenum disulphide sheets as adsorbents, *Journal of Molecular Liquids*. 263 (2018) 526–533. doi:10.1016/j.molliq.2018.04.149.
- [9] F. Jia, Q. Wang, J. Wu, Y. Li, S. Song, Two-Dimensional Molybdenum Disulfide as a Superb Adsorbent for Removing  $Hg^{2+}$  from Water, *ACS Sustainable Chemistry & Engineering*. 5 (2017) 7410–7419. doi:10.1021/acssuschemeng.7b01880.
- [10] K. Ai, C. Ruan, M. Shen, L. Lu,  $MoS_2$  Nanosheets with Widened Interlayer Spacing for High-Efficiency Removal of Mercury in Aquatic Systems, *Advanced Functional Materials*. 26 (2016) 5542–5549. doi:10.1002/adfm.201601338.
- [11] Y. Gao, C. Chen, X. Tan, H. Xu, K. Zhu, Polyaniline-modified 3D-flower-like molybdenum disulfide composite for efficient adsorption/photocatalytic reduction of Cr(VI), *Journal of Colloid and Interface Science*. 476 (2016) 62–70. doi:10.1016/j.jcis.2016.05.022.
- [12] C.-B. Ma, Y. Du, B. Du, H. Wang, E. Wang, Investigation of an eco-friendly aerogel as a substrate for the immobilization of  $MoS_2$  nanoflowers for removal of mercury species

- from aqueous solutions, *Journal of Colloid and Interface Science*. 525 (2018) 251–259. doi:10.1016/j.jcis.2018.04.079.
- [13] N. Baghban, E. Yilmaz, M. Soyak, Nanodiamond/MoS<sub>2</sub> nanorod composite as a novel sorbent for fast and effective vortex-assisted micro solid phase extraction of lead(II) and copper(II) for their flame atomic absorption spectrometric detection, *Journal of Molecular Liquids*. 234 (2017) 260–267. doi:10.1016/j.molliq.2017.03.079.
- [14] N. Baghban, E. Yilmaz, M. Soyak, A magnetic MoS<sub>2</sub>-Fe<sub>3</sub>O<sub>4</sub> nanocomposite as an effective adsorbent for dispersive solid-phase microextraction of lead(II) and copper(II) prior to their determination by FAAS, *Microchimica Acta*. 184 (2017) 3969–3976. doi:10.1007/s00604-017-2384-z.
- [15] M.J. Aghagoli, M.H. Beyki, F. Shemirani, Facile synthesis of Fe<sub>3</sub>O<sub>4</sub>/MoS<sub>2</sub> nanohybrid for solid phase extraction of Ag(I) and Pb(II): kinetic, isotherm and thermodynamic studies, *International Journal of Environmental Analytical Chemistry*. 97 (2017) 1328–1351. doi:10.1080/03067319.2017.1414204.
- [16] Y. Song, M. Lu, B. Huang, D. Wang, G. Wang, L. Zhou, Decoration of defective MoS<sub>2</sub> nanosheets with Fe<sub>3</sub>O<sub>4</sub> nanoparticles as superior magnetic adsorbent for highly selective and efficient mercury ions(Hg<sup>2+</sup>) removal, *Journal of Alloys and Compounds*. 737 (2018) 113–121. doi:10.1016/j.jallcom.2017.12.087.
- [17] Y. Liu, K. Ai, L. Lu, Polydopamine and its derivative materials: Synthesis and promising applications in energy, environmental, and biomedical fields, *Chemical Reviews*. 114 (2014) 5057–5115. doi:10.1021/cr400407a.
- [18] H. Deng, X. Li, Q. Peng, X. Wang, J. Chen, Y. Li, Monodisperse magnetic single-crystal ferrite microspheres, *Angewandte Chemie - International Edition*. 44 (2005) 2782–2785. doi:10.1002/anie.200462551.
- [19] H.-P. Peng, R.-P. Liang, L. Zhang, J.-D. Qiu, Facile preparation of novel core-shell enzyme-Au-polydopamine-Fe<sub>3</sub>O<sub>4</sub> magnetic bionanoparticles for glucosesensor, *Biosensors and Bioelectronics*. 42 (2013) 293–299. doi:10.1016/j.bios.2012.10.074.
- [20] Y. Xie, B. Yan, H. Xu, J. Chen, Q. Liu, Y. Deng, H. Zeng, Highly regenerable mussel-inspired Fe<sub>3</sub>O<sub>4</sub>@Polydopamine-Ag core-shell microspheres as catalyst and adsorbent for methylene blue removal, *ACS Applied Materials and Interfaces*. 6 (2014) 8845–8852. doi:10.1021/am501632f.
- [21] Q. Fang, S. Duan, J. Zhang, J. Li, K.C.F. Leung, Dual shelled Fe<sub>3</sub>O<sub>4</sub>/polydopamine hollow microspheres as an effective Eu(III) adsorbent, *Journal of Materials Chemistry A*. 5 (2017) 2947–2958. doi:10.1039/c6ta09968h.
- [22] S. Zhang, Y. Zhang, G. Bi, J. Liu, Z. Wang, Q. Xu, H. Xu, X. Li, Mussel-inspired

- polydopamine biopolymer decorated with magnetic nanoparticles for multiple pollutants removal, *Journal of Hazardous Materials*. 270 (2014) 27–34. doi:10.1016/j.jhazmat.2014.01.039.
- [23] D.H.K. Reddy, K. Seshaiiah, A.V.R. Reddy, M.M. Rao, M.C. Wang, Biosorption of Pb<sup>2+</sup> from aqueous solutions by *Moringa oleifera* bark: Equilibrium and kinetic studies, *Journal of Hazardous Materials*. 174 (2010) 831–838. doi:10.1016/j.jhazmat.2009.09.128.
- [24] Q. Wang, G. Ren, F. Jia, S. Song, Preparation and Characterization of Nanoscale Zero-Valent Iron-Loaded Porous Sepiolite for Decolorizing Methylene Blue in Aqueous Solutions, *JOM*. 69 (2017) 699–703. doi:10.1007/s11837-017-2269-y.
- [25] W. Wang, Y. Zhao, H. Bai, T. Zhang, V. Ibarra-Galvan, S. Song, Methylene blue removal from water using the hydrogel beads of poly(vinyl alcohol)-sodium alginate-chitosan-montmorillonite, *Carbohydrate Polymers*. 198 (2018) 518–528. doi:10.1016/j.carbpol.2018.06.124.
- [26] F. Liu, Y. Jin, H. Liao, L. Cai, M. Tong, Y. Hou, Facile self-assembly synthesis of titanate/Fe<sub>3</sub>O<sub>4</sub> nanocomposites for the efficient removal of Pb<sup>2+</sup> from aqueous systems, *Journal of Materials Chemistry A*. 1 (2013) 805–813. doi:10.1039/c2ta00099g.
- [27] P. Wu, W. Wu, S. Li, N. Xing, N. Zhu, P. Li, J. Wu, C. Yang, Z. Dang, Removal of Cd<sup>2+</sup> from aqueous solution by adsorption using Fe-montmorillonite, *Journal of Hazardous Materials*. 169 (2009) 824–830. doi:10.1016/j.jhazmat.2009.04.022.
- [28] R.J. Umpleby, S.C. Baxter, Y. Chen, R.N. Shah, K.D. Shimizu, Characterization of molecularly imprinted polymers with the Langmuir - Freundlich isotherm, *Analytical Chemistry*. 73 (2001) 4584–4591. doi:10.1021/ac0105686.
- [29] W. Zhang, Z. Li, X. Dai, X. Zhang, Y. Yang, H. Sun, K. Du, Enhanced hydrogen evolution reaction on few-layer MoS<sub>2</sub> nanosheets-coated functionalized carbon nanotubes, *International Journal of Hydrogen Energy*. 40 (2015) 8877–8888. doi:10.1016/j.ijhydene.2015.05.062.
- [30] M. Franz, H.A. Arafat, N.G. Pinto, Effect of chemical surface heterogeneity on the adsorption mechanism of dissolved aromatics on activated carbon, *Carbon*. 38 (2000) 1807–1819. doi:10.1016/S0008-6223(00)00012-9.
- [31] Z. Reddad, C. Gerente, Y. Andres, P. Le Cloirec, Adsorption of Several Metal Ions onto a Low-Cost Biosorbent: Kinetic and Equilibrium Studies, *Environmental Science & Technology*. 36 (2002) 2067–2073. doi:10.1021/es0102989.
- [32] A. Sari, M. Tuzen, M. Soylak, Adsorption of Pb(II) and Cr(III) from aqueous solution on Celtek clay, *Journal of Hazardous Materials*. 144 (2007) 41–46. doi:10.1016/j.jhazmat.2006.09.080.

- [33] C.J. Madadrang, H.Y. Kim, G. Gao, N. Wang, J. Zhu, H. Feng, M. Gorrng, M.L. Kasner, S. Hou, Adsorption behavior of EDTA-graphene oxide for Pb(II) removal, *ACS Applied Materials and Interfaces*. 4 (2012) 1186–1193. doi:10.1021/am201645g.
- [34] X. Huang, M. Pan, The highly efficient adsorption of Pb(II) on graphene oxides: A process combined by batch experiments and modeling techniques, *Journal of Molecular Liquids*. 215 (2016) 410–416. doi:10.1016/j.molliq.2015.12.061.
- [35] Y. Zhang, B. Cao, L. Zhao, L. Sun, Y. Gao, J. Li, F. Yang, Biochar-supported reduced graphene oxide composite for adsorption and coadsorption of atrazine and lead ions, *Applied Surface Science*. 427 (2018) 147–155. doi:10.1016/j.apsusc.2017.07.237.
- [36] H.K. Boparai, M. Joseph, D.M. O’Carroll, Kinetics and thermodynamics of cadmium ion removal by adsorption onto nano zerovalent iron particles, *Journal of Hazardous Materials*. 186 (2011) 458–465. doi:10.1016/j.jhazmat.2010.11.029.
- [37] Y.M. Hao, C. Man, Z.B. Hu, Effective removal of Cu(II) ions from aqueous solution by amino-functionalized magnetic nanoparticles, *Journal of Hazardous Materials*. 184 (2010) 392–399. doi:10.1016/j.jhazmat.2010.08.048.
- [38] F. Jia, C. Liu, B. Yang, S. Song, Applied Surface Science Microscale control of edge defect and oxidation on molybdenum disulfide through thermal treatment in air and nitrogen atmospheres, *Applied Surface Science*. 462 (2018) 471–479. doi:10.1016/j.apsusc.2018.08.166.
- [39] C. Liu, F. Jia, Q. Wang, B. Yang, S. Song, Two-dimensional molybdenum disulfide as adsorbent for high-efficient Pb(II) removal from water, *Applied Materials Today*. 9 (2017) 220–228. doi:10.1016/j.apmt.2017.07.009.
- [40] F. Jia, C. Liu, B. Yang, X. Zhang, H. Yi, J. Ni, S. Song, Thermal Modification of the Molybdenum Disulfide Surface for Tremendous Improvement of Hg<sup>2+</sup> Adsorption from Aqueous Solution, *ACS Sustainable Chemistry & Engineering*. 6 (2018) 9065–9073. doi:10.1021/acssuschemeng.8b01412.

*The main content of this chapter was published as “Journal of Molecular Liquids 282 (2019): 598-605.”.*

## CHAPTER IX

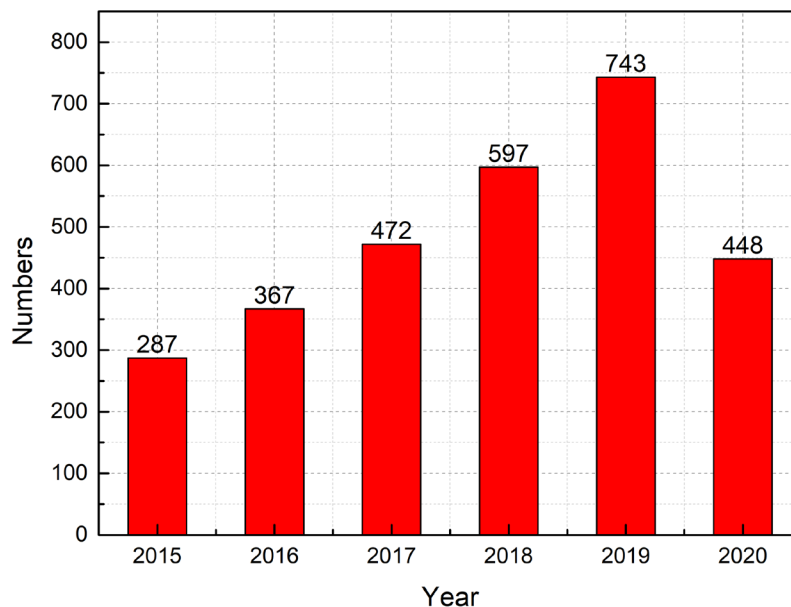
### Conclusions

- (1) With the in-depth study in this work, MoS<sub>2</sub> nanosheets were developed for the desalination and heavy metals removal from water, which might provide one promising solution to alleviate freshwater resources' problem faced by human beings.
- (2) Magnetic MoS<sub>2</sub> nanosheets, prepared by the in-situ growth of nano Fe<sub>3</sub>O<sub>4</sub> on the PDA-functionalized MoS<sub>2</sub> nanosheets, possessed excellent solar-to-heat conversion capacity and excellent recyclability, thereby can be used as photo-absorbers in volumetric evaporation system for high-performance solar steam generation.
- (3) With low cost, facile construction pathway and good mechanical flexibility, the MPU-PPU evaporator with DLS (top layer: MoS<sub>2</sub> nanosheets embed in PU sponge; bottom layer: PU sponge modified by hydrophilic PDA), exhibited high evaporation efficiency and desalination performance, showing a bright application prospect for solar desalination.
- (4) A novel strategy was used to prepare high-quality MoS<sub>2</sub> aerogels. The excellent solar-to-heat conversion, porous networks for vapor escape, good hydrophilicity for continuous water supply and low thermal conductivity for effective heat localization of this MoS<sub>2</sub> aerogel render it an excellent evaporator with excellent solar evaporation efficiency and desalination performance.
- (5) Overcoming the poor water wettability facing MoS<sub>2</sub> nanosheets by the modification of PDA, MoS<sub>2</sub>/PDA-4 nanocomposites exhibited the highest specific capacitance, the lowest inner resistances and excellent electrochemical stability, which greatly enhanced its capacitive deionization performance.
- (6) With high specific area and abundant exposed sulfur atoms on its surface, MoS<sub>2</sub> nanosheets exfoliated from bulk molybdenite have proved to be an outstanding nano-adsorbent with high adsorption capacity of Cd<sup>2+</sup> ions from water.
- (8) Overcoming the difficulty of solid-liquid separation facing nanoscale MoS<sub>2</sub>, Fe<sub>3</sub>O<sub>4</sub>@polydopamine (PDA)-MoS<sub>2</sub> core-shell nanospheres turned out to be an outstanding adsorbent for the removal of Pb<sup>2+</sup> from water, which meet the requirement for its practical applications.
- (9). Generally, due to more effective heat management, using MoS<sub>2</sub> nanosheets in the interfacial solar systems had better evaporation performances than in the volumetric evaporation system.



## CHAPTER X

### Perspectives and future work



Statistics of papers on solar desalination in recent years. (Source: Web of Science (Core Collection); Keywords: Solar desalination or solar steam generation; Date: 2020.06.25)

Due to its aforementioned advantages, solar desalination will become one of the research hotspots in the field of desalination in the next 5-10 years.

However, there are two problems facing the current solar desalination technology: (1) Salt ion crystallization is easy to occur on the surfaces of the evaporator, and the salt bulk can strongly reflect sunlight and block vapor escape channels, severely reducing the continuity and efficiency of the vapor generation process; (2) The latent heat of condensation of the steam is often not used and directly released to the atmosphere through the cover plate, causing energy waste.

In this case, our future work will include: (1) Design and preparation of a salt-resistant evaporator which can automatically overcome the problems of salt precipitation; (2). To build water-energy-environment nexus in the solar desalination process, such as: (a). Attach the latent heat of condensation to the thermoelectric generator to convert it into electrical energy for storage. (b). Store the latent heat of condensation by means of phase-change energy storage materials, and heat the evaporator in the absence of sunlight. (c). Develop salt self-resistant evaporator to treat heavy metal wastewater and other complex sewage.

## APPENDIX

### Publications

#### 1. Articles published in international journals during the Ph.D. studying

- (1) **Qingmiao Wang**, Feifei Jia, Anhua Huang, Yi Qin, Shaoxian Song, Yanmei Li, Mario Alberto Corona Arroyo. "MoS<sub>2</sub>@sponge with Double Layer Structure for High-Efficiency Solar Desalination." *Desalination* (2020). (Impact factor: **6.035**)
- (2) **Qingmiao Wang**, Feifei Jia, Shaoxian Song and Yanmei Li. "Hydrophilic MoS<sub>2</sub>/Polydopamine (PDA) Nanocomposites as The Electrode for Enhanced Capacitive Deionization." *Separation and Purification Technology* (2019): 116298. (Impact Factor: **5.107**)
- (3) **Qingmiao Wang**, Lai Peng, Yuanyu Gong, Feifei Jia, Shaoxian Song, and Yanmei Li. "Mussel-inspired Fe<sub>3</sub>O<sub>4</sub>@ Polydopamine (PDA)-MoS<sub>2</sub> core-shell nanosphere as a promising adsorbent for removal of Pb<sup>2+</sup> from water." *Journal of Molecular Liquids* 282 (2019): 598-605. (Impact Factor: **4.561**)
- (4) **Qingmiao Wang**, Lang Yang, Feifei Jia, Yanmei Li, and Shaoxian Song. "Removal of Cd (II) from water by using nano-scale molybdenum disulphide sheets as adsorbents." *Journal of Molecular Liquids* 263 (2018): 526-533. (Impact Factor: **4.561**)
- (5) Chang, Liu, **Qingmiao Wang**, Feifei Jia, and Shaoxian Song. "Adsorption of heavy metals on molybdenum disulfide in water: A critical review." *Journal of Molecular Liquids* (2019): 111390. (**Co-first author**, Impact Factor: **4.561**)
- (6) Jia, Feifei, Kaige Sun, Bingqiao Yang, Xian Zhang, **Qingmiao Wang**, and Shaoxian Song. "Defect-rich molybdenum disulfide as electrode for enhanced capacitive deionization from water." *Desalination* 446 (2018): 21-30. (Impact Factor: **6.035**)

## **2. Articles to be published in international journals during the Ph.D. studying**

(1) **Qingmiao, Wang**, Yi Qin, Qijing Guo, Feifei Jia, Yanmei Li, Shaoxian Song. "Facile preparation of 3D MoS<sub>2</sub> aerogel for highly efficient solar desalination." Submitted to *ACS Applied Materials&Interfaces*. Current status: **The Second Revision Finished**.

(2) **Qingmiao, Wang**, Yi Qin, Feifei Jia, Shaoxian Song, Yanmei Li. "Recyclable Fe<sub>3</sub>O<sub>4</sub>@Polydopamine (PDA) Nanofluids for Highly Efficient Solar Evaporation." Submitted to *Green energy and Environment*, current status: **Revision Finished**.

(3) **Qingmiao, Wang**, Yi Qin, Feifei Jia, Yanmei Li, Shaoxian Song. "Magnetic MoS<sub>2</sub> Nanosheets as Recyclable Solar-Absorbers for High-performance Solar Steam Generation." Submitted to *Renewable Energy*, current status: **Revision Finished**.

(4) **Qingmiao Wang**, Yi Qin, Feifei Jia, Yanmei Li, Shaoxian Song "One-step Preparation of Solar Absorber with Double Layer Structure for High-Efficiency Solar Desalination". Submitted to "Desalination". Current status: **Under Resubmission**.